



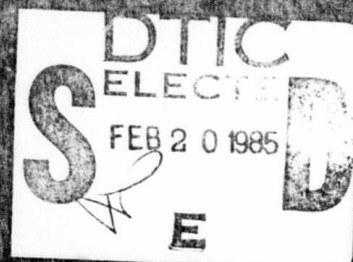
AD-A150 461

FINAL REPORT

LASER HOT SPOT MACHINING

SPONSOR: Defense Advanced Research
Project Agency (DoD)

PRINCIPAL INVESTIGATORS: Michael Bass
Stephen M. Copley



This document has been approved
for public release and sale; its
distribution is unlimited.

FINAL REPORT

LASER HOT SPOT MACHINING

SPONSOR: Defense Advanced Research Project Agency (DoD)
DARPA Order No. 4006
Contract No. MDA 903-80-C-0436
Issued by Department of Army
Defense Supply Service
Washington, DC 20310

CONTRACTOR: University of Southern California
CONTRACT PERIOD: July 1, 1980 - June 30, 1983

PRINCIPAL INVESTIGATORS: Michael Bass
Stephen M. Copley

Accession For	
NTIS GRA&I	<input checked="" type="checkbox"/>
DTIC TAB	<input type="checkbox"/>
Unannounced	<input type="checkbox"/>
Justification	<i>per</i>
By	
Distribution/	
Availability Codes	
Dist	Avail and/or Special
A-1	

DTIC
ELECTE
S **D**
FEB 20 1985
E



APPROVED FOR PUBLIC RELEASE,
DISTRIBUTION IS UNLIMITED (A)

The original "Statement of Work" sent to Major Harry Winsor on April 24, 1980 was modified on the basis of results we obtained through our participation in the DARPA/AFML/GE Advanced Machining Research Program, DARPA Order No. 3770, Contract No. F 33615-79-C-5119. A revised work statement and the reasons for the revisions were presented to Dr. Robert Green in a letter dated July 19, 1982.

The research carried out in this program is described in two dissertations included in Appendices 1 and 2.

R. J. Wallace, "A Study of the Shaping of Hot Pressed Silicon Nitride with a High Power CW Carbon Dioxide Laser," Ph.D. dissertation, University of Southern California (1983).

R.K.C. Hsu, "Shaping Articles by Vaporization with a CO₂ Laser," Ph.D. dissertation, University of Southern California (1984).

Publications based on preliminary results of this research included in previous reports.

S. M. Copley, M. Bass, B. Jau and R. J. Wallace, "Shaping Materials with Lasers" in Laser Materials Processing, M. Bass, Ed., North Holland Publishing Co. (1983).

S. M. Copley, "Laser Shaping of Materials" in Lasers in Materials Processing, F. A. Metzbower, Ed., American Society for Metals, Metals Park (1984).

The following papers are currently being prepared for publication:

R. J. Wallace, M. Bass and S. M. Copley, "Effect of Beam Polarization on the Shape of Grooves in Si₃N₄ Produced by Laser Machining" to be submitted to J. Appl. Phys.

R. J. Wallace and S. M. Copley, "Laser Machining of Si₃N₄: I. Energetics" to be submitted to J. Am. Ceram. Soc.

R. J. Wallace and S. M. Copley, "Laser Machining of Si₃N₄: II. Shaping and Materials Properties" to be submitted to J. Am. Ceram. Soc.

R.K.C. Hsu and S. M. Copley, "Shaping Articles by Vaporization with a CO₂ Laser" to be submitted to Trans. ASME.

Reprints will be sent to the Sponsor as an addendum to this report when they become available.

APPENDIX I

A STUDY OF THE SHAPING OF HOT PRESSED SILICON NITRIDE

WITH A HIGH POWER CW CO₂ LASER

by

Russell John Wallace

A Dissertation Presented to the
FACULTY OF THE GRADUATE SCHOOL
UNIVERSITY OF SOUTHERN CALIFORNIA
In Partial Fulfillment of the
Requirements for the Degree
DOCTOR OF PHILOSOPHY
(Materials Science)

March 1983

UNIVERSITY OF SOUTHERN CALIFORNIA
THE GRADUATE SCHOOL
UNIVERSITY PARK
LOS ANGELES, CALIFORNIA 90007

This dissertation, written by

Russell John Wallace

*under the direction of his... Dissertation Com-
mittee, and approved by all its members, has
been presented to and accepted by The Graduate
School, in partial fulfillment of requirements of
the degree of*

DOCTOR OF PHILOSOPHY

B. S. Quaid

Dean

Date March 18, 1983

DISSERTATION COMMITTEE

Stephen M. Capley

Chairman

David B. Wilton

ACKNOWLEDGEMENTS

I gratefully acknowledge the Defense Advanced Research Project Agency who supported this research under DARPA Order No. 4006, Contract No. MDA 908-80-C-0436.

Dedicated to my parents
Niel R. Wallace and Ilda M. Wallace

TABLE OF CONTENTS

DEDICATION	ii
LIST OF FIGURES	vi
LIST OF TABLES	xi
ABSTRACT	xii
Chapter I. INTRODUCTION	1
A. Scope of Thesis Research	8
Chapter II. EXPERIMENTAL DESIGN	12
A. Introduction	12
B. Experimental Set-up	13
1. Laser	13
2. Beam Handling	20
3. Focusing System	21
4. Translation System	24
C. Sample and Sample Preparation	30
1. Sample Properties	30
2. Sample Preparation	36
D. Laser Characteristics	37
Chapter III. SINGLE GROOVE FORMATION STUDY - PART I	46
A. Introduction	46
B. Results	47
1. Curvatures versus Translation Direction	47
2. Entrance and Exit Shapes	49
	iii

3. Spatial Distribution of Intensity	53
4. Polarization of Beam	56
5. Absorption versus Polarization	62
C. Discussion	67
1. Curvature Mechanism	67
2. Calculated Absorption	72
Chapter IV. SINGLE GROOVE FORMATION STUDY - PART II	76
A. Introduction	76
B. Results	77
1. Effect of Speed and Power	77
2. Effect of Gas	84
3. Effect of Focus	88
C. Discussion	94
1. Factors Affecting Material Removal Rates	95
2. Mechanism of Reaction	98
3. Energy Balance	99
4. Mechanism of Absorption	107
Chapter V. OVERLAPPED GROOVE FORMATION STUDY	117
A. Introduction	117
B. Results	119
1. Beam Guiding - Surface Roughness	119
2. Material Removal Rate	127
3. Additional Features of Laser Machined Surfaces	135
4. Flexural Strength	135
D. Discussion	145

1. Overlapped Grooves	145
2. Flexural Strength	151
3. Economics	169
Chapter VI. SUMMARY	178
A. Summary - Conclusions	178
1. Single Groove Formation - Part I	178
2. Single Groove Formation - Part II	179
3. Overlapped Groove Formation	180
REFERENCES	182

LIST OF FIGURES

II.1.	Apparatus for laser shaping of ceramic materials	14
II.2.	Schematic representation of specific chamber and rotating translation stage	26
II.3.	Specific heat capacity as a function of temperature for Si_3N_4	32
II.4.	Thermal diffusivity as a function of temperature for Si_3N_4	33
II.5.	Thermal expansion as a function of temperature for Si_3N_4	34
II.6.	Double slit arrangement for spatial distribution determination	41
II.7.	Spatial distribution at focus with Gaussian overlay	43
II.8.	Spatial distribution at focus with Gaussian overlay	44
III.1.	Cross section illustrating curving behavior. $\theta=0^\circ$ translation direction	48
III.2.	Cross section illustrating curving behavior. $\theta=180^\circ$ translation direction	50
III.3.	Cross section at entrance. $\theta=90^\circ$	51
III.4.	Cross section at exit. $\theta=90^\circ$	52

III.5.	Hypothesized curving mechanism involving the spatial distribution of intensity	55
III.6.	Cross section with $\phi=0^\circ$	58
III.7.	Cross section with $\phi=42^\circ$	59
III.8.	Cross section with $\phi=72^\circ$	60
III.9.	Cross section with $\phi=90^\circ$	61
III.10.	Infrared reflection as a function of wavelength for Si_3N_4	66
III.11.	Mechanism of polarization induced curvature	68
III.12.	Proposed shape of groove bottom near exit surface	71
III.13.	Reflectance as a function of angle of incidence for Si_3N_4 at $\lambda=10.6 \mu\text{m}$	75
IV.1.	Material removal rates as a function of ϕ	78
IV.2.	Material removal rates as a function of scan speed and incident power for $\phi=0^\circ$...	79
IV.3.	Material removal rates as a function of scan speed and incident power for $\phi=90^\circ$..	80
IV.4.	Cross section as a function of scan speed for $\phi=0^\circ$	81
IV.5.	Cross section as a function of scan speed for $\phi=90^\circ$	83
IV.6.	Variation in cross section with constant parameters	85

IV.7.	Cross section as a function of gas environment	87
IV.8.	Effects of focal position on material removal rate. 12.7 cm lens	89
IV.9.	Effects of focal position on material removal rate. 6.35 cm lens	90
IV.10.	Effects of focal position on cross sec- tion. $\phi=0^\circ$	92
IV.11.	Effects of focal position on cross sec- tion. $\phi=90^\circ$	93
IV.12.	Temperature distribution on the surface of the sample	104
IV.13.	Isotherms within the laser heated sample .	105
IV.14.	Reflectance as a function of wavelength and temperature for NaCl	110
V.1.	Distortion of cross section due to beam guiding	121
V.2.	Multiple pass cross section with a feed of 0.022 cm	122
V.3.	Multiple pass cross section with a feed of 0.0178 cm	123
V.4.	Multiple pass cross section with a feed of 0.015 cm	124
V.5.	Multiple pass cross section with a feed of 0.010 cm	125

V.6.	Material removal rates as a function of feed and velocities	129
V.7.	Width and feed/width at beam guiding onset as a function of scan speed and ϕ orien- tation	132
V.8.	Surface profile trace of a sample machined with a scan velocity of 238 cm sec^{-1} , $\phi=0^\circ$ and a feed of 0.00378 cm	134
V.9.	SEM photomicrograph illustrating the solidified silicon layer	136
V.10.	Fracture surface of laser machined sample	142
V.11.	Detail of fracture surface in Fig. V.10 ..	143
V.12.	SEM photomicrograph illustrating cracks in silicon layer	144
V.13.	Probability of fracture versus MOR for $\phi=0^\circ$ laser machined samples and diamond machined samples	154
V.14.	Probability of fracture versus MOR for $\phi=90^\circ$ laser machined samples and diamond machined samples	155
V.15.	Schematic representation of crack system in a multiphase body with residual load and uniform applied stress	163
V.16.	Stress intensity factor versus crack depth for the edge-notched crack of Fig. V.15	168

V.17.	Dimensions of ceramic turbine blade used	
	in economic study	175

LIST OF TABLES

II.1.	Laser performance characteristics	15
II.2.	Sample material properties	35
III.1.	Absorption versus angle of incidence	64
V.1.	Four-point flexure strength of NC-132 Si_3N_4	139
V.2.	Material removal rates comparison between laser and diamond machining	172
V.3.	Economic comparison between laser and diamond machining for ceramic turbine blade	176

→ *The first dissertation investigated* ABSTRACT

The shaping of hot pressed Si_3N_4 with a high power CW CO_2 laser, was investigated. The laser was used to heat the surface of a workpiece forming a groove by vaporization. Shaping was accomplished by overlapping the grooves. For both singly and multiply overlapped grooves, cross section sizes and shapes, and material removal rates were determined for a wide range of incident powers (315 to 940 W) and sample scan speeds (5 to 240 cm s^{-1}). Initial examination of cross section shapes revealed some grooves to be curved. This behavior was subsequently found to be directly related to the angle between the \vec{E} vector of the partially polarized incident beam and the velocity vector of the sample and occurs due to an observed difference in reflectivity for the beam's TE and TM components.

Results are given showing that groove shapes and material removal rates are independent of irradiation environment. This suggests that decomposition is responsible for the removal of material. The consideration of the thermodynamic values for the decomposition reaction and an estimate of conductive losses to the substrate during groove formation suggest that at least 0.28 of the incident power should be absorbed. This value is higher

→ next p.

than would be expected due to normal infrared absorption. Part of this increase can be attributed to the presence of a Si film, and part to the temperature dependence of Reststrahl absorption. There was also some experimental evidence that plasma coupling effects may be partly responsible.

→ An analysis of multiple overlapping grooves indicated, in some cases, that the shape of the overlapped groove differs significantly from that of the single pass groove. Based on these results an improved method of predicting material removal rates and surface roughness is presented. The high material removal rates attained in laser machining compared to those experienced in diamond grinding lead to a favorable economic evaluation of the former. To further evaluate the potential of this shaping process, 4-point bend specimens were tested with laser machined surfaces. The results indicated a reduction in strength of 36% accompanied by greatly reduced scatter. Both reductions may be attributed to the presence of excess Si left by the decomposition reaction.

to p. xi of
appendix II

I. INTRODUCTION

Among the large group of directed energy sources commonly used in material processing only the laser is able to produce very high power density without extreme environmental restriction. The ability of the laser to transfer energy to a material, thereby causing an increase in its temperature, depends more critically than for other directed energy sources on the properties of the material to be processed (e.g., surface structure, reflectivity, and bulk absorption).¹ Although the electron beam technique is able to produce a similar power density to the laser and is less sensitive to material properties, it does normally require that the workpiece be processed in a vacuum. This requirement can create difficulty when using certain materials, particularly those that outgas vigorously during heating. Because the laser possesses the important and unique advantage of being able to project its easily controllable energy over a large distance without being attenuated in the presence of air or other gasses, it has found a wide variety of applications in the field of materials processing formerly done by other directed energy heat sources.^{2,3} In addition, because of its unique properties, the laser has been successful in

opening up completely new applications in the field of material processing such as the machining of Si_3N_4 , which is the subject of this research.

Fundamentally, the laser is a source of energy that can be focused to a very small spot size thus giving very high power density. The absorption of energy from the high power density beam creates a very rapid increase in the temperature of a material being irradiated. The extent of heating in the material is generally determined by the input power density, interaction time, and both the optical and thermal properties of the sample. Depending on the values of these parameters, the transfer of energy from the laser beam to the sample creates three regimes of heating: 1) heating without a phase change in the material, 2) laser induced melting, and 3) laser induced vaporization.⁴⁻⁷ Most material processing applications involve the last two.

The use of the laser in the melting regime has been generally limited to metal systems. Typical applications include microstructural refinement, alloying, cladding,⁸⁻¹⁰ cutting with a gas jet assist,¹¹⁻¹³ and most importantly welding.¹⁴⁻¹⁶ Because laser induced vaporization generally requires energies that are an order of magnitude higher than melting, applications to metal systems in the vaporization regime have been limited. The most successful applications in the vaporization regime have been with

non-metals (e.g., polymers) due to the lower energy generally needed for vaporization, their smaller thermal conductivity and higher absorption.²

Many applications involving the use of the laser are successful because the incident power levels can be accurately controlled and the beam focused to a small spot size so that the total heat input can be minimized in obtaining the desired temperature increase. As a result, thermal distortion is reduced and excessive heating of adjacent material is minimized giving a small heat affected zone.⁷

Of particular interest and the subject of this research is the use of lasers to process difficult to machine materials. In this regard, the laser has become an established machine tool for very hard and brittle materials such as ceramics.^{1,2,7} Generally, the interaction occurs in the vaporization regime and until now has been limited with respect to types of materials and machining operations. Diamonds, alumina, silicon, and glass have been the most widely used hard, brittle materials machined by lasers, while operations have been limited to drilling, scribing, and cutting operations.

The use of lasers to drill holes in hard materials has reached commercial status.² For example, there has been a need to produce holes that range from 0.03 to 1.3 mm in diameter in diamonds which are then used as dies for the extrusion of wire. This is an application where

laser processing offers significant advantage over competing techniques because conventional means are very tedious and costly. Conventional drilling usually requires diamond-tipped, hardened steel drill bits, which are used with a diamond slurry in an abrasive operation. For holes less than 0.25 mm in diameter or where the depth is greater than the diameter, drilling of this type often results in breakage of the drill and high tool wear rates. The process is slow and can take up to 7 hours to drill up to a depth of 12.7 mm.¹⁷ In contrast laser drilling can be used to machine such small holes easily with one or a few pulses from the laser without danger of fracturing.⁴

The hole drilling technique using a laser has also been extended to other materials, specifically alumina. Alumina is widely used in the electronic industry and is also a very difficult material to drill while in the fully fired state.^{18,19} Lasers have been used to produce holes for attachments of leads to an integrated circuit substrate.

Another need of the electronic industry that has taken advantage of laser machining is the production of alumina substrates and the separation of silicon wafers into complex shapes.²⁰⁻²⁴ These items are often used in integrated circuits. Conventional methods are expensive and slow and usually involve diamond sawing or scribing of the substrate. Three approaches have been taken in

separating substrates into complex shapes using the laser depending on the geometry of the cuts. If only straight line cuts are required either hole drilling or scribing can be used. The thin plates can be either pierced with a line of holes spaced at small intervals or scribed with a continuous groove into the surface but not all the way through the workpiece. The workpiece can then be separated along the line created by the laser. Because one does not cut all the way through the material, hole drilling and scribing can be carried out at higher speeds with less damage due to heating and thermal stresses than through cutting of the material. It has also been shown that the cuts obtained when hole drilling and scribing are employed are of a higher quality than those obtained by diamond scratching followed by breaking.¹ When non-straight lines are required through cutting by the laser is used. Through cutting although slower than drilling or scribing is an alternative when very complex shapes are needed.

The use of the laser to process hard and brittle ceramic materials has the advantage of increased material removal rates, no tool wear, and no force so fixturing is not required. Because the laser forms narrow cuts, there is low material loss and owing to the very small heat affected zones often material can be produced which requires no further finishing of the edge after completion of the operation.² For some ceramics, the laser has been

used to machine the material in its hard, brittle fired state. Previously because of their brittleness, ceramics produced from powders were often machined in their "green" state, i.e., before firing, but this leads to reduced dimensional tolerances. This problem can be overcome by using laser processing.⁷

Although the laser has proven to be very successful for these hard and brittle materials, as a tool to produce holes and in scribing and in cutting thin sections, its uses as a method to remove large amounts of materials resulting in shaping has not been exploited. Laser shaping of this type could be based on the overlapping of grooves created by the laser beam as it scans the surface of the sample thereby removing a layer of material.

Previously demonstrated by the investigator was the feasibility of carrying out several shaping operations based on the overlapping of grooves, including turning, threading, and milling with various silicon compound ceramics.^{25,26} The silicon compound ceramics, Si_3N_4 , SiAlON, and SiC, were investigated because they are candidate materials for high temperature applications. They have excellent oxidation resistance, thermal shock resistance and high temperature strength,²⁷⁻²⁹ but because of their high hardness (2200 Knoop), these materials can be shaped only at low rates by diamond grinding or ultrasonic machining.^{30,31} This high hardness along with their

inherent brittleness have been major roadblocks to their use at high temperatures but make them ideal potential candidates for laser shaping.

Although the previous work did demonstrate the feasibility of shaping by overlapping grooves, it did not fully investigate machining by this method. The purpose of the present investigation, based upon these feasibility studies, is to elucidate additional aspects of the laser machining operation and also to determine the origin of several previously documented but unexplained observations; observations which are detailed in the following sections.

A. Scope of Thesis Research

This research is an extension of previous investigations^{25,26} and can be divided into three parts. The first and second parts deal with the formation of single grooves, while the third part deals with the overlapping of grooves leading to shaping. This study unlike the previous work was restricted to one silicon compound ceramic, hot pressed silicon nitride (Si_3N_4). More detailed information about the materials selected can be found in Sec. II.C. Also contained in Chap. II are details relating to the experimental set-up and the characteristics of the laser used in this research.

To fully understand shaping by overlapping grooves one requires knowledge and data on the formation of single grooves. In addition to shaping, the formation of single grooves is of interest with regard to the simple cut off of material, which would be a useful operation during laser machining. Cut off involves a deep single pass groove produced by the laser's interaction with the material. Initial experiments involving single pass grooves gave an unexpected result in that grooves were often curved. Therefore the first part of the present investigation was undertaken to study the origin of this effect. Chapter III contains the results and a discussion of this

research. This investigation indicated a dependence of the shape of the laser machined grooves in Si_3N_4 on the angle ϕ between the velocity vector of the sample and the electric vector of the partially polarized incident laser beam. When $\phi=0^\circ$, the groove is symmetrical with a cross-section that is the narrowest and deepest observed at any angle. When ϕ equals 90° , the groove is again symmetrical but with a wide shallow cross-section. For $0^\circ < \phi < 90^\circ$, the groove cross section was curved.

Once the origin of curving in single pass grooves was determined, the second part of the investigation was carried out. This research is described in Chap. IV, which presents additional data on the formation of single pass grooves in silicon nitride. Groove cross sections and material removal rates were determined for a wide range of incident beam powers and sample scan speeds. The material removal rate Z ($\text{cm}^3\text{sec}^{-1}$) is the product of the area of the groove cross section and the speed at which the sample was translated. Groove formation was studied in several different atmospheres and under different focusing conditions. This was done to develop a better understanding of the energy balance involved in the reaction causing the material removal and the mechanism of absorption of the beam power.

The final part of this research is described in Chap. V and deals with the overlapping of grooves. Based

on preliminary data on groove cross sections, a model was previously developed that predicts the surface roughness R and the material removal rate Z for surfaces produced by overlapping laser vaporized grooves. According to this model, which considers both speed and groove spacing, Z and R decrease as the groove spacing decreases. Subsequently, it was found that although the predicted behavior occurs over a wide range of groove spacings, at very small groove spacings the opposite behavior occurs. The final part of this research deals with the origin of this unexpected effect.

The previous analysis assumed that the shape of a single pass groove cut by the laser would be repeated during multiple overlapping, even though the laser is removing material at the edge of a previously machined groove rather than from a flat surface. In the results presented in Chap. V, it is shown that in some situations the shape of the overlapping groove differs significantly from that of the single pass groove. Based on these results, more accurate methods of predicting Z and R are presented.

In the previous work the effects of laser machining on mechanical properties was not determined. Because Si_3N_4 lacks fracture toughness,³² K_{IC} of 3.25 to $4.8 \text{ MN m}^{-3/2}$, it is highly dependent on the presence of flaws or stress raisers. It was expected that laser machining would decrease strength because by its very

nature laser machining produces well defined overlapped grooves that can act as stress raisers. Also, micro-cracks may be produced as a result of laser induced thermal stresses. To investigate these effects, 4-point bend specimens were tested with laser machined surfaces. The results given in Sec. V.B.4 indicate an over all reduction in the modulus of rupture but also greatly reduced scatter.

The selection of laser machining to shape Si_3N_4 would also involve economic considerations. These considerations are discussed in Sec. V.C.3, and it is concluded that laser machining is a technologically feasible method for the shaping of Si_3N_4 .

The final section, Chap. VI contains a summary and conclusions of this research.

II. EXPERIMENTAL DESIGN

A. Introduction

This chapter contains information about the experimental set-up, laser characteristics, sample choices, and sample preparation. In this chapter, there are two aspects of prime importance. The first is the experimental information. It is this information which allows one to draw conclusions, apply the author's theories, and reproduce part or all of the experiment. The second is information not directly related to the experiment but which provides insight into why the experiment was designed in the manner specified.

B. Experimental Set-up

The major part of this research involves translating a sample at constant velocity in a controlled environment under a focused laser beam causing material to be removed from the workpiece.

The apparatus used in this experiment is schematically illustrated in Fig. II.1. The system can be separated into four sub-systems consisting of the laser, beam handling system, focusing system, and sample translation system. These sub-systems are discussed in detail in the following sections. In addition to the laser machining apparatus other experimental apparatus were used during the course of this research, such as the atmosphere chamber and the 4-point flexure testing fixture. Because these apparatus have particular relevance to only specific parts of the research they are not discussed here but rather in the relevant sections.

B.1 Laser

The results in this paper were obtained employing a Photon Sources³³ Model 1003 continuous wave CO₂ laser, with a maximum output of 1250 W at a wavelength of 10.6 μm . The performance characteristics of this laser are given in Table II.1. This laser is a good choice for material

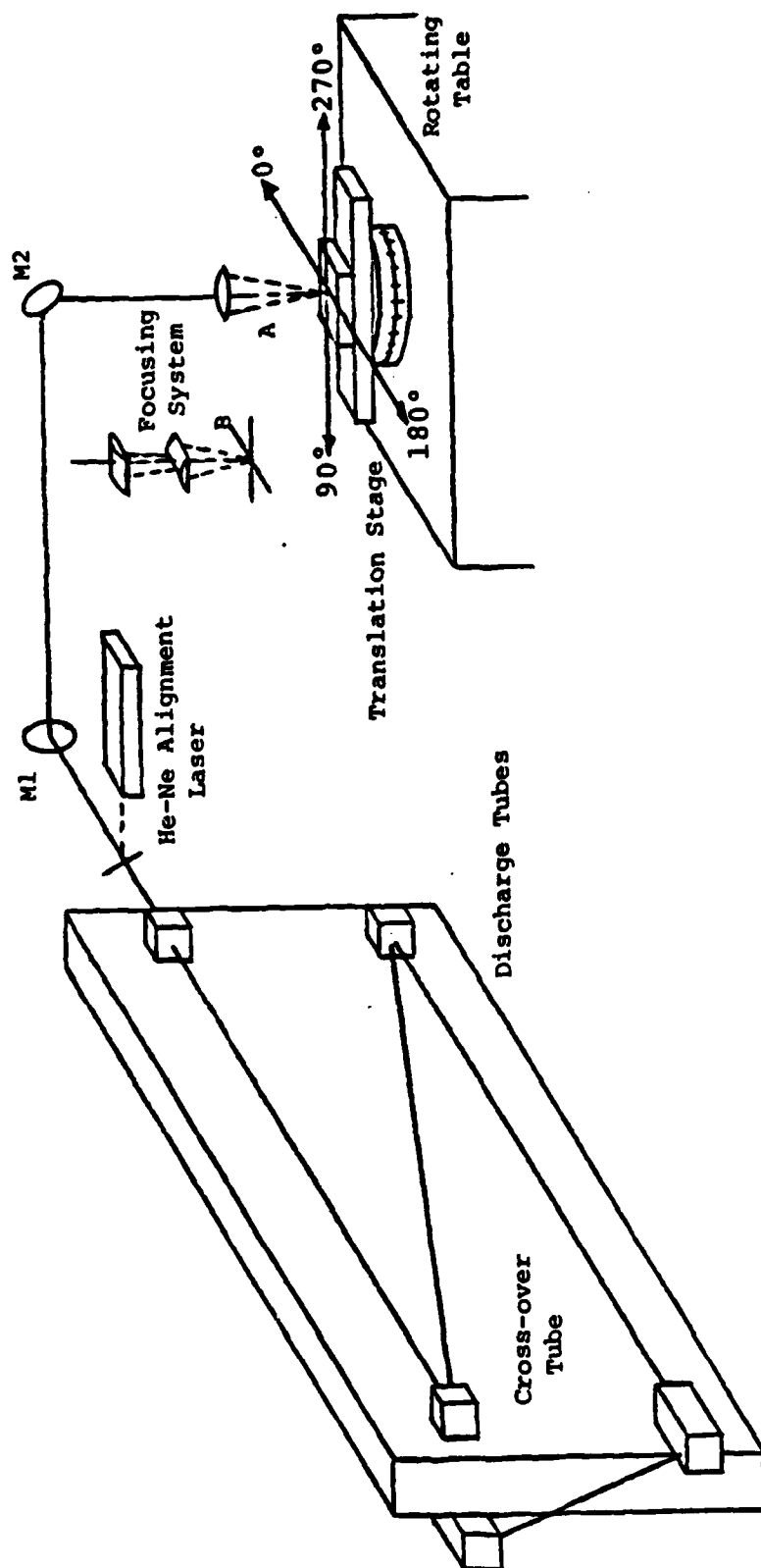


Fig. II.1. Apparatus for laser shaping of ceramic materials.

Photon Sources Model 1003 Laser

Wavelength:	10.6 micrometers
Output Power Range:	125 to 1250 watts
Output Power Stability:	2 percent, 8 hours
Mode Stability:	95 percent minimum TEM ₀₀
Active Discharge Length:	18 meters
Beam Diameter:	1.8 centimeters (e^{-2})
Beam Divergence:	2.2 milliradians
Minimum Pulse Duration:	100 microseconds
Maximum Repetition Rate:	1 kHz

Table II.1. Laser performance characteristics.³³

processing applications because of the high operational efficiency (5-10%) and the high average output powers obtainable with CO₂ lasers.³⁴ Other favorable characteristics of this particular model include long term power and mode stability as shown in Table II.1. This stability was required because preliminary results indicated an apparent sensitivity to some laser parameters. Some of the important factors influencing the output beam's stability and how the Model 1003 deals with these factors will be discussed below.

The Photon Sources Model 1003 is in the family of conventional CO₂ lasers used in material processing which operates by producing a longitudinal DC electric discharge in a slowly flowing, low pressure mixture of carbon dioxide, nitrogen, and helium. This technique produces 50 to 80 W per meter of discharge length.³³ Therefore lasers with a high output power require very long cavity designs. The Model 1003 laser attains high power while retaining reasonable outer dimensions by folding the cavity back upon itself creating a double "Z" arrangement. The two "Z" shaped resonators, each having six plasma tubes, are optically coupled through an isolated crossover tube as shown in Fig. II.1. This arrangement gives an active discharge length of 18 m and leads to a maximum power of 1250 W but requires the use of eight mirrors within the cavity.

The multiple mirrors constitute a liability because, as is well known, a very small amount of tilt due to misalignment of optical elements in a laser resonator can cause a significant perturbation to the beam and can lead to an asymmetric output beam and loss in output power.⁴ These problems if not caused by erroneous alignment of the optical cavity when setting up the laser are often caused by a lack of dimensional stability. To partially overcome this problem the Model 1003 uses a large granite slab that provides a stable platform for the optical resonator.

To help maintain stability all mirror mounts are of the ball-and-socket configuration, providing maximum bearing surface and a solid mirror assembly. Although stable once adjusted the mount design does not lend itself to easy adjustment of the mirrors which is required to tune the laser resonator to different output modes. Ideally, the laser resonator output should be the TEM₀₀ Gaussian fundamental mode. The TEM₀₀ energy profile has several advantages over higher order or multimode outputs including having the smallest focus, and a symmetrical intensity profile.³

Attempts were made to tune the resonator, the mirror geometry of which consists of a spherical/flat configuration, to the TEM₀₀ mode. This was done by directing the output beam, chopped to reduce total average power onto

an infrared sensitive thermal image screen. The area impinged upon by the laser becomes darker in proportion to the distribution of the energy density. By observing the image on the screen and adjusting the output mirror, the output beam can be changed to the desired mode. During this tuning, the laser always exhibited multi-mode behavior and generally had its highest power output when the output beam was asymmetric. Considerable effort was made to adjust the beam to a symmetric profile but this was never quite achieved as will be shown in Sec. II.D.

Periodic checks were made during the experiments using thermal sensitive paper and they showed that the output mode was very stable and did not change. The mode stability can be attributed to the already mentioned granite slab and solid mirror mounts and also to the resonator cooling system. Any heat generated by the discharge can cause misalignment of the optical cavity due to thermal warping. The Model 1003 uses a cooling system consisting of circulating, high dielectric strength oil in a closed loop through an internal Freon controlled heat exchanger. The cooling system maintains the plasma tubes, cathodes, and mirror mount assemblies at room temperature. To further isolate the laser from the lab environment, the entire laser is enclosed within a steel enclosure.

The laser's output power was designed to be

controlled by varying the discharge current giving an output power range of 125 to 1250 W with a stability of $\pm 2\%$ over many hours as specified in Table II.1. Practical experience indicated that output powers below 300 W were not stable. This was because the Model 1003's gas mixing system which can individually set the flow rate of carbon dioxide, helium, and nitrogen was adjusted so that the laser would produce maximum output power. This gas mixture is rich in nitrogen which tends to adversely effect the discharge at lower powers. Because this experiment utilized the upper power output range the low power instability did not prove to be a problem.

Although the Model 1003 can be externally electronically gated up to 1 kHz at variable duty cycles, this experiment always used the continuous wave mode. The laser was also equipped with an external beam shutter that blocked the beam path, diverting the beam by means of an electrically operated mirror into an energy sink. The shutter allows the laser to be energized and stabilized at the desired power output before the beam is delivered to the sample. To verify the desired power levels the laser was equipped with an internal meter that could monitor the power output. This monitoring was accomplished by placing a power meter behind the rear laser window. The window was designed to transmit 0.4% of the energy inside the laser cavity. This power meter system

monitored the power output continually during sample irradiation. More detailed information about the characteristics and mode of the laser is found in Sec. II.D.

B.2 Beam Handling

The beam handling system is also illustrated in Fig. II.1. It consists of two turning mirrors (M1,M2) and the He-Ne alignment system. Upon opening the shutter the output beam leaves the laser enclosure and proceeds 0.5 m to M1. Mirror M1 causes the beam to be directed 7.3 m in the horizontal plane and at a right angle to the output of the laser to the second turning mirror M2. Mirror M2 directs the beam down into the focusing system. This arrangement gives a laser to sample distance of 8.2 m.

For this experiment M1 was a water cooled copper mirror while M2 was an air cooled molybdenum mirror. Both mirrors were mounted into 2-axis mirror mounts that allow for the precision angular adjustments required to align the beam. Although M1 was water cooled this was not necessary and was not used for this experiment due to the relatively short beam on times and long intervals between irradiations. Though the copper mirrors have slightly higher initial reflectance than molybdenum mirrors they have limited usefulness in that they are not very resistant to tarnishing.³⁵ Tarnishing will effect the level of power that can be delivered by the beam handling

system. During this experiment the mirrors were frequently inspected and did not show any deterioration of this type. Practical experience indicates that molybdenum mirrors are a better choice for use in laser material processing application where particulates, oil mists or other contaminants may be present in the environment.

In an effort to help retard the deterioration of the mirrors but more importantly as a safety measure the entire beam path was enclosed with steel tubes and Plexiglass chambers. These enclosures did not provide an air tight seal but did afford complete safety protection. Lasers of this power can easily cause severe burns to both eyes and skin upon exposure to the output beam.⁴ Precautions were always taken particularly for eye protection.

Because the beam from a CO₂ laser has a wavelength of 10.6 μm , it is invisible to the naked eye. Therefore, to aid in alignment of the optical system a small He-Ne laser was employed. The He-Ne beam could be remotely accuated and placed co-axially with the CO₂ beam before the first turning mirror. This allows adjustment of all external optical elements in the beam handling system without the danger or problems associated with using the high power CO₂ beam in the alignment process.

B.3 Focusing System

The purpose of the focusing system was to accurately

position the focusing lens along the beam axis. The system used in this experiment was the commercially available Photon Sources Model 450 Viewing Delivery System.

The lens and lens holder assembly is attached to a heavy-duty precision slide mechanism which is anchored directly to the beam bender mirror (M2) assembly. The slide mechanism allows the lens to be moved up or down, a motion that allows the focus to be coincident with the top of the sample or at any known distance above or below the sample. The Model 450 is equipped with a dial indicator which displays the position of the focusing lens with an accuracy of 25.4 μm over the full 7.6 cm travel of the mechanism.

The Model 450 focusing system permits the viewing of the sample at high magnification. The system has the internal adjustment needed to make the focus of the microscope viewing system and the focus of the laser beam coincident. The viewing system has a relatively high magnification and therefore a very narrow depth of focus. This narrow depth of focus allows for accurate positioning of the lens system to the top of the samples. This is accomplished by moving the total lens system until the sample is in focus using the viewing system. From this position the dial indicator can then be used for those irradiations that require the beam's focus to be above or below the top of the sample.

The Model 450 is designed for sequential viewing only. It cannot be used for viewing while the irradiation is taking place. Although the Model 450 is very good for relocating focus when many samples are used one drawback is that it is only accurate for the person that originally aligns the optical focus for the microscope due to the variations in vision for different operators.

The Model 450 also employs a gas delivery system which allows a stream of gas to be delivered coaxially with the focused laser beam. The area below the lens forms a chamber to which gas can be introduced and only escape through the gas jet nozzle mounted below the inlet chamber. This gas nozzle can be independently moved toward or away from the lens along the axis of the focused beam. Typically, this gas jet is used directly in the laser material interactions process but for this research it was only used to shield the focusing lens from products produced by the vaporization reaction. To reduce the possible effect of the jet of gas on groove formation, a large nozzle diameter was employed. The nozzle was raised relative to the sample surface and the inlet gas pressure to the chamber was kept as low as possible. To assure precise centering of the focused beam through the nozzle, the inlet chamber and viewing system to which the nozzle assembly is attached can also be moved by means of a precision dovetail mechanism in two axes about the focusing

lens.

In addition to the Model 450 lens system another lens system, designated B, is also depicted in Fig. II.1. It was used in Chap. III. Lens system B involves the use of two optical elements in their own alignment system and replaced the Model 450 Viewing Delivery System. The lens system description and function is discussed in more detail in Sec. III.B.3.

Except where noted a standard plano-convex lens was used for all laser machining in this research. The lens was 3.8 cm in diameter with a 12.7 cm focal length and was mounted in a Photon Sources compatible lens mount. The optical components of all focusing systems used in this experiment were zinc selenide and had an anti-reflective dielectric coating. Zinc selenide was a good choice for this experimental set-up because it transmits light down to 0.5 μm in the visible region and therefore permits the use of the He-Ne alignment system.³⁵ The lens proved durable throughout the experiment and showed none of the signs of deterioration which are commonly seen in high power laser optics.

B.4 Translation Stage

This research required the following characteristics of the specimen translation stage:

- 1) Variability of speed over a wide range

- 2) Controlled environment
- 3) The ability to overlap single pass grooves with the amount of overlap (feed) being variable
- 4) Variability of sample translation vector

These requirements were met by the arrangement shown in Fig. II.2 where the "turntable" stage is schematically illustrated.

The turntable was coupled through a variable ratio system to a reversible variable speed DC motor. This system permitted a sample placed on the outer edge of the turntable to be translated under the focusing system, over a wide range of speeds typically unobtainable with a standard linear stage. For single pass irradiations the upper range of the speed was limited only by the ability to open and close the shutter within a single revolution so as to irradiate the sample only once. For this experiment a rotational speed of $13.9 \text{ rad sec}^{-1}$ corresponding to a sample scan speed of 125 cm sec^{-1} at the 9 cm radius sample position was found to be the upper limit. The lowest speed was limited by the DC motor which did not run smoothly below a sample scan speed of 5 cm sec^{-1} with the gear ratio used. Although the turntable motor controller had a readout of motor RPM all low velocities were independently measured with a stop watch and higher velocities were calibrated using a strobe tachometer.

To control the irradiation environment the sample

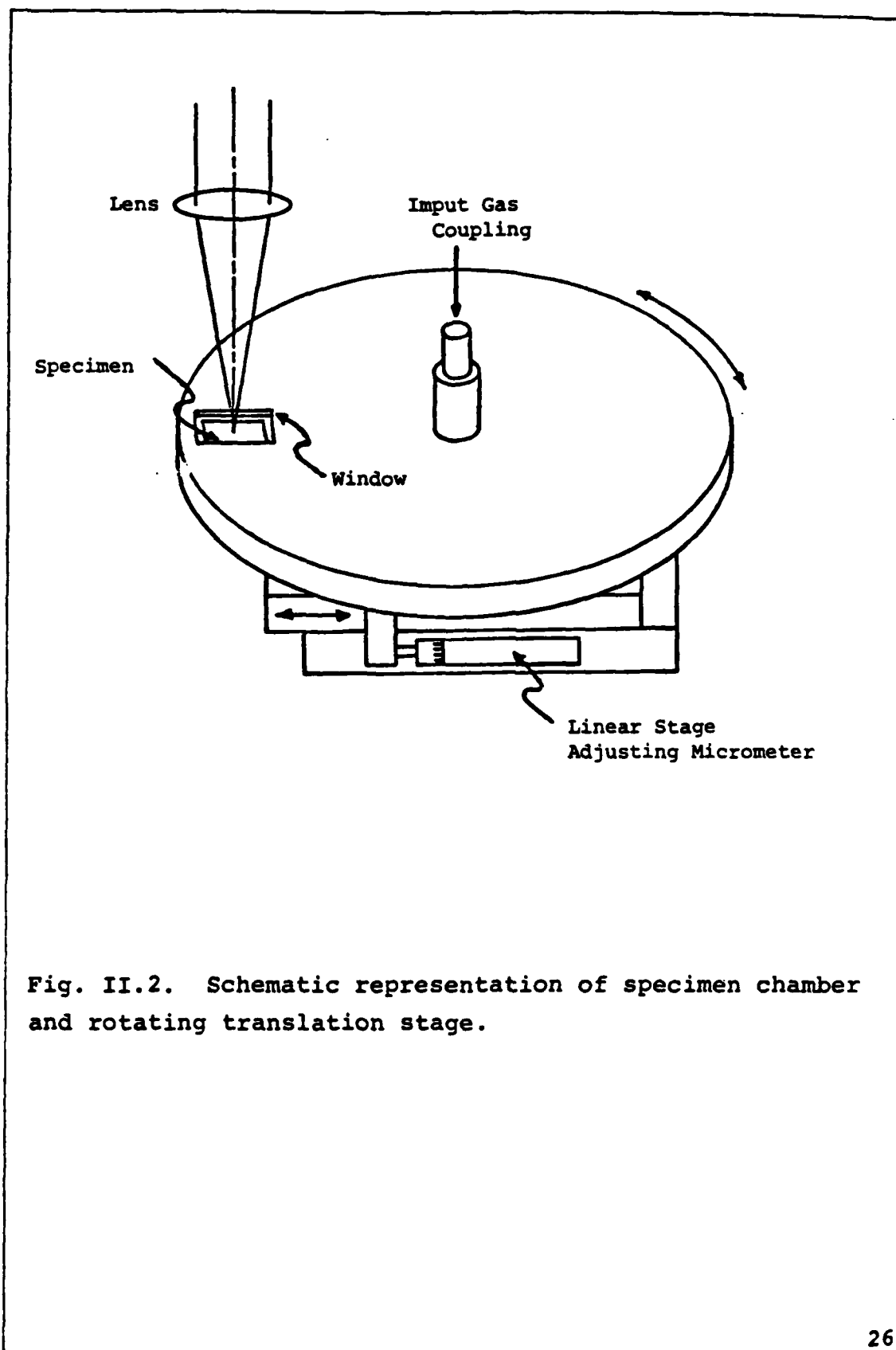


Fig. II.2. Schematic representation of specimen chamber and rotating translation stage.

was placed in a window region slightly below the smooth upper surface of the turntable as shown in Fig. II.2. The interior of the turntable was hollow; the hollow chamber being connected to a gas inlet through a rotating gas coupling. As the sample was rotated, gas was introduced into the chamber and could only escape through the window area thereby surrounding the sample by a low velocity gas flow. This method allows control of the gas environment without subjecting the specimen's surface to any direct high speed gas flow. As previously mentioned the nozzle that shields the focusing lens was modified for the same reasons. For all irradiations the nozzle always contained the same type of gas as the rotating stage. Most sample irradiations were done in an O_2 -rich flowing gas environment with N_2 and He being selectively used.

In Chap. V there was a need to continuously overlap the laser machined grooves to various degrees. This was done by mounting the "turntable" stage on a micrometer controlled linear stage. The micrometer was driven by a variable speed DC gearhead motor. The amount of overlap was determined by the speed of the linear stage and the angular velocity of the turntable. For cases where only a few overlapping grooves were needed the DC motor was removed and the micrometer was manually adjusted after each pass. While single pass speeds were limited to

approximately 125 cm sec^{-1} owing to the necessity of shuttering, the overlapped machined samples did not have this limitation. Thus, some of the samples in Sec. V were laser machined at a velocity of 250 cm sec^{-1} although this required a change in the ratio of the turntable drive system.

Variation in the direction of the sample translation with respect to the polarization of the incident beam was accomplished by mounting both the "turntable" and linear stage on a horizontal rotating indexing table. The indexing table allowed the sample velocity vector to be directed at any angle θ in the horizontal plane with the angles and direction being defined in relation to the focused laser beam as shown in Fig. II.1. Direction reversal was possible because the DC motor driving the turntable was reversible.

Although the translation stage used in this experiment did meet all the functional requirements, it did have some drawbacks. The most obvious was that the grooves were not laser machined in a straight-line manner but formed arcs corresponding to the radius of the turntable. Another drawback was the variation in sample speed arising from variations in turntable radius. The speeds cited in the following sections refer to the speeds at the 9 cm radius position on the sample, although the actual speed of each groove, which was normally within 5% of the cited

value, was used in all calculations involving speed such as the calculations of material removal rates. Neither of these drawbacks proved to be of critical importance in this experiment.

Not shown in Fig. II.1 is the vacuum nozzle which was placed approximately 5 cm from the focused beam. Its purpose was to remove the vapor and dust generated in forming the grooves from the work area.

C. Sample and Sample Preparation

This research was restricted to one silicon compound ceramic, hot pressed silicon nitride. Silicon nitride was utilized because of the following factors: previous successes in laser machining of Si_3N_4 , limitations of current shaping capabilities using conventional machining, and the future usefulness of this material for structural applications. The Si_3N_4 selected was a Norton Company³² product, NC-132 which has become the standard for advanced ceramic materials.

C.1 Sample Properties

NC-132 is a uniaxially hot pressed silicon nitride which is nearly isotropic. The flexural strength of this material shows little variation (<20%) with direction in the billet. Its thermodynamic properties vary less than 5% when measured parallel to and perpendicular to, the hot pressing axis. NC-132 has a fine-grained microstructure with beta Si_3N_4 being the major crystalline phase. The maximum grain size is on the order of 3 μm and there are small pores dispersed throughout the matrix. The pores are typically smaller than 2 μm in diameter.

Thermal properties for NC-132 as a function of temperature were derived from Norton's technical

literature.³⁵ The thermal diffusivity D is shown in Fig. II.3; volumetric specific heat capacity C_p is presented in Fig. II.4; and thermal expansion is presented in Fig. II.5. The plot of thermal diffusivity involved the extrapolation of the curve from 1146 to 1878°C. The plot of specific heat capacity involved a similar extrapolation from 1425 to 1878°C. Because of the large temperature dependence shown in Figs. II.3 and II.4, the values used in this experiment were the integrated averages of the published and extrapolated data from 25 to 1878°C. These values are listed in Table II.2 and used in Secs. IV.C.3 and IV.C.4. Sections IV.C.2 and IV.C.3 contain more detailed information about the high-temperature thermodynamics of the silicon nitride system.

Other properties were obtained from various sources as described elsewhere in the text. The values of flexure strength for NC-132 from both the literature and those experimentally obtained in this research are discussed in Secs. V.B.4 and V.C.2. Section V.C contains a discussion including material removal rates of conventional machining techniques commonly used with NC-132 hot pressed silicon nitride.

The reflectivity of NC-132 at the $\lambda=10.6 \mu\text{m}$ was measured during the course of this experiment and was correlated with published information. This correlation leads to a calculated optical index of refraction for

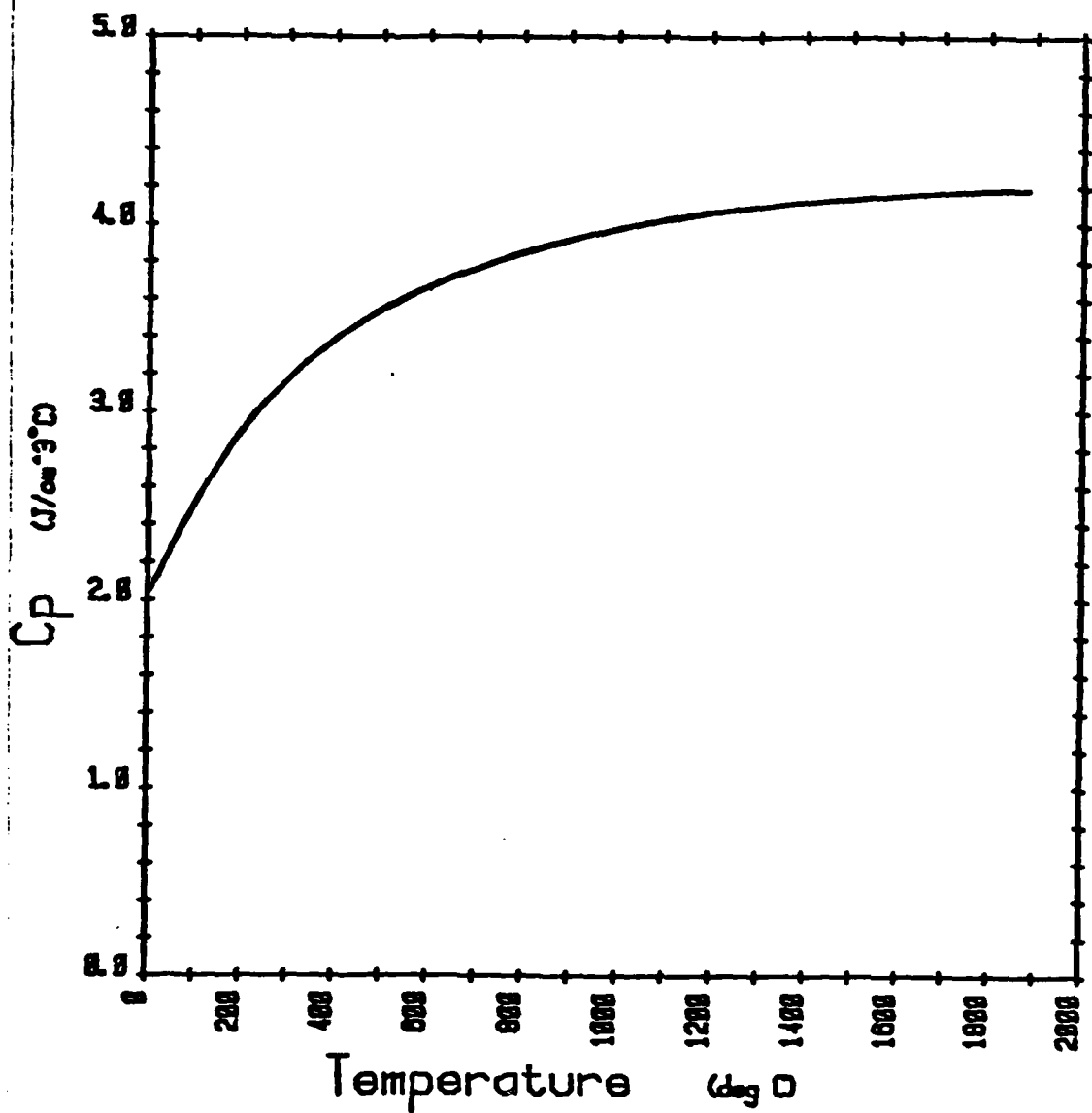


Fig. II.3. Specific heat capacity as a function of temperature for Si_3N_4 .

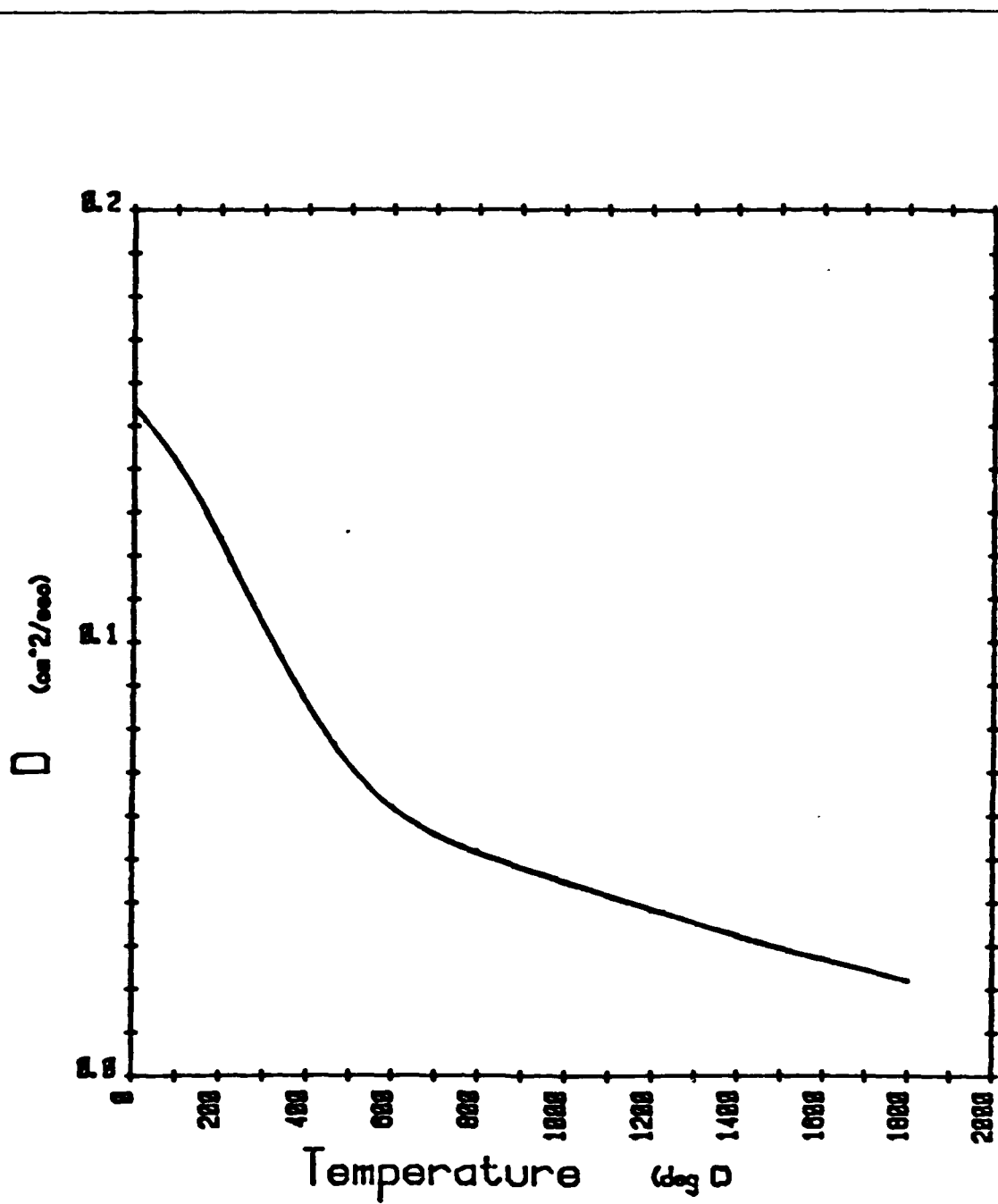


Fig. II.4. Thermal diffusivity as a function of temperature for Si_3N_4 .

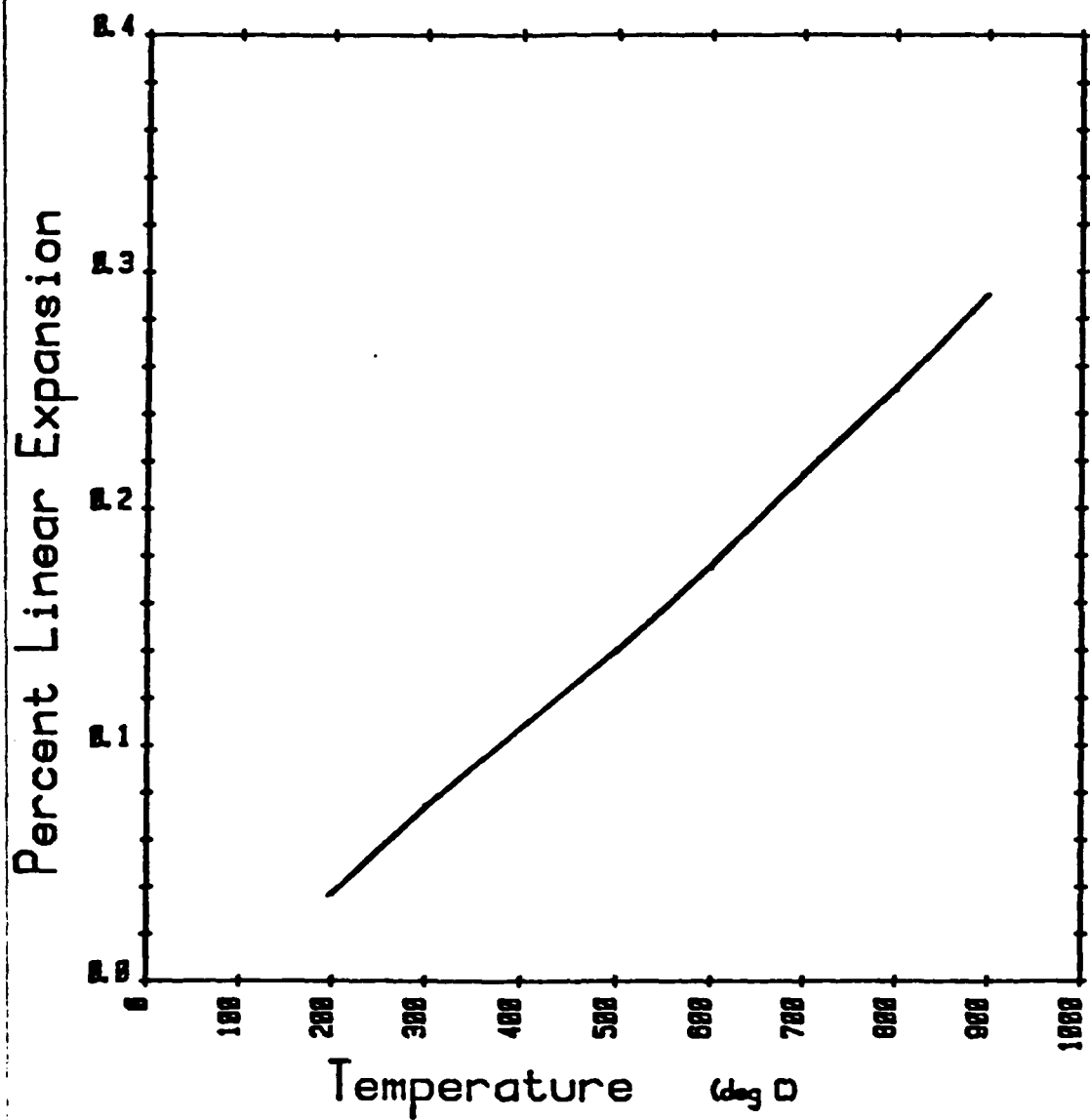


Fig. II.5. Thermal expansion as a function of temperature for Si_3N_4 .

Norton's NC-132 Hot Pressed Silicon Nitride			
Property	Units		
Density	gm cm ⁻³		3.25
Hardness	Kg mm ⁻²		2200
Strength (4pt)	MN m ⁻²		694 R.T.
Specific Heat	J cm ⁻³ C ⁻¹		3.72
Thermal Diffusivity	cm ² sec ⁻¹		0.058
Chemistry	Wt %	Mg	0.51
		Ca	0.01
		Fe	0.15
		Al	0.11
		O ₂	2.41
		W	2.70

Table II.2. Sample material properties.

NC-132 at $\lambda=10.6 \mu\text{m}$ and is discussed in Sec. III.C.2. Related information is found in the discussion of the various mechanisms of absorption of the incident laser radiation in Sec. IV.C.4.

C.2 Sample Preparation

For this study two billets of NC-132 were obtained from the Norton Company. Each billet was produced from Norton's powder lot HN19. Analytical data for this lot was supplied by Norton and is detailed in Table II.2. The density of both billets was measured and found to be 3.25 g cc^{-1} . In addition both billets were examined by x-ray to ensure radiographic uniformity.

Samples of $0.45 \times 0.64 \times 2.54 \text{ cm}$ were sectioned from the $15 \times 15 \times 0.64 \text{ cm}$ billet of NC-132. The top surfaces had a uniform surface roughness produced by grinding using a 320 grit diamond wheel. After the samples were laser machined they were resectioned for examination using a high speed wafer saw with a 220 grit diamond blade. The calculated areas for groove cross sections were determined from photomicrographs using a polar planimeter.

D. Laser Characteristics

In order to fully comprehend the laser material interaction, the characteristics of the laser beam must be understood. This information is needed not only for theoretical modeling but also when others compare their findings to the laser-material interaction data of this experiment. When the interaction involves a focused beam, as it does in this research, information about the unfocused profile is of little importance, except that it is usually the unfocused beam that is used to tune the laser to the desired mode as previously stated in Sec. II.B.1. Unless many assumptions are made, such as the beam is in the TEM₀₀ mode and no error is introduced due to mirror or lens aberration, the information gained about the unfocused beam cannot be used to easily calculate focused beam characteristics. Therefore focused characteristics must be measured directly. Unfortunately some of these characteristics are experimentally difficult to measure due to the high powers and intensity associated with the focused beams of lasers used for processing of materials.

In general the two following characteristics should be known at the point of the laser-material interaction:

- 1) beam power P

2) spatial distribution of intensity of the
focused beam $I(r)$

With knowledge of P and $I(r)$ other parameters such as focused spot size and peak intensity $I(0)$ can then be calculated.

Of the two main characteristics the beam power was the easiest to measure. The beam power at the focus is a function of the laser output power and losses due to the mirrors and focusing lenses in the beam handling and focusing systems. The losses were periodically measured using a Coherent³⁶ Model 213 power meter after the final lens. With the losses known the laser output could be adjusted so that the desired amount of power was delivered to the sample. Although the laser has an internal monitoring system as previously mentioned all powers reported in this thesis refer to those measured after the final lens. During this research the incident powers ranged from 315 to 940 W.

The measurement of the focused beam intensity profile is not as easily accomplished. Measurement techniques that are suitable for unfocused beams do not give accurate results when applied to focused beams. Three common methods are used to measure the distribution of intensity. They are generally referred to as: thermal imaging, direct burning, and slit scanning. Only slit scanning appeared to have the accuracy needed for this research.

The slit scanning technique involves the direct measurement of beam power through an aperture which transmits only a small portion of the total beam area. A scan across the entire beam diameter produces a power versus position trace which can be used as an indication of the spatial distribution of the beam intensity. This technique requires that the size of the aperture must be small enough to adequately resolve the true detail of the intensity distribution yet large enough to transmit sufficient energy for detection. In order to produce an accurate recording of the intensity distribution by continuous scanning, the maximum translation rate of the aperture must be appropriately matched to the response time of the detection and data recording system.

When this scanning technique is applied to the focal plane where intensity density are on the order of 5 MW cm^{-2} the small apertures ($25\mu\text{m}$) required are prone to damage unless translated very quickly. However, fast translation requires the use of a fast detector. The need for a fast detector and the difficulty in making the small durable aperture made the fast translating slit technique undesirable in this investigation. The technique finally used in this experiment, developed in part by the investigator, involved the modification of the aperture thereby allowing slow aperture translation and similarly the use of a slow pyroelectric detector.

The modified system involves the use of two slits oriented at right angles to each other at fixed distances apart as shown in Fig. II.6. The upper slit is wider than the lower slit. When the converging laser beam is directed down through the slits the upper slit only allows a "slice" of the beam to reach the bottom slit. As the bottom slit is then translated through this slice of the beam the detector below both slits measures the intensity profile as a function of position. By adjusting the position of the slits relative to the lens the maximum transmission of power can be found and it is at this point the focal plane of the lens is coincident with the bottom slit. This apparatus can therefore also be used to locate the focal plane of the lens for subsequent experiments. This system works because the upper slit reflects the bulk of the beam energy and reduces the very high intensity that the second slit would normally encounter. Both slits are made of copper with their top surfaces highly polished to make them highly reflective to the incident radiation thereby again reducing the possibility of damage due to heating.

A complete series of intensity profiles was made with the double slit arrangement using the standard 12.7 cm focal length lens. This series consisted of scans made in the plane perpendicular to the beam and centered on the axes. This was accomplished by rotating the double slit assembly about the beam axes using the horizontal rotating

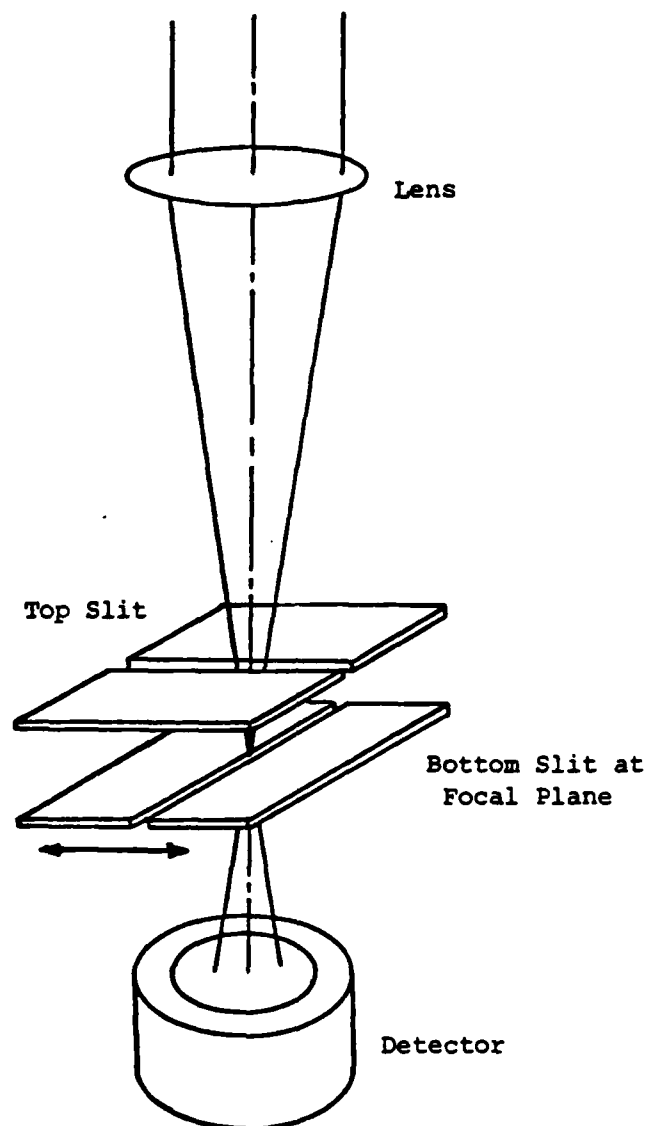


Fig. II.6. Double slit arrangement for spatial distribution determination.

indexing table mentioned in Sec. II.B.4. The direction of the beam intensity profiles can be related to the directions shown in Fig. II.1. This series of beam scans indicates that the focused beam had an asymmetric distribution similar to that observed in the unfocused beam. The focused beam could be best described as being elliptical. If one chooses to pick the width at the e^{-2} intensity level then the elliptical focused beam would have a minor axis of 190 μm and a major axis of 280 μm with an average diameter of 230 μm . Figures II.7 and II.8 show the intensity distribution along both axes which are situated at 90° to one another. Also shown in Figs. II.7 and II.8 are Gaussian overlays for comparison. Using the overlays it was calculated that the intensity profiles of Figs. II.7 and II.8 were approximately 90% Gaussian.

With the parameters used to generate the Gaussian overlays one can also calculate the approximate peak power density $I(0)$. Using a beam diameter based on the Gaussian overlay of Fig. II.7 with an incident power of 942 W, one obtains a peak power density of 4.15 MW cm^{-2} ; similarly Fig. II.8 would give 7.68 MW cm^{-2} . These two values lead to an average power density of 5.92 MW cm^{-2} .

In addition to the beam power and focused beam intensity profile the polarization of the incident beam was also measured during the course of the experiment. The polarization has particular relevance to Chap. III and is

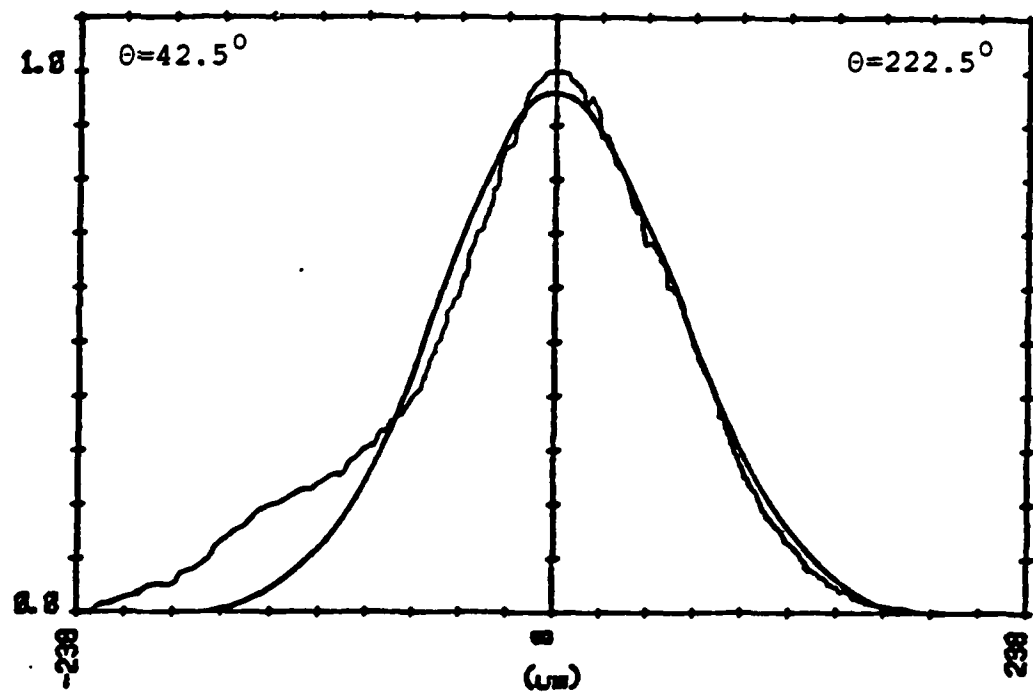


Fig. II.7. Spatial distribution at focus with Gaussian overlay.

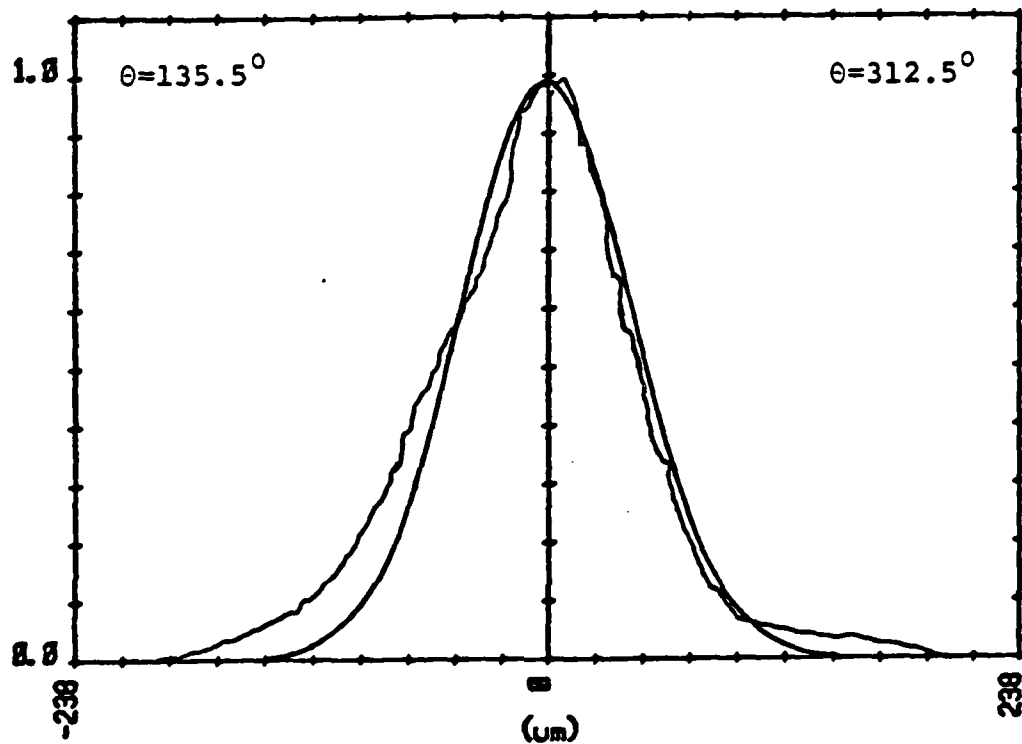


Fig. II.8. Spatial distribution at focus with Gaussian overlay.

discussed in Sec. III.B.4.

III. SINGLE GROOVE FORMATION STUDY - PART I

A. Introduction

As stated in Chap. I to fully understand shaping by overlapping grooves one requires knowledge and data on the formation of single grooves. This chapter details the specific investigation undertaken to study the origin of previously observed unexpected single pass behavior. Examination of sections perpendicular to the laser vaporized grooves in Si_3N_4 had revealed that these grooves were often curved. Within this chapter observation of this behavior was documented and several possible explanations were experimentally tested. Subsequently, it was found that the shape of the groove cross section is directly related to the partially polarized incident beam.

B. Results

B.1 Curvatures Versus Translation Direction

The curved behavior described in Secs. I.A and III.A can be seen in the groove cross section shown in Fig. III.1. The sample was translated in the 0° direction at 5 cm sec^{-1} using 560 W. This behavior was seen over a wide range of speeds with Fig. III.1 typical of low speeds. As the translation speed was increased for the same power the groove became shallower with the curvature eventually disappearing; however, the groove remained asymmetric with one wall being steeper than the other. When the speed was increased beyond 100 cm sec^{-1} only a slightly asymmetric shape can be found in the sectioned sample. Varying the power has the same effect. For a fixed velocity vector, decreasing the incident power reduced the extent of the curving as well as the depth of the groove.

Although the direction of curvature was very consistent for a fixed velocity vector and the material was believed to be nearly isotropic, the sample's orientation was changed while maintaining the same velocity vector in an effort to vary the direction of curvature. All experiments involving changes in sample orientation gave negative results, i.e., the direction of curvature was not



H 0.1 mm

$\oplus v_s$

Fig. III.1. Cross section illustrating curving behavior.
 $\phi=0^\circ$ translation direction.

changed. Also, the experiments showed that the direction of curving was independent of the angle of incidence as well as being independent of the type of cover gas used.

One experiment that did cause the direction of curvature to change involved the reversal of the velocity vector. An example of this behavior can be seen in Fig. III.2 where all parameters are the same as those used in Fig. III.1 except the direction of translation was changed by 180° . Note that the velocity vector V_s is indicated on every figure with a sectioned groove and refers to the motion of the sample. One can see from Figs. III.1 and III.2 that not only is the direction of curvature reversed but the shape is also reversed to the point of being a mirror image. This effect was seen for the whole velocity range investigated.

B.2 Entrance and Exit Shapes

Section III.B.1 referred to curving behavior of a sectioned groove when not influenced by end effects. Observations of the changes in groove curvature where the laser first enters or leaves the Si_3N_4 sample revealed the entrance to the groove had a curved cross section, while the exit had a symmetric or straight cross section (see Figs. III.3 and III.4).

Successive cross sections performed in the region near the entrances showed that the curved groove cross



┃ 0.1 mm

⊙ v_s

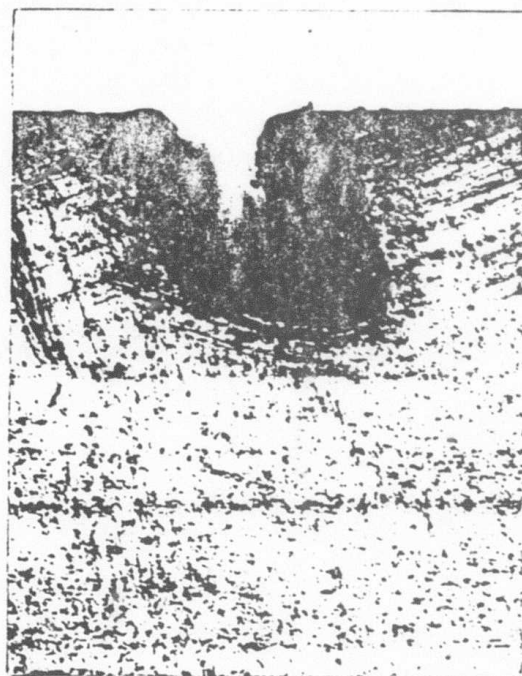
Fig. III.2. Cross section illustrating curving behavior.
 $\theta=180^\circ$ translation direction.



I 0.1 mm

⊙ V_s

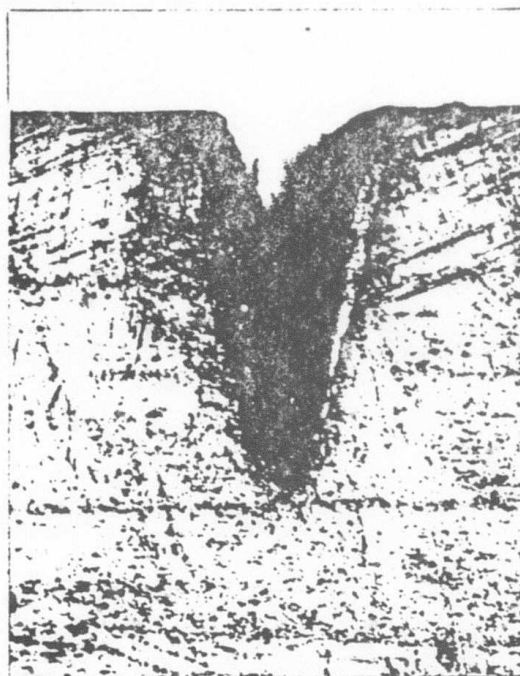
Fig. III.3. Cross section at entrance. $\phi=90^\circ$.



┌┐ 0.1 mm

⊙ V_s

Fig. III.3. Cross section at entrance. $\phi=90^\circ$.



— 0.1 mm

⊕ v_s

Fig. III.4. Cross section at exit. $\phi=90^\circ$.

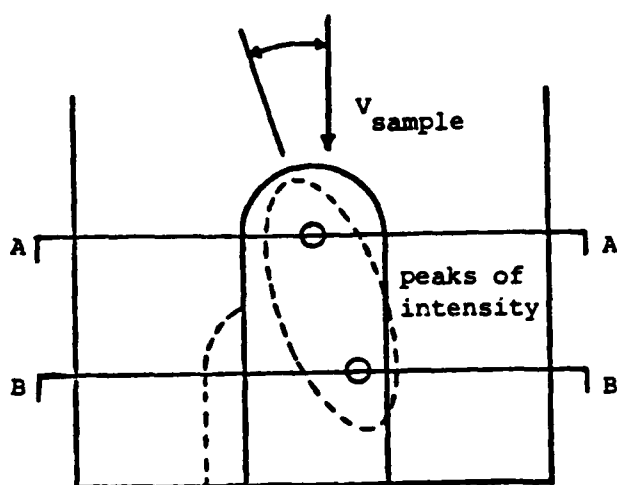
section as seen in Fig. III.3 is very representative in both shape and amount of the curvature observed throughout the length of the groove. In addition, later experiments showed that curvature versus translation direction in the previous section is exactly mimicked at the entrance to the groove, although the fine details of the groove are harder to observe in the unsectioned samples because material produced by the vaporization had been deposited on the entrance surfaces.

Behavior observed in the exit region of the groove is more complicated. For the velocity vector and power corresponding to Fig. III.4 successive cross sections starting back from the exit surface showed that the curvature seen throughout the groove begins to become more symmetric about 0.5 mm from the exit surface of the sample. In the region where this straightening takes place the groove becomes slightly shallower. After becoming this, the groove becomes deeper while still maintaining a symmetric profile just as it leaves the surface. This final lengthening of the exit surface can be seen in Fig. III.4. This behavior was seen over a wide range of velocities and powers though the distance from the end at which the straightening took place did vary with these parameters.

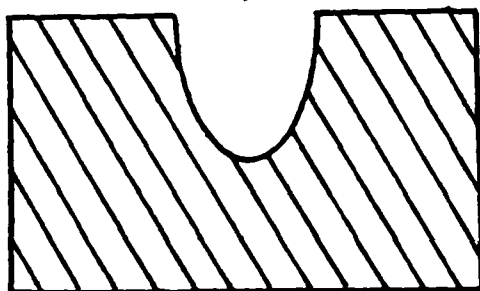
B.3 Spatial Distribution of Intensity

It was first hypothesized that the curved groove cross section was due to an asymmetrical spatial distribution of intensity within the output beam. As stated in Sec. II.D beam scans of the focused beam showed similar asymmetry. The focused beam could be best described as being elliptical. The origin of the curved groove cross section, according to this hypothesis, can best be explained by regarding the focused beam profile as two closely spaced peaks of intensity. The line connecting the peaks would then correspond to the major axis of the ellipse.

If this line is at an angle to the translation direction as shown in Fig. III.5 the first peak of intensity will begin to create a groove as shown in Fig. III.5, section AA. As the translation continues the second peak of intensity will not impinge the smooth top surface but rather the wall of the groove created by the first peak. The second peak will be guided by reflection from the wall to create the curvature of the groove as seen in section BB of Fig. III.5. If the direction of translation is reversed it is easy to see that the direction of curving would switch to the other side, which would be consistent with the general behavior seen in Figs. III.1 and III.2. By the above hypothesis, the shape of the groove should remain the same throughout the sample. This behavior was observed except where the beam leaves the sample.



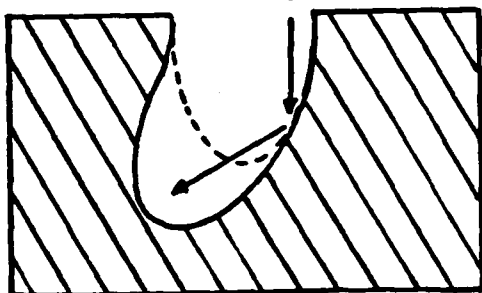
↓ first peak



Section AA

Groove created by first peak

↓ second peak



Section BB

The section peak is guided by the wall created by the first peak

Fig. III.5. Hypothesized curving mechanism involving the spatial distribution of intensity.

To verify this model, control of the intensity variation was necessary while maintaining all other parameters at constant values. This control was obtained with the arrangement depicted in lens system B of Fig. II.1. Two cylindrical lenses of different focal lengths ($f_1=25.4$ cm, $f_2=12.7$ cm) were oriented at 90° with respect to each other and positioned at a distance d equal to f_1 minus f_2 apart. By slightly varying d , a line of intensity could be produced. Rotation of the lens assembly was used to vary the angle. Many scans were made varying the angle between the line of intensity and the translation vector in an effort to affect the direction of curvature. In no case was it possible to vary the curvature. Based on this result and the failure of the intensity model to explain the groove shape where the laser beam exits the sample it was concluded that asymmetry in the spatial distribution does not provide an adequate explanation for the curved cross section of the single pass groove.

B.4 Polarization of Beam

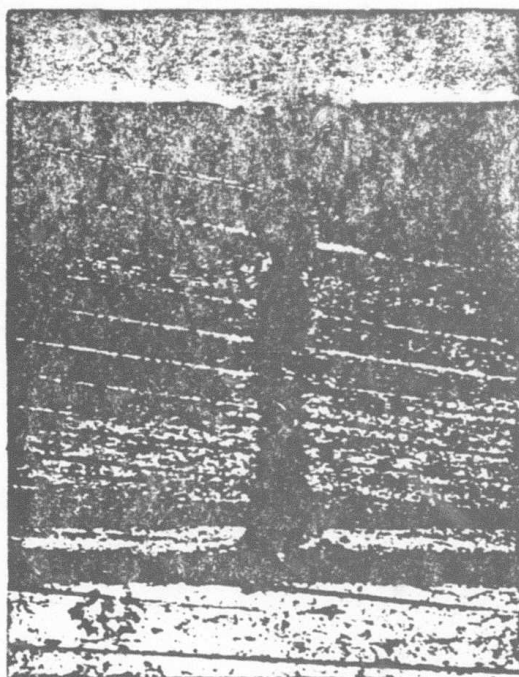
Polarization is known to effect the removal of materials in metal systems although the extreme curvature observed here has not been previously reported.³⁷ It is well known that laser beams are often partially polarized due to the use of internal Brewster windows. The laser used in this experiment has no such windows, however, it

does employ internal turning mirrors which could give rise to polarization of the beam.

A measurement of the beam was undertaken using a double Brewster window polarizer. The beam was chopped and masked and the polarizer placed after the final turning mirror. These measurements indicated that the beam was indeed polarized with the electric vector \vec{E} pointed in the 80° and 198° direction of Fig. II.1. The 18° value correlated with the orientation of the internal mirrors at each end of the cross-over tube which were 18° from the vertical direction as shown in Fig. II.1.

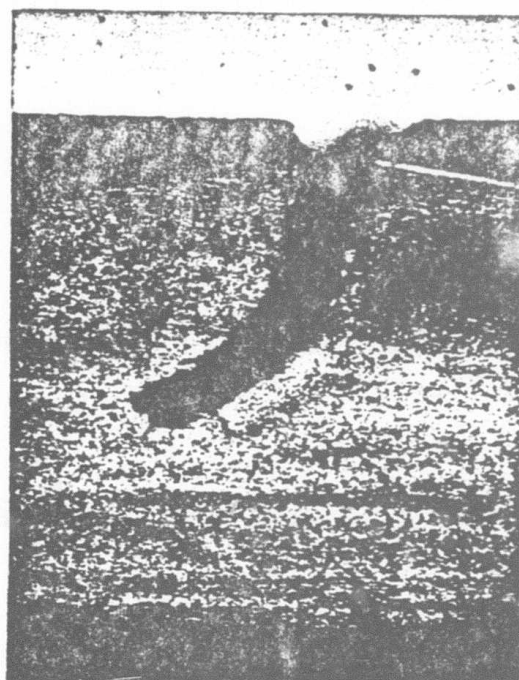
Experiments were undertaken to study the curving effect in relationship to the polarization. Samples were translated for various values of the angle ϕ , the angle between \vec{E} and \vec{V}_s . This was done by rotation of the index table below the translation stage. A direct correlation was seen as shown in Figs. III.6 to III.9. When the angle $\phi=0$, or when \vec{E} and \vec{V}_s were parallel, the grooves had straight cross sections. In this case the grooves were more narrow and deep than observed at any angle ϕ (Fig. III.6).

When ϕ equals 90° , the groove was again symmetric but very different in character from the groove for $\phi=0^\circ$. At $\phi=90^\circ$ it was wide and shallow. At very low speed at $\phi=90^\circ$ the groove was wider below the surface than above (see Fig. III.9). At angles ϕ between 0° and 90°



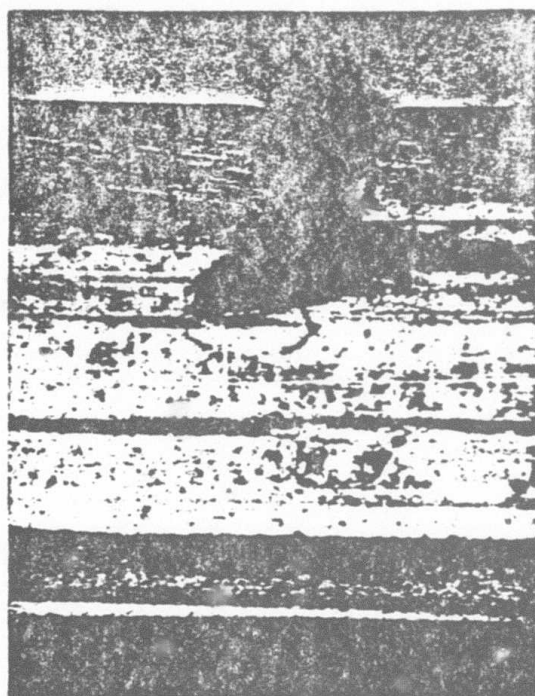
H 0.1 mm $\oplus v_s$

Fig. III.6. Cross section with $\phi=0^\circ$.



⊥ 0.1 mm ⊕ v_s

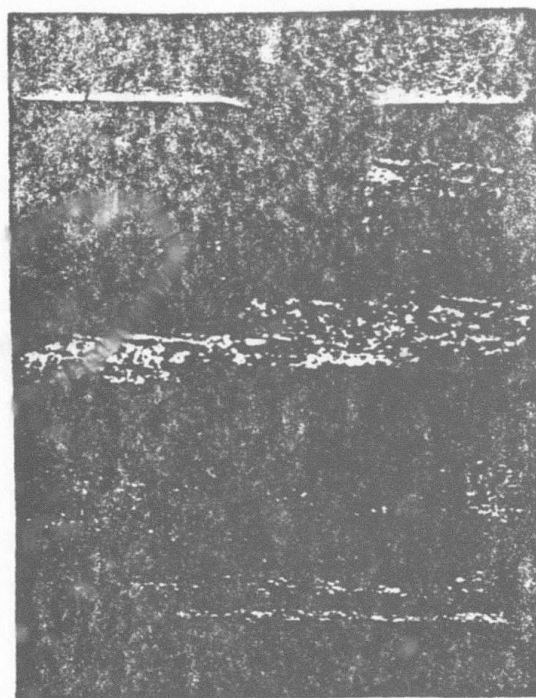
Fig. III.7. Cross section with $\phi=42^\circ$.



H 0.1 mm

$\oplus V_s$

Fig. III.8. Cross section with $\phi=72^\circ$.



0.1 mm $\oplus V_s$

Fig. III.9. Cross section with $\phi=90^\circ$.

curving was observed. As the angle was increased from 0° , the groove changes from a long straight profile to a gentle curve. With further increases in ϕ , the curvature of the groove became more pronounced, the depth decreased and the width increased as seen in Fig. III.7. As ϕ approached 90° , the shape became more angular as the groove widened and its depth further decreased. This behavior can be seen in Fig. III.8 where ϕ equals 72° .

The groove profile is extremely sensitive to the angle ϕ when ϕ nears the values of 0° or 90° . The cross section can go from symmetric to asymmetric if the angle is varied by as little as 5° . Whenever the value of ϕ is varied through 0° or 90° , the direction of curvature changes. This behavior is consistent with that shown in Figs. III.1 and III.2. Also, whenever two grooves are made with ϕ 's that are oppositely directed, they have the same profile but the direction of the curvature is reversed.

B.5 Absorption Versus Polarization

The strong correlation of polarization angle and groove curvature suggests that a dependence of absorption on polarization may exist and dominate the interaction of the beam with the groove walls. Thus, a study was done to measure the absorption for two different cases of polarization. In the first case, the electric vector of the

incident beam was perpendicular to the plane of incidence (transverse electric, TE); in the second, the electric vector was parallel (transverse magnetic, TM). In both cases absorption versus angle of incidence β was measured.

A 1.27x3.81 cm polished Si_3N_4 sample and a small CO_2 laser with an output of 10 W were used in the study. The sample was mounted so that the absorption for various incidence angles for the two cases, TE and TM, could be measured.

The absorption was calculated by a reflection method. This method assumes that the absorption is equal to 1 minus the quotient of the measured reflected power divided by the measured input power. A Coherent Model 210 power meter was used to measure both powers. Because of the power meter head size, incidence angles smaller than 10° could not be measured. Also, due to the small sample size incidence angles larger than 60° could not be measured. The results are given in Table III.1. In the reflection method, it is very difficult to measure all the reflected light because of scattering. This was thought to be occurring because microscope examination of the polished sample showed roughness that appeared to be due to grain pullout.

A second experiment was undertaken to measure absorption using a calorimetric method which was not affected by scattering.³⁸ The temperature of a sample thermally

Angle of Incidence (deg)	Absorption			
	(Reflection Method)		(Calorimetry)	
	TM	TE	TM	TE
0°			0.113	0.113
10°	0.175	0.183		
20°	0.185	0.174	0.118	0.102
40°	0.196	0.145	0.137	0.067
60°	0.249	0.118	0.191	0.035

Table III.1. Absorption versus angle of incidence.

isolated from its surroundings was measured as a function of time. If a laser beam of constant intensity impinges on the sample, energy will be absorbed causing a rise in temperature, which can be measured using a thermocouple attached to the sample. The experimental data was reduced by the "two-slope" method.³⁹ In this technique the slope of the temperature-time curve is corrected for sample heat losses to the surroundings in calculating the absorption coefficient. The results are also shown in Table III.1. Note that this method allows the absorption at 0° angle of incidence to be measured. The values of absorption as measured by calorimetry were lower than those measured by the reflection method. This difference was due to the scattering losses which affect the results using the latter method. The calorimetric values are used as the correct values.

In addition, reflectance versus wavelength was independently commercially measured using a similar reflection method at an incidence angle of 20° for the same sample.⁴⁰ The results of this measurement are shown in Fig. III.10. The $10.6\text{ }\mu\text{m}$ value was consistent with the value obtained by this investigation's reflection method.

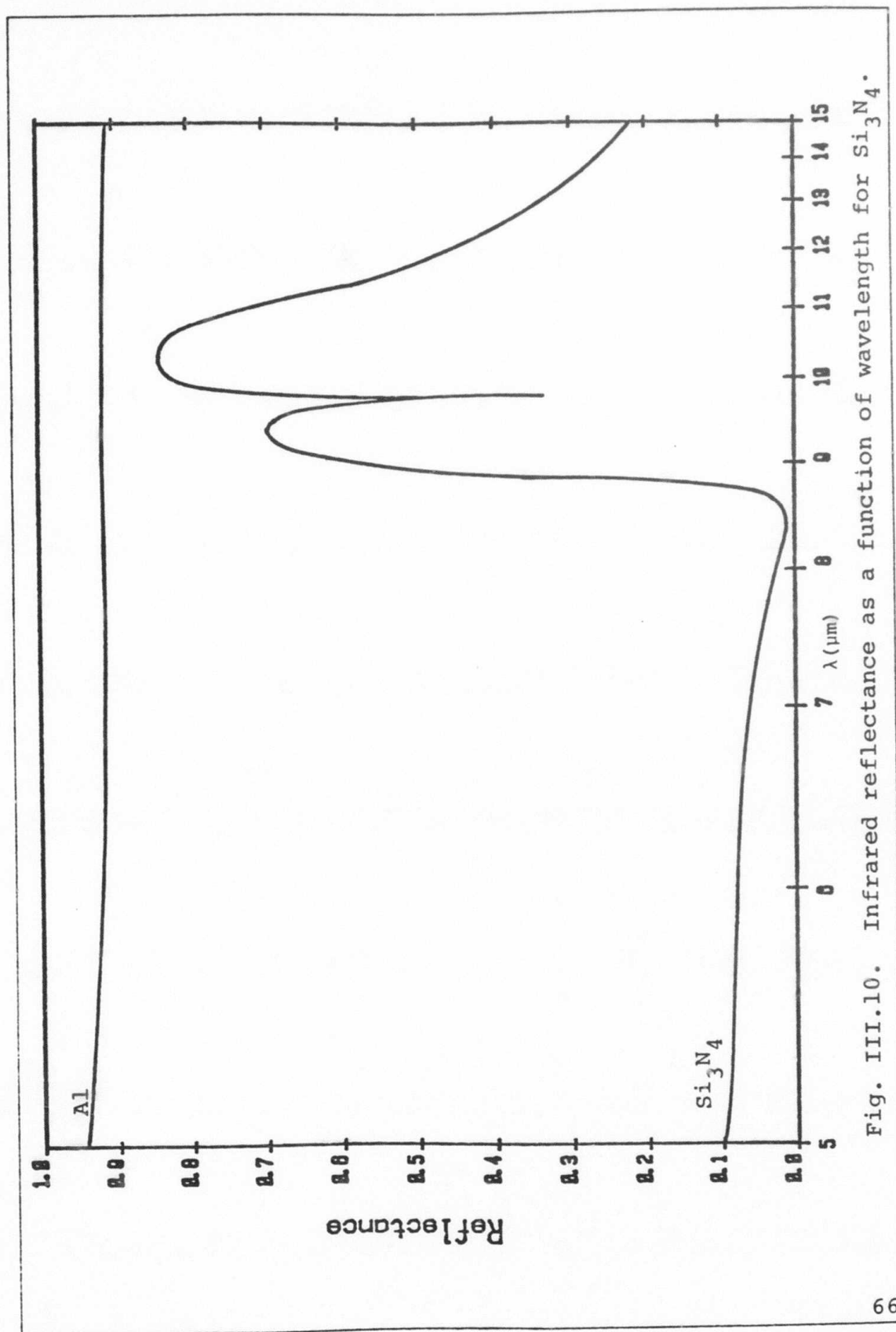


Fig. III.10. Infrared reflectance as a function of wavelength for Si_3N_4 .

C. Discussion

C.1 Curvature Mechanism

The mechanism which is believed to cause polarization induced curvature in a single pass groove is illustrated in Fig. III.11. Shown is the angular relationship between the velocity vector and the \vec{E} vector of the incident beam. Also shown are two reflection vectors designating the TM and TE reflection. The TM reflection is produced when the incident beam's \vec{E} vector is in the plane of incidence while the TE reflection is produced when the \vec{E} vector is perpendicular to the plane of incidence. For steady-state cutting represented in Fig. III.11, the focused beam will interact with the slanted wall of the groove and be reflected. Although the whole front surface reflects the light, for simplicity only the two reflections mentioned previously are shown, and because the \vec{V}_s vector is defined as 45° from the \vec{E} vector, the direction of the reflected vector is symmetric around the velocity vector as shown in Fig. III.11. Although the direction of reflections is symmetric the magnitude of the TE and TM reflections will not be. As the data obtained in Sec. III.B.5 shows, and Fresnel's law predicts, for any angle of incidence larger than 0° , the magnitude of the TE reflection will be

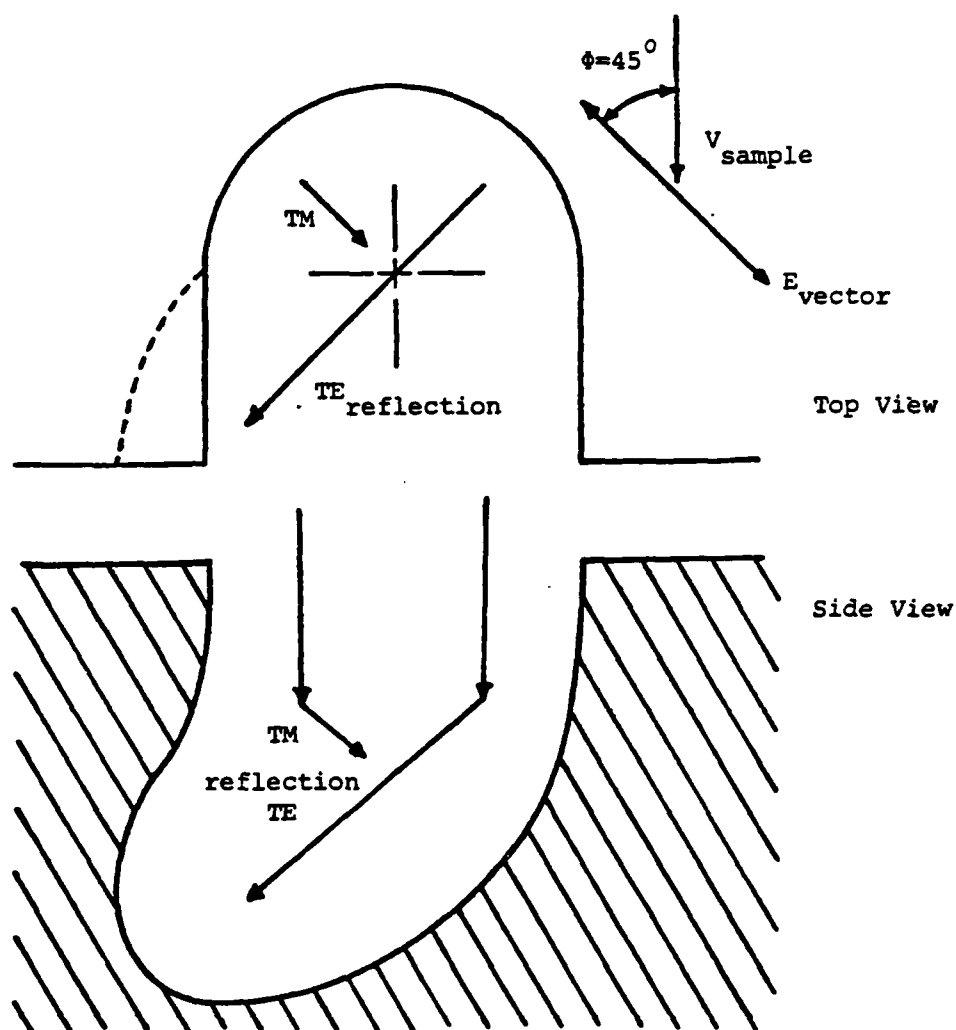


Fig. III.11. Mechanism of polarization induced curvature.

the largest. This increase in magnitude is represented schematically by the increased length of the TE vector in Fig. III.11. After the initial reflections both the TE and TM reflections are directed down and across to the opposing wall where the energy will be absorbed. But since the intensity of the light reflected as TE rays is larger than that reflected as TM rays more energy will be deposited and therefore more material removed in this area. The uneven reflection and subsequent non-symmetric energy deposition creates the curved cross section.

Figure III.11 simplifies the true situation of the laser beam interacting with the sample, because it does not illustrate the multiple reflection of the beam off the wall as it penetrates the material. Also the diagram does not represent the cross section modification due to the energy absorbed by the front wall in the region of the origin of the TM reflection but this would just add to the non-symmetric energy absorption causing the curving. Although a simplification, Fig. III.11 and the mechanism it represents can be used to explain satisfactorily the observations and behavior reported in Secs. III.B.1 and III.B.4. When the direction of translation is reversed or when ϕ is changed from plus to minus the direction of curvature is also reversed. When ϕ is 0° , there will be two TE reflections; one on each side of the groove and a TM reflection off the front surface directed along the bottom of the

groove. Since the magnitude of the two TE reflections on the sides are equal the groove created should be symmetric and the TM reflection at the front represents a high absorption in the region thus creating a long straight cross section. When $\phi=90^\circ$ there are two TM reflections on the sides and a TE reflection in the front. The two TM reflections representing high absorption at the walls create a wide groove that is still symmetric. At all other angles, $0^\circ < \phi < 90^\circ$, the reflections are no longer symmetric and curving will take place.

The mechanism also predicts the groove front should be curved in the plane perpendicular to the top surface of the sample and parallel to the velocity vector as shown in position A of Fig. III.12. The mechanism requires that the light is reflected down the front of and back along the bottom of the groove. This front curve behavior has been seen during laser welding of quartz.⁴¹ It is also this curved front that gives rise to the unusual behavior described in Sec. III.B.2, where the groove approaches the exit surface. Just as the tip of the groove crosses the exit surface the cross section curving mechanism will start to break down since there is no front surface with which the beam can interact (position B, Fig. III.12). This accounts for the straightening of the groove at a relatively large distance from the end compared to the beam diameter. At this point the main part of the beam

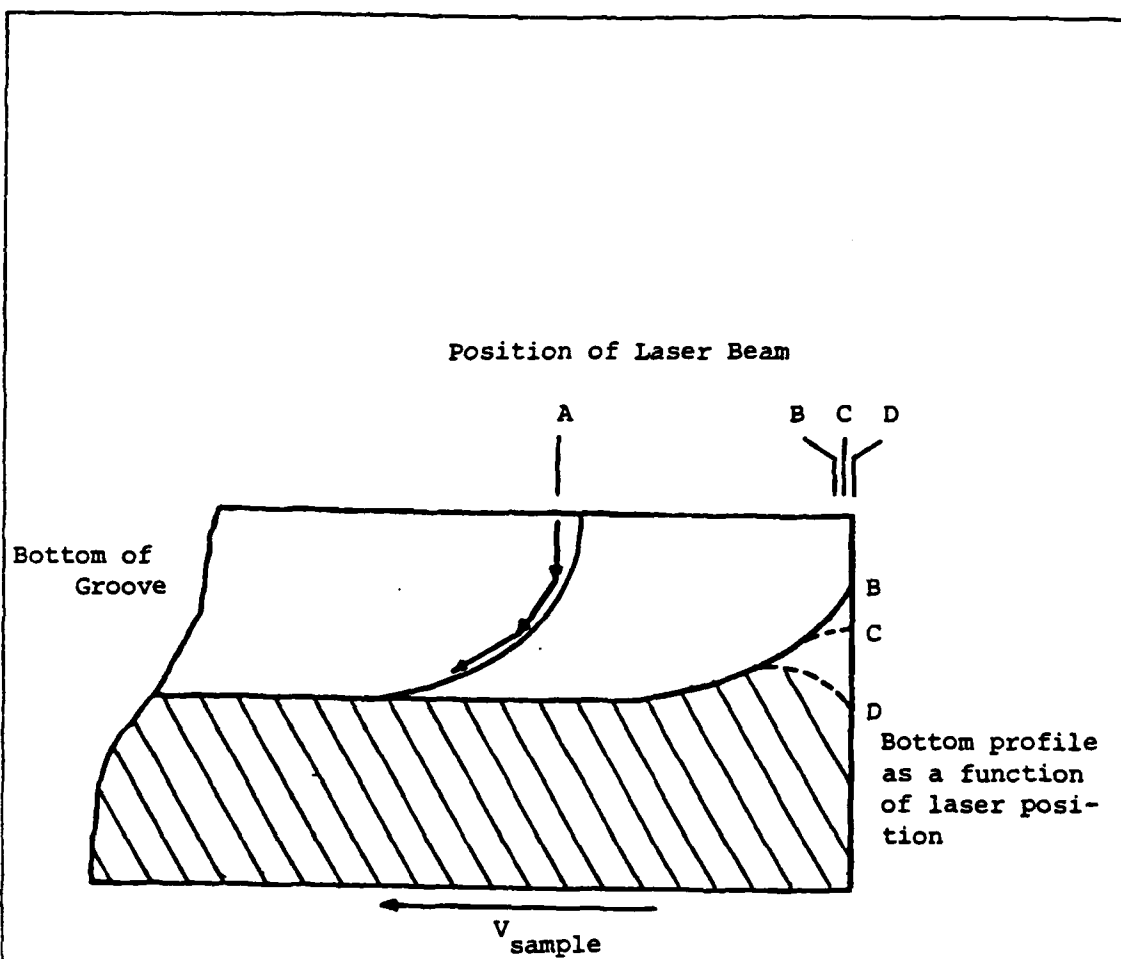


Fig. III.12. Proposed shape of groove bottom near exit surface.

would, in a sense, overtake the curved front. The front becomes modified by the end surface as seen in position C, Fig. III.12. In this position the beam hits this surface at a smaller angle of incidence so that it is no longer reflected back into the groove but rather ahead of itself and down the exit surface (position D) creating the effect seen in Fig. III.4, a long straight groove.

C.2 Calculated Absorption

From Figs. III.11 and III.12 and the cross section of the other grooves shown, it can be seen that the angle of incidence of the beam with the groove walls is probably 75° to 80° , rather than 60° , which was the largest angle for which the absorption was reported in Sec. III.B.4. The reflectance of the TE and TM beams can be calculated using the following complex equation⁴²

$$\text{Reflectance}_{(TE)} = \left(\frac{\cos\beta - N\cos\gamma}{\cos\beta + N\cos\gamma} \right) \left(\frac{\cos\beta - N\cos\gamma}{\cos\beta + N\cos\gamma} \right)^* \quad (\text{III.1})$$

$$\text{Reflectance}_{(TM)} = \left(\frac{-N\cos\beta + \cos\gamma}{N\cos\beta + \cos\gamma} \right) \left(\frac{-N\cos\beta + \cos\gamma}{N\cos\beta + \cos\gamma} \right)^* \quad (\text{III.2})$$

where β is the angle of incidence; $\cos\gamma = (1 - \sin^2\beta/N^2)^{1/2}$, and N is the complex index of refraction ($n+ik$).

Reizman and Van Gelder⁴³ give the optical index of refraction of Si_3N_4 as 1.96 to 2.02 in the visible region.

The use of this value at $\lambda=10.6 \mu\text{m}$ is not possible, because as stated in Sec. III.B.5, a reflectance versus wavelength curve was experimentally determined and it indicates that there is a Reststrahl band centered at $\lambda=10.6 \mu\text{m}$. This infrared absorption band can cause the value of n to deviate considerably from the visible value.⁴⁴ Haggerty and Cannon⁴⁵ have listed values of the optical properties at $\lambda=10.6 \mu\text{m}$ as $n=2.1$ and $k=6.95$. Their n value was derived from an extension of the Reizman and Van Gelder work but because of the Reststrahl band is incorrect. The k value was derived by Haggerty and Cannon from a bulk absorption measurement. It can be shown that $k=\alpha_b\lambda/4\pi$ where α_b is the bulk absorption coefficient.⁴² Haggerty and Cannon experimentally calculated $\alpha_b=8.24 \times 10^4 \text{ cm}^{-1}$ which then gives a k value of 6.95 for Si_3N_4 .

Assuming their value of k is correct, one is able to calculate n using either Eqs. (III.1) or (III.2) and the data of Sec. III.B.4. For the case of normal incidence ($\beta=0^\circ$) both Eqs. (III.1) and (III.2) give the same result namely

$$\text{Reflectance} = \frac{(1-n)^2 + k^2}{(1+n)^2 + k^2} \quad (\text{III.3})$$

Using a reflectance of 0.89 derived from Table III.1 and $k=6.85$, Eq. (III.3) requires a value of 1.5 for n . Using these values of n and k with Eqs. (III.1) and (III.2) a

plot of reflectance as a function of angle of incidence can be calculated for both the TE and TM polarization. This plot is shown graphically in Fig. III.13. Also plotted is the data from Table III.1 obtained using the calorimetric method. There is fairly good agreement between the two for the range $\beta=0^\circ$ to 60° . Examination of Fig. III.13 in the region where the initial reflections are thought to be taking place $\beta=75^\circ$ to 85° reveals that there would be a great difference between the magnitudes of the two reflections. The maximum difference is at $\beta=82^\circ$ where the reflectance for the TM polarization is only 0.65 while the TE would be 0.98. This indicates that the TM polarization is absorbed 17.5 times as much as the TE polarization. This large difference is consistent with the proposed mechanism.

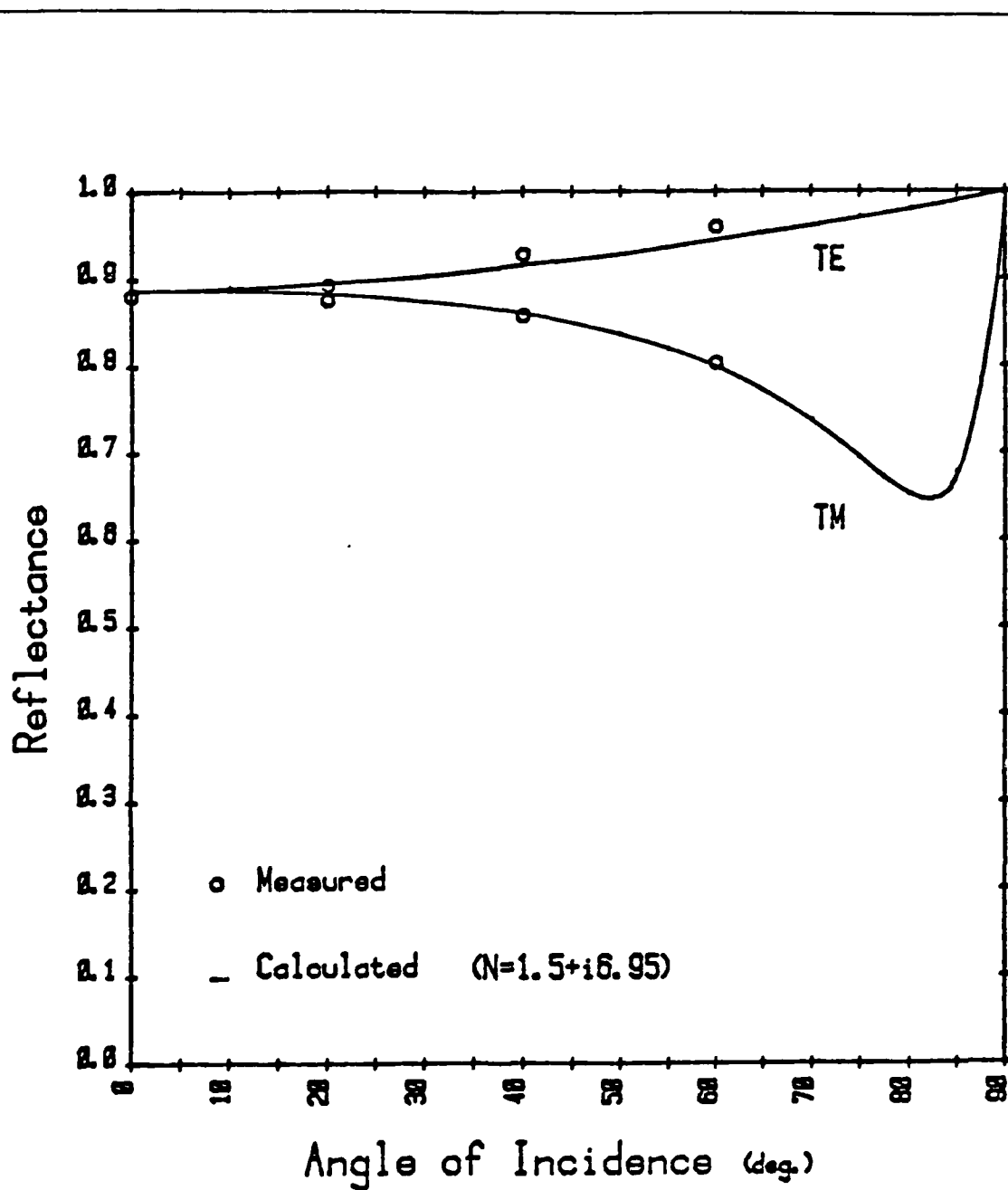


Fig. III.13. Reflectance as a function of angle of incidence for Si_3N_4 at $\lambda=10.6\mu\text{m}$.

IV. SINGLE GROOVE FORMATION STUDY - PART II

A. Introduction

Chapter III investigated the dependence of the shape of laser machined grooves in Si_3N_4 on the angle (ϕ) between the velocity vector of the sample with respect to the incident beam and the electric vector of the incident beam, which is partially polarized. When $\phi=0^\circ$ the groove has a triangular cross section extending perpendicular to the surface, which is the narrowest and deepest observed at any angle. When ϕ equals 90° , the groove is wide and shallow with a rounded bottom. For $0^\circ < \phi < 90^\circ$, the groove cross section was curved.

In this chapter the investigation has obtained additional data on the formation of single grooves in silicon nitride. Groove cross sections and material removal rates have been determined for a wide range of incident beam powers and beam scan speeds. Groove formation has been studied in several different atmospheres and under different focusing conditions. The objective has been to develop a better understanding of the energy balance involved in the reaction resulting in material removal and of the mechanism of absorption of the beam power.

B. Results

Although Chap. III investigated the dependence of the shape of laser machined grooves on ϕ , the variation of material removal rate with ϕ was not determined. This variation was presently determined and is shown in Fig. IV.1 for the $0^\circ < \phi < 90^\circ$ and a speed of 4.2 cm sec^{-1} . At $\phi=0^\circ$, the material removal rate is greatest. It decreases gradually with increasing ϕ reaching its least value at $\phi=90^\circ$. The difference in Z observed between the $\phi=0^\circ$ and $\phi=90^\circ$ orientations decreases as the speed is increased (see Figs. IV.2 and IV.3).

Because of the slight dependence of Z on ϕ , even at low speeds only the $\phi=0^\circ$ and $\phi=90^\circ$ orientations were investigated. It was felt that results for these orientations would reveal all phenomena that might be occurring and that material removal rates for the angles ϕ between 0° and 90° probably could be predicted by extrapolating from measured end points.

B.1 Effect of Speed and Power

For the two orientations of ϕ , a series of scans was performed varying incidence powers and scan speeds. The material removal rates were determined for these scans and are plotted in Figs. IV.2 and IV.3. Figures IV.4 and

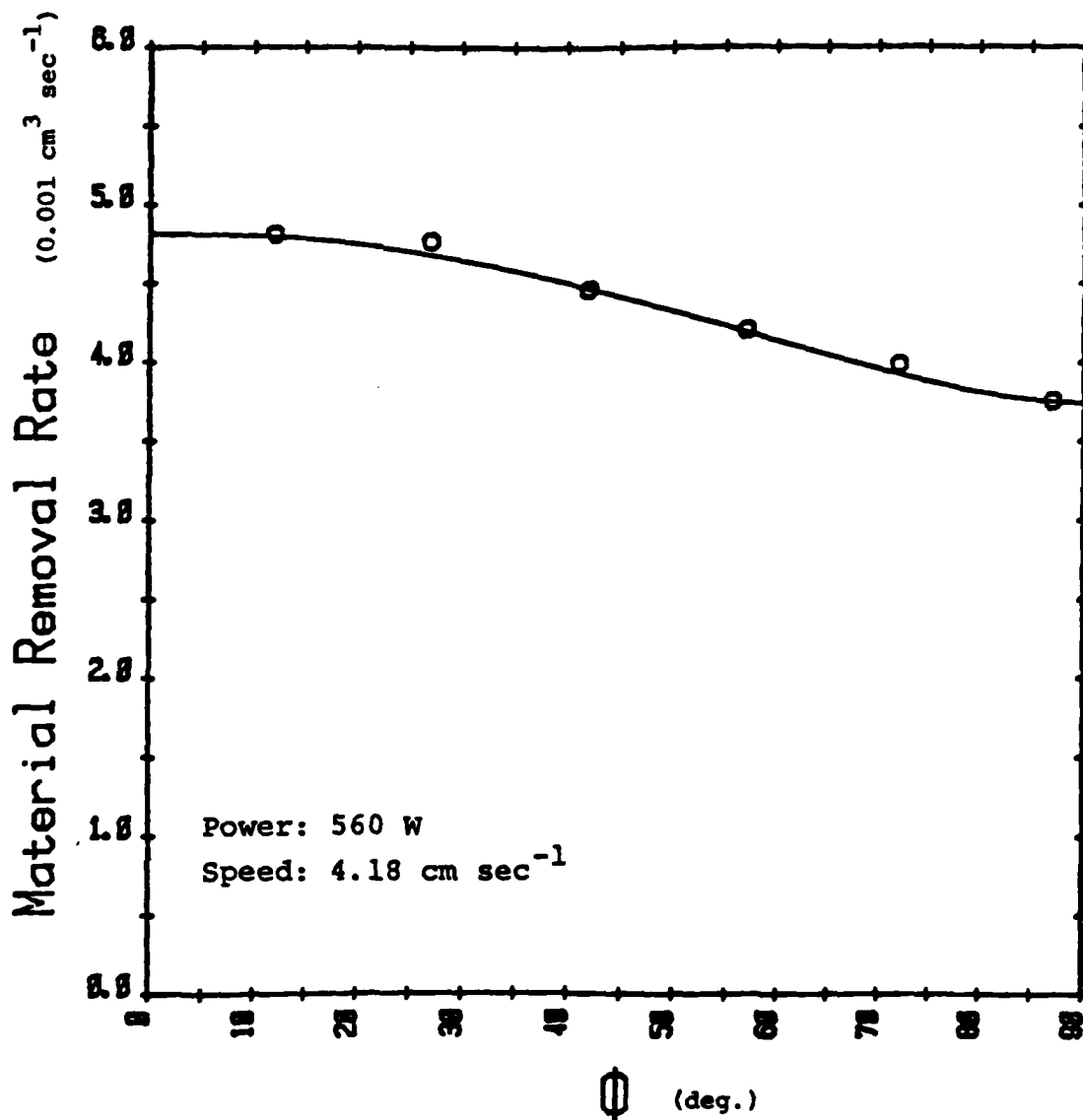


Fig. IV.1. Material removal rates as a function of ϕ .

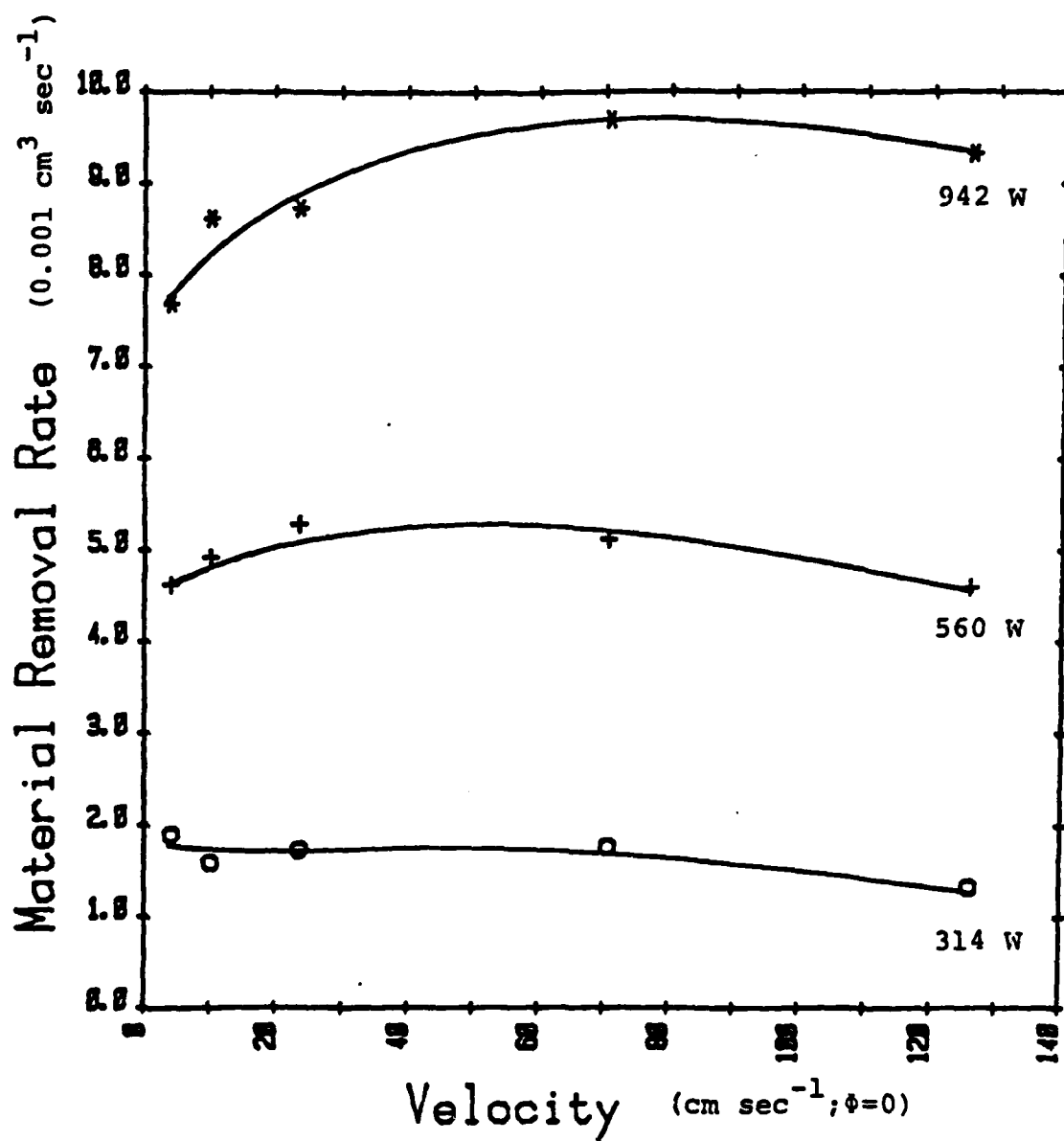


Fig. IV.2. Material removal rates as a function of scan speed and incident power for $\phi=0^\circ$.

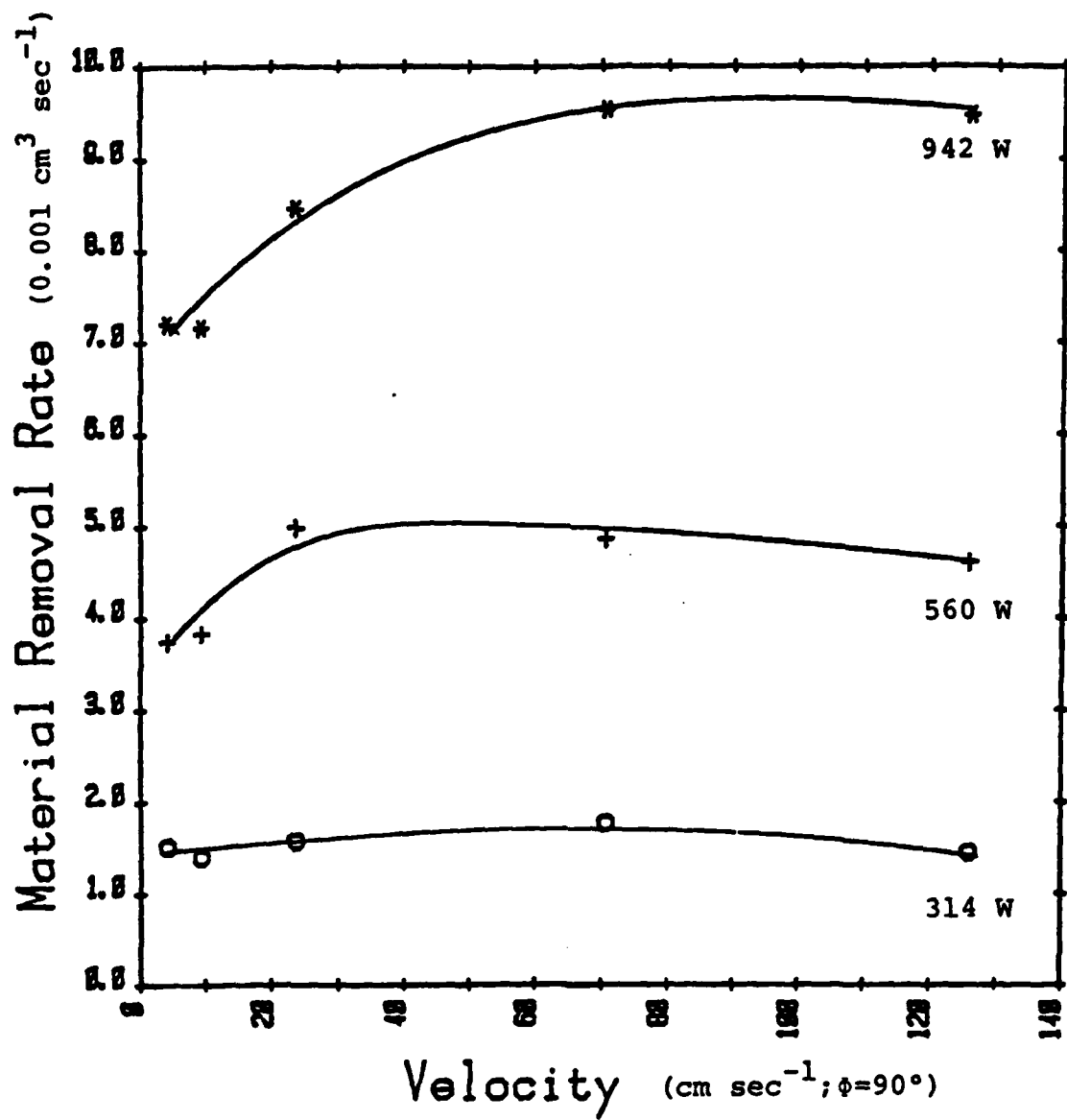


Fig. IV.3. Material removal rates as a function of scan speed and incident power for $\phi=90^\circ$.

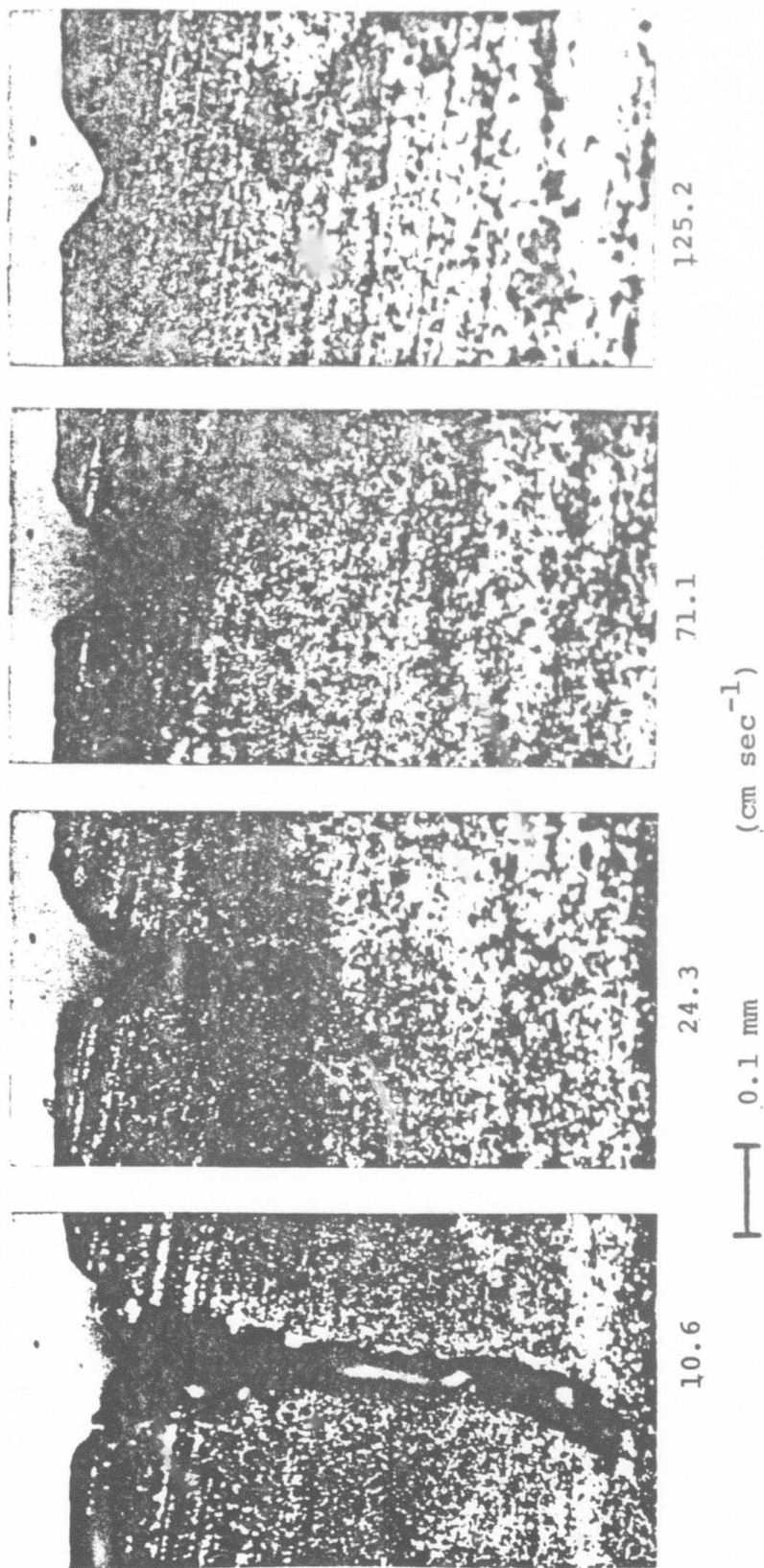


Fig. IV.4. Cross section as a function of scan speed for $\phi=0^\circ$.

IV.5 show typical photomicrographs of groove cross sections for the 560 W scans in Figs. IV.2 and IV.3 respectively.

Two significant trends are seen in the data presented in Figs. IV.2 and IV.3. One trend is the gradual decrease in material removal rates at high speeds, which is least evident at the highest power level. The second is the decrease in material removal rate with decreasing speed at low speeds; this effect is most evident at the highest power level. At lower power levels the effect is reduced to the point where there is no decrease for the 314 W scans. In fact the material removal rate increases with decreasing speed for the $\phi=0^\circ$ orientation at 314 W. Since there are effects that tend to decrease the material removal rate in both the high and low speed ranges, there is a range where material removal rates are maximized.

For both orientations the 560 W scans show a maximum in the 30 to 70 cm sec^{-1} speed range with material removal rates of $4.9 \times 10^{-3} \text{ cm}^3 \text{ sec}^{-1}$ for $\phi=90^\circ$ and $5.2 \times 10^{-3} \text{ cm}^3 \text{ sec}^{-1}$ for $\phi=0^\circ$ orientation. As the incident power is increased, the speed range where maximum material removal rate occurs also increases and shifts to higher values. For the 942 W scans the maximum appears around 70 to 110 cm sec^{-1} with material removal rates on the order of $9.6 \times 10^{-3} \text{ cm}^3 \text{ sec}^{-1}$ for both orientations. For the 314 W scans, the material removal rate does not decrease significantly at lower speeds and the value of Z is $1.8 \times 10^{-3} \text{ cm}^3 \text{ sec}^{-1}$ over a

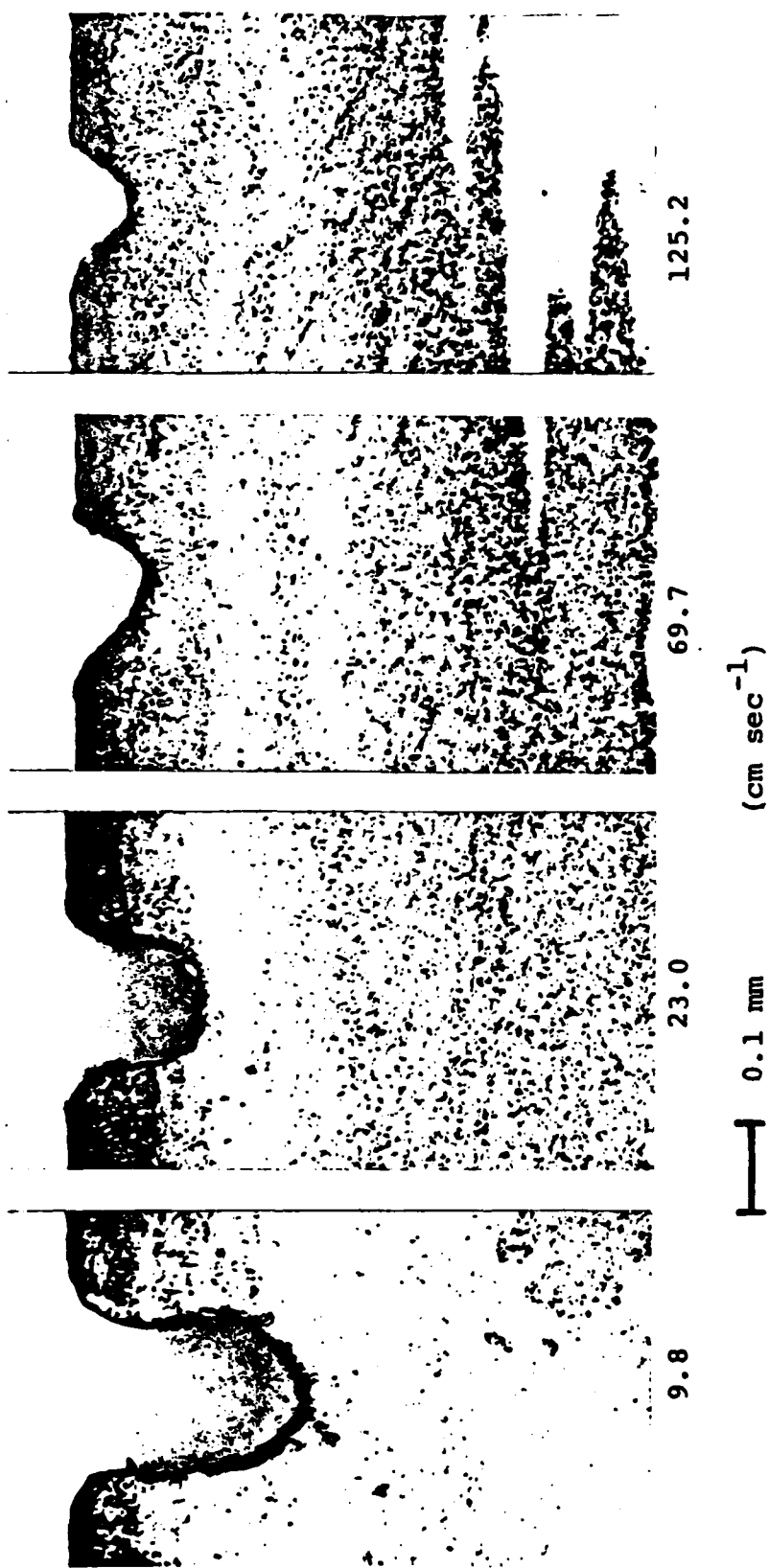


Fig. IV.5. Cross section as a function of scan speed for $\phi=90^\circ$.

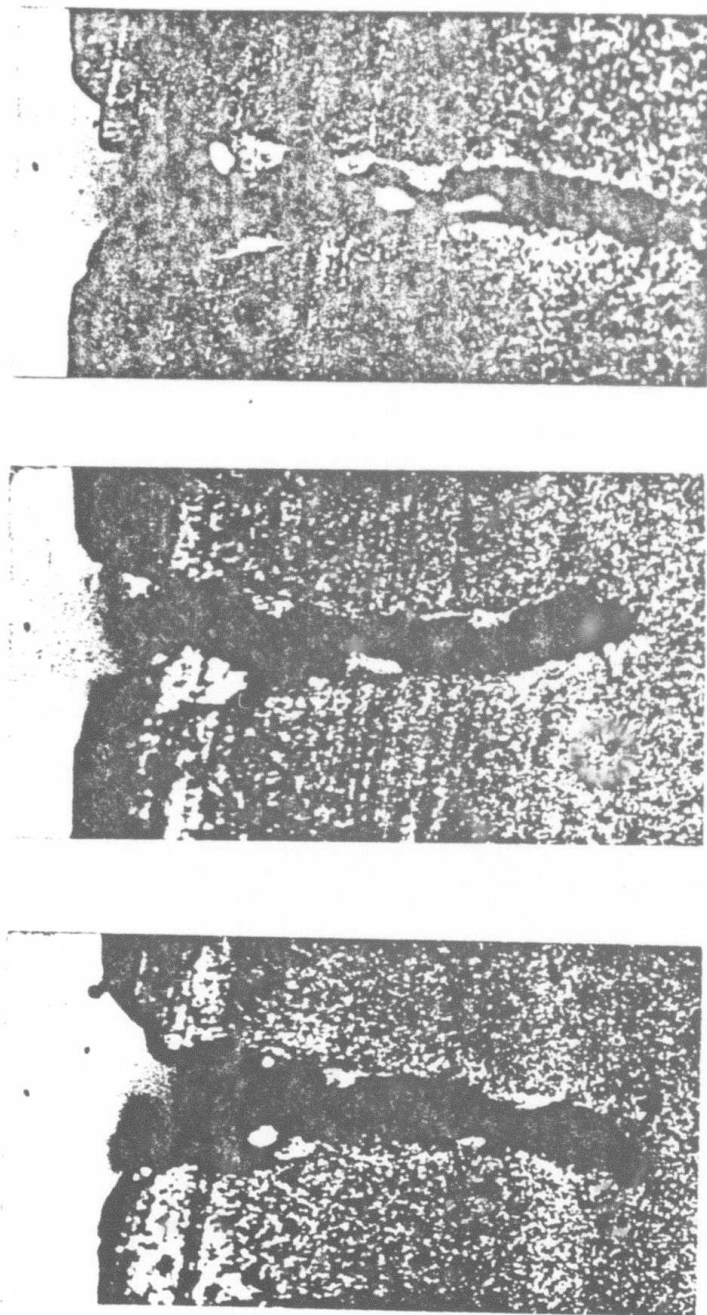
wide speed range centered around 70 cm sec^{-1} .

The difference in material removal rates for the two orientations $\phi=0^\circ$ and 90° has already been mentioned. As seen in Figs. IV.2 and IV.3 this difference becomes smaller as the speed is increased. Also, the groove shapes shown in Figs. IV.4 and IV.5 become similar at the higher speeds although the $\phi=0^\circ$ groove retains a more angular shape even at the highest velocity shown.

As stated previously, for both the $\phi=0^\circ$ and 90° orientations one would expect a symmetrical groove shape based on the polarization induced curvature mechanism, but the groove for the 10.6 cm sec^{-1} scan in Fig. IV.4 is curved. Figure IV.6 shows examples of the variation in cross section for three different grooves with the same parameters, $\phi=0^\circ$, 560 W, and 9.2 cm sec^{-1} . Successive cross sections within the same groove show similar variations with the direction of the curvature shifting back and forth, although the average groove shape is symmetric. This instability in the cross sections is observed primarily in the $\phi=0^\circ$ orientation and usually only in the deepest grooves.

B.2 Effects of Gas

The atmosphere used in laser machining the grooves described in Figs. IV.2 and IV.3 was oxygen. Similar experiments were performed using He and N_2 . Based on



V_s 9.2 cm sec⁻¹; $\phi=0^0$

0.1 mm

Fig. IV.6. Variation in cross section with constant parameters.

previously reported increases in groove depth when a high velocity jet of O_2 was substituted for one of N_2 , it was expected that the material removal rate for He and N_2 would be lower.²⁶ In contrast to the earlier results, however, no detectable differences in groove cross section were detected when the environment was varied, see Fig. IV.7. It appears that the previously observed increase was due to slight unintentional changes in nozzle orientation.

Although no difference in material removal rate was observed when the gas environment was changed, there were differences observed in the ejected material deposited on the top surface of the sample near the groove as well as on the wall of the sample holder. For both the He and N_2 gas environment a brown powder was observed while for the O_2 environment a whitish powder was deposited. It is likely, based on the known colors of SiO_2 and Si_3N_4 , that the white powder is SiO_2 and the brownish powder is Si_3N_4 , however, no chemical analysis was performed to positively identify the powders.

Because the current results differed from previously reported results on the effect of gas environment, the experiments were repeated using a closed chamber to insure that the environment around the sample was pure. The chamber was operated in two modes: one with a static gas environment and the other with the pure gas continually flowing during sample irradiation. The latter mode was

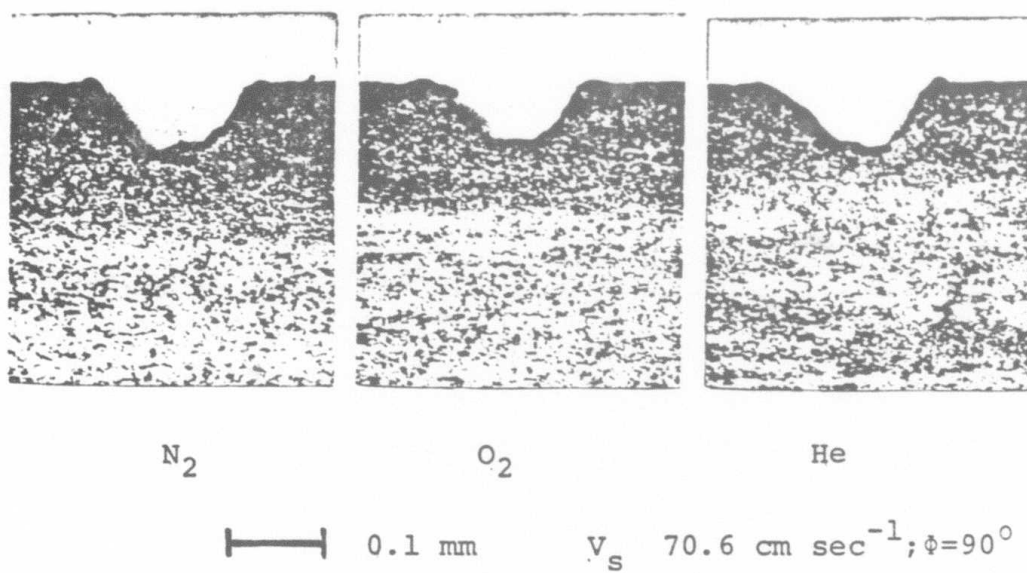


Fig. IV.7. Cross section as a function of gas environment.

more satisfactory because less ejected material was deposited on the NaCl windows with the flowing system. All experiments using the chamber verified that for Si_3N_4 , the material removal rate was the same for O_2 , N_2 , and He atmospheres.

B.3 Effect of Focus

An experiment was conducted where the focal plane which normally was positioned at the top surface was moved both above and below the surface of the sample. Material removal rates were determined for both the $\phi=0^\circ$ and $\phi=90^\circ$ orientations, and for several velocities at 520 W. The results of the focal plane experiment for the laser machining parameters of $\phi=0^\circ$ and 70.6 cm sec^{-1} are given in Fig. IV.8. The determination of material removal rate versus position of focal plane was first done with the standard 12.7 cm focal length lens. It was observed that slightly more material was removed when the focal plane was located above the surface of the sample than when it was located an equal amount below. The experiment was repeated using a 6.4 cm focal length lens with the hope of magnifying the effect due to the smaller focal depth. These results are shown in Fig. IV.9. The difference in material removal rate became much more pronounced using the 6.4 cm lens. The results for the $\phi=90^\circ$ orientation were similar. Throughout this experiment the position of the focal plane

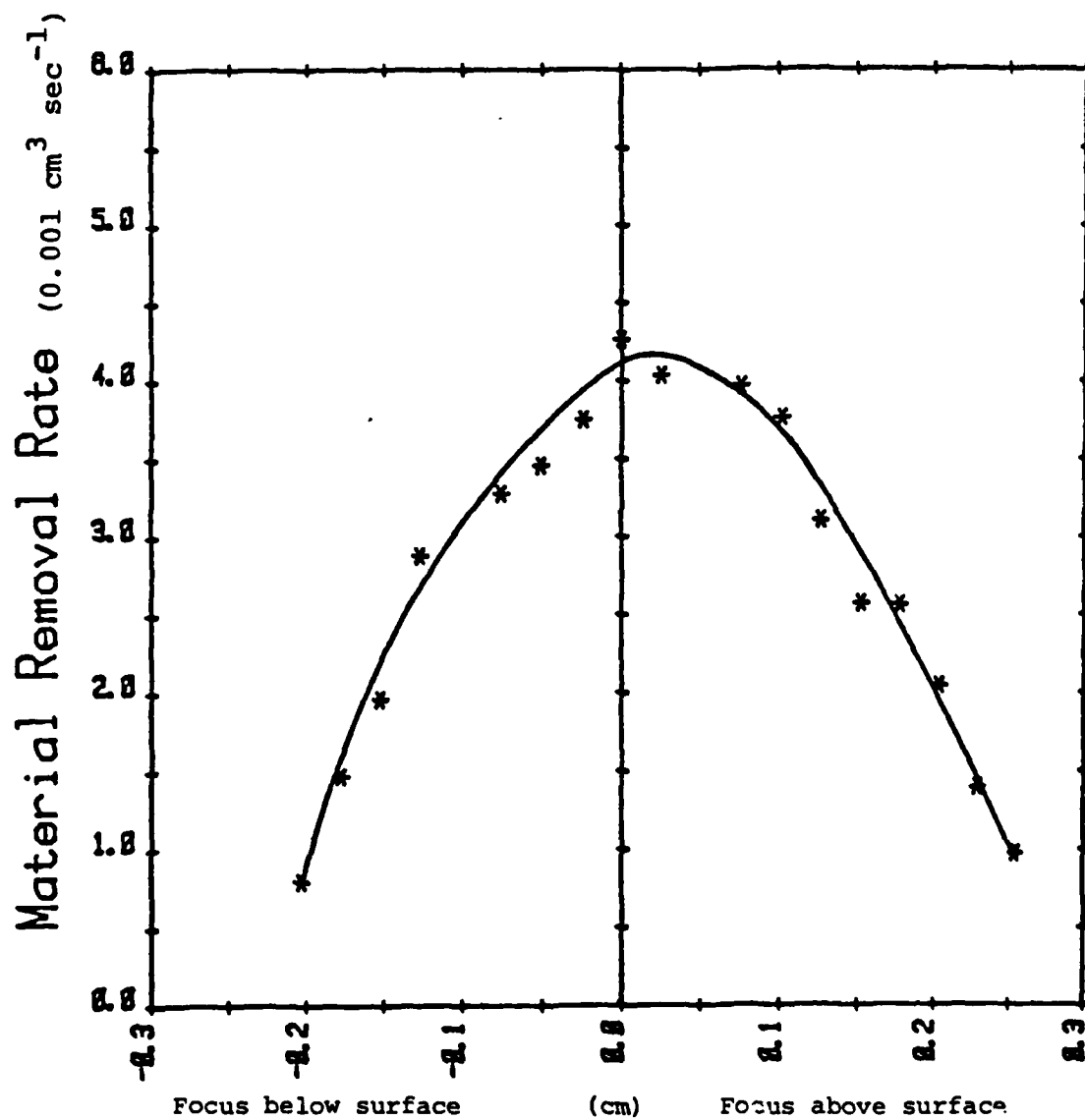


Fig. IV.8. Effects of focal position on material removal rates. 12.7 cm lens.

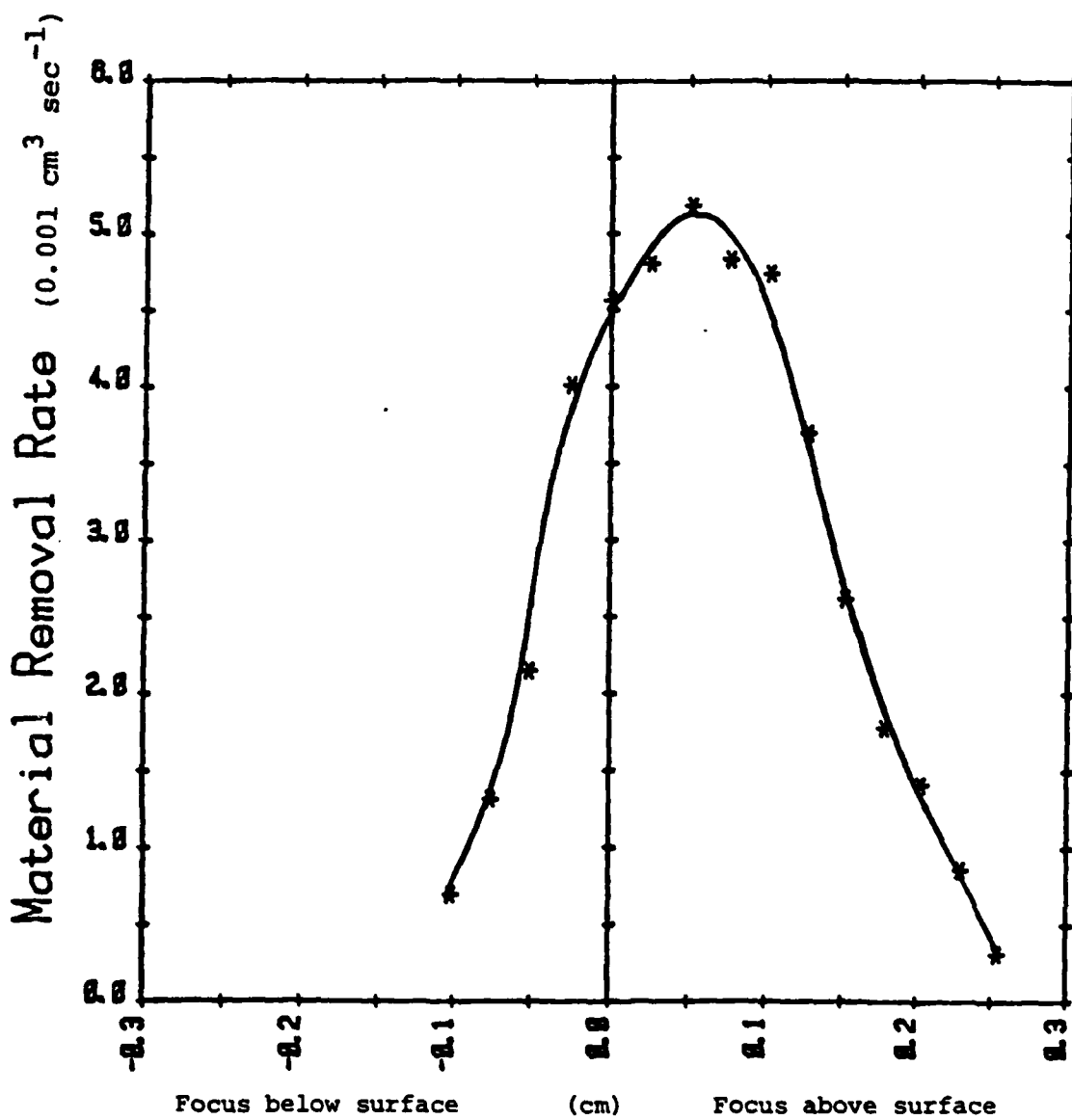


Fig. IV.9. Effects of focal position on material removal rates. 6.35 cm lens.

was repeatedly verified using a slit scanning technique described in Sec. II.D.

Examination of the results for the 6.4 cm focal length lens reveals an unexpected behavior; namely, more material is removed when the focal plane is a critical distance above the sample than when it is located at the surface on the sample (see Fig. IV.9). Approximately 11% more material was removed when the focal plane was raised 0.05 cm. This result implies that more laser beam power is absorbed when the focus is above the sample surface.

A comparison of cross sections produced by the 635 cm focal length lens for various locations of the focal plane shows that when the focus is above the surface and in the region where material removal rate is highest, the width of the groove at the top surface is narrower and the wall steeper than when the focus is at the surface. This shape is observed in both orientations and is quite different from the wide shallow groove shapes seen when the focus is an equal distance below the surface (see Figs. IV.10 and IV.11).

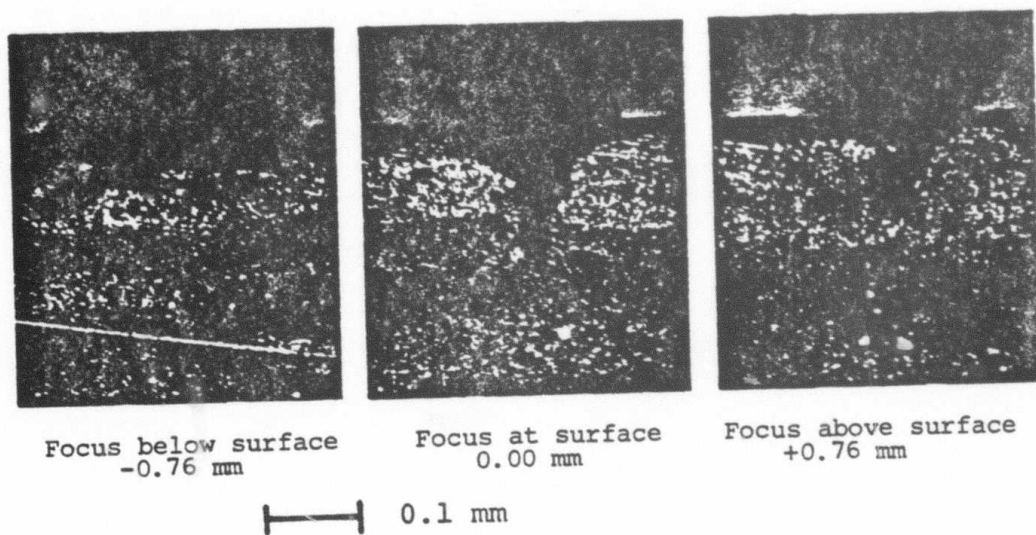


Fig. IV.10. Effects of focal position on cross section.
 $\phi=0^\circ$.

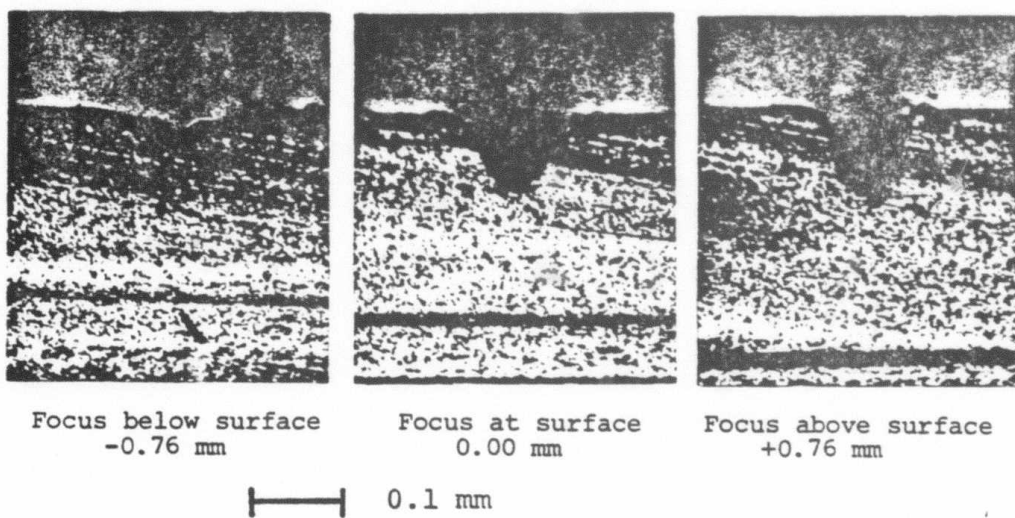


Fig. IV.11. Effects of focal position on cross section.
 $\phi=90^\circ$.

C. Discussion

For a completely efficient process of material removal due to laser heating, where all the incident power is utilized for vaporization, the material removal rate should depend only on incident power. To remove a volume of material from the workpiece, the temperature of the surface must be raised beyond a critical temperature where the kinetics of the vaporization reaction become rapid enough so that the rate of vaporization is limited by the incident power. For a fixed volume of material the amount of energy that is required to heat the volume to the critical temperature plus the heat to vaporize is also fixed. Thus for constant incident power, a constant material removal rate independent of sample speed would be predicted.

The results presented in Figs. IV.1, IV.2, and IV.3 indicate that the material removal process is not completely efficient and must involve losses. The losses will be classified as either reflective or conductive. The factors affecting reflective losses include: the optical properties of the material, beam polarization, groove shape and size, ejecta, and plasma interaction. Factors affecting conductive losses include thermal properties, scan speed, and groove shape and size.

Section IV.C.1 shows how these losses can be included

in a straightforward energy balance model to understand the dependence of Z on power, ϕ orientation, and scan speed. In Sec. IV.C.2 the vaporization reaction is identified. In Sec. IV.C.3 the energy required to heat and vaporize the material is calculated, and an estimate of the minimum fraction of incident energy absorbed is made. This analysis suggests that the fraction absorbed is greater than would be expected from normal infrared absorption mechanisms. In Sec. IV.C.4, possible explanations for the high values of α are discussed such as the presence of an absorption enhancing silicon film layer, the occurrence of temperature dependent Reststrahl bands and plasma effects.

C.1 Factors Affecting Material Removal Rates

Referring to Figs. IV.2 and IV.3 it can be seen that at high scan speeds, the material removal rate decreases gradually, with increasing speed. This decrease can be explained on the basis of the total energy deposited per unit area which decreases with increasing speed. If one translates the sample fast enough, the irradiated volume near the surface will not absorb enough energy to raise its temperature to the point where the vaporization reaction is rapid enough for appreciable material to be removed.

The reduction in material removal rate with

decreasing speed in Figs. IV.2 and IV.3 is thought to be the result of two factors. The first factor consists of the blocking of incoming light by ejecta. As the groove becomes deeper at lower velocities, Si droplets that are formed near the bottom of the groove are blown up into the incoming beam preventing the beam's energy from reaching the bottom of the groove. The deeper the groove the longer will be the path through the ejected material that the incoming beam must penetrate. Consequently, less energy is absorbed by the sample resulting in a lower material removal rate. The second factor is conductive loss. As already discussed, the removal of material requires that the temperature be raised to a critical value. But, since the material to be removed is in thermal contact with its surroundings the temperature of the whole region is raised by thermal conduction. If the sample is slowly translated there is more time for the energy to be conducted away from the volume being irradiated and because of this loss an increase in incident energy is needed to remove the same amount of material.

The lowest power level group, 314 W, shows the least effect of reducing velocity on material removal rate probably due to the smaller groove cross sections for this group. Nevertheless, if the sample is translated slowly enough ($<4 \text{ cm sec}^{-1}$) to obtain very deep grooves, one would still expect a drop in material removal rate similar

to those seen in the higher power scans.

The behavior shown in Fig. IV.1 is more complicated and probably involves several additional factors that influence energy loss. One important factor determining the dependence of Z on ϕ at low speed is the geometry of the groove. As the speed is lowered, the cross sectional area of the grooves must become larger to maintain the same material removal rate. As shown in Figs. IV.4 and IV.5, the grooves tend to become deeper rather than wider because the width is restricted by the diameter of the focussed laser beam with the $\phi=0^\circ$ grooves being much deeper and narrower than the $\phi=90^\circ$ grooves. With this deepening, one would expect the incident light to be more effectively trapped in the groove. This mechanism would tend to increase material removal rate and may be responsible for the higher material removal rates of grooves with a very deep narrow cross section ($\phi=0^\circ$) compared to those with a wide shallow cross section ($\phi=90^\circ$).

The larger material removal rates associated with the deeper grooves, Fig. IV.1, could also be due to polarization. As previously described for orientations near $\phi=0^\circ$ the beam is reflected off the side walls and absorbed by the front wall as the groove is being machined. On the other hand, for orientations near $\phi=90^\circ$ the laser beam is reflected off the front surface. The front surface reflection causes the beam to be guided down and back

into the already machined groove so that it is deposited over a larger area away from the region of material removal and therefore is not as effective in causing vaporization.

Because of the relatively wide range of velocities over which material rates are near a maximum value, see Sec. IV.B.1, it is possible to vary the shape and depth of the groove as shown in Figs. IV.4 and IV.5 without appreciably affecting the material removal rate. This behavior would allow greater flexibility when applying the laser machining process in typical Si_3N_4 applications.

C.2 Mechanism of Reaction

The observation that the material removal rate is the same in He, O_2 , and N_2 (see Sec. IV.B.2) suggests that decomposition is responsible for the removal of material. A review of the high temperature thermodynamics of the silicon nitride system indicates that at temperatures above 1413°C , the decomposition reaction is



while below 1413°C the following reaction applies⁴⁶⁻⁴⁹



Equation (IV.2) is not expected to play a significant role in the removal of material in laser machining due to the low equilibrium pressure of nitrogen over the

temperature range of the reaction and the difficulty of transporting N_2 through the solid reaction layer. For example at 1413°C Pehlke and Elliott found the equilibrium pressure of N_2 to be only 0.001 atmospheres.⁴⁷

The thermodynamic data for Eq. (IV.1) is summarized in the 1979 JANAF Tables.⁴⁹ The temperature of decomposition, which is defined and calculated as the point at which the decomposition pressure of nitrogen reaches 1 atmosphere, is 1878°C . Below this temperature, a thin layer of liquid silicon forms but the reaction is suppressed by this layer which acts as a diffusion barrier. At temperatures greater than 1878°C , the production of subsurface nitrogen at a pressure greater than 1 atmosphere causes the liquid Si layer to be blown off. The upper temperature limit for Eq. (IV.1) is the boiling point of liquid silicon, which is 3241°C . Beyond that temperature sublimation will occur.

C.3 Energy Balance

With the vaporization reaction known one is then able to calculate the energy required to heat and decompose the material contained within the grooves. This information can be used to estimate a minimum value for the fraction in incident power absorbed α for the experimental parameters used in this experiment. The total energy H_D required to decompose Si_3N_4 initially at room temperature

is given by the sum of the energy needed to raise the sample from room temperature to the critical temperature 1878°C , and the energy required to decompose the material at 1878°C . The value of H_D can be found using the following equation:

$$H_D = C_p T + H \quad (\text{IV.3})$$

where

C_p = volumetric specific heat	$3.72 \text{ J cm}^{-3} \text{ }^{\circ}\text{C}^{-1}$
H = heat of reaction	$2.00 \times 10^4 \text{ J cm}^{-3}$
T = temperature increase	1853°C

Substitution of these values into the equation for H_D indicates that $2.7 \times 10^4 \text{ J cm}^{-3}$ is required to both heat and then decompose the Si_3N_4 initially at room temperature. Using this value for the total energy times the material removal rates for the various input powers from Figs. IV.2 and IV.3 one can then calculate the minimum power needed to remove the material. A material removal rate of $1.8 \times 10^{-3} \text{ cm sec}^{-1}$ for the 314 W scan leads to a minimum power of 48.6 W which is required to create the groove. Similarly, the 560 W and 942 W scans need a minimum power of 138 W and 261 W respectively. The material removal rates used to calculate these minimum powers corresponds to the 70 cm sec^{-1} scans of Figs. IV.2 and IV.3 and were chosen because they are near or at the maximum material removal rate at all power levels. From the calculated

minimum powers the minimum absorption can then be found by dividing the minimum powers to create the groove by their respective input powers. The absorption for the 314 W scans is $48.6/314$ or $\alpha=0.155$. Similar calculations give an α equal to 0.246 for the 560 W scans and 0.277 for the 942 W scan.

To further refine the value of the absorption obtained above one can make an estimate of the conductive losses incurred because the volume being removed is in thermal contact with its surroundings. An estimate of the conductive losses requires knowledge of the temperature distribution within the irradiated sample. There have been several analyses published on the temperature distribution produced by a laser beam scanning a surface at constant velocity.⁵⁰⁻⁵² For this work the solution of Cline and Anthony was utilized.⁵¹ Cline and Anthony give an integral solution for the three dimensional temperature distribution produced by a Gaussian heat source scanning a semi-infinite half plane. As in most thermal analyses, Cline and Anthony assume constant thermal properties as well as constant optical absorption values and do not take into account the heats of melting or vaporization. Even with this drawback a reasonable lower bound can be set for the conductive losses.

The coordinate system used by Cline and Anthony is fixed with respect to the material: the laser beam

impinges on the surface $z=0$ at time $t=0$ and moves in the x -direction at a velocity v . Cline and Anthony describe the temperature distribution at a point x,y,z produced by a beam scanning the surfaces at a speed v by the equation:

$$T(x,y,z,v) = \frac{P_A}{C_p D R} f(X,Y,Z,V)$$

where P_A = absorbed power

C_p = volumetric specific heat

D = thermal diffusivity

R = focussed beam radius

f = dimensionless temperature

$V = \frac{Rv}{D}$ dimensionless velocity

and

$$X = \frac{x}{R} \quad Y = \frac{y}{R} \quad Z = \frac{z}{R}$$

The dimensionless temperature is obtained from the integral

$$f = \int_0^\infty \frac{\exp(-F)}{(2\pi^3)^{\frac{1}{2}} (1+\mu^2)} d\mu$$

where

$$F = \frac{(X + \frac{VR\mu^2}{2D})^2 + Y^2}{2(1+\mu^2)} + \frac{Z^2}{2\mu^2} \quad \text{and} \quad \mu^2 = \frac{2Dt'}{R}$$

In order to predict the temperature distribution, values for C_p and D are required. The thermodynamic values used were the integrated averages of published data from

25 to 1878°C. This required the extrapolation of some data to 1878°C. The values obtained and used were $C_p = 3.72 \text{ J cm}^{-3} \text{ }^\circ\text{C}^{-1}$ and $D = 0.058 \text{ cm}^2 \text{ sec}^{-1}$ (see Sec. II.C).

The Cline and Anthony distribution predicts that the maximum temperature at any point within the substrate will be on the surface ($z=0$) along the line of translation ($y=0$) and just behind the center of the beam ($x=x_1$). The value of x_1 is determined by C_p , D , R , and v for the scan speed of 70 cm sec^{-1} , x_1 is equal to -0.00575 cm . The value of the temperature at this position then becomes a linear function of the absorbed power with all other parameters fixed. Cline and Anthony's equations predict that to raise the temperature of the material at x_1 to the critical temperature 1878°C requires that 52 W of power be absorbed, illustrated in Figs. IV.12 and IV.13.

The above analysis indicates that when using a sample scan speed of 70 cm sec^{-1} a minimum of 52 W are needed to heat a groove of zero cross section to the critical temperature. Therefore, 52 W can be regarded as a lower bound for the power required to heat the material contained within any 70 cm sec^{-1} groove independent of groove size. When this new value for heating, 52 W, is combined with the power needed to decompose a groove of specific size, given by HZ, one can obtain a lower bound for power absorbed by the sample to remove material. When this value is divided by the incident power a lower bound for the

$P_{beam} = 100W$
 $BeamArea = 52\mu$
 $Sp\ Heat = 3.72J/cm^3sC$
 $Th\ Diff = 0.058cm^2/sec$
 $Velocity = 70.81cm/sec$
 $Y = 0.00cm$
 $Z = 0.00cm$

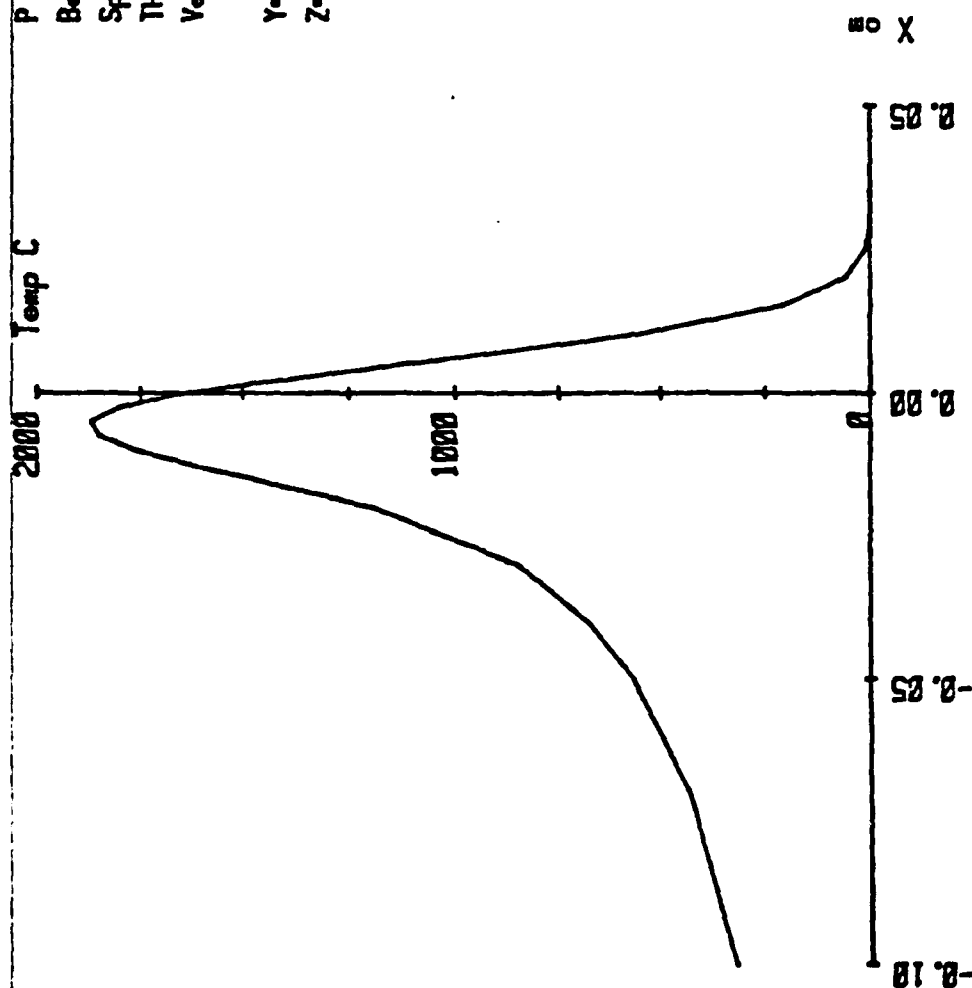


Fig. IV.12. Temperature distribution on the surface of the sample.

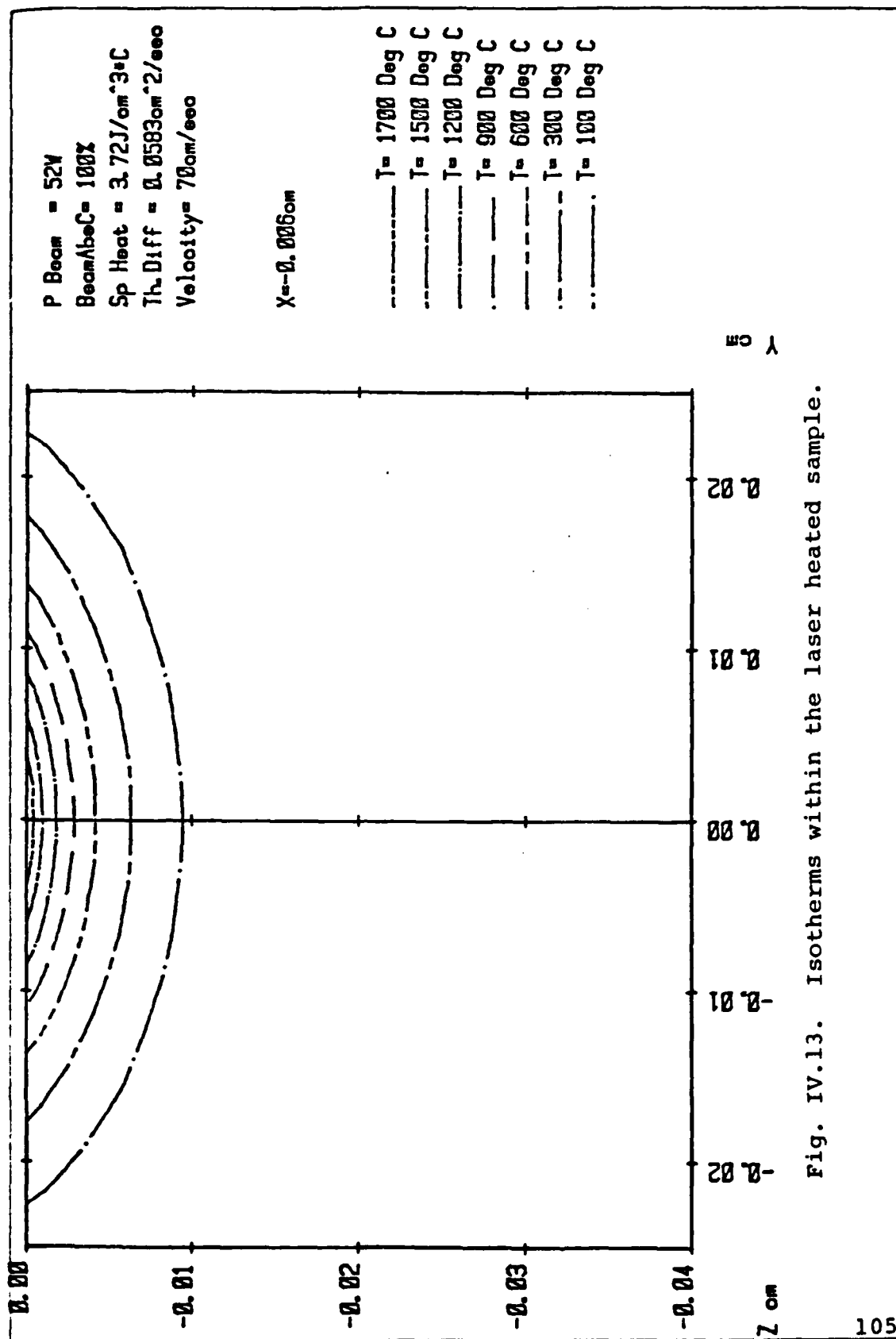


Fig. IV.13. Isotherms within the laser heated sample.

fraction of incident power absorbed α can then be calculated. For the 314 W, 70 cm sec⁻¹ scans the material removal rate is 1.8×10^{-3} cm³ sec⁻¹ which leads to an α of:

$$\alpha = (52W + (2 \times 10^4 \text{ J cm}^{-3}) (1.8 \times 10^{-3} \text{ cm}^3 \text{ s}^{-1})) / 314W^{-1} = 0.28$$

This is nearly twice the minimum absorption ($\alpha=0.16$) calculated when using the Eq. (IV.3) approach.

For the 560 W scan the use of the Cline and Anthony derived lower bound leads to only a minor increase in α from 0.25 to 0.28. This is due to the large value of Z associated with the 560 W scan. For a Z equal to 7.4×10^{-3} cm³ sec⁻¹ both approaches, Eq. (IV.3) and the Cline and Anthony derived lower bound and would give the same values for α . Finally for larger Z the Eq. (IV.3) approach would give the best lower bound for α , i.e., $\alpha=0.28$ for the 942 W scan.

This estimate of $\alpha=0.28$ represents only a minimum absorption due to the decomposition reaction and a minimum estimate of conductive losses. One would expect that the losses due to conduction would become larger as the groove cross section increases with higher incident powers. Furthermore, the actual absorption could be higher due to radiative and conductive losses to the atmosphere, although previous calculations have shown that these effects tend to be small.

C.4 Mechanism of Absorption

The value of 0.28 for the absorption is much larger than one would expect from the optical properties of Si_3N_4 as measured and calculated. As previously stated in Sec. III.C.2 the complex index of refraction was calculated to be $N=1.5+i6.95$ at $\lambda=10.6 \mu\text{m}$. This value of N leads to a normal incidence absorption of 0.11. The difference in absorption between the 0.11 value predicted by the optical properties and the apparent minimum value of 0.28 seen in the actual runs could be due to several mechanisms including light trapping, silicon film layer, Reststrahl bands, and plasma effects. These absorption enhancing mechanisms are discussed in the following sections.

Light Trapping

As previously stated, groove geometry can effect absorption by trapping incident light. But because the increased absorption was observed at 314 W, of the 70 cm sec^{-1} scans, where grooves produced are very shallow, light trapping would not be likely.

Silicon Film

One explanation for an increase in absorption is that a silicon byproduct of the decomposition reaction forms on the surface. Droplets of this substance were seen on the laser machined grooves. The silicon would have a different optical absorption than Si_3N_4 at $10.6 \mu\text{m}$. Published data on silicon give the index as $n=3.42$ at

$\lambda=10.6 \mu\text{m}$ which leads to an absorption of 0.28.⁵³⁻⁵⁴ This value is equal to the minimum absorption of the sample previously calculated. But one would expect the contribution due to the silicon to have effect only after the threshold of the reaction that produces silicon is reached. Depending on the environment the threshold is in the 1413 to 1873°C range. Up to this temperature range $\alpha=0.11$ for pure Si_3N_4 should apply. Cline and Anthony's equation indicates that it would require 354 W of incident power with an absorption rate of 0.11 to reach the bottom temperature range for the production of silicon. Therefore the increase in absorption due to the silicon cannot be completely responsible for the high absorption levels at the lowest powers of the 70 cm sec^{-1} scans.

Reststrahl Bands

The apparent increase in the absorption can also be related to the unique optical behavior of Si_3N_4 near $10.6 \mu\text{m}$. As previously reported in Sec. III.B.5 a reflectance versus wavelength measurement indicated that the Si_3N_4 sample exhibits a Reststrahl or infrared lattice band centered at $\lambda=10.6 \mu\text{m}$. Due to phonon-photon coupling, incident electromagnetic waves with wavelengths lying in the Reststrahl band will not propagate but are reflected at the boundary of the medium. It has been experimentally determined that the Reststrahl bands are affected by temperature. It is this functional dependence that is

possibly responsible for the increase in absorption of the Si_3N_4 sample. The Reststrahl bands are known to respond in two ways to a temperature rise. The first involves the lowering of the peak and the second relates to an overall shift relative to the wavelength. Typical examples of this behavior of NaCl are shown in Fig. IV.14. Both these effects would increase the absorption of Si_3N_4 at $\lambda=10.6 \mu\text{m}$.

The reduction in the peak reflectivity with increased temperature is attributed to the increased coupling and diffusion of the resonant lattice wave into numerous other secondary lattice vibrations. Although most previous investigations⁵⁵⁻⁵⁷ of the effects of temperature on Reststrahl bands generally have been confined to cubic ionic crystals rather than covalently bonded hexagonal structures like Si_3N_4 , they can serve as indicators of the changes in Reststrahl band absorption with temperature that might be expected for the Si_3N_4 material. For NaCl, Hass⁵⁵ showed the effects of temperature on the magnitude of the maximum reflection. At room temperature, the absorption was found to be 0.11. With an increase in temperature of only 340°C the absorption increased to 0.30, finally increasing to 0.48 with a sample temperature of 710°C . If this reduction in reflectivity also occurs in Si_3N_4 the lowering of the Reststrahl band effect would be large enough to account for the increase in absorption.

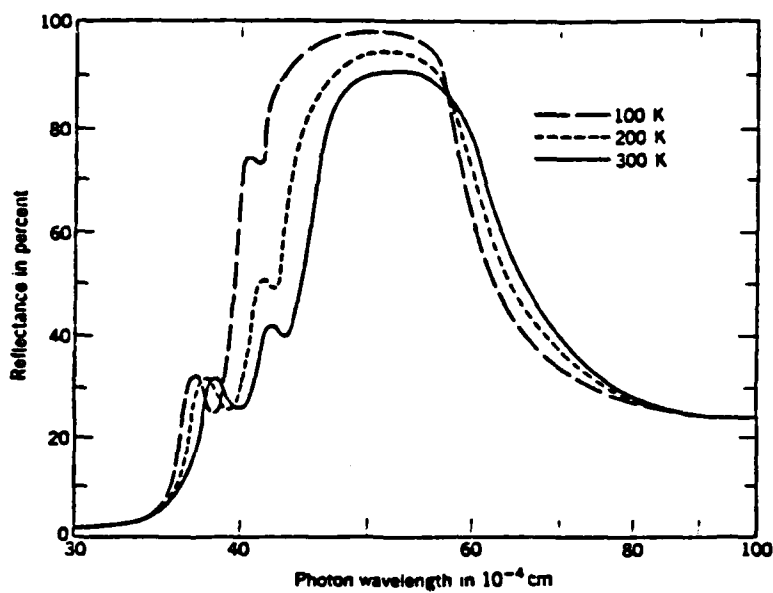


Fig. IV.14. Reflectance as a function of wavelength and temperature for NaCl.⁵⁵

In addition to the lowering of the peak there is also another mechanism associated with the Reststrahl band that can add to an increase in absorption. As the temperature of the sample is increased there is a shift in the central frequency of the Reststrahl band towards the longer wavelengths. This shift is due to a change in force constants arising from the anharmonicity of the crystal bonding. For a fixed incident wavelength any shift in the band will cause the reflectivity to either rise or fall depending on the location of the incident wavelength relative to the band. In this experiment the incident wavelength is centered on the band at room temperature and any shift in the band due to a temperature increase will cause a decline in reflectivity.

Although the magnitude of the shift versus temperature is not known for Si_3N_4 , based on work on other materials⁵⁵⁻⁵⁷ as a guideline and assuming Si_3N_4 behaves in the same manner it is estimated that an increase in temperature from 25 to 948°C could cause an increase in absorption from the room temperature value of 0.11 to 0.24. This increase in absorption does not take into account a broadening of the band with increased temperature which has been observed in many investigations.^{55,56} This broadening effect would tend to reduce the increase in absorption due to the shift.

Both the reduction in peak reflectivity and the

resonate shift occur at the same time and their absorption increase would be additive, and could easily account for the apparent absorption of 0.28 seen in the laser machining experiment. It should be noted that both effects described ignore the fact that the reflectance versus wavelength curve for Si_3N_4 has two closely spaced bands. However, this type of behavior is not uncommon and should not affect the general behavior of the curve with temperature.

Plasma

The previously mentioned factors, which involve the lowering and shifting of the Reststrahl bands resulting in an increase in absorption by effecting simple infrared absorption mechanisms, may not be the only mechanisms responsible for the increased absorption. The results presented in Sec. IV.B.3 give some indirect evidence that the increased energy absorption may be due to plasma enhancement. The plasma more effectively absorbs the incident energy and then transfers its energy to the sample.⁵⁸

One would expect the material removal rate versus focal distance curve to be symmetric around the 0.00 cm position in Figs. IV.8 and IV.9. The incidence energy distribution is equal at the surface for two focal positions that are an equal distance from the 0.00 cm position. The angle of incidence of the incoming beam will be different for the two positions but the maximum

difference is calculated to be only 15.25° for the 6.35 cm lens. Because the incidence angles are near normal and the effect of uneven material removal rates were seen in both orientations $\phi=0^\circ$ and 90° , the asymmetric behavior shown in Figs. IV.8 and IV.9 is probably not related to either polarization or light trapping.

Although the intensity is equal at the surface for the two focal positions that are at an equal distance from the 0.00 cm position the intensity above the surface is not. When the focal plane is above the surface, any plasma that is produced at the surface rises into the region of the focus and therefore a higher intensity region. In this position the plasma can absorb a large part of the energy. When the focus is below the surface the same plasma produced at the surface rises into an ever increasing intensity region. Because of the higher material removal rates for the former case there is a strong suggestion that plasma waves (LSC) are being produced in the higher intensity region above the surface. Normally, an intensity on the order of 10^9 w/cm^2 is required for breakdown of clear air by a CO_2 ($\lambda=10.6 \mu\text{m}$) laser pulse but breakdown at a solid surface can be achieved with much lower peak fluxes, e.g., on the order of 10 kw cm^{-2} .^{59,60}

Although it appears that the asymmetric behavior related to plasma enhancement is greatly reduced for the

12.7 cm focal lens curves, this is not totally unexpected because the magnitude of intensity at focus is four times larger for the 6.35 cm length than the 12.7 cm lens. And, it has been shown that the thermal coupling coefficient α' increases as the incident laser flux is increased.⁵⁸ There is a point where the thermal coupling coefficient will begin to fall off with further increases in incident laser flux. This is the threshold for laser-supported detonation (LSD) plasma wave ignition. The decrease in α' is attributed to an increase in the plasma front propagation velocity with intensity. The intensities in this experiment are thought not to be sufficient to reach the threshold for LSD because one would expect a discontinuity in the curves of Fig. IV.9. If the incident intensity were above the LSD threshold at focus the defocusing would lower the intensity to the LSC region at some point causing a change in slope of α' versus incident intensity. No such point is apparent in the curves of Fig. IV.9. Therefore the intensities used in this experiment are felt to be lower than the laser supported detonation wave threshold.

It has been previously shown in metal targets that under specific conditions of LSC plasma production 3 to 10 times as much thermal energy can be deposited in the sample as would be deposited by normal infrared absorption.⁶¹ The physical mechanism of this increased

absorption has not yet been established. Two possible mechanisms have been considered. The first involves thermal conduction from the laser-heated plasma; the second, the absorption of thermal radiation in the ultra-violet region emitted by the hot plasma. These are based on the experimentally observed behavior of continued heating of the sample for a few microseconds after the end of the laser pulse and heating of the sample beyond the area of the focussed laser beam. Most investigations of thermal coupling and plasma properties involve the use of a pulsed laser while the situation currently being considered involves CW laser irradiation. Correlating the results is very difficult because the operating characteristics of the lasers and target materials involved are frequently very different. The work of McKay et al.⁶¹ using an Al target showed that target heating by thermal radiation alone appeared to be insufficient to explain the enhanced absorption observed and they concluded that thermal conduction must contribute significantly to target heating.

There is no simple way of knowing the relative magnitude that each absorption enhancement mechanism plays in the laser machining of Si_3N_4 . Light trapping probably does not play a role in the lower power scans but can become effective for the deeper grooves of the higher powers. The silicon film would increase the absorption for

all situations where grooves are created but it does not account for the increase in α that must take place before the creation of any silicon layer at the lowest power. Of all the mechanisms proposed only the lowering and or shifting of the Reststrahl bands can account for an increase in absorption before any groove is created and therefore the Reststrahl band must be important to the overall absorption enhancement. Finally increases due to a plasma process again can only occur after the creation of the groove as proceeded. But the increase in material removal rate when the focus is above the surface for the 6.35 cm lens curve, Fig. IV.9, indicates that the absorption enhancement due to plasma processes is probably also very important.

V. OVERLAPPED GROOVE FORMATION STUDY

A. Introduction

This chapter deals with the overlapping of laser vaporized grooves leading to shaping. A model has been previously developed that predicts the surface roughness R and the material removal rate Z for surfaces produced by overlapping laser vaporized grooves.²⁶ According to this model, which considers the effects of varying incident power, scan speed and groove spacing (feed), both Z and R decrease as the groove spacing decreases. Subsequently, it was found that although the predicted behavior occurs over a wide range of groove spacings at very small groove spacings, the opposite behavior occurs. This investigation was undertaken to determine the origin of this unpredicted behavior.

The previous analysis assumed that the shape of a single pass groove cut by the laser would be repeated during multiple overlapping even though the laser is removing material at the edge of a previously machined groove rather than from a flat surface. In this investigation, it was found that under certain situations the shape of the overlapping groove differs significantly from that of the single pass groove. Based on this result,

more accurate methods of predicting Z and R are presented.

In the previous work, the effect of laser machining on mechanical properties was not determined. Because Si_3N_4 lacks fracture toughness, $K_{IC}=3.25$ to $4.8 \text{ MN m}^{-3/2}$, its strength is highly dependent of the presence of flaws or stress raisers. It was expected that laser machining would decrease strength because by its very nature laser machining produces well defined overlapped grooves that can act as stress raisers. Also, microcracks may be produced as a result of laser induced thermal stresses. To investigate these effects, 4-point bend specimens were tested with laser machined surfaces. The results indicated an overall reduction in the modulus of rupture accompanied by a greatly reduced scatter.

The selection of laser machining to shape Si_3N_4 involves economic considerations. These considerations are discussed and it is concluded that laser machining is a technologically feasible method for the shaping of Si_3N_4 .

B. Results

B.1 Beam Guiding - Surface Roughness

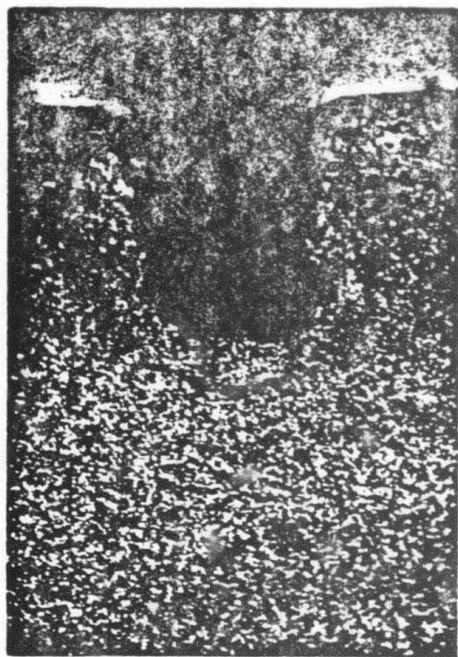
An investigation was undertaken to study the origin of the increase in roughness with a decreasing feed observed at small feeds. A number of specimens were machined with a laser using a series of different feeds. One incident power level, 560 W, and several different single groove scan speeds ranging from 9.1 to 238 cm sec⁻¹ were employed. The investigation was carried out for two scan orientations, $\phi=0^\circ$ and 90° where ϕ is the angle between the electric vector in the focused laser beam and the velocity vector of sample translation. It has been shown in Chap. III that the two orientations produce distinctly different single pass groove cross sections because of polarization effects.

For all parameters of the experimental matrix three types of surfaces were produced: surfaces with single pass grooves, surfaces with two overlapping grooves, and surfaces with multiple overlapping grooves. The largest feed investigated corresponded to the situation where adjacent grooves did not show the effect of interaction. For feeds where interaction did occur both the two pass and multiple overlapping grooves were distorted due to

beam guiding.

A typical example of this type of distortion is shown in Fig. V.1. Figure V.1(a) shows a symmetric single pass cross section, while Fig. V.1(b) illustrates the nonsymmetric cross section of a two pass groove. Each pass was made by translating the specimen in the same direction and employing the same speed and power as in Fig. V.1(a). The groove spacing, which was determined by the feed was 0.015 cm. This type of behavior was seen throughout the range of velocities investigated for both ϕ orientations and plays a very large role in determining the finish attained in laser machining by multiple overlapping of grooves.

In the use of multiple overlapped grooves, the beam guiding effect creates two types of surfaces. The first, which was previously observed, is characterized by an increase in roughness with decreasing feed. The second is characterized by deep initial grooves followed by a region of grooves of moderate depth and then a region where the grooves become shallow as the end of the cut is approached. Both these effects are illustrated in Figs. V.2 to V.5, which show multiple pass groove cross sections for a series of feeds. The grooves which were formed at a low speed (9.1 cm sec^{-1}) and the $\phi=90^\circ$ orientation, are very representative of those seen at higher velocities and the $\phi=0^\circ$ orientation.



A. Single Pass



B. Two Pass ($f=0.015$ cm)



0.1 mm

V_s 9.1 cm sec⁻¹; $\phi=90^\circ$

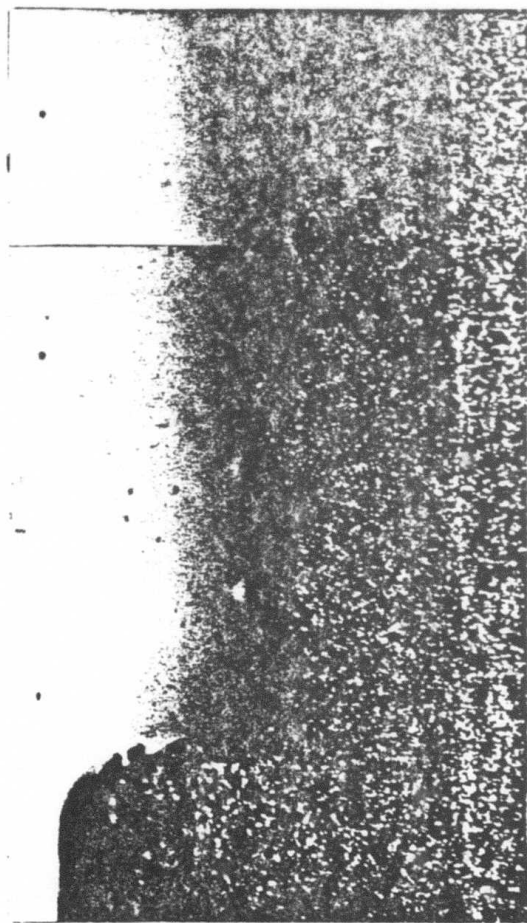
Fig V.1. Distortion of cross section due to beam guiding.



— 0.1 mm

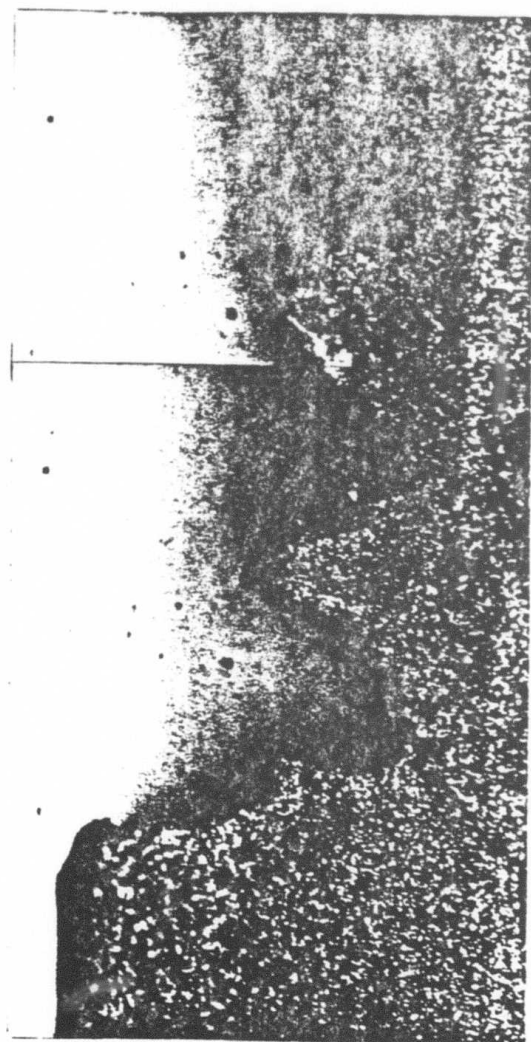
V_s 9.1 cm sec⁻¹; $\phi=90^\circ$

Fig. V.2. Multiple pass cross section with a feed of 0.022 cm.



 0.1 mm
 V_s 9.1 cm sec⁻¹; $\phi=90^\circ$

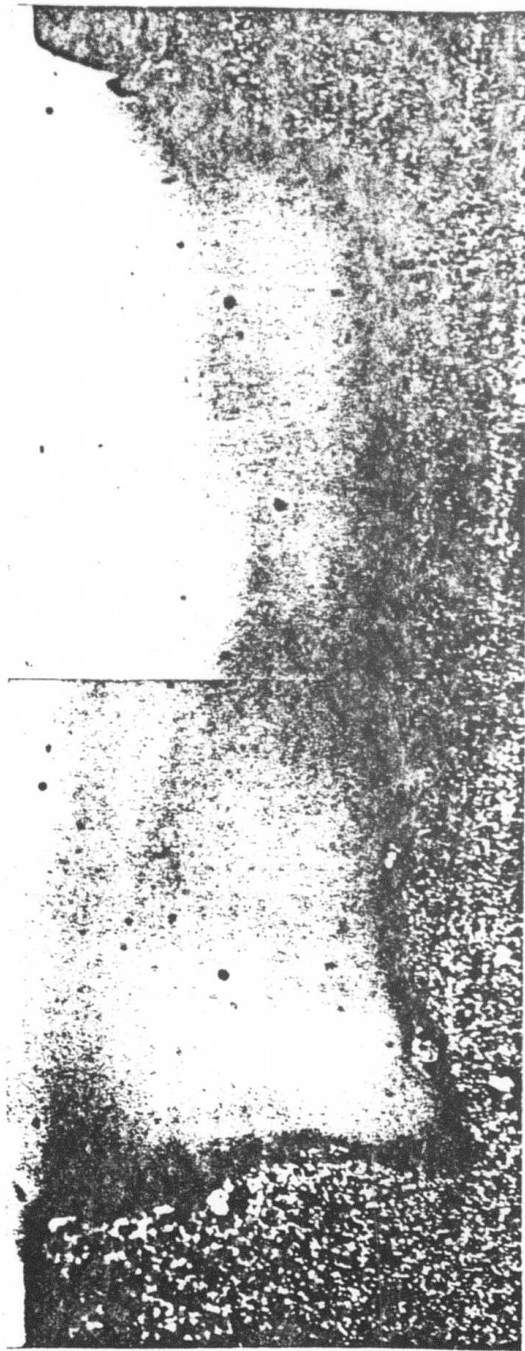
Fig. V.3. Multiple pass cross section with a feed of 0.0178 cm.



— 0.1 mm

V_s 9.1 cm sec⁻¹; $\phi=90^\circ$

Fig. V.4. Multiple pass cross section with a feed of 0.015 cm.



— 0.1 mm

V_s 9.1 cm sec⁻¹; $\phi=90^\circ$

Fig. V.5. Multiple pass cross section with a feed of 0.010 cm.

The single pass groove cross section corresponding to power, speed, and ϕ orientation used in Figs. V.2 to V.5 are shown in Fig. V.1(a). Figure V.2 shows the bottom surface of a multiple pass laser machined sample, machined at a feed of 0.022 cm. At this feed, a scalloped bottom surface as would be expected from the repetition of the single pass groove was observed. As the feed was reduced to 0.0178 cm, Fig. V.3, the scallops seen in Fig. V.2 were almost completely removed and the surface became very smooth. Further reduction of the feed would be expected to further increase the degree of smoothness, however, this was not observed. Once the feed becomes significantly smaller than the width of a single pass groove the beam guiding effect becomes important. Figure V.4 shows an example of increasing surface roughness with decreasing feed. A feed reduction from 0.0178 cm in Fig. V.3 to 0.015 cm in Fig. V.4 creates a large increase in roughness.

In Fig. V.4 the first laser machined groove is on the left. Only a small ridge from the first pass remains. During the second pass, the groove spacing is sufficiently small to cause a large portion of the laser beam to be guided to the left by the walls of the first groove giving a cross section similar to Fig. V.1(b). During the third pass the effective groove spacing has been increased because the beam was guided to the left during the second pass. Thus the third groove is not guided by the

previously machined surface and is similar to a single pass groove. The fourth pass is then guided similarly to the second pass and the process repeats giving the highly contoured profile cross section in Fig. V.4. It should be noted that this gives a repetitive groove shape, the spacing of which is not equal to the feed.

The second type of multiple pass surface varies in depth as shown in Fig. V.5 for a feed of 0.010 cm. This surface is very typical of that produced by laser machining where the feed is reduced to the point that every groove after the first is always guided to the left by the previous grooves. This creates a depression of the type shown in Fig. V.5. For very small feeds, the depression can become very deep relative to a single pass groove and also can undercut the wall formed by the first pass. Such undercutting is only slightly evident in Fig. V.5. As one moves to the right from the initial depression, there is a region in which the depth remains constant. From this region the bottom surface gradually rises. This gradual rise occurs over a distance corresponding to many passes. Further information regarding the occurrence of beam guiding is given in Sec. V.B.2.

B.2 Material Removal Rate

In addition to the investigation of the origin of the increased roughness, material removal rates (Z) were

determined for the various groove spacings. The material removal rate was previously calculated for single pass grooves. This was done by multiplying the area of the single pass groove, as measured from a photomicrograph with a polar planimeter by the sample translation speed. For multiple overlapping grooves, the average material removal rate equals the total area of material removed times the sample translation speed divided by the number of passes. The results are shown in Fig. V.6, where the material removal rate is plotted for different feeds and velocities in the $\phi=0^\circ$ orientation. Both $\phi=0^\circ$ and 90° orientations gave similar results.

In Fig. V.6 it can be seen that laser machining of Si_3N_4 produces a constant material removal rate over a wide range of feeds. It was found that this constant rate was equal to the material removal rate for a single pass groove for the same power, scan speed, and ϕ orientation. For each curve corresponding to a different velocity, there is a point beyond which the material removal rate begins to decrease with decreasing feed. The feed corresponding to the onset of this decrease decreases with increasing velocity. For the 9.12 cm sec^{-1} velocity curve, the onset is $11 \times 10^{-3} \text{ cm}$. This value is reduced to approximately $3 \times 10^{-3} \text{ cm}$ for the 238 cm sec^{-1} translation speed curve. This decrease in material removal rate is not related to the decrease predicted by the machining

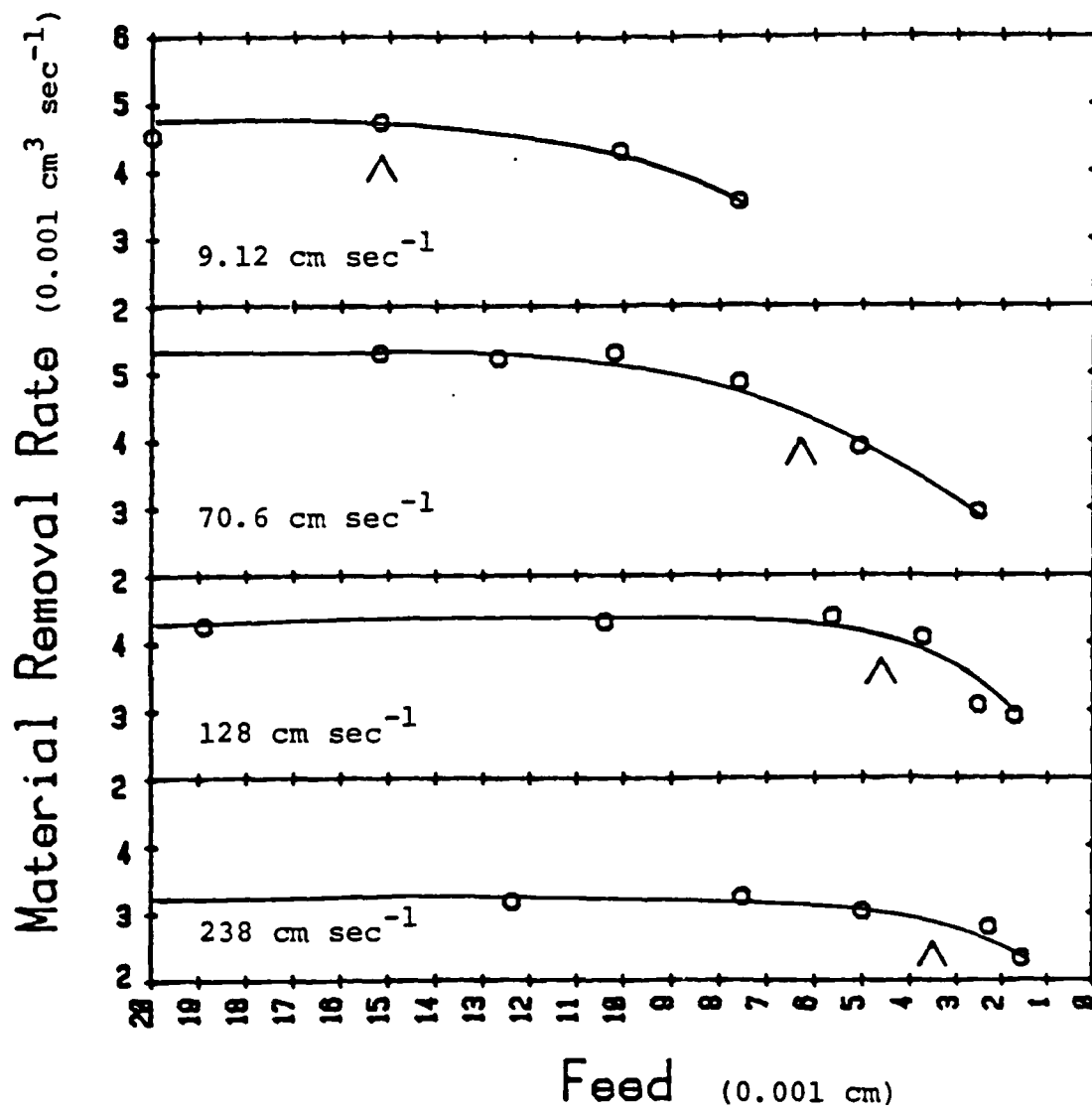


Fig. V.6. Material removal rate as a function of feed and velocities.

analysis previously proposed which assumed the shape of a single pass groove would be repeated during multiple overlapping but rather it is also a result of beam guiding. Because of the beam guiding by the already machined walls, the incident energy is deposited over a larger area at small feeds than at large feeds and, therefore, is not as effective in removing material.

A problem associated with determining material removal rates at very fine feeds where the onset of decreasing Z is observed is the previously mentioned variation in groove depth from the initial to the final grooves. Measurement in the initial region of deep grooves would give high values of Z while measurement near the shallow region near the end of the cut would give low values of Z .

The variation in groove depth associated with the non-steady state regions of the initial and final grooves along with the lower material removal rates makes machining with very fine feeds undesirable. Therefore, the values of groove overlap where the onset of light guiding was observed for the various velocities and orientations were determined. The onset was defined as either when the bottom surface cross section was no longer repetitive corresponding to the feed or when the groove depth varied from the initial to the final grooves. The arrows in Fig. V.6 indicate the values of groove overlap determined

for the various scan speeds of the $\phi=0^\circ$ orientation. The numerical value of groove overlap represented by the arrows in Fig. V.6 is the average of adjacent feeds that do and do not exhibit beam guiding behavior. For situations where the difference between feeds was larger than 0.05 cm the numerical value for the onset was taken to be the value of the feed where beam guiding was first observed. For example, for the experimental parameters used in Figs. V.2 to V.5 this definition of the onset of light guiding leads to a groove overlap of 0.0165 cm.

Because the onset of beam guiding is associated with the overlapping of grooves, it is convenient to compare the groove overlap at onset to the width of a single pass groove. In this case the width is defined as the width of the groove at the e^{-2} value of the depth. For the experimental parameters used in Figs. V.2 to V.5 (9.42 cm sec^{-1} ; $\phi=90^\circ$) the width was 0.01846 cm which when divided into the value of groove overlap at the onset of light guiding gives a ratio, δ , of 0.0894. Similarly δ was determined for other velocities and orientations and is plotted as a function of translation speed in Fig. V.7. The groove widths used to obtain δ are also given in Fig. V.7 as a function of velocity.

In Fig. V.7 one can see that δ for the 9.12 cm sec^{-1} , $\phi=0^\circ$ case is 0.987 which is 14% higher than for the $\phi=90^\circ$ orientation. This increase in δ for the $\phi=0^\circ$ orientation

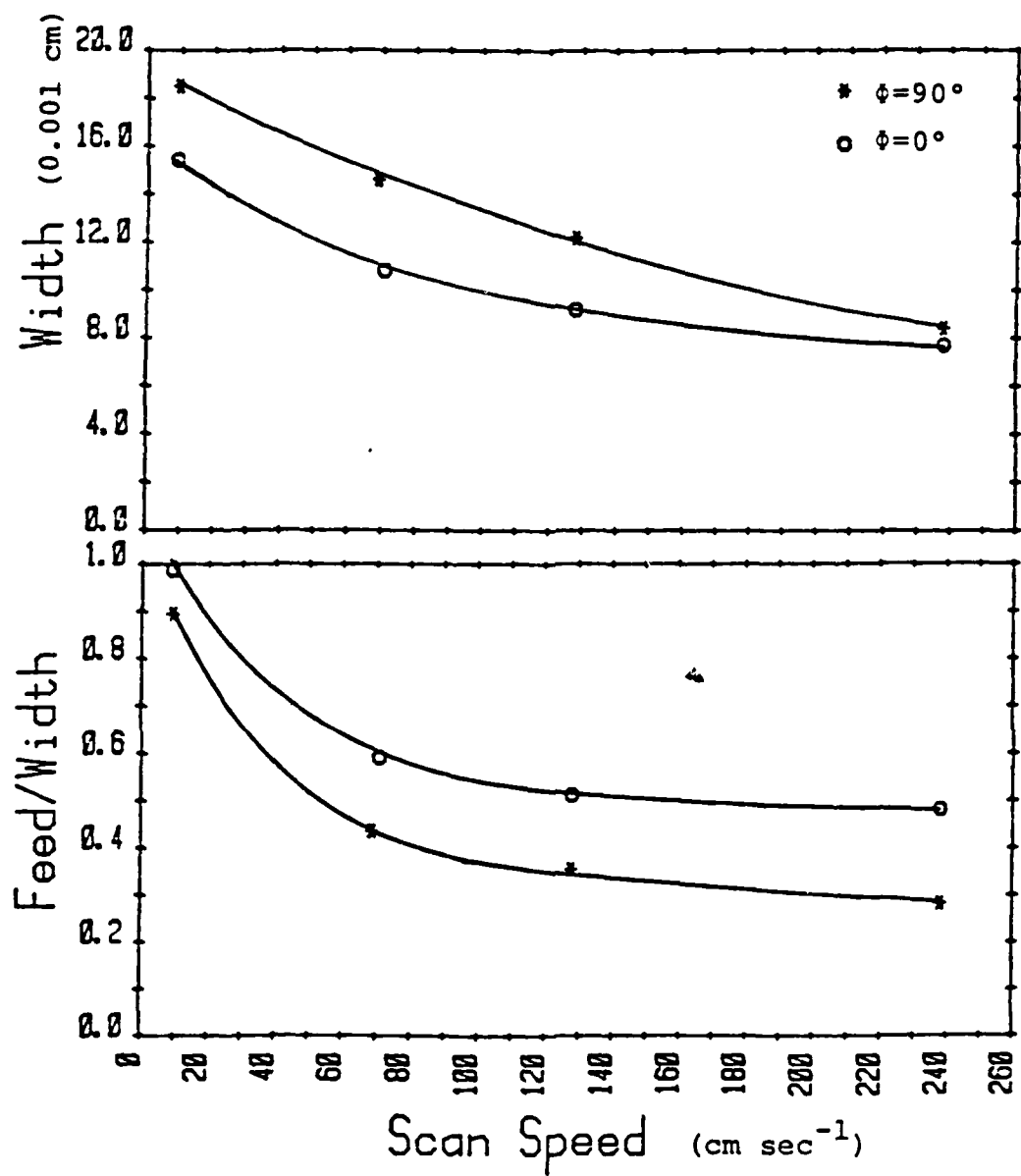


Fig. V.7. Width and feed/width at beam guiding onset as a function of scan speed and ϕ orientation.

was observed at all scan speeds but was largest at highest velocities. For the 238 cm sec^{-1} scan, δ was 70% larger for the $\phi=0^\circ$ orientation than for the $\phi=90^\circ$ orientation. Another notable feature in Fig. V.7 is the decrease in δ for both orientations with increasing scan speed at high scan speeds, the value of δ becomes a constant approaching 0.5 for $\phi=0^\circ$ and 0.3 for the $\phi=90^\circ$ orientation.

When not affected by light guiding the bottom surface follows the conventional behavior of obtaining smoother surfaces with reduced feed, but the minimum feed for laser machining is determined by the ratio δ . Therefore, the smallest δ is desirable, which as Fig. V.7 indicates is associated with the faster translation speeds. Unfortunately, the creation of smoother surfaces with higher translation speeds is done at a cost of lower material removal rates. It has been previously demonstrated in Sec. IV.B.1 that for a fixed incident power there is an optimum translation speed giving a maximum material removal rate. Therefore one must balance these two requirements to obtain the most efficient laser machining process. For example, the smoothest surface obtained in this investigation was with the 238 cm sec^{-1} scan giving a surface roughness of $2.88 \text{ }\mu\text{m}$, see Fig. V.8 showing a surface profile trace. This smoothness was obtained at the cost of a 35% reduction in material removal rate over the optimum removal rate seen at 70 cm sec^{-1} .

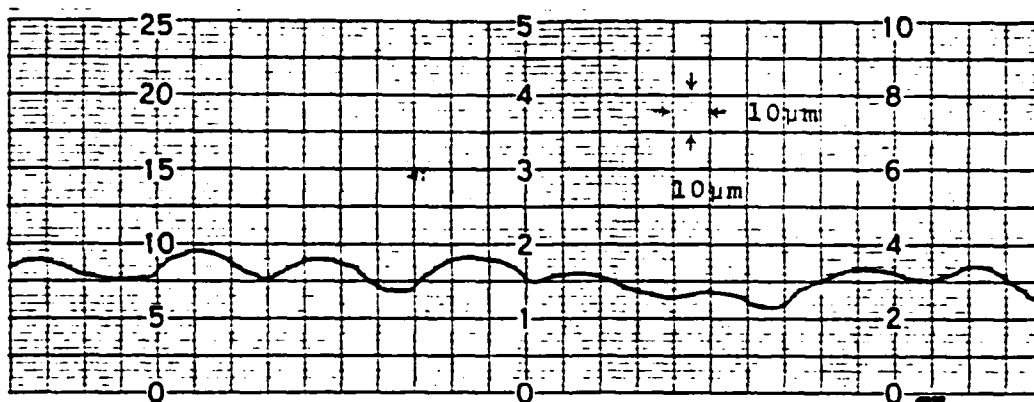


Fig. V.8. Surface profile trace of a sample machined with a scan velocity of 238 cm sec^{-1} ; $\phi=0^\circ$ and a feed of 0.00378 cm .

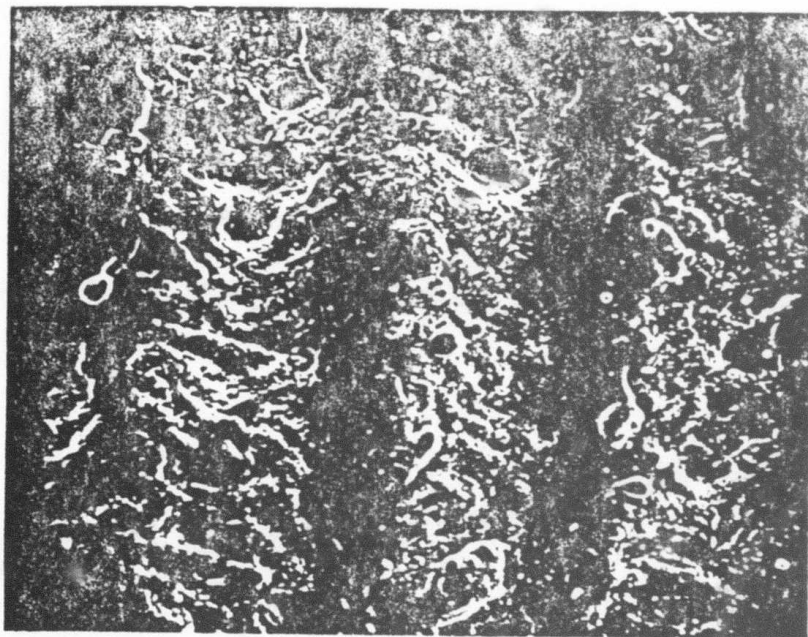
B.3 Additional Features of Laser Machined Surfaces

Another feature of the laser machined surface is a silicon layer formed as a product of the Si_3N_4 decomposition reaction. Although much of the liquid silicon product is blown off the surface by gaseous nitrogen, which is also a product, some wets the surface, and tends to solidify as a continuous smooth layer on the side of the groove most recently formed by the laser beam. Figure V.9 shows a region covered by the silicon layer along with a rougher adjacent region. Energy dispersive x-ray analysis (EDX) showed qualitatively that both the wetted and rough regions contained more silicon than the bulk Si_3N_4 with the rough area being the lower of the two.

For grooves formed at high speeds, the silicon layer is continuous and its depth is fairly uniform but for those formed at lower speeds silicon forms spherical globules. These globules produce additional roughness at the surface.

B.4 Flexural Strength

Specimens with various laser machined surfaces were tested in 4-point bending. The test matrix consisted of seven sets of samples, A through G. The first set, A, was produced using only conventional diamond grinding and was used as a standard which could be compared to previously published results⁶² to verify the present experimental procedures. All sets were tested using a 4-point flexural



┌─┐ 10 μm

Fig. V.9. SEM photomicrograph illustrating the solidified silicon layer.

strength testing fixture designed to reduce errors in the bend test.⁶³ This included rounded steel knife edges rounded to a radius of 3.18 mm, provisions for the alignment of the bearing surfaces, and an outer and inner span of 2.54 cm and 1.27 cm, respectively. All tests were conducted at room temperature in air using an Instron⁶⁴ Model TTC with a constant cross head speed of $0.0508 \text{ cm min}^{-1}$.

All bend specimens had the same direction, $0.669 \times 0.417 \times 3.5 \text{ cm}$, with the long edges of the tension surface bevelled, 0.0794 cm at a 45° angle. The samples only had their tension surface laser machined with all other surfaces being ground employing a 520 grit resinoid bonded synthetic diamond wheel and an infeed of 0.000762 cm per pass. The final grinding was done parallel to the long axis of the specimen. Because of the sensitivity of NC-132 to flaws and stress raisers, the smoothest possible laser machined surface was used. This was obtained with a scan speed of 238 cm sec^{-1} and an incident power of 560 W. For this scan speed, a groove overlap of 0.00378 cm was chosen so that the laser machining would not be influenced by the beam guiding effect previously discussed.

Sets B and C were laser machined using the $\phi=90^\circ$ orientation while sets D, E, F, and G used the $\phi=0^\circ$ orientation. Sets C and D were longitudinally machined, i.e., their grooves were parallel to the long axis of the sample. Sets B, D, F, and G were laser machined in the transverse

direction. The three sets D, F, and G were exactly the same. Sets F and G were used to determine if any strength loss due to laser machining could be recovered with a finishing pass by diamond grinding. The laser machined surface of set F was diamond ground as previously described until the features of the laser machined surface became invisible to the unaided eye. Set G was machined in a similar manner but with one extra finishing cut of 0.000792 cm to remove microcracks which might have been created by laser machining.

A summary of the 4-point flexure strength measurements is presented in Table V.1, which lists the number of samples tested, average bend strengths, standard deviations, and Weibull⁶⁵ distribution characteristics.

Table V.1 indicates the average strength of the laser sample as compared to that of set A, 694 MN m^{-2} , was reduced by 30.6 to 41.9%. Sets B and D which were laser machined in the transverse direction showed the biggest decrease. Set B ($\phi=90^\circ$) had an average flexure strength of 423 MN m^{-2} while set D ($\phi=0^\circ$) had an average flexure strength of 403 MN m^{-2} . Sets C and E were laser machined in the longitudinal direction. Set C was machined using the $\phi=90^\circ$ orientation while set E had the $\phi=0^\circ$ orientation. Set C had a strength of 462 MN m^{-2} while set E had a strength of 482 MN m^{-2} . The closeness of these values suggests that at the speed of 238 cm sec^{-1} used in this

	Sets							
	PI*	A	B	C	D	E	F	G
Machining Tool								
D-Diamond (Grit)		D(320)	D(520)	L	L	L	L	L
L-Laser							D(520)	D(520)
Machining Direction								
T-Transverse	L	L	T	L	T	L	T	T
L-Longitudinal								
ϕ -Orientation			90°	90°	0°	0°	0°	0°
Number of Samples	50	10	10	10	10	10	9	9
Average Strength (MN m ⁻²)	632	694	423	462	403	482	643	683
Standard Deviation (MN m ⁻²)	59	56	12	15	11	14	52	70
Weibull Strength (MN m ⁻²)	658	720	430	469	408	489	668	715
Weibull Slope	12.6	12.6	34.4	33.0	39.0	36.0	12.5	9.8
*Previous Investigation ⁶²								

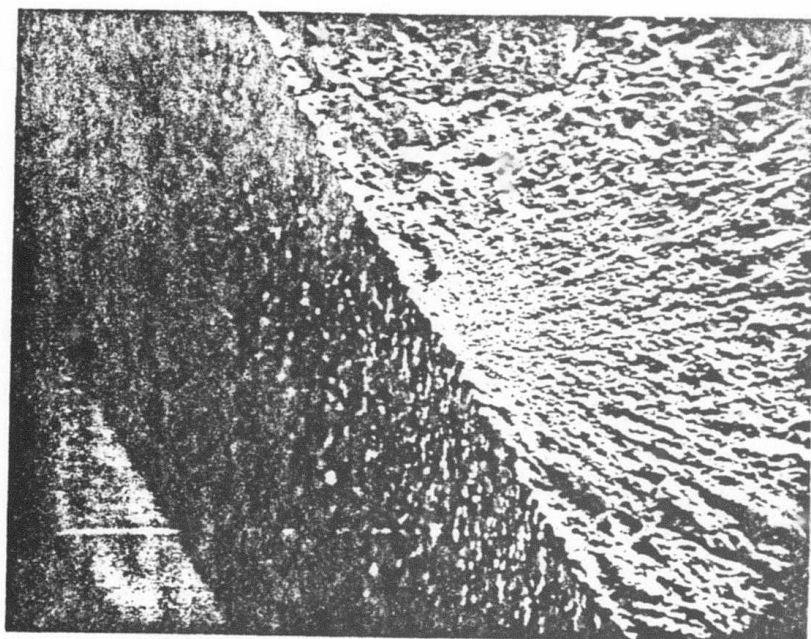
Table V.1. Four-point flexure strength of NC-132 Si₃N₄.

investigation, the resultant groove shapes of the two orientations were very similar. The average strength values of sets F and G listed in Table V.1 show that the reduction due to laser machining can be recovered by diamond grinding. Not only is the average strength increased but also the standard deviation is increased to the value observed in sets A and PI. The standard deviations of the laser machined sets in Table V.1 show a marked decrease in comparison to the diamond machined sets. The previous investigation, set PI, and sets A, F, and G have standard deviations of 9.4, 8.0, and 10.3% of their average strengths, respectively while sets B, C, D, and E have standard deviations that range from 2.7 to 3.3% with an average of 2.9%. Correspondingly the Weibull slope which is a measure of the variability of strength of the material with a larger value being associated with the least variability also varied significantly. Sets PI and A both had slopes of 12.6 while the laser machined sets B, C, D, and E had values of 34.4, 33.0, 39.2, and 36.1, respectively. This along with the observed reduction in strength suggests that the laser machined samples had a narrow distribution of flaw sizes but that the flaws were larger than in the diamond ground samples.

Optical and SEM examinations were not able to reveal exact origins of fracture but did show that the fracture origins were associated with the surface and were not close

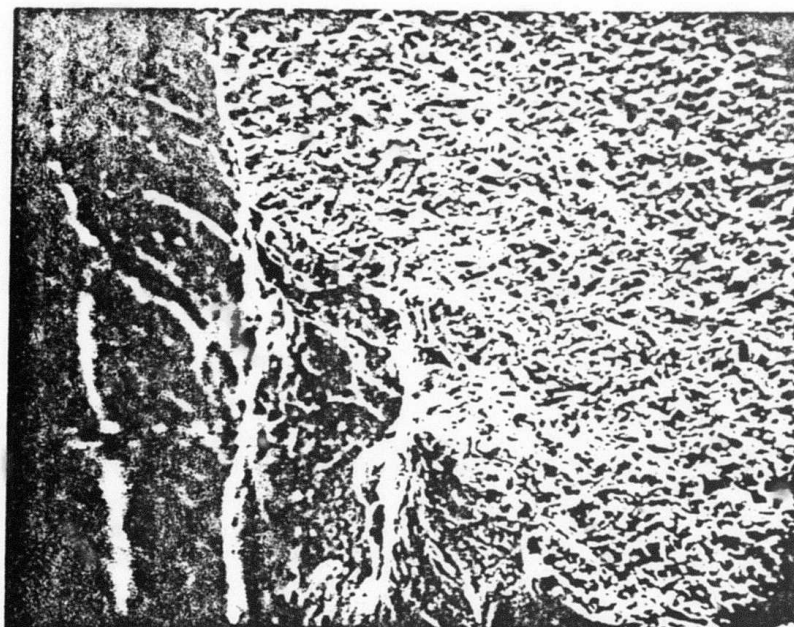
to the chamfered edges, Figs. V.10 and V.11. SEM photographs also showed that the "wetted" silicon had very narrow cracks.

Although these cracks were somewhat random in direction the majority were perpendicular to the groove direction and extended across the width of the "wetted" silicon. This type of cracking can be seen in Fig. V.9 and in more detail in Fig. V.12.



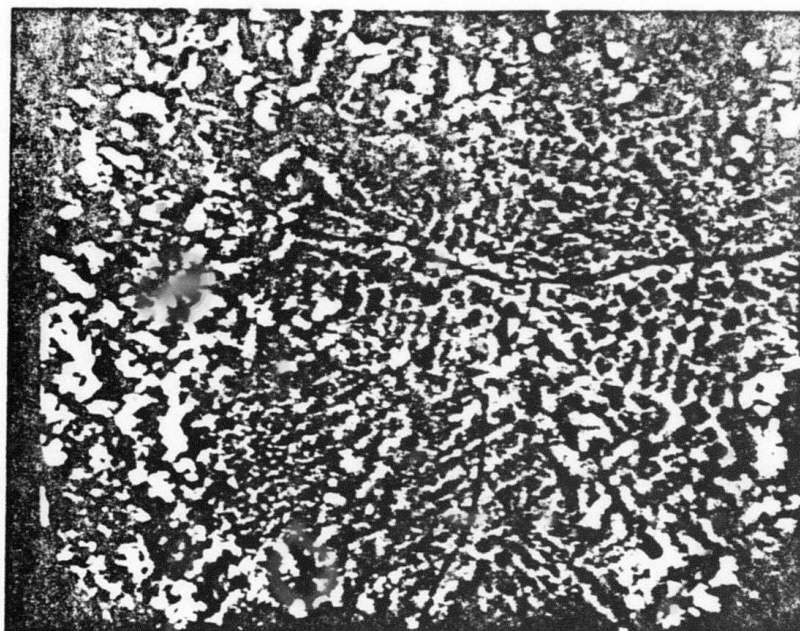
— 0.5 mm

Fig. V.10. Fracture surface of laser machined sample.



— 10 μm

Fig. V.11. Detail of fracture surface in Fig. V.10.



— 2 μm

Fig. V.12. SEM photomicrograph illustrating cracks in silicon layer.

C. Discussion

C.1 Overlapped Grooves

As Secs. V.B.1 and V.B.2 have illustrated, beam guiding effects play an important role in determining the finish of laser machined surfaces. These effects could possibly limit the usefulness of lasers in shaping Si_3N_4 . The unsymmetrical groove cross sections formed by two passes are similar to curved grooves formed by single passes.

In an earlier investigation, Chap. III, it was shown that the curving of grooves formed by single passes was caused by polarization of the laser beam. An alternative to the polarization explanation also considered curving due to beam guiding. This alternative was based on the idea that an unsymmetrical intensity distribution might cause the material initially vaporized to be offset from the main path of the beam. It was proposed that the main part of the beam would then be guided by the unsymmetrical groove front resulting in a curved cross section. This alternative explanation, however, was not able to explain all observations related to groove curving. Also, an attempt to demonstrate it by manipulating the beam intensity with cylindrical lenses to form an elliptical beam

cross section with the long axis of the ellipse making an acute angle with the groove direction was unsuccessful. Although rejected as an explanation for the curving of single pass grooves, the idea of beam guiding provides a satisfactory explanation for unsymmetrical cross sections of two pass grooves. The failure of the previous attempt to demonstrate this mechanism in single pass grooves was probably due to the failure of the elliptical beam to establish a sufficiently offset initial groove front.

The results described in Sec. V.B.2 indicate that it is difficult to compare material removal rates and surface roughness obtained by laser machining to those obtained by standard single point cutting. This arises from the fundamental difference between the conventional cutting tool and the "tool" used in laser machining, the focused laser beam. The conventional cutting tool removes only material that intersects the tool cross section. As the feed or groove spacing is decreased the area of intersection also becomes smaller and thus the material removal rate becomes less. This differs from laser machining where the tool is a fixed amount of power directed toward a sample surface. All this power interacts with the surface regardless of whether or not some of the surface was previously removed. In general, this causes the material removal rate to remain constant independent of the groove spacing and the surface roughness to vary in a complicated manner with feed.

From a machining standpoint, the observation of a constant material removal rate independent of feed presents a unique situation. The material removal rate can be easily predicted from that of single pass grooves. The single pass material removal rates have been discussed previously in terms of incident power, scan velocity, and orientation. If the material removal rate remains constant as the feed is decreased, then the average groove depth must become deeper. Therefore, the depth of the machined surface is not only a function of incident power, scan velocity, and ϕ orientation but also of feed. It should be noted that it is average depth that is being referred to here, and there may be specific grooves that are much deeper than adjacent ones due to beam guiding effects.

In Sec. V.B.2 conditions for the onset of beam guiding were discussed. It was pointed out that whenever the feed corresponds to the width of the groove beam guiding and non-steady state groove formation will occur near the initial and final grooves. This results from energy being deposited on the preceding groove starting with the second pass. For cases where beam guiding is not predominant these effects were observed only slightly in the first and last grooves, or, not at all. (See Figs. V.2 and V.3 for moderate feeds, where approximately steady state behavior was observed in the first grooves).

Referring to Fig. V.7, the increase in the ratio δ

for the $\phi=0^\circ$ orientation compared to the $\phi=90^\circ$ orientation is an important feature which was seen at all scan speeds. This behavior is expected because in the $\phi=0^\circ$ orientation more of the incident light is reflected by the walls of the groove and thus more easily guided, as previously described. Similarly, one can expect that the "steepness" of the groove walls would also be a factor. Steeper walls would more easily guide the incident light, which would lead to an increase in δ . For example, the walls of the 9.42 cm sec^{-1} , $\phi=90^\circ$, single pass groove shown in Fig. V.1 are almost perpendicular to the surface. This groove when overlapped, gave a δ of 0.894. In contrast the fastest scan speed groove, formed at 237 cm sec^{-1} , had walls inclined 33° from the top surface for the $\phi=90^\circ$ orientation and had a δ of 0.282.

Considering another measure of wall steepness, namely the ratio of depth to width for a single pass groove, a direct correlation can be found with the ratio δ for the faster scan speeds included in Fig. V.7. At 128 cm sec^{-1} and 237 cm sec^{-1} for both orientations, δ is equal to the value of the depth divided by the width to within 13%. For the data included in Fig. V.7 this relationship appears to break down when the value of depth to width reaches 0.55 to 0.60. In Fig. V.7 this corresponds to the $\phi=0^\circ$ orientation for the 61 cm sec^{-1} scans and both orientations for the 9 cm sec^{-1} scans. Contributing to this breakdown

is the fact that the depth to width is not truly representative of the wall steepness of the deep grooves associated with the slower scan velocities because they vary from a triangular shape.

For δ values where beam guiding is not predominant, the resulting machined surface is made up of overlapping grooves spaced according to the feed. Thus, the smoothest surface is attained with the fastest scan speed and smallest feed. Of course, there are both machine limits and material removal rate limits to the fastest scan speed that can be used. These limits then define the maximum smoothness that can be obtained by laser machining.

Observing these limits, one can then predict the smoothness of the laser machined surface by conventional analysis. For the fastest scan speed included in Fig. V.6, the single pass groove cross section can be modeled as an equilateral triangle. For overlapping grooves, the surface roughness R is equal to the following:⁶⁶

$$R = \frac{R_{\max}}{4} \quad (V.1)$$

where R_{\max} is the vertical distance from peak to valley of the resulting idealized machined surface. Because the ratio of feed to width is equal to the ratio of depth to width for the fastest scan speed the following equality exists: feed/width equals depth/width equals 0.5, for the

$\phi=0^\circ$ orientation. It follows that R_{\max} equals 0.5 times the depth which when combined with Eq. (V.1) and the measured depth of the 238 cm sec^{-1} , $\phi=0^\circ$ orientation grooves, $38.5 \text{ }\mu\text{m}$, leads to a predicted surface roughness of $4.81 \text{ }\mu\text{m}$. The value of R corresponds to N8-N9 using the ISO-roughness grade numbers.⁶⁶ The predicted value of roughness, $4.81 \text{ }\mu\text{m}$ is slightly higher than the measured value of $2.88 \text{ }\mu\text{m}$ for the 238 cm sec^{-1} , $\phi=0^\circ$ orientation scan. This difference is probably due to modeling the groove cross section as a sharp triangle rather than as a triangular shape with rounded corners. This analysis neglects groove shape modification due to a slight amount of beam guiding and modification covered by the residual silicon.

In addition to modifying the final surface roughness, the residual silicon can also cause the surface to have long range irregularities. A solidified silicon deposited from one pass will affect the subsequent passes by presenting an irregular surface to the laser beam.

C.2 Flexure Strength

The 4-point flexure strength results presented in Sec. V.B.4 show that the strength of the laser machined samples was significantly decreased compared to conventionally diamond ground samples. In addition, the strength of this investigation's ground samples was greater than those tested in previous investigations. An analysis of this difference requires the use of the Weibull distribution, a distribution widely used in the analysis of brittle materials strength data.⁶⁷

While the Gaussian distribution is applied widely in engineering problems, there is no experimental or theoretical justification for using it in fracture problems. The Gaussian distribution has long tails on each side of the mean and does not represent normal fracture data.

Weibull's theory assumes that the cumulative probability of fracture $F(\sigma)$ for the strength σ of a material is given by

$$F(\sigma) = 1 - \exp(-B) \quad (V.2)$$

where B is given by

$$B = \int_V n_1(\sigma) dv + \int_S n_2(\sigma) ds \quad (V.3)$$

where V and S are the volume and surface of the sample, and $n_1(\sigma)$ and $n_2(\sigma)$ are functions relating the probability

of failure to the stress level, σ . Both $n_1(\sigma)$ and $n_2(\sigma)$ are functions of the form

$$\begin{aligned} n(\sigma) &= ((\sigma - \sigma_\mu) / \sigma_0)^m & \sigma > \sigma_\mu \\ n(\sigma) &= 0 & \sigma < \sigma_\mu \end{aligned} \quad (V.4)$$

where σ_μ , σ_0 , and m , the three parameters describing the function, are defined as follows:⁶⁷

- 1) σ_μ is known as the threshold stress or lower limiting stress. It is the stress below which the failure probability is zero. Generally it is set equal to zero unless there are physical reasons to expect an upper limit to the size of the flaw or there has been some proof testing.
- 2) σ_0 is the characteristic Weibull strength. For specified values of m , σ_μ , and specimen size the mean fracture stress increases with increasing σ_0 . If σ_μ is zero and the specimen is of unit size subjected to a stress σ_0 , the specimen will have a cumulative probability of fracture equal to $1 - 1/e$ or 0.632.
- 3) m is the Weibull modulus. It is a measure of the variability of the quantity $(\sigma - \sigma_\mu)$. A high value of m yields a narrow range of stress over which failure is likely to occur.

The Weibull theory assumes that m , σ_0 , and σ_μ are all

material properties depending on the microstructure.

Equation (V.3) explicitly contains a size effect since B depends on the limits over which the integration is performed. In Eq. (V.3), both volume and surface flaws are taken into account, although previous investigators⁶⁸ have shown that NC-132 failure is primarily due to the surface flaws. In this case, the volume term in Eq. (V.3) can be neglected and Eq. (V.2) can be combined with (V.3) and (V.4) to give the equation

$$F(\sigma) = 1 - \exp^{-(\sigma/\sigma_0)^m} \quad (V.5)$$

By fitting the modulus rupture (MOR) data to Eq. (V.5), using the least squares procedure, the Weibull parameters listed in Table V.1 were calculated (graphically shown in Figs. V.13 and V.14).

Comparing set A to the data of previous investigations in Table V.1, one finds that the results are very similar although in the previous investigations lower average and Weibull characteristic strengths were observed. This could be due to several factors including specimen size effects, strength anisotropocity, and surface treatments. Davies and others⁶⁷⁻⁷⁰ have shown that when surface flaws predominate the magnitude of the size effect depends primarily on m and the mean strengths, σ_{m1} and σ_{m2} , for two samples with surface area S_1 and S_2 . The relationship takes the form

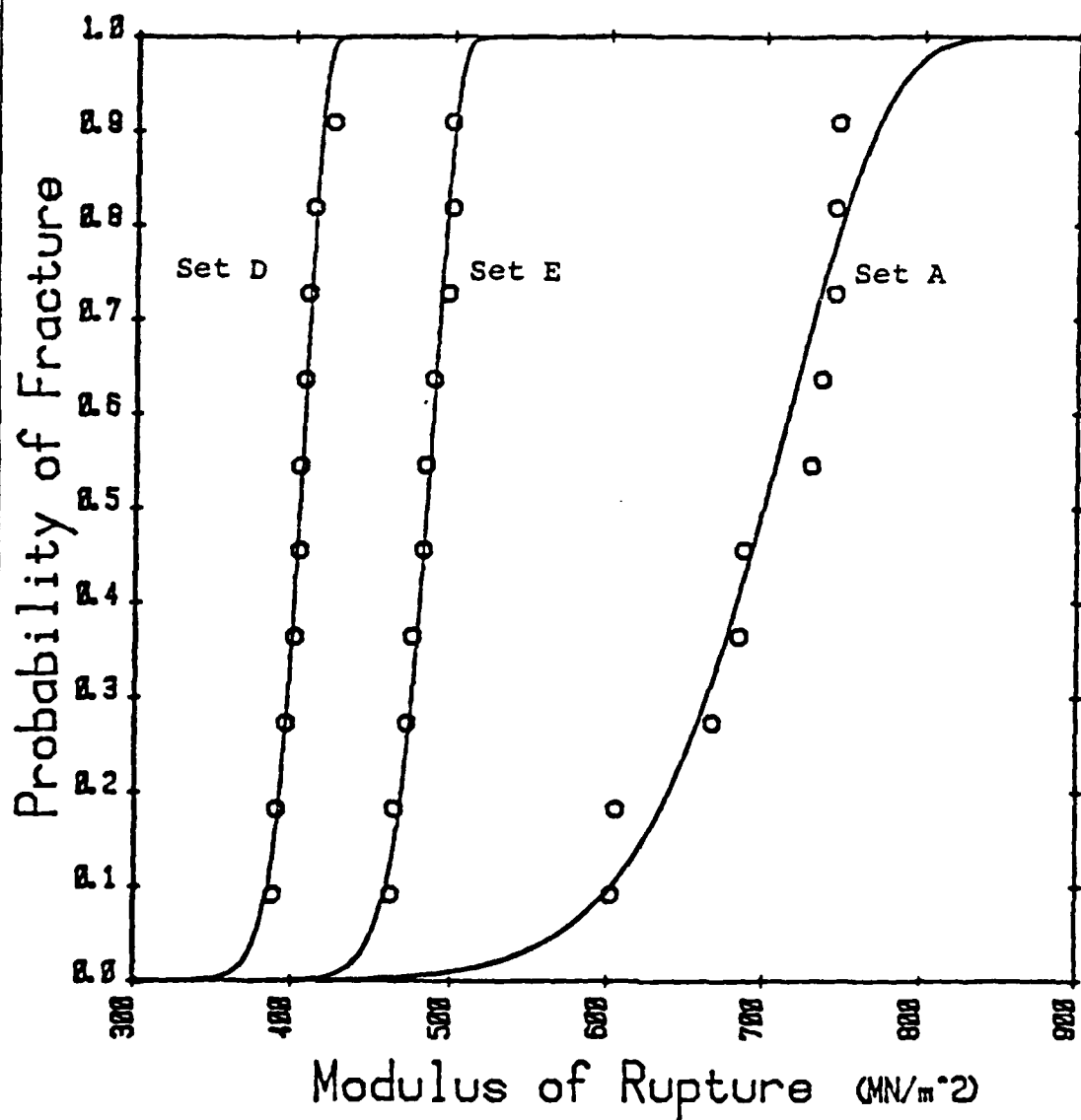


Fig. V.13. Probability of fracture versus MOR for $\phi=0^\circ$ laser machined samples and diamond machined samples.

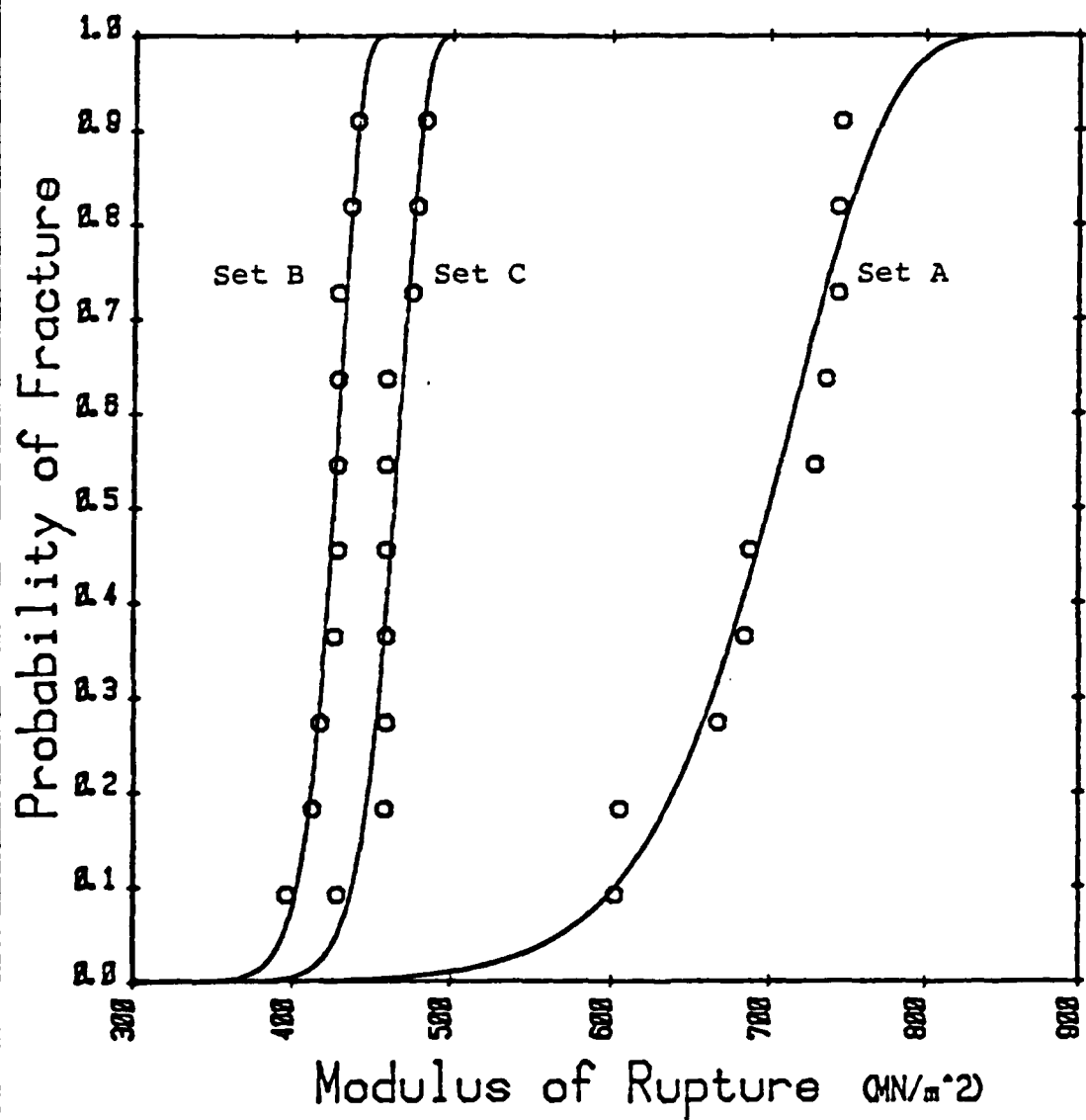


Fig. V.14. Probability of fracture versus MOR for $\phi=90^\circ$ laser machined samples and diamond machined samples.

$$\sigma_{m1}/\sigma_{m2} = (S_1/S_2)^{-(1/m)} \quad (V.6)$$

when $\sigma_u = 0$.

Using $m=12.6$ and the known values of S_1 and S_2 for sets A and PI, Eq. (V.6) would then indicate that if the specimen size of set PI were the same as set A, set PI would have a mean strength of 652 MN m^{-2} . This would still be smaller than the observed value of 694 MN m^{-2} for set A, and therefore, the size effect cannot completely account for the difference between the two sets.

This remaining difference between sets A and PI could be due to flexure strength anisotropocity previously observed³² in NC-132. Depending on the test bar length, orientation and loading force factor orientation relative to the billet pressing axis, the mean strength can vary by as much as 18%. Sets A through G had both their long axes and loading force vectors in the billet plane. In the previous investigation the orientation of the test bars is unknown but because of their size it is likely that they had the same testing orientation as sets A through G. Thus, it does not appear that flexure strength anistropy can account for the remaining difference between sets A and PI.

Another source for the remaining difference in strength between sets PI and A could be different surface

treatments. Set A was conventionally surfaced using a 520 grit diamond wheel while a 320 grit wheel was used for set PI. This difference in grit size could account for the difference in average strength. Richerson and Yonushonis⁶² investigated the effects of processing conditions on NC-132. Using ultrasonic machining they observed an increase in average strength of 9% when 320 grit B₄C was replaced with 600 grit B₄C. Thus, it appears likely that the difference in strength not accounted for by the sample size effect can be attributed to the different surface treatment.

As stated previously in Sec. V.B.4, the average strength of the laser machined sample when compared to that of set A reduced from 30.6 to 41.9% with the transversely laser machined samples showing the largest decrease in strength. This decrease for the transverse set was expected. Richerson and Yonushonis have shown in surface grinding with 320 grit diamond wheels there is a large decrease in strength for the transverse direction. Both their transversely and longitudinally diamond ground samples had strengths similar to sets B, D, and A. Their transversely diamond ground samples had an average strength of 434 MN m⁻².

Considering the similarity in strength of the transversely laser machined surfaces and those produced by diamond grinding one might expect the strengths of

longitudinally laser machined surfaces to be similar to those of the longitudinally diamond ground samples. However, this is not the case since there is only a moderate increase in strength of the longitudinally laser machined samples with respect to the transversely laser machined samples. This fact suggests a fundamental difference in the resulting surface microstructure produced by the two types of machining.

Unfortunately, Richerson and Yonushonis only give the average strengths and not the standard deviations. This is important because aside from the overall drop in strength the other notable characteristic of laser machined samples is their reduced standard deviation. As stated previously, the diamond machined samples had standard deviations that were approximately 8.7% of their average strength while the laser machined samples had standard deviations that ranged from 2.7 to 3.3% of their average strength with an average of 2.9%. The Weibull slope exhibited similar behavior with m equalling 12.6 for the diamond machined sets and an average of 35.7 for laser machined samples. This would indicate a material with a narrow distribution of flaw sizes. Petrovic et al.⁷¹ showed that when surface flaws of controlled size and shape were produced, by a Knoop indentation, in hot pressed Si_3N_4 there was a reduction in fracture stress by a factor of approximately 2 and a reduction in the scatter (standard

deviation) by a factor of 4. Their results are very similar in magnitude to the results obtained when comparing laser machined samples to the diamond machined sets.

Rice⁷² also studied the effect of grinding direction on the strength of ceramics. He lists a value of 655 MN m^{-2} for longitudinally ground hot pressed Si_3N_4 and a value of 359 MN m^{-2} for transversely ground samples. Unlike Richerson and Yonushonis's results, standard deviations are given and listed as 9.5% for the longitudinal direction and 3.8% for the transverse direction. These values for transversely ground samples are similar in both magnitude and scatter to the values for the transverse laser machined sets. Unfortunately, Rice's results are based on a very small number of tests. Heckel and Heigl⁷³ also investigated the effect of grinding direction on the strength of Si_3N_4 but tested reaction-bonded silicon nitride specimens. The average strength of the transversely ground samples was reduced by 32% with respect to the longitudinally ground samples as compared to the 45% observed by Rice and 35% listed by Richerson and Yonushonis. But in contrast, Heckel and Heigl saw no decrease in scatter between the two grinding orientations with a Weibull slope of 14.0 for the longitudinally ground samples and 12.9 for the transversely ground samples.

It was proposed by Rice that the variation of strength with grinding direction was associated with

grinding striations or grooves which would act as stress concentrators. Thus, stressing a sample with the grooves in the longitudinal direction would not increase the stress experienced by the material while stressing with grooves in the transverse direction would result in the maximum stress concentration. However, there are several observations which indicate that the grinding grooves are normally not a major factor contributing to the anisotropy of strength. Investigation of the shape of the grooves showed that theoretically calculated stress concentrations would not be great enough to account for the strength anisotropy. Also, it has been shown that the strength anisotropy remains in samples after the grooves have been subsequently removed by further treatment.⁷⁴ Further, fracture surface analysis showed that the grooves often do not appear to be as deep as the flaws causing fracture. The results of a substantial amount of study related to this problem showed that there are basically two different sets of flaws extending into the body from a surface generated by grinding. Typically, both sets of flaws extend to similar depths. The flaws formed parallel to the grinding grooves are longer than those formed perpendicular to them, which is consistent with the observed strength anisotropy.⁷⁵ In both sets the most severe flaws are generally associated with a particularly deep grinding groove.

As summarized in Sec. V.B.4, SEM examination of the

laser machined surfaces revealed no cracks in the Si_3N_4 but did show that the thin "wetted" silicon layer had shallow randomly oriented cracks. An analysis based on fracture mechanics will now be presented to determine whether or not the presence of these cracks can provide an adequate explanation for the reduction in strength as well as the reduction in scatter of strength values observed in Si_3N_4 .

To simplify the analysis, uniform applied stress, edge-notched crack depths that are much smaller than the specimen thickness, and uniform elastic constants are assumed. With these assumptions, the appropriate stress intensity factor for this case is then given by the equation:⁷⁶

$$K_a = Y_a \sigma_a (C')^{\frac{1}{2}} \quad (\text{V.7})$$

where Y_a is a crack geometry parameter which for the edge-notched crack is 1.99, σ_a is the applied stress, and C' is the depth of the crack. Using the observed value of maximum silicon layer thickness for the crack depth, $C' = 4 \times 10^{-6}$ m, and setting $\sigma_a = 472 \text{ MN m}^{-2}$, the observed breaking stress for the longitudinal laser machined samples, Eq. (V.7) gives a $K_a = 1.88 \text{ MN m}^{-3/2}$. This value is much smaller than the reported range of values³² for K_{IC} , 3.25 to $4.8 \text{ MN m}^{-3/2}$. This indicates that the cracks in the silicon are too small to be responsible for fracture

at the observed applied stress.

Although the cracks in the silicon are not large enough to cause fracture, the effects of these cracks when combined with the effects of residual stress due to a thermal expansion mismatch between the silicon and Si_3N_4 layer may be large enough to account for the reduced strength. As the surface is laser machined, the liquid silicon produced in the decomposition reaction solidifies upon cooling. Because the thermal expansion coefficient of the silicon layer is larger than the Si_3N_4 substrate,^{32,77} cooling places the silicon layer in bi-axial tension and the substrate below the layer of compression. The silicon layer also exerts a force, P_r , on the Si_3N_4 at the silicon layer edge.⁷⁸ This force can propagate cracks in the substrate as schematically illustrated in Fig. V.15. Again, one can use the fracture mechanics approach to analyze the situation in Fig. V.15. The stress intensity factor K_r due to the residual load acting at the mouth of the crack in the substrate is given by⁷⁶

$$K_r = Y_r (2P_r C^{-1/2}) \quad (\text{V.8})$$

where Y_r is the appropriate geometrical factor, and P_r is the residual load per unit crack length. This stress intensity factor can be added to the stress intensity factor K_a due to the uniform applied stress, which for the geometry of Fig. V.15 is given by

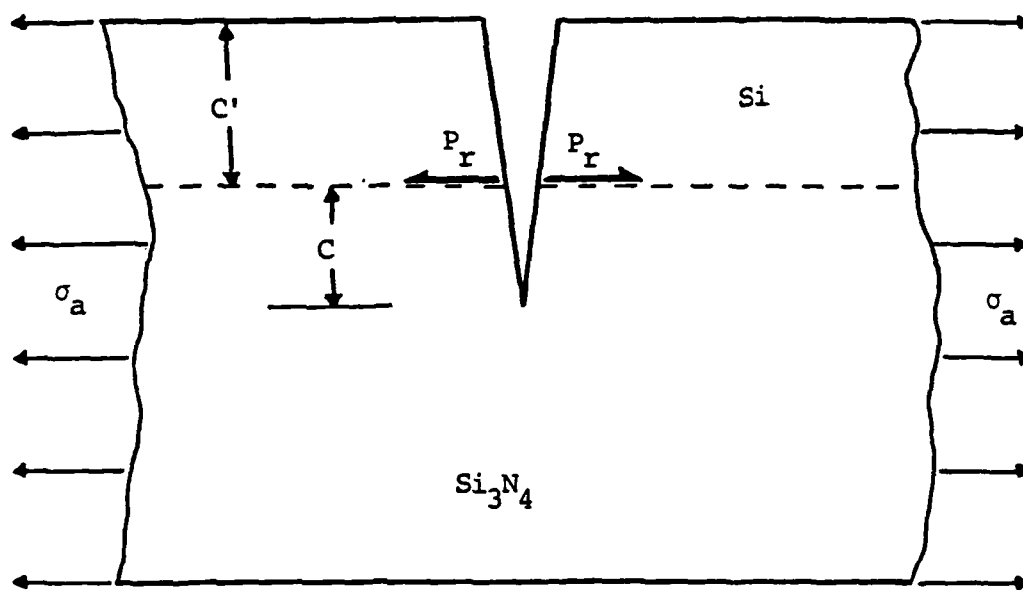


Fig. V.15. Schematic representation of crack system in a multiphase body with residual load and uniform applied stress.

$$K_a = Y_a \sigma_a (C' + C)^{\frac{1}{2}} \quad (V.9)$$

Thus, the crack shown in Fig. V.15 is subjected to a net stress intensity factor given by

$$K_I = K_a + K_r = Y_a \sigma_a (C' + C)^{\frac{1}{2}} + Y_r (2P_r C^{-\frac{1}{2}}) \quad (V.10)$$

By inserting $K_I = K_{IC}$ into Eq. (V.10) and rearranging one can obtain the following expression for the applied stress at fracture as a function of crack length.

$$\sigma_a = \frac{K_{IC}}{Y_a (C' + C)^{\frac{1}{2}}} \left(1 - \frac{2Y_r P_r}{K_{IC} C^{\frac{1}{2}}} \right) \quad (V.11)$$

By differentiating Eq. (V.11) with respect to C one obtains the equation

$$\frac{d\sigma_a}{dC} = \frac{-K_{IC}}{Y_a 2 (C' + C)^{\frac{3}{2}}} + \frac{Y_r P_r}{Y_a} \left(\frac{1}{(C' + C)^{\frac{3}{2}} C^{\frac{1}{2}}} + \frac{1}{(C' + C)^{\frac{1}{2}} C^{\frac{3}{2}}} \right) \quad (V.12)$$

which can be set equal to zero to find the crack depth C_m at the maximum stress. The value of C_m is found by solving the following cubic equation, derived from Eq. (V.12) after setting $d\sigma_a/dC=0$

$$\left(\frac{K_{IC}}{2Y_r P_r} \right)^2 C^3 - 4C^2 - 4CC' - C'^2 = 0 \quad (V.13)$$

Finally, substituting C_m into Eq. (V.11) yields the value of maximum stress (σ_{am}). For $\sigma > \sigma_{am}$, the crack system ($C+C'$) will become unstable and fracture will occur. The approach used in this analysis is similar to that of Marshall and coworkers^{79,80} who investigated the influence of residual stresses induced by sharp indenters.

To evaluate C_m and σ_{am} , a value for P_r , the residual load generated by the silicon layer is needed. This is calculated by assuming that all the stress in the silicon layer, when converted to force per unit crack length, acts to wedge the crack open as shown in Fig. V.15. Of course, the stress is actually transferred to the substrate by shear at the Si_3N_4 -silicon interface acting over a distance approximately equal to the silicon layer thickness. To estimate the stress, and thus P_r , one can use the elastic solution, for the plate composite, which is given by⁸¹

$$\sigma_{si} = \frac{(E_{Si_3N_4} / (1 - \nu_{Si_3N_4})) \Delta \alpha \Delta T}{(E_{Si_3N_4} / E_{Si}) ((1 - \nu_{Si}) / (1 - \nu_{Si_3N_4})) + 1} \quad (V.14)$$

In this equation E and ν denote Young's modulus and Poisson's ratio, respectively, $\Delta \alpha = \alpha_{Si} - \alpha_{Si_3N_4}$ where

$\alpha_{\text{Si}, \text{Si}_3\text{N}_4}$ is the thermal expansion coefficient and ΔT is the change in temperature. In deriving Eq. (V.14), it was assumed that the thickness of the stressed region in the Si_3N_4 is equal to the thickness of the silicon layer.

Substituting the following physical properties into Eq. (V.14)

$$E_{\text{Si}_3\text{N}_4} = 325 \text{ GN m}^{-2} \quad (\text{Ref. 32})$$

$$E_{\text{Si}} = 200 \text{ GN m}^{-2} \quad (\text{Ref. 82})$$

$$\nu_{\text{Si}} = \nu_{\text{Si}_3\text{N}_4} = 0.3$$

$$\Delta\alpha = 1.0 \times 10^{-6} \text{ } ^\circ\text{C}^{-1} \quad (\text{Ref. 32, 77})$$

$$\Delta T = 1385^\circ\text{C}$$

gives a stress of 245 MN m^{-2} in the silicon due to cooling. When this stress is multiplied by the thickness of the silicon layer one then obtains the force per unit crack length P_r needed to solve Eqs. (V.11) and (V.13). A silicon layer thickness of $4 \times 10^{-6} \text{ m}$ multiplied by 245 MN m^{-2} gives a P_r of 980 N m^{-1} .

Evaluating Eq. (V.13) and subsequently Eq. (V.11) using the following values

$$C' = 4 \times 10^{-6} \text{ m}$$

$$P = 980 \text{ N m}^{-1}$$

$$K_{\text{IC}} = 3.25 \text{ MN m}^{-3/2}$$

$$Y_r = 0.734$$

$$Y_a = 1.99$$

yields $C_m = 2.52 \times 10^{-6}$ m and $\sigma_{am} = 461$ MN m⁻², the crack length in the Si₃N₄ and the maximum applied stress for which the crack system will become unstable and fracture will occur, respectively. The value of the calculated stress is very close to the observed strength of the laser machined sample 427 MN m⁻¹.

One result of the preceding analysis is that the initial depth of the crack (C) in the Si₃N₄ no longer plays a part in determining strength. A plot of K_I , K_a , and K_r as a function of crack depth (C) in the Si₃N₄, Fig. V.16, indicates that in the absence of an applied load the residual stresses have their most important effect at small crack lengths. The crack will initiate and grow due to the residual load until K_r drops to K_{IC} , and then remains stable, see point I Fig. V.16. To induce further crack growth, it is necessary to apply a stress. In the region to the right of point I on the line K_{IC} the crack growth is stable under increasing applied stress because increases in K_a are offset by decreases in K_r . When the crack length reaches C_m , position II Fig. V.16, at a stress of σ_{am} , $K_a + K_r$ becomes larger than K_{IC} and the crack system becomes unstable. For this analysis the point at which crack growth becomes unstable is therefore independent of the initial crack size. Although C_m and σ_{am} at fracture are not dependent on the initial value of C, σ_{am} is dependent

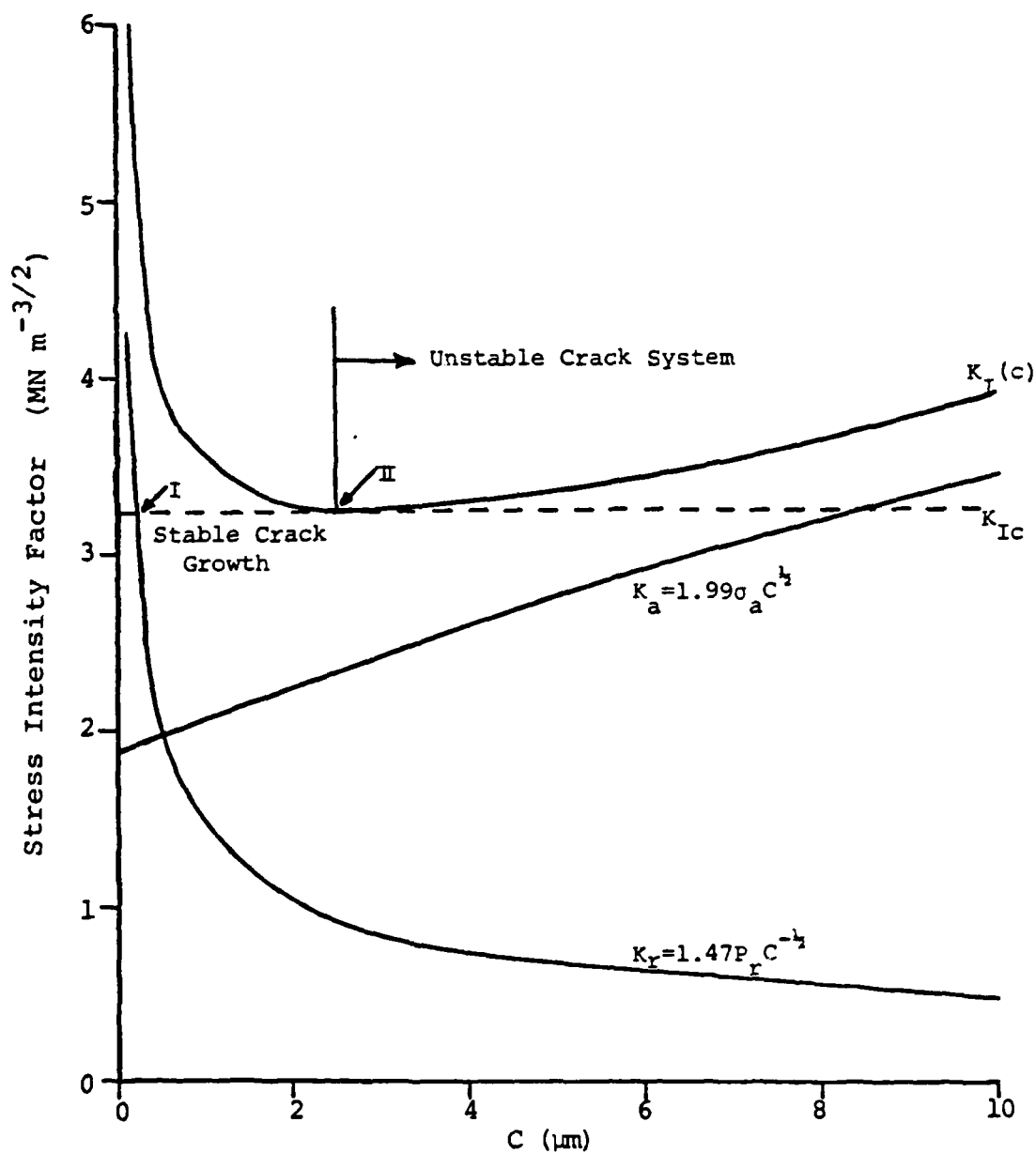


Fig. V.16. Stress intensity factor versus crack depth for the edge-notched crack of Fig. V.15. ($P_r = 980 \text{ N m}^{-1}$, $\sigma_a = 461 \text{ MN m}^{-2}$, $K_{IC} = 3.25 \text{ MN m}^{-3/2}$, $C' = 4 \times 10^{-6} \text{ m}$).

on C' , the depth of the silicon layer, not only from the K_a term of Eq. (V.10) but also P_r in the second term of Eq. (V.10).

Therefore, the reduced scatter observed in the strength values of the laser machined samples must be attributed to the uniform maximum thickness of the silicon layer.

The proposed mechanism does not explain the differences in strength observed with different machining orientations. It may be as suggested by Rice in the case of grinding that the grooves act as stress raisers.⁷²

This effect would be greatest for grooves in the transverse direction. Unfortunately, there is no stress intensity analysis available that considers a beam with periodic notches with the correct geometry and it is improper to use single notch values because they represent a higher degree of stress concentration than a series of closely spaced notches of the same kind as the single notch.⁸³ Thus it is not possible to make an accurate estimate of the magnitude of this effect.

C.3 Economics

While one major concern in evaluating the potential of shaping NC-132 with a laser is the quality of the resulting surface, another is the economic feasibility. The most straightforward economic study would be the

comparison of material removal rates between the laser and conventional grinding methods. In what follows, this comparison is made and the actual costs of manufacturing a NC-132 turbine blade are also determined.

While data which can be employed to estimate material removal rates for laser machining can be found in Chaps. IV and V, values of removal rates for conventional machining methods cannot be as easily obtained. Material removal rates for diamond grinding depend on several factors such as grit size, bonding material, cooling fluids and slurries, wheel size, previous wear and contact pressure between the work piece and the diamond wheel. The first few factors can be specified and held constant but the last two, previous wear and contact pressure, are extremely variable. Studies have shown that removal rates can vary significantly over the life of a diamond tool, with the larger values of Z being associated with newer tools.⁸⁴ The contact pressure is normally determined by the operator based on his feeling as to the amount of pressure needed to remove material without breaking the tool or the machined part. Due to the variability in these factors, values for material removal rates are not often quoted. Fortunately, some values have been published by the Norton Company.^{31,85}

The single pass grooves produced by the laser can best be compared to a conventional slicing operation with

a thin diamond blade. The removal of material from a surface as described in Chap. V can most closely be equated to a surface machining operation using a wide diamond wheel. A comparison of these types of operations can be found in Table V.2 where values of material removal rates for both slicing and surfacing are listed along with comparable laser machining values.

For a slicing operation the material removal rate for laser cutting was obtained from Chap. IV and represents the maximum value of Z seen for the parameters used, $9.3 \times 10^{-3} \text{ cm}^3 \text{ sec}^{-1}$, which was observed with an incident power of 942 W and a scan speed of 70.6 cm sec^{-1} . For the surface operation the material removal rate for the laser machining was chosen from this chapter to be $3.4 \times 10^{-3} \text{ cm}^3 \text{ sec}^{-1}$ and corresponds to an incident power of 560 W, scan speed of 238 cm sec^{-1} and a feed of 0.00378 cm. Although this was not the maximum material removal rate seen for this incident power, it was chosen to correspond to the conditions used in laser machining the flexure test bars. Both values are not maximum values for laser machining operations and could easily be increased by increasing the incident power, however, they can be used as an indication of values easily obtainable in laser machining.

Referring to Table V.2, values for slicing and surfacing with the surface grinder, Ref. 31, can be considered maximum values. They were obtained in machining

Operation: Slicing

Machine	Tool	Wheel-Grit	Removal Rate ($\text{cm}^3 \text{s}^{-1}$)	Ref.
Surface Grinder	Diamond	0.05"x6" -150	5.46×10^{-3}	31
Surface Grinder	Diamond	0.05"x10"-150	0.75×10^{-3}	85
Laser	Power:942W	Scan Speed:70 cm s^{-1}	9.30×10^{-3}	

Operation: Surfacing

Machine	Tool	Wheel-Grit	Removal Rate ($\text{cm}^3 \text{s}^{-1}$)	Ref.
Surface Grinder	Diamond	0.5"x6"-150	10.90×10^{-3}	31
Surface Grinder	Diamond	0.5"x6"-150 (Rough)	3.75×10^{-3}	85
Surface Grinder	Diamond	0.5"x6"-320 (Finish)	1.28×10^{-3}	85
Pantograph	Dia. Points	0.13"x.63"-150 (Rough)	0.09×10^{-3}	84
Pantograph	Dia. Points	0.13"x.63"-320 (Finish)	0.045×10^{-3}	84
Laser	Power:560W	Scan Speed:238 cm s^{-1}	3.40×10^{-3}	

Table V.2. Comparison of laser and diamond machining material removal rates.

billets where the risk of breakage due to high contact pressure is minimal. The same situation applies to those values obtained from Ref. 85, although they appear to be more conservative and probably represent more typical removal rates for operations involving billets.

For slicing operations Table V.2 indicates that the use of laser machining represents a 12.4-fold improvement in material removal rate over typical diamond methods. In addition to this increase the width of laser created grooves are generally equal to the width of the focussed beam which is smaller by a factor of 4 than the width of the diamond blades used in Table V.2. Therefore, when only the cut-off of material is required, the amount of material removed is reduced by a factor of 4. Consequently the time needed to perform the cut-off operation is reduced by 4 and in this special case there would be an improvement of approximately 50 times obtained by using the laser rather than a diamond tool.

For the surfacing operations shown in Table V.2 a removal rate of $3.75 \times 10^{-3} \text{ cm}^3 \text{ sec}^{-1}$ was obtained by conventional machining and a rate of $3.4 \times 10^{-3} \text{ cm}^3 \text{ sec}^{-1}$ by laser machining, however, conventional machining again involved only the machining of billets where the application of high contact pressure would not present a problem. More complicated shapes such as airfoils require the use of a pantograph profile grinder. These grinders use small

diamond coated rods called points which are rotated from 5,000 to 100,000 rpm. In contour grinding the material removal rates are much less than in the surface grinding of billets as illustrated by Table V.2. For rough grinding with the pantograph grinder typical removal rates are $0.09 \times 10^{-3} \text{ cm}^3 \text{ sec}^{-1}$. Assuming that laser machining can do similar contouring at a rate similar to that observed in surfacing, using the laser could result in a 37.7 times increase in materials removal rate compared to conventional methods.

Baker⁸⁴ conducted an economic study involving the manufacture of a turbine blade using the pantograph operation. If, employing his data, one substitutes laser machining for pantograph grinding of the roughing cuts, an idea of the significance of increasing the materials removal rate can be obtained. The dimensions of the ceramic blade used in this analysis are given in Fig. V.17. The cost calculations are listed in Table V.3. Baker's study involved the use of an abrasive slurry of B_4C to aid the diamond points and improved the material removal rates over those shown in Table V.2. The production costs shown in Table V.3 do not contain the normal overhead costs, rejection costs, and set up. Referring to Table V.2 if the laser is used for only the rough machining operation a cost reduction of 62% is obtained in the cost per blade.

The estimate of time required for laser machining

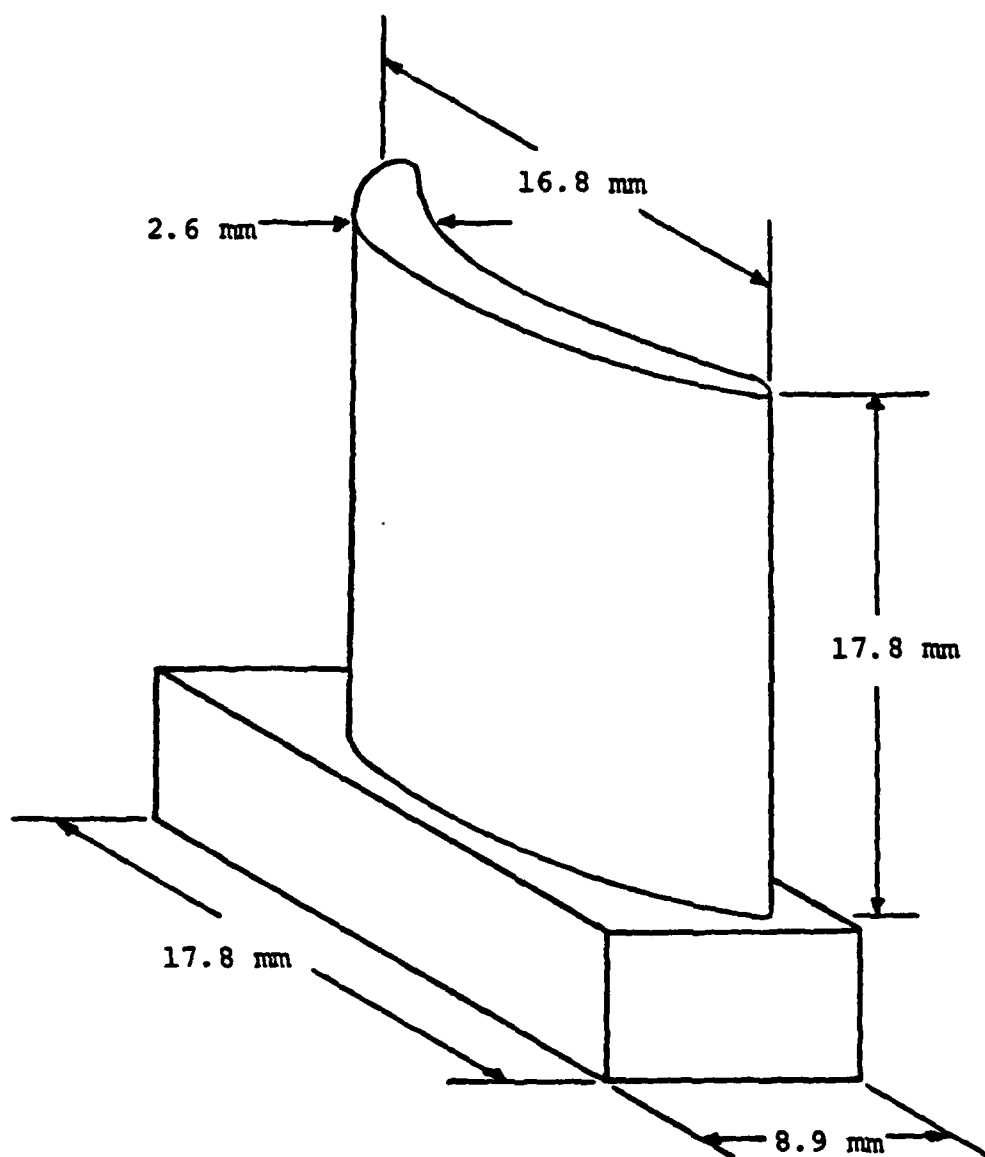


Fig. V.17. Dimension of ceramic turbine blade used in economic study.

Operation	Dia. Points	Tool Grit Slurry	$\text{cm}^3 \text{ sec}^{-1}$	Hours	No. of Spindles Used
<u>Diamond Machining:</u>					
Rough Cut	120	240	0.27×10^{-3}	2.5	2
Finish	240	400	0.14×10^{-3}	1.0	1
Miscellaneous				$\frac{0.5}{4.0}$	$\frac{3}{3}$
				<u>Cost</u> Labor/Hour	
				1 Spindle	\$29
				<u>Production Cost</u>	\$87
				Total	\$167
<u>Laser/Diamond Machining:</u>					
Rough Cut-Laser	(560W-238cm s^{-1})		3.40×10^{-3}	0.2	
Finish	240	400	0.14×10^{-3}	1.0	1
Miscellaneous				$\frac{0.5}{1.7}$	$\frac{1}{1}$
				<u>Cost</u> Labor Hour	
				1 Spindle	\$29
				<u>Production Cost</u>	\$34
				Total	\$63

Table V.3. Economic comparison between laser and diamond machining for ceramic turbine blade.

the blade is probably optimistic in that it does not allow for "off" time that would be required to allow the blade to cool from heating due to conduction nor does it allow for time needed to reposition the turbine blade during the laser machining. Even if the time required for laser machining is increased by a factor of 5 to 1 hour there would still be a reduction in cost of 52% over the diamond machining.

A further increase can be realized because unlike the diamond slicing operation the laser machined grooves are not limited to a straight line therefore large sections of the initial block can be removed intact. The removal of bulk pieces would dramatically increase the overall effective removal rate further increasing the economic advantage of laser machining.

VI. SUMMARY

A. Summary - Conclusions

The shaping of hot pressed silicon nitride with a high power CW CO₂ laser was investigated. The major portion of this research involved translating a Si₃N₄ sample at constant velocity in a controlled environment under a focused laser beam. The laser was used to heat the surface of the workpiece forming a groove by vaporization. Shaping was accomplished by overlapping the grooves.

This investigation was divided into three parts. The first and second parts deal with the formation of single pass grooves, while the third part deals with the overlapping of grooves leading to shaping. These parts are summarized individually in the following sections.

A.1 Single Groove Formation - Part I

1) Examination of sections perpendicular to laser vaporized grooves in Si₃N₄ has revealed these grooves are often curved. The curvature becomes more pronounced at low speeds and high incident power and reverses direction if the scan direction is reversed.

2) The shape of the curved grooves was found to be independent of the distribution of intensity within the

focused incident beam.

3) The shape of the curved grooves is directly related to the angle ϕ between the electric vector of the partially polarized beam and the velocity of the sample. A mechanism is proposed which explains the curved shape of single pass grooves in terms of the difference in reflectivity between the TM and TE beam components for large angles of incidence.

4) Calculations of values of reflectance for the TM and TE components as a function of the angle of incidence verify that a large difference exists at $\lambda=10.6 \mu\text{m}$. These calculations were based on a value of k reported by Haggarty and Cannon⁴⁵ and measurements of absorption carried out as part of this investigation.

A.2 Single Groove Formation - Part II

1) Groove cross sections and material removal rates were determined for a wide range of incident beam powers (315 to 940 W) and beam scan speeds (5 to 125 cm sec⁻¹). In addition the effects of varying ϕ were also studied. Factors affecting the behavior observed in material removal rate are discussed including optical properties, beam polarization, ejecta, and groove shape and size.

2) Groove formation was studied in several different gaseous environments (O_2 , N_2 , and He) and it was found that the material removal rate was independent of the

environment used. This result is evidence that the decomposition reaction, $\text{Si}_3\text{N}_4(\text{s}) \rightarrow 3\text{Si}(\text{l}) + 2\text{N}_2(\text{g})$, is responsible for the removal of material in laser machining of Si_3N_4 .

3) Based on the energy balance involved in the reaction responsible for the removal of material and an estimate of conductive losses to the substrate during groove formation, an absorption coefficient of at least 0.28 is calculated. This is much higher than would be expected due to normal infrared absorption.

4) Possible explanations for the increased α are discussed including the presence of an absorption enhancing silicon film and occurrence of temperature dependent Reststrahl absorption. Also, some experimental evidence that plasma effects may be partly responsible for the increase in α is discussed.

A.3 Overlapped Groove Formation

1) Groove cross sections and material removal rates were determined for multiple overlapped grooves of various spacings for a wide range of scan speeds (9.1 to 238 cm sec^{-1}), and for both the $\phi=0^\circ$ and 90° orientations at one incident power (560 W).

2) An analysis of multiple overlapping grooves indicated, in some cases, that the shape of the overlapped groove differs significantly from that of the single pass

groove. This distortion is caused by beam guiding and can be related to groove overlap and single pass groove width.

3) The results showed that material removal rates remain constant independent of the groove spacing. It was found that this constant rate was equal to the material removal rate for a single pass groove for the same power, scan speed, and ϕ orientation.

4) Specimens with various laser machined surfaces were tested in 4-point bending. The results indicated an overall reduction of 30 to 40% in the modulus of rupture relative to diamond ground surfaces accompanied by greatly reduced scatter. Both reductions may be attributed to the presence of excess silicon left by the decomposition reaction.

5) The high material removal rates attained in laser machining compared to those experienced in diamond grinding lead to a favorable economic evaluation of the former. For slicing operations laser machining represents a 12-fold improvement, and for surfacing operations involving thin or complicated parts a 38-fold increase in material removal rate is predicted as compared to conventional diamond grinding methods.

REFERENCES

1. C. Ruffler and K. Gurs, Opt. Laser Technol. 4, 265 (1972).
2. C.D. Desforges, Engineering 217 (10), I (1977).
3. R.W. Walker, Photonic Spectra 16 (9), 65 (1982).
4. J.F. Ready, Industrial Application of Lasers. (Academic, San Francisco, 1978).
5. J.F. Ready, Effects of High Power Laser Radiation. (Academic, San Francisco, 1971).
6. W.W. Duley, CO₂ Lasers - Effects and Applications. (Academic, San Francisco, 1976).
7. M. Pasturel and R. Saunders, Electro-Optical Systems Design 8 (5), 23 (1976).
8. S.L. Engel, Society of Manufacturing Engineers Technical Paper No. MR 76-857 (1976).
9. T.F. Zaveoz, M.A. Saifi, and M. Notis, Appl. Phys. Lett. 26, 165 (1975).
10. F.D. Seamar and D.S. Gnanamuth, Metal Progress 108 (3), 67 (1975).
11. E.V. Lock and R. Hella, I.E.E.E. J. Quantum Electron. QE-10, 179 (1974).
12. W. Duley and J.N. Gansalves, Opt. Laser Technol. 6, 78 (1974).
13. V.P. Babenko and V.P. Tychinskii, Sov. J. Quantum Electron. 2, 399 (1973).
14. R.J. Conti, Welding J. 48, 800 (1969).
15. E.L. Baardsen, D.J. Schmatz, and R.E. Bisaro, Welding J. 54, 227 (1973).

16. J.E. Anderson and J.E. Jackson, Welding J. 44, 1018 (1965).
17. J.P. Epperson, R.W. Dyer, and J.C. Grzywa, West. Elec. Eng. 10, 2 (1966).
18. J. Longfellow, Ceram. Bull. 50, 251 (1971).
19. Y. Nakada and M.A. Giles, J. Am. Ceram. Soc. 54, 354 (1971).
20. M.A. Saifi and R. Borutta, Ceram. Bull. 54, 986 (1975).
21. U.C. Paek and V.J. Zaleckas, Ceram. Bull. 54, 585 (1975).
22. R.M. Lumley, Ceram. Bull. 48, 850 (1969).
23. J. Longfellow, Ceram. Bull. 52, 513 (1973).
24. R. Belland, Electron Packaging and Production 15 (1), 56 (1975).
25. S.M. Copley, M. Bass, and R.J. Wallace, Proceedings of 2nd International Symposium on Ceramic Machining and Finishing. National Bureau of Standards Publication No. 562 (1978), pp. 283-292.
26. R.J. Wallace, M. Bass, and S.M. Copley, Physical Processes in Laser Materials Interaction. (To be published by Plenum, New York).
27. G.R. Forger, Mater. Eng. 87 (3), 30 (1978).
28. A.F. Mclean, Ceram. Bull. 52, 464 (1973).
29. A. Paluszny, Mater. Sci. Eng. 15, 39 (1974).
30. R.K. Bart, E.W. Hauch, and M.L. Torti, American Society of Mechanical Engineers Publication No. 75-GT-99 (1975).
31. D.W. Richerson and M.W. Robare, Proceedings on 2nd International Symposium on Ceramic Machining and Finishing. National Bureau of Standards Publication No. 562 (1978), pp. 209-222.
32. "NC-132 Hot Pressed Silicon Nitride," (Norton Company Industrial Ceramic Division, Worcester, MA).

33. Photon Sources Inc., Livonia, MI.
34. I.J. Spalding, Opt. Laser Technol. 10, 29 (1978).
35. "Infrared Optics Catalog" (II-VI Incorporated, Saxonburg, PA).
36. Coherent Radiation Inc., Palo Alto, CA.
37. F.O. Olsen, "Cutting with Polarized Laser Beams" Ph.D. Thesis, Lyngby, Denmark (1979).
38. M. Hass, J.D. Dawisss, H.B. Rosenstock, and J. Babisking, Appl. Opt. 14, 1128 (1975).
39. T.J. Meravec and E. Bernal, Appl. Opt. 17, 1938 (1979).
40. Newport Thin Film Lab., Santa Ana, CA.
41. J.G. Sickman and R. Morijn, Phillips Res. Rep. 23, 367 (1968).
42. G.R. Fowles, Introduction to Modern Optics. (Holt, San Francisco, 1968).
43. F. Reizman and W. Van Gelder, Solid-State Electron. 10, 625 (1967).
44. D.L. Decker and R.L. Wild, Physical Review B 4, 3425 (1971).
45. J.S. Haggerty and W.R. Cannon, National Technical Information Service No. AD-A063-064 (1978).
46. S.C. Singhal, Ceramurgia Int. 2, 123 (1976).
47. R.D. Pehlke and J.F. Elliot, Trans. AIME 215, 781 (1959).
48. H.D. Batha and E.D. Whitney, J. Amer. Ceram. Soc. 56, 365 (1973).
49. JANAF Thermochemical Tables. National Bureau of Standards Publication No. 37 (1971).
50. D. Rosenthal, Trans. ASME 68, 849 (1946).
51. H.E. Cline and T.R. Anthony, J. Appl. Phys. 48, 3895 (1977).

-
52. Y. Arata, H. Marvo, and I. Miyamoto, "Application of Lasers for Material Processing." Translated from: Japan Welding Society, April 1978.
 53. P. Ehrenreich, *Phy. Rev.* 129, 1550 (1963).
 54. H.W. Icenogle, B.C. Platt, and W.L. Wolf, *Appl. Opt.* 15, 2348 (1976).
 55. M. Hass, *Phys. Rev.* 117, 1497 (1960).
 56. I.F. Chang and S.S. Mitra, *Phys. Rev. B* 5, 4094 (1972).
 57. J.R. Jaspers, A. Kahan, and J.N. Plendl, *Phys. Rev.* 146, 526 (1966).
 58. S. Marcus, J.E. Lowder, and D.L. Mooney, *J. Appl. Phys.* 47, 2966 (1976).
 59. L.R. Hettch, T.R. Tucker, J.T. Schriempf, R.L. Stegman, and S.A. Metz, *J. Appl. Phys.* 47, 1415 (1976).
 60. R.L. Stegman, J.T. Schriempf, and L.R. Hettch, *J. Appl. Phys.* 44, 3675 (1973).
 61. J.A. McKay, R.D. Bleach, D.J. Nagel, J.T. Schriempf, R.B. Hall, C.R. Pond, and S.K. Manlief, *J. Appl. Phys.* 50, 323 (1979).
 62. D.W. Richerson and T.M. Yonushonis, Proceedings of the 1977 DARPA/NAVSEA Ceramic Gas Turbine Demonstration Engine Program Review. Battelle Lab. Report No. MCIC-78-36 (1978), pp. 193-217.
 63. R.G. Hoagland, C.W. Marshall, and W.H. Duckworth, *J. Am. Ceram. Soc.* 59, 189 (1976).
 64. Instrom Corp., Canton, MA.
 65. W. Weibull, *J. Appl. Mech.* 18, 293 (1951).
 66. G. Boothroyd, Fundamentals of Metal Machining and Machine Tools. (McGraw-Hill, San Francisco, 1975).
 67. D.G.S. Davies, *Proc. Br. Ceram. Soc.* 22, 429 (1974).

68. D.J. Tree and H.L. Kington, Proceedings of the 1977 DARPA/NAVSEA Ceramic Gas Turbine Demonstration Engine Program Review. Battelle Lab. Report No. MCIC-78-36 (1978), pp. 41-75.
69. D. Lewis III and S.M. Oyler, J. Am. Ceram. Soc. 59, 507 (1976).
70. G.K. Bansal, W.H. Duckworth, and D.E. Miesz, J. Am. Cer. Soc. 59, 472 (1976).
71. J.J. Petrovic, L.A. Jacobson, P.K. Talty, and A.K. Vasudevan, J. Am. Ceram. Soc. 58, 113 (1975).
72. R.W. Rice, The Science of Ceramic Machining and Surface Finishing. National Bureau of Standards Publication No. 348 (1972), pp. 365-376.
73. K. Heckel and H. Heigl, Third International Conference on Mechanical Behavior of Material. Pergamon Press, New York (1979), pp. 27-33
74. R.W. Rice and J.J. Mecholsky, Naval Research Lab. Report No. 4077 (1979).
75. J.J. Mecholsky, S.W. Freiman, and R.W. Rice, J. Am. Ceram. Soc. 60, 114 (1977).
76. H. Tada, P. Paris, and G. Irwin, The Stress Analysis of Cracks Handbook. (Del Research Corp., Hellertown, Penn., 1973).
77. Y.S. Tovlovkin, Thermophysical Properties of Matter, Vol. 13. (Plenum, New York, 1970).
78. S.T. Gulati and H.E. Hagy, J. Am. Ceram. Soc. 65, 1 (1982).
79. D.B. Marshall, B.R. Lawn, and P. Chantikul, J. Mater. Sci. 14, 2225 (1979).
80. D.B. Marshall and B.R. Lawn, J. Am. Ceram. Soc. 63, 532 (1980).
81. F. Laszlo, J. Iron Steel Inst. 148, 173 (1943).
82. C.R. Barrnett, W. Nix, and A.S. Tetelman, Principles of Engineering Materials. (Prentice-Hall, Englewood Cliffs, New Jersey, 1973).

-
83. R.E. Peterson, Stress Concentration Factors. (Wiley, New York, 1974).
 84. S.H. Baker, National Technical Information Service No. AD-A034-757 (1976).
 85. "Guidelines for Slicing and Grinding," (Norton Co. Industrial Ceramic Division, Worcester, MA).

APPENDIX II

SHAPING ARTICLES BY VAPORIZATION WITH A CO₂ LASER

by

Ralph Kein Chung Hsu

**A Dissertation Presented to the
FACULTY OF THE GRADUATE SCHOOL
UNIVERSITY OF SOUTHERN CALIFORNIA**

**In Partial Fulfillment of the
Requirements for the Degree**

DOCTOR OF PHILOSOPHY

(Mechanical Engineering)

April 1984

UNIVERSITY OF SOUTHERN CALIFORNIA
THE GRADUATE SCHOOL
UNIVERSITY PARK
LOS ANGELES, CALIFORNIA 90089

This dissertation, written by

.....RALPH KEIN CHUNG HSU.....

*under the direction of h...I.S..... Dissertation
Committee, and approved by all its members,
has been presented to and accepted by The
Graduate School, in partial fulfillment of re-
quirements for the degree of*

DOCTOR OF PHILOSOPHY

.....*William L. Spitzer*.....
Dean

DateApril 27, 1984.....

DISSERTATION COMMITTEE

.....*Stephen H. Copley*.....
Chairperson

.....*Michael Bess*.....

.....*Gregory A. Shillett*.....

**DEDICATED TO MY PARENTS PAUL YEU CHUNG HSU, CLARE SUE YING
HSU AND MY SISTER CHRISTABELLE.**

Acknowledgement

I would like to take this opportunity to thank Professor Stephen M. Copley for his support and guidance throughout my graduate studies at the University of Southern California. His encouragement and comments were most valuable in aiding me in completing the research project and writing my dissertation.

I would also like to thank the staffs from the Center for Laser Studies, Mechanical Engineering Department, Materials Science Department, and the School of Engineering's Machine Shop for their cooperation in routine day to day matters making my graduate studies at USC very pleasant and enjoyable. Their enthusiasm and willingness to help are deeply appreciated.

I am also grateful to the Defense Advanced Research Project Agency who supported this research under DARPA Order No. 4006, Contract No. MDA 903-80-C-0436.

TABLE OF CONTENTS

CHAPTER 1

1.1 Introduction	1
-------------------------------	----------

CHAPTER 2

2.1 Laser System And Materials Removal Techniques	4
2.2 Laser Beam Delivery System	10
2.3 Beam Characterization	12
2.4 He-Ne Beam Alignment System	16
2.5 CNC System And Positioning Tables	18
2.6 Programming Shapes Into CNC Positioning System	24
2.7 Procedures In Setting Up Coordinate System In Software	28
2.8 Choice Of Model Material	31
2.9 Procedures In Setting Focus On Workpiece	33

CHAPTER 3

3.1 Important Variables	35
3.2 Shaping Experiments	44
3.3 Effects Of Tilting Workpiece	54
3.4 Layer Removal On A Tilted Workpiece	65

3.5 Studies On Machining A Tilted Workpiece	69
3.6 Machining Shapes With Tilting About One Axis	72
3.7 Studies In Machining Workpiece Tilted About 2 Axis	79
3.8 Application To Si_3N_4	88

CHAPTER 4

4.1 Assessment Of Laser Shaping Process	92
---	----

CHAPTER 5

5.1 Conclusion	97
----------------------	----

LIST OF REFERENCES	98
--------------------------	----

APPENDIX	100
----------------	-----

A.I.1 Interface Control Commands and Schematics	101
A.II Software Listings	
A.II.1 Program For Beam Scan Experiment	107
A.II.2 Program To Determine Focal Plane on Workpiece	108
A.II.3 Program For Cutting Trails In Regions Of Focus (Normal Incidence)	109
A.II.4 Program For Tilted/Orientation Studies	112
A.II.5 Program For Machining Step	114

A.II.6 Program To Machine convex quad In Graphite	117
A.II.7 Program To Machine Concave quad In Graphite	120
A.II.8 Program To Machining Workpiece With 2 Rotation	123

List of Figures

1.1.1 Contour Approximation By Steps(layers)	2
2.1.1 Block Diagram Of Machining System	6
2.1.2 Velocity Effects On Material Removal	8
2.2.1 Laser Beam Delivery System	11
2.3.1 Schematic For Beam Scan Experiment	13
2.3.2 Beam Shape In The Region of Focus	14
2.3.3 Convention In Measuring Angle Between Electric Vector And Workpiece Translation Direction	15
2.4.1 He-Ne Beam Alignment System	17
2.5.1 CNC System And PDC Controller	19
2.5.2 Z Translation Table With Focussing Mechanism	21
2.5.3 Positioning Tables Assembly	22
2.5.4 Tilting Mechanism Assembly	23
2.6.1 Coordinate System In Base And Reference Frames	25
2.6.2 Generalized Flowchart In Programming A Shape Using(step) Layer Approximation	26
2.7.1 Reference Marks For Alignment	29
2.9.1 Convention In Defining Amount Of Defocus	34
3.1.1 Timing Relationship Between Laser Pulses And Motion Of Workpiece Under Pulse-Move Procotol	36
3.1.2 Timing Relationship Between Laser Pulses And Motion Of Workpiece Under Constant Velocity	38
3.1.3 Grooves Machined With A Normal Incidence Beam At Various Focus and Polarization Orientation	41

3.2.1 Layer Removal Technique To Form Step	45
3.2.2 Distortion In Step	46
3.2.3 Sloped Side-Wall Formation	48
3.2.4 Step Machined With Velocity Vector Parallel To Electric Vector	50
3.2.5 Step Machined With Velocity Vector Perpendicular To Electric Vector	51
3.2.6 Increase Absorption On Side-Wall By Tilting Workpiece	52
3.3.1 Tilt Angle About X Axis	55
3.3.2 Tilt Angle About Y Axis	56
3.3.3 Grooves Machined At Various Tilt Angles And Polarization Orientation	58
3.3.4 Effects Of Tilting On Incidence Angles At Side-Walls Of Grooves ..	61
3.3.5 Shapes Of Groove Development At 0 and 90 degrees To E Vector .	62
3.3.6 Shapes Of Groove Development At 45 and 135 degrees To E Vector	63
3.5.1 Layers Machined At Various Polarization Orientations(at focus) With Tilt = 30 Degree	71
3.5.2 Layers Machined At Various Polarization Orientations (Defocus = ~2 MM) With Tilt = 30 degree	71
3.6.1 Stock Before And After Machining	73
3.6.2 Workpiece Mounted On Tilt Platform	74
3.6.3 Step Machined With Tilting And Defocusing	76
3.6.4 Convex Quadrant(Graphite)	77
3.6.5 Concave Quadrant(Graphite)	78
3.7.1 Sign Conventions In Tilt Angles	80
3.7.2 Surfaces Of Interest In Shaping An Orthogonal Corner	81
3.7.3 xz Plane	83

3.7.4 yz Plane	84
3.7.5 xy Plane	85
3.7.6 Schematic Of 4 Quadrant Orientation Approach	87
3.8.1 Convex Quad(silicon nitride)	90
3.8.2 Concave Quad(silicon nitride)	91
4.1.1 Difficulties In Machining A Slot	93
A.1.1 External Laser Power Control Interface Circuit	102
A.1.2 Interface Board Layout In PDC	103
A.1.3 Laser Status Monitor Buffer	104
A.1.4 Home And Limit Switches For Translation Tables	105
A.1.5 Opto-electronic Home Switches For Translation Table & Actuation Cam	106

List of Tables

2.1.1 Laser Specifications	5
3.8.1 Operating Conditions	89

ABSTRACT

In order to understand,

→ A laser machining process for shaping non-solid of revolution shapes with a high power carbon dioxide laser operating in pulse mode was studied and developed. Graphite was used as the model material to develop the process and it was demonstrated that the process can successfully be adapted to machine silicon nitride.

Materials were removed, a layer at a time and by controlling the boundaries of the layers; a contour shape can be formed. A detail parametric study was conducted to determine the controlling variables in machining grooves and layers. The effects of angle of beam incidence and polarization on groove shape was studied and analysed on the basis of Fresnel's Law of Reflection.

Distortion introduced by reflections at the end of a layer was analysed and corrected by reorientation (tilting) of the workpiece with respect to the optical axis of the laser beam. Smoother surface finishes were obtained by defocussing the laser beam so the focal plane was above the workpiece.

Step, convex and concave shapes were machined successfully in graphite and silicon nitride by laser machining with the developed process. Furthermore, a blind orthogonal corner was machined successfully in graphite by tilting the workpiece about two axis demonstrating the possibility in machining a more general shape.

1.1 Introduction

Previous work of Wallace, Copley and Bass has established the feasibility of shaping ceramic articles with a high power CW CO₂ laser.¹⁴ A threaded workpiece of hot pressed Si₃N₄ was shaped with a laser beam on a lathe modified for laser machining to demonstrate the potential of machining ceramics in a turning configuration. The mechanism of removing material in laser machining involves vaporizing the material with the intense laser beam to form a groove. A straight forward analysis was developed based on the overlapping of grooves that predicts surface roughness and effective material removal rate as a function of process parameters. More recently, Wallace has carried out a detailed investigation of laser shaping of Si₃N₄.⁶ He has studied the effect of beam polarization on the shape of grooves,¹⁵ the energetics of groove formation¹⁶ and the shaping of articles by overlapping grooves.¹⁷ This work has been summarized in a recent review article by Copley.¹⁸

The purpose of this investigation is to develop an approach for producing a general shape with a high power laser and to assess its potential. To produce a general shape, material is removed by the laser beam a layer at a time exerting precise control over the boundaries of the removed layers. Figure 1.1.1 is a schematic drawing showing the formation of a contoured surface by the layer removal process.

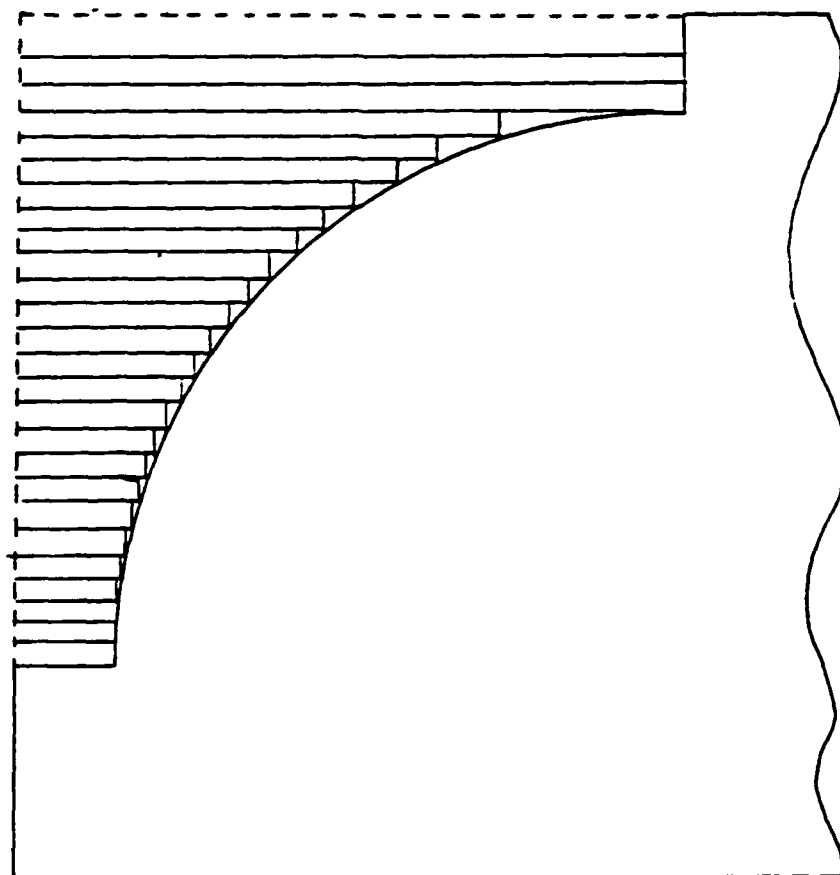


Fig. 1.1.1 CONTOUR APPROXIMATION BY STEPS (LAYERS)

The potential for laser shaping appears to be great for some materials that are difficult to shape by conventional grinding processes. *Ceramics such as SiC, Si₃N₄, and AlN* are examples of materials that can be shaped successfully with this process. It is foreseeable that a complete category of materials, which are difficult to machine with conventional processes, having properties that couple well with the high power laser and that vaporize under intense heat, would be good candidates for this laser machining process.

2.1 Laser System and Materials Removal Techniques

The high power carbon dioxide laser used in this study is a Photon Source Model 1003 laser. The laser has a maximum output of 1250W continuous power at 10.6 microns. It is also equipped with a programmable digital controller to operate the laser in pulsed mode and in a variety of other modes electronically. A detailed description of the laser system's construction, controls, and characteristics can be found in the manufacturer's manuals.² Table 2.1 is a brief listing of the specifications of the Model 1003 laser.

Figure 2.1.1 is a block diagram of the systems employed in the laser machining process. The laser beam is stationary and the workpiece is translated in the X-Y direction in this process. The focussing lens assembly is mounted on a translation table which moves in the Z direction. Material is removed by irradiating the workpiece in a controlled layer by layer method. A layer is removed by overlapping grooves. Grooves can be formed by irradiating the surface of the material with a CW beam or with a pulsed beam to produce an overlapping series of holes. In previous work, the workpiece was rotated making beam speeds of 10 - 100 cm/s possible. In this study the use of the X-Y translation stage limited beam velocities to less than 5 cm/s. Since the depth of the layer removed depends on the amount of energy absorbed locally, maintaining a suitable layer depth at such a low beam velocity required decreasing the power. However, it was found that the high power laser was not stable when operated at CW powers of less than 450W. Thus, an

Photon Sources Model 1003 Laser

Wavelength:	10.6 micrometers
Output Power Range:	125 to 1250 watts
Output Power Stability:	2 percent, 8 hours
Mode:	TEM₀₁*
Active Discharge Length:	18 meters
Beam Diameter:	1.8 centimeters (1/e²)
Beam Divergence:	2.2 milliradians
Minimum Pulse Duration:	100 microseconds
Maximum Repetition Rate:	1 kHz

Table 2.1 Laser Performance Characteristics².

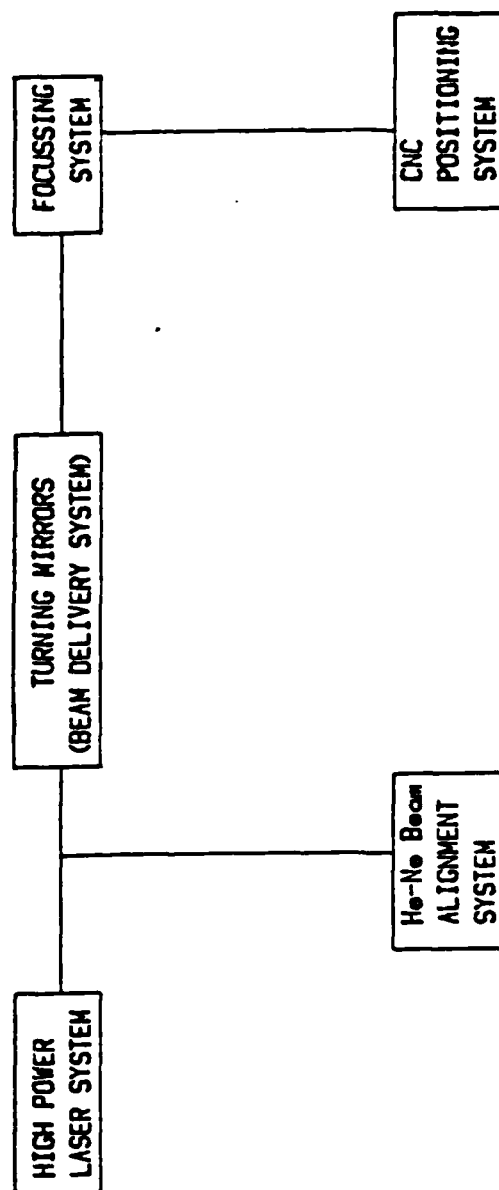
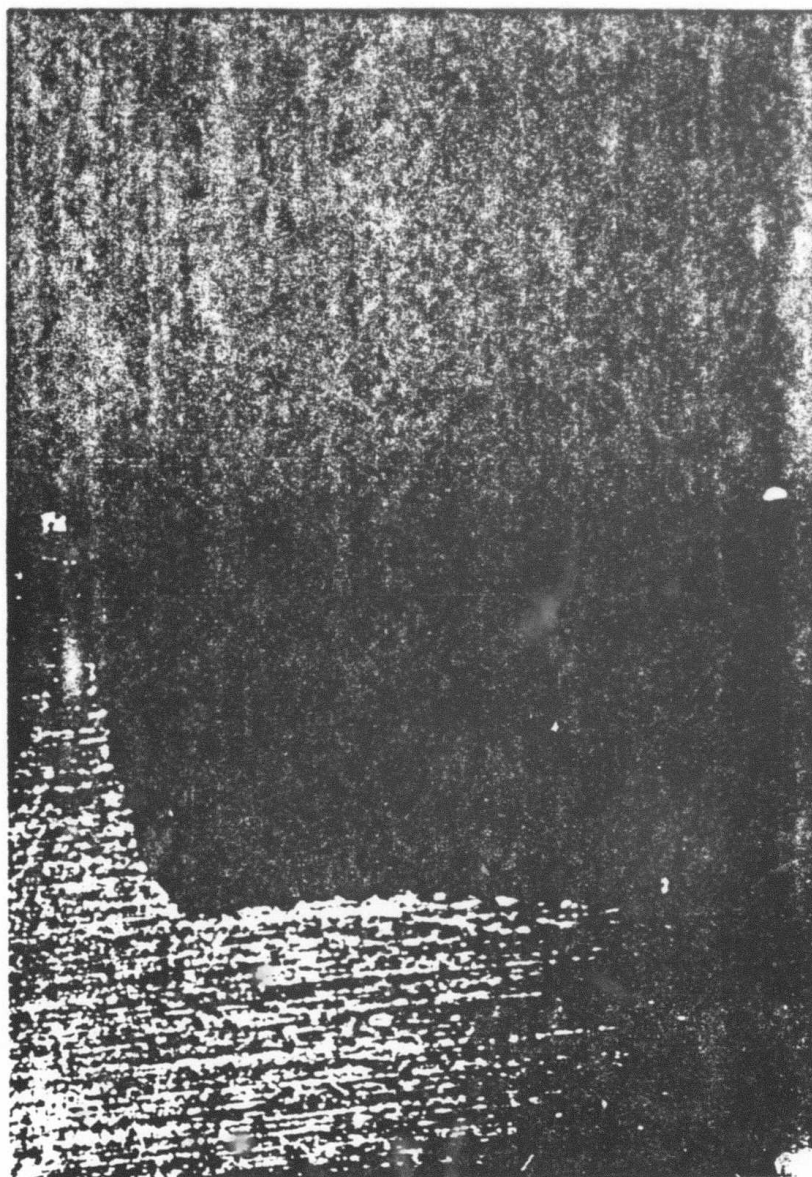


Fig. 2.1.1 BLOCK DIAGRAM OF MACHINING SYSTEM

alternative approach was adopted; namely, operating the laser in a repetitively pulsed mode.

If the depth of the layer being formed is to be constant, it is necessary to deposit equal amount of energy at all locations being irradiated. One obvious approach is to maintain constant beam velocity throughout the shaping operation. However, this approach poses difficulties because the mechanical system requires time to accelerate the workpiece from rest to constant velocity due to inertia. During the acceleration of the workpiece from rest, the irradiation time with a repetitively pulsed beam is longer than that when the workpiece has attained constant velocity. The variation in velocity will result in an undesirable variation of the depth of the groove being formed. Figure 2.1.2 is a photograph showing the effects of velocity in machining a slot in graphite with overlapping grooves. The undercut on each side of the bottom is due to the acceleration and deceleration of the workpiece. More complicated control schemes such as modulating the power of the beam according to the velocity of translation have been considered but the response time and the duration taken for the beam to stabilize at a certain power will again cause grooves with variable depth to be formed.

Two alternative techniques in operating the laser were developed and used in these studies to avoid some of the control problems. The laser was operated either in repetitively pulsed mode or under a pulse-move protocol depending on the shaping operation. Operating the laser in a pulsed mode with a simple pulse-move protocol eliminates the control



TRANSLATION DIRECTION

Fig. 2.1.2 VELOCITY EFFECTS ON MATERIAL REMOVAL

problems associate with operating the laser in the repetitively pulsed mode. The protocol insures that each laser pulse is completed before the workpiece is moved to the next location. In cases when it is possible to have ramp up/down distances to build up speed of the workpiece to constant velocity before laser pulsing is initiated, the repetitively pulsed mode is employed. This alternative technique has higher material removal rate compare to the pulse-move approach.

The Z axis(focussing lens) is operated in an open-loop control fashion. The incremental change in Z after each layer is removed was determined experimentally and was programmed into the CNC controller for the machining process. Deviation of the actual depth of cut from the programmed values during machining are not sensed or compensated for in this control algorithm. A closed-loop control algorithm would be superior but was considered to be too complicated and difficult to implement for this process at this time. A sensing system which can operate in the vicinity of a plasma plume without interfering with the shaping process would have to be developed to close the loop for this machining process. In the closed-loop control algorithm, the actual depth of material removed would be measured with a sensor and supplied to the CNC controller for the contouring computations. Variations in the depth of cut would be compensated for during machining with this algorithm.

2.2 Laser Beam Delivery System

The laser beam is delivered to the workstation by two turning mirrors M1, and M2 as shown in Fig. 2.2.1. The mirror, M1, is a water-cooled copper mirror installed in a 2 axis mirror mount located at the beam exit port from the laser system enclosure. It bends the laser beam 90 degrees in the horizontal plane pointing it in the direction of the workstation.

The mirror, M2, is an air-cooled molybdenum mirror mounted in the turn head at the workstation. It bends the horizontal beam from M1, 90 degrees vertically down through the focussing mechanism towards the X, Y translation tables. The beam path between the two turning mirrors is enclosed with aluminum conduit tubings for safety reasons.

The focussing mechanism is installed on the Z translation table between M2 and the X, Y translation tables of the CNC system. The focussing lens and a gas delivery system are mounted to this mechanism. The gas delivery system provides a path to deliver a stream of gas coaxially with the focussed beam. The gas can exit only through the jet nozzle mounted at the bottom of the inlet chamber of the gas delivery system. One of the main purposes of this gas is to provide a shield for the focussing lens from the products produced by the vaporizing action of the laser beam. In some cases, a reactive gas is used for gas-assisted machining processes.

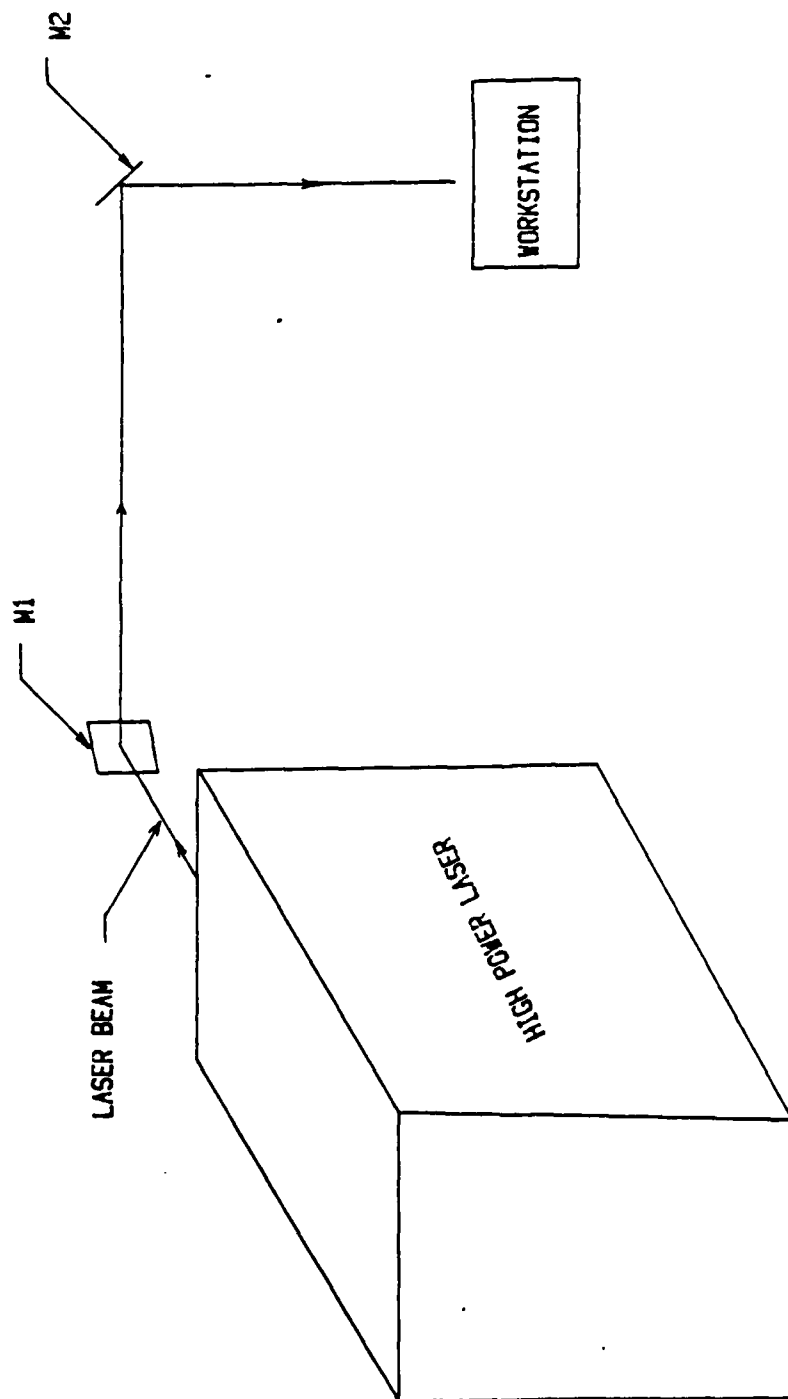


Fig. 2.2.1 LASER BEAM DELIVERY SYSTEM

2.3 Beam Characterization

The profile spatial distribution of the focussed laser beam in the region of the focal plane is determined via a single slit, beam-scan experiment. The width of the slit was approximately 20 microns. A schematic diagram showing the experimental set-up is given in Fig. 2.3.1.

A scan across the beam diameter produces a power versus position trace which can be used to determine the spot size of the beam. The translation speed and slit opening are carefully matched to the response time of the detector for an accurate recording of the beam profile.

A series of scans in the region of the focal plane were made and the respective spot sizes calculated by the $1/e^2$ convention were plotted in Fig. 2.3.2.

The polarization of the laser beam was measured with a polarizer. The beam was chopped and the polarizer was placed after the second turning mirror. The measurement indicates that the electric vector E pointed in the the 18 degrees direction as shown in Fig. 2.3.3.

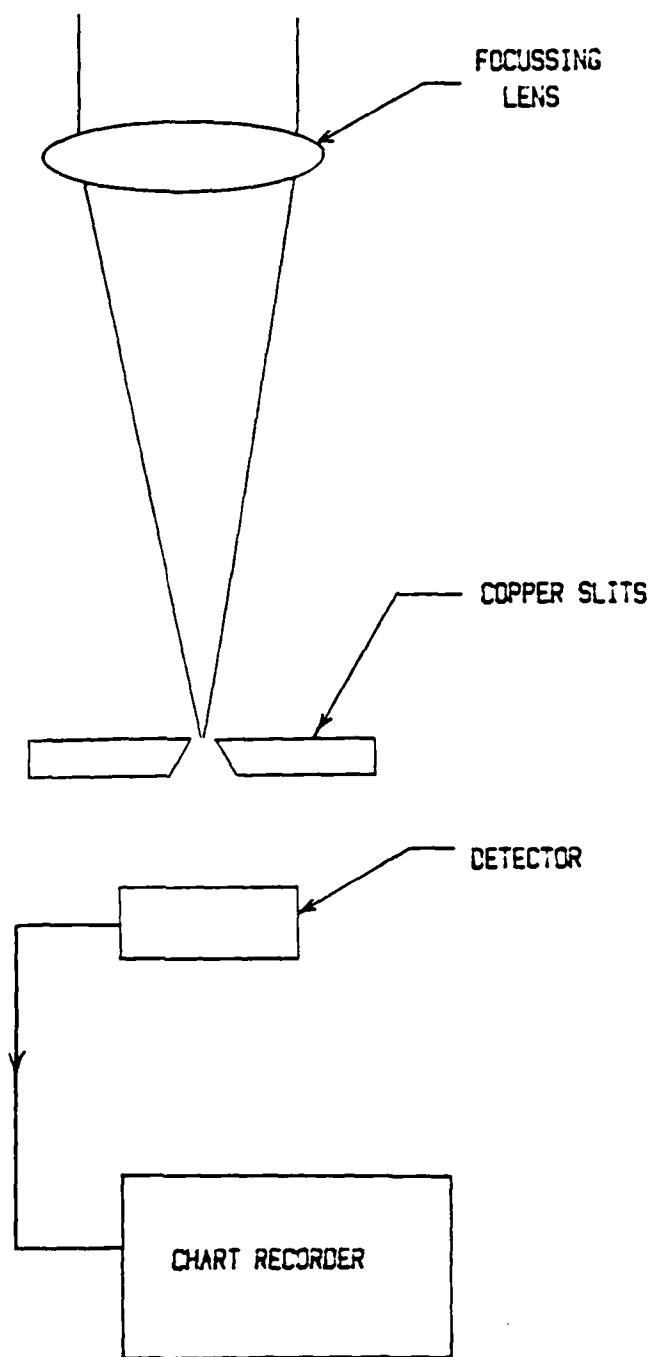


Fig. 2.3.1 SCHEMATIC FOR BEAM SCAN EXPERIMENT

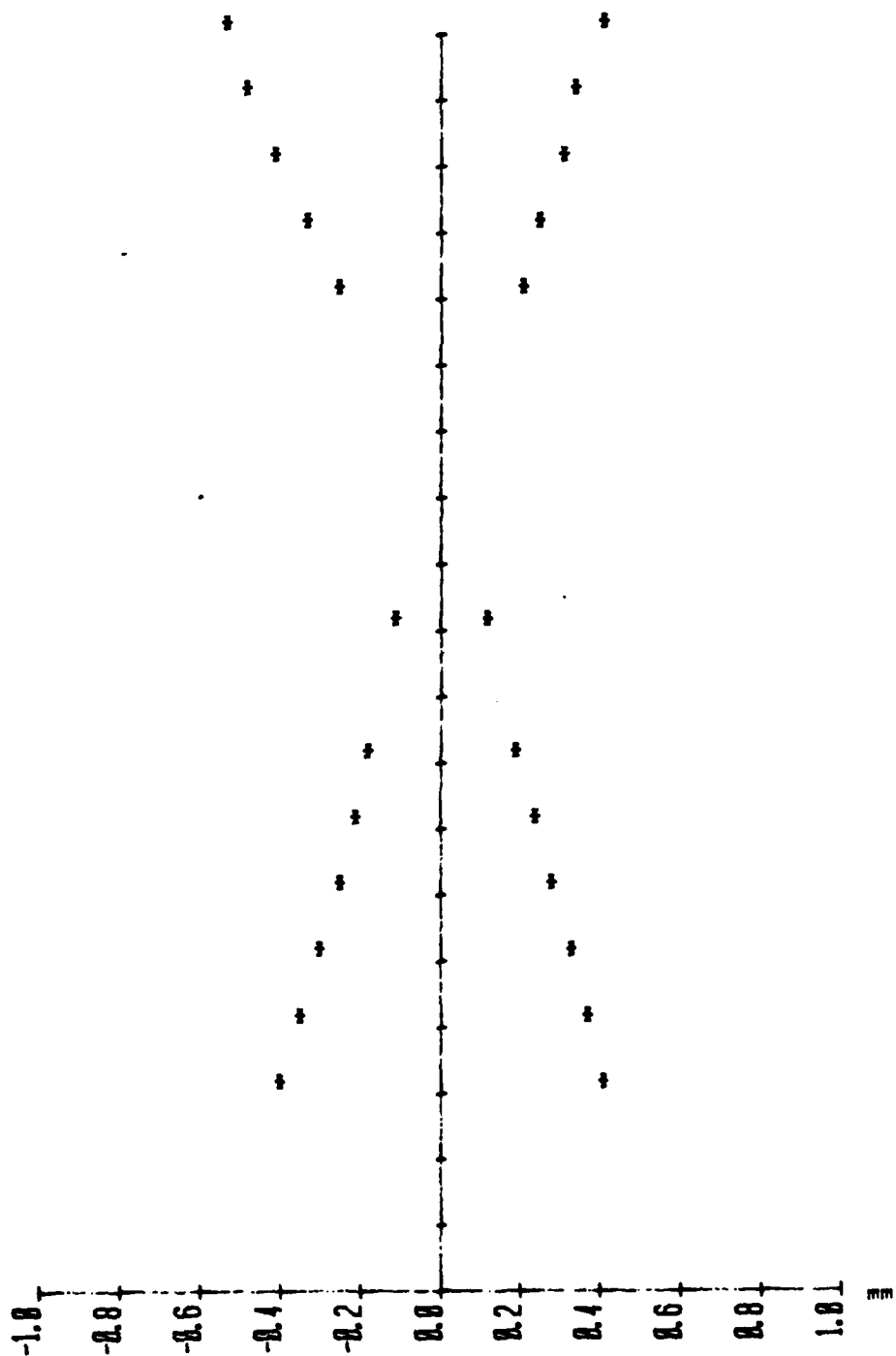


Fig. 2.3.2 BEAM SHAPE IN THE REGION OF FOCUS
VERTICAL AXIS 0.5 mm/div (1/e² plot)

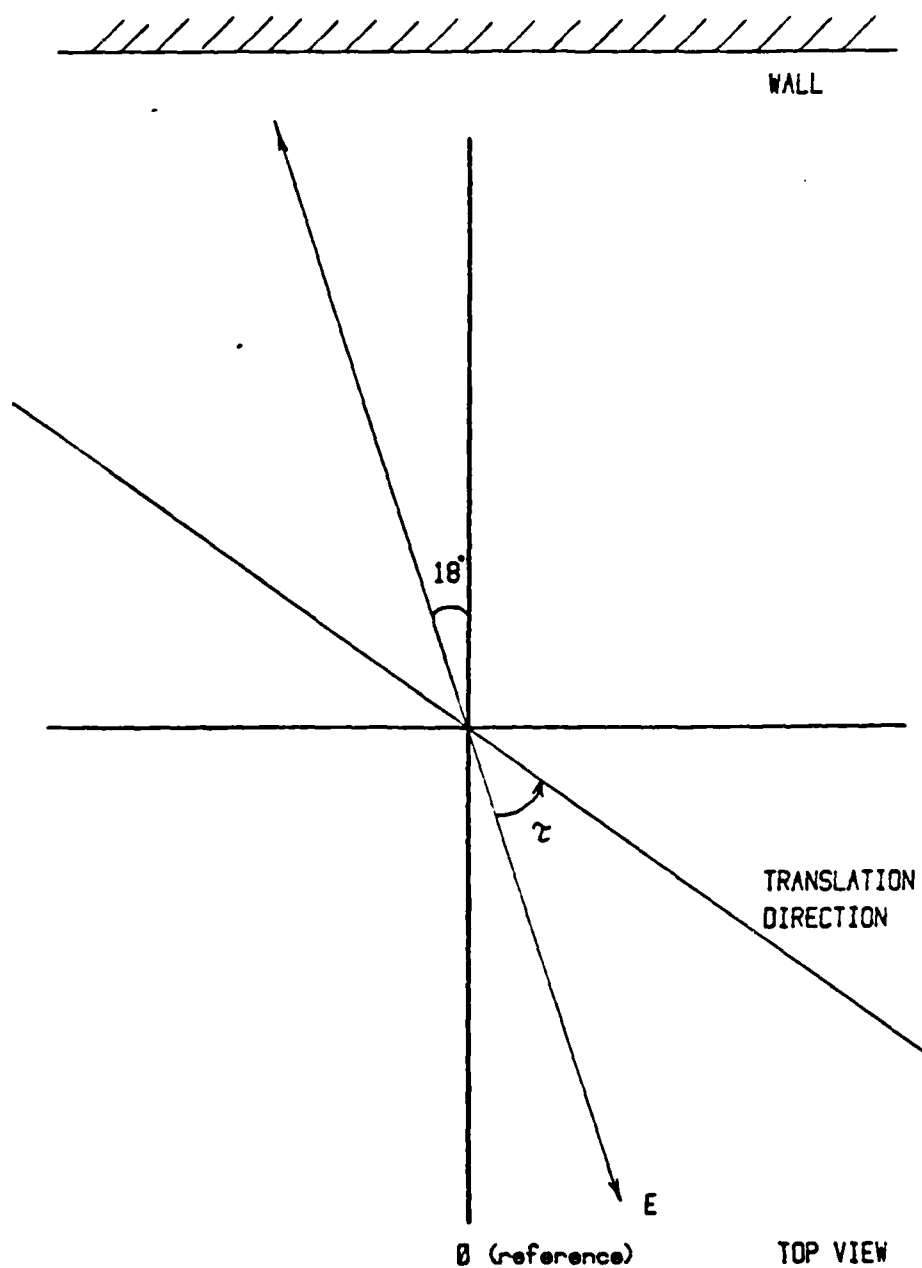


Fig. 2.3.3 CONVENTION IN MEASURING ANGLE BETWEEN ELECTRIC VECTOR AND WORKPIECE TRANSLATION DIRECTION

2.4 He-Ne Beam Alignment System

The 10.6 micron carbon dioxide laser beam is in the infra-red region of the electromagnetic spectrum and is invisible to the naked eyes. A remotely acutuated He-Ne laser is incorporated into the system to assist the optical alignment procedures in the machining process. The He-Ne laser emits a red color light and is coaxially aligned with the main carbon dioxide laser beam. When an alignment procedure such as positioning of the workpiece is needed, the He-Ne laser beam is switched in remotely by inserting a mirror in the beam path between M1 and the beam exit of the laser system. Figure 2.4.1 is a photograph of the He-Ne Beam alignment system. The visible beam is carefully aligned to the carbon dioxide laser beam so all external optical adjustments can be done with the He-Ne beam. When the necessary alignment procedures are completed, the He-Ne beam is switched out of the beam path so the high energy beam can be turned on.

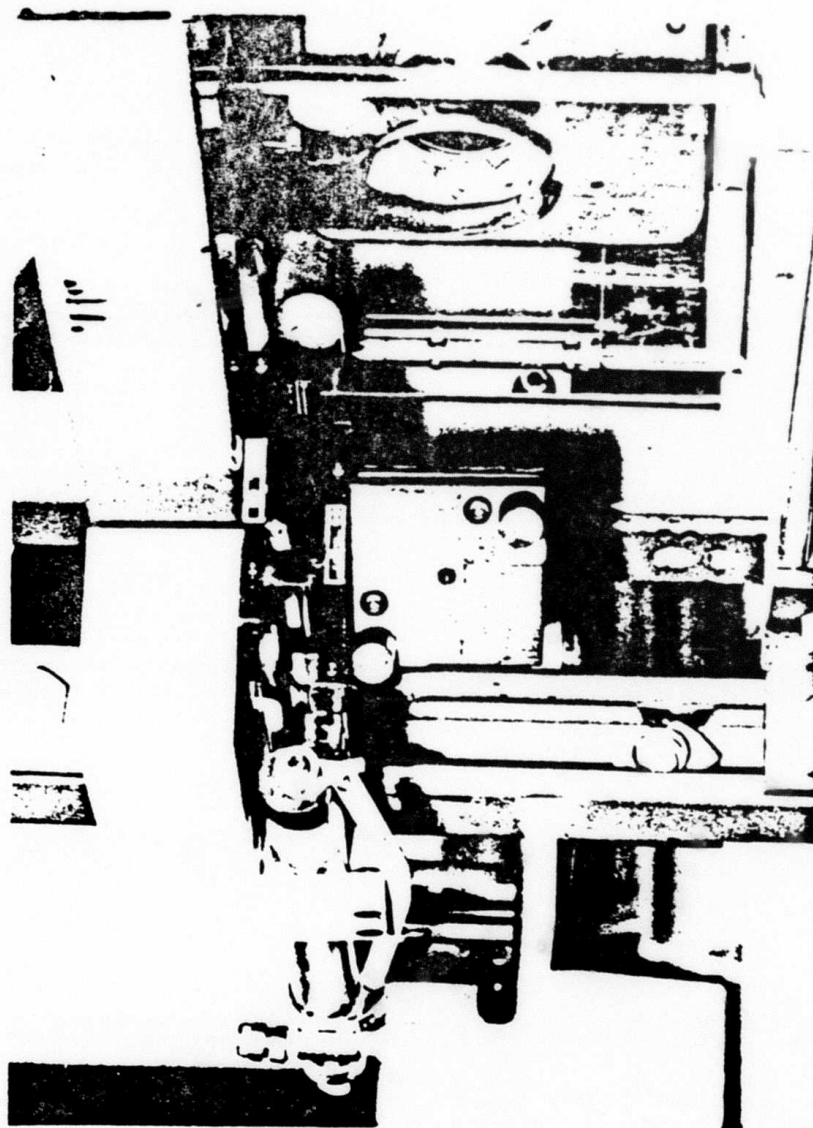


Fig. 2.4.1 He-Ne BEAM ALIGNMENT SYSTEM

2.5 CNC System and Positioning Tables

The Anomatic II computer numerical control positioning system employed in this study is capable of operating 5 axes simultaneously. However, it has been configured only to operate the X, Y and Z axis at the current time. Detail specifications giving the capabilities and construction of the system can be found in the manuals provided by the manufacturer.³ In the course of this investigation, the Anomatic II system was interfaced to a programmable digital controller(PDC) by the author so that some of the laser control function could be incorporated into computer programs written for the CNC systems. Figure 2.5.1 is a picture of the CNC system with the laser's PDC controller.

Laser power, program sequence on/off, and safety shutter on/off functions can be actuated by the CNC controller if desired. Operation details and schematics for the interfaces are included in Appendix I.

The Z axis translation table assembly was purchased from Anorad Corporation.[3] It has 70 mm of travel, and a 25 lines/mm linear encoder for position feedback. The mounting brackets and accessories to integrate the table into the laser machining system were designed and fabricated at USC. The X, Y tables were reconditioned and modified for use with the Anomatic II CNC positioning system. These tables have a travel of 140 mm, 1 mm pitch leadscrews and 100 lines/rev rotary encoders for position feedback. The maximum speed attainable on the X, Y tables are 5 cm/s. All axes are equipped with

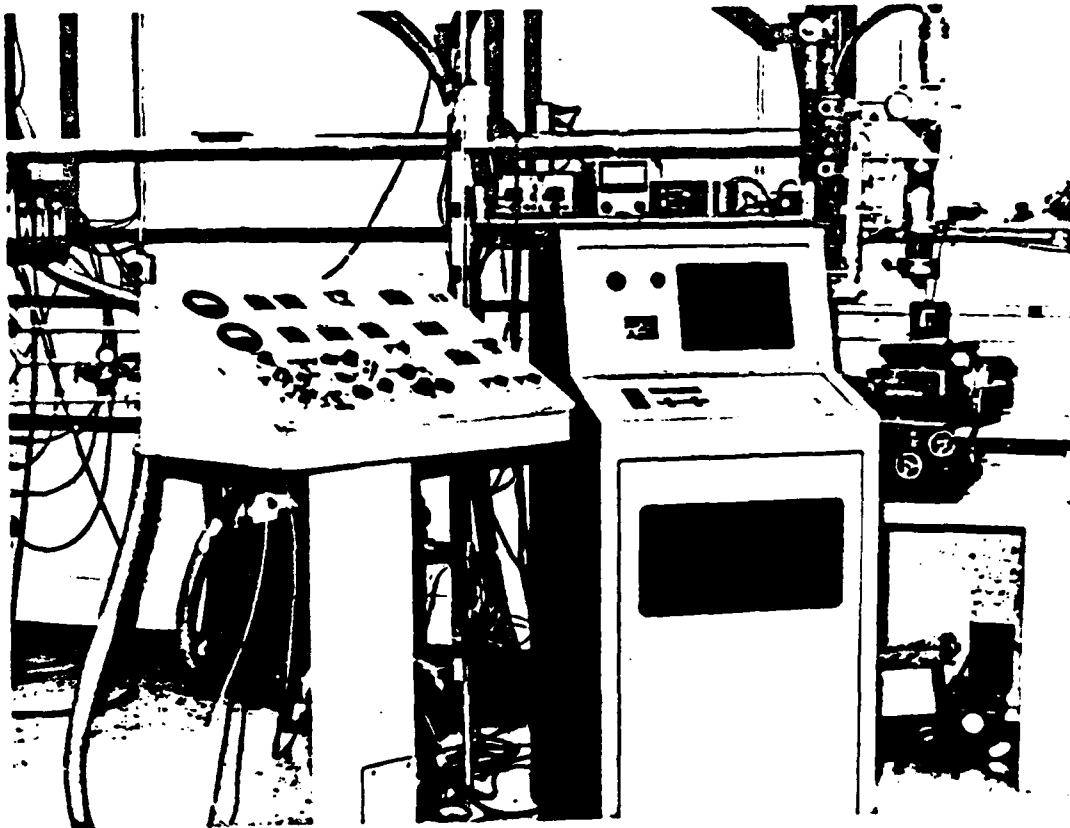


Fig. 2.5.1 CNC SYSTEM AND PDC CONTROLLERS

20X logic cards for their position feedbacks. Tachcometers mounted at the end of the drive motors provide velocity feedback of the respective axis. The computer controlled X, Y table assembly was mounted on a manual X-Y- ϕ mounting table allowing more flexibility in positioning the assembly. In addition, a Newport elevator platform was mounted on top of the X, Y table assemblies for ease of raising or lowering the tilting mechanism.¹⁰ Figure 2.5.2 is a picture of the Z translation table with the focussing mechanism and Fig. 2.5.3 is a picture of the various table assemblies.

The tilting mechanism was assembled with two Newport rotary mounts for rotation about X and Y axis. The axes of rotation of the two mounts intersect each other. The workpiece mounting platform was bolted to the X rotation mount and a hold down bracket was bolted to the base of the Y rotation mount. The complete mechanism was secured to the elevator platform by bolting down the hold down bracket to the platform. Figure 2.5.4 is a picture of the tilting mechanism assembly mounted to the elevator platform.

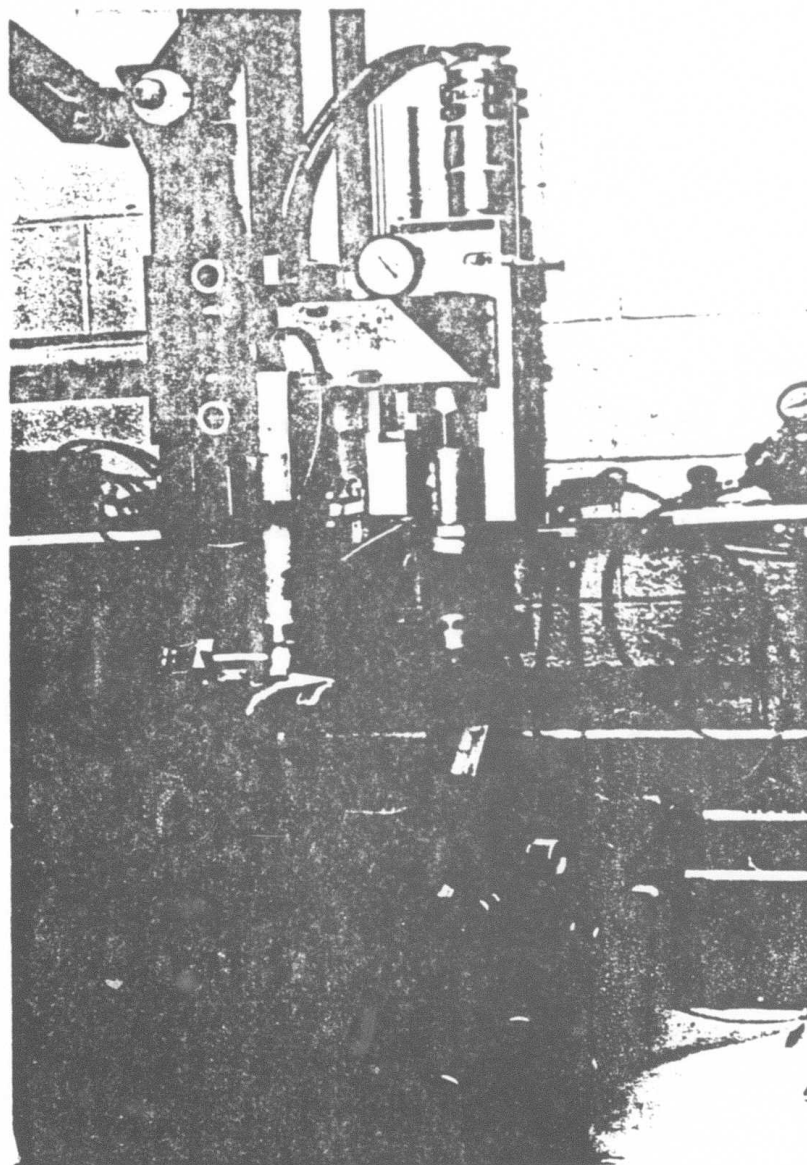


Fig. 2.5.2 Z TRANSLATION TABLE WITH FOCUSING MECHANISM

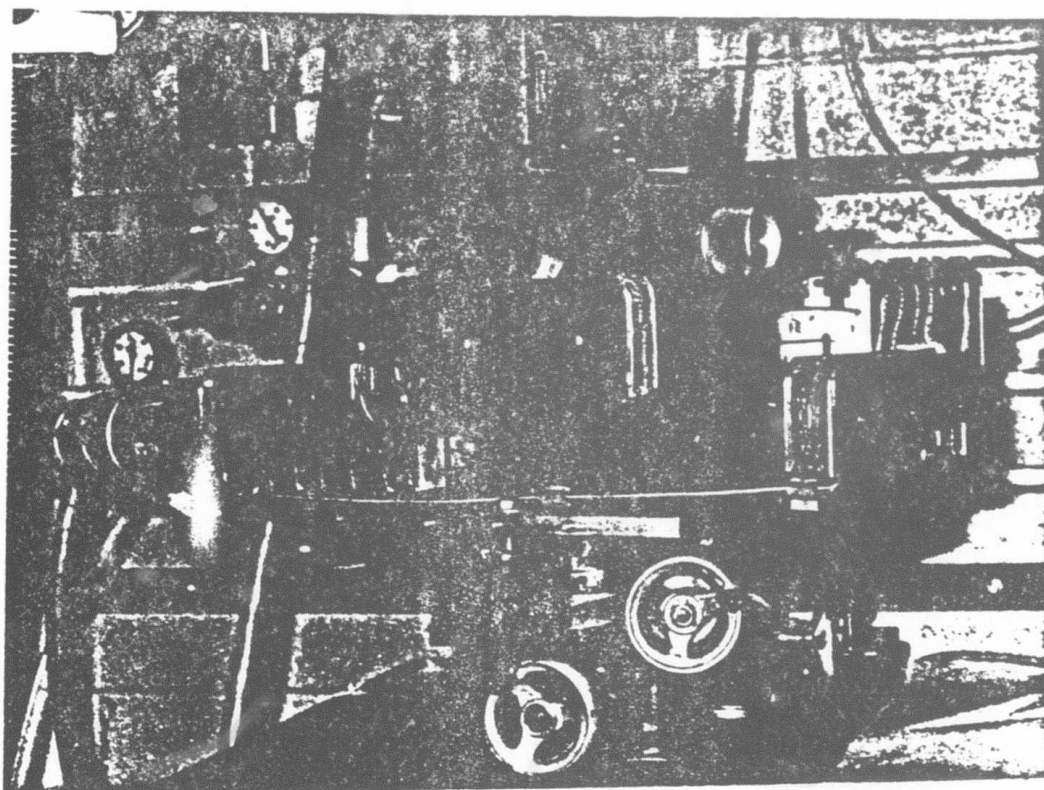


Fig. 2.5.3 POSITIONING TABLES ASSEMBLY

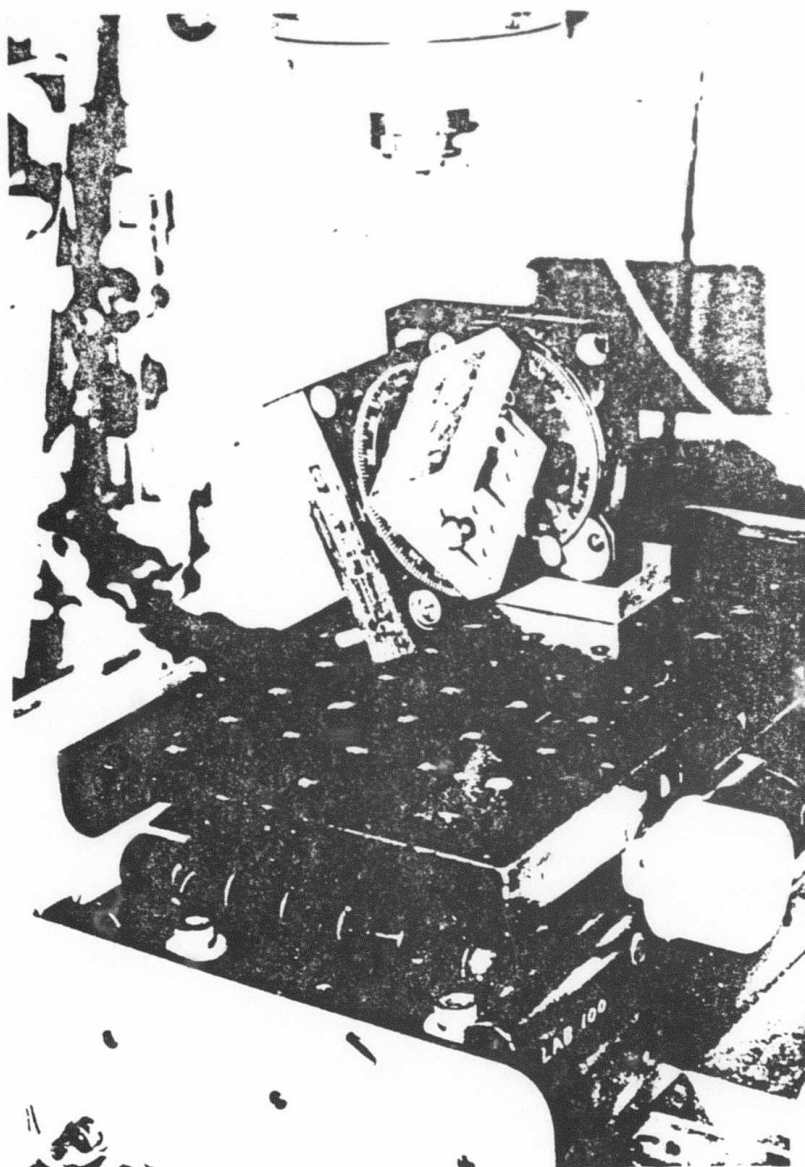


Fig. 2.5.4 TILTING MECHANISM ASSEMBLY

2.6 Programming shapes into the CNC machining system

The programming techniques used to define shapes to be machined for the Anomatic system are similar to those of any numerically controlled system used to generate a three dimensional shape. The shape to be made is defined in a set of orthogonal axes, namely X, Y and Z. The outline of the part is generated by stepwise approximation. Figure 2.6.1 is a diagram showing the reference and base frames of the coordinate systems used. The reference frame is a set of coordinates imbedded in the tilting mechanism to simplify the description of the shape to be made. The origin of the base frame was carefully chosen to be at the intersection of the X, Y rotational axis of the rotation table assemblies in order to simplify the transformation computations. Layers of materials are removed starting from the top of the stock to form the desired shape. Figure 2.6.2 shows a generalized flowchart in programming a shape using the layer approximation.

Step(1) of the program, "initialize variables and system", sets the stepsize, tilt angle, laser power, translation speed, amount of defocus, translation distances, starting positions, and the position vector P in the base frame pointing to the origin of the reference frame.

Step(2) of the program, "calculate translation vector", calculates the translation vector T as defined by Eq. 3.4.4 and Eq. 3.4.7 in Sect. 3.4.

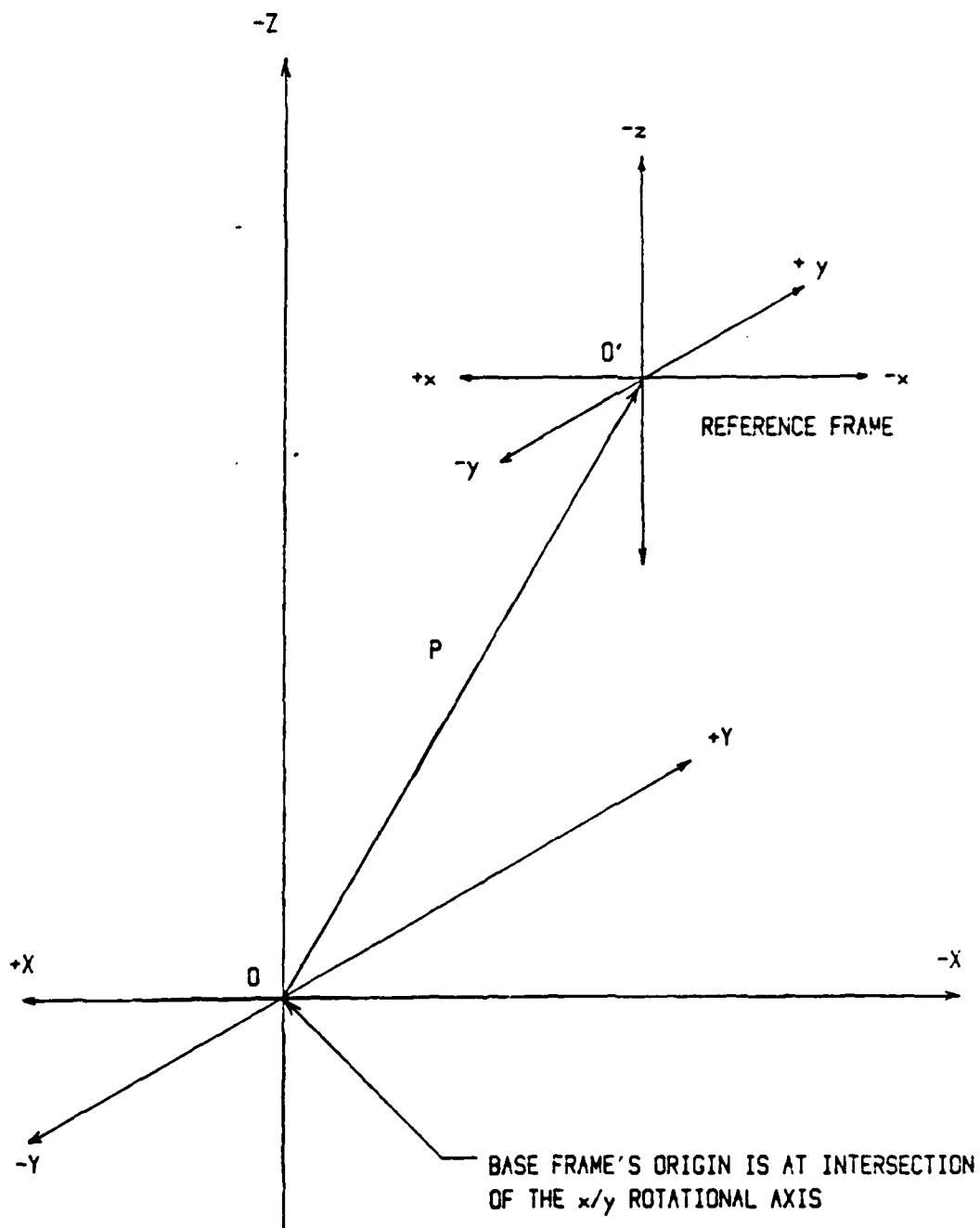


Fig. 2.6.1 COORDINATE SYSTEMS IN BASE AND REFERENCE FRAMES

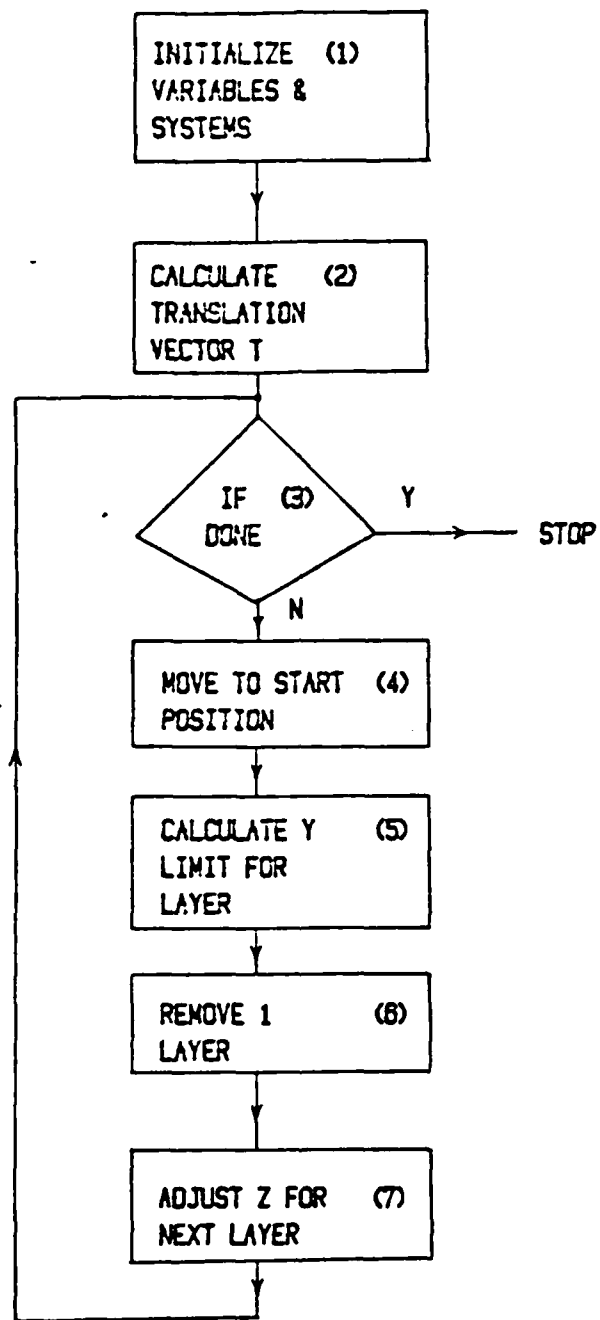


Fig 2.6.2 GENERALIZED FLOWCHART IN PROGRAMMING A SHAPE USING(STEP) LAYER APPROXIMATION

Step(3) of the program, "if done", checks if the last layer has been machined. If yes, the machining process is completed.

Step(4) of the program, "move to start position", computes and moves the workpiece to the proper starting position in the base frame.

Step(5) of the program, "calculate Y limit for layer", calculates the Y dimension of the layer to be removed. The Y limits vs Z distance plot will give a stepwise approximation of the profile of the shape to be formed.

Step(6) of the program, "remove 1 layer", fires the laser and moves the workpiece accordingly so that the layer of material is removed as specified. The workpiece is moved according to the pulse-move protocol or continuously pulsed and translated at a constant velocity.

Step(7) of the program, "compute and adjust Z for the next layer", computes and adjusts the focussing lens (Z axis) to the proper position in the base frame to machine the next layer.

Steps (3) through (7) are repeated until the machining process is completed. The flowchart represents the general format in programming a shape into the CNC system. The shapes to be formed are defined in the calculated limits in each of the X and Y layers being removed.

2.7 Procedures to set up coordinate system in software

It is of great importance that the physical position of the reference and base frames in the positioning hardware agrees with that in the CNC system's software. The set up procedures are described in the following paragraphs.

The alignment procedures are done with the He-Ne laser alignment system and a 127 mm(5 in) focal length salt lens.

The elevator platform is adjusted such that it is 76.2 mm(3 in) above the Y translation table. The tilt mechanism is mounted as shown in Fig.2.5.4. The rotational axes are parallel to the X-Y tables' translation direction respectively. The tilt angles are set to zero on both mounts. The X, Y and Z tables are sent home¹ and the position counters in software are zero. The X, Y tables are moved to the middle of their travel, and the Z axis is jogged down manually so that a focussed He-Ne spot can be seen on the mounting platform of the tilting mechanism. The X, Y table assembly is manually positioned by adjusting the cranks of the X-Y tables on the base mount till the He-Ne spot is aligned with the cross-hair mark on the mounting platform. The alignment procedures in setting up the origin in the X, Y plane of the baseframe is completed.

The thickness of the stock to be used in the machining must be known to set up the proper Z coordinate system. Figure 2.7.1 shows the respective dimensions used in the set up procedures. The top of the

¹ A fixed reference position in each of the translation tables.

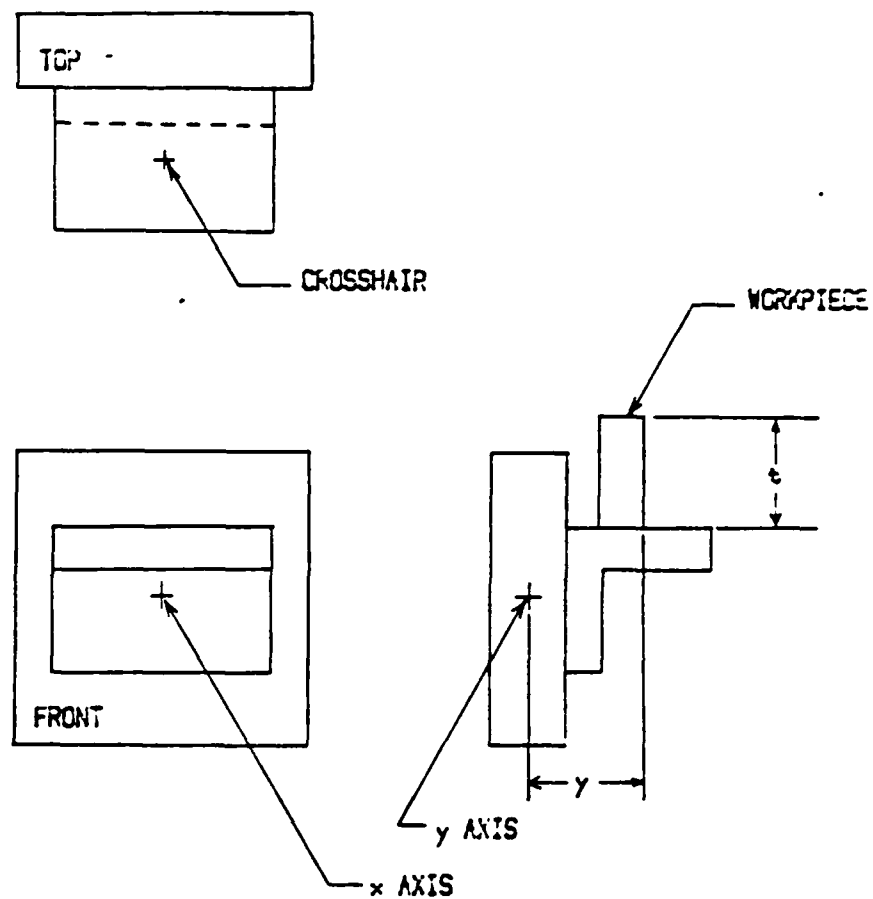


Fig. 2.7.1 REFERENCE MARKS FOR ALIGNMENT

mounting platform has been set to be 25mm above the X rotational axis. With a rectangular block of thickness t , the Z distance of the top of the workpiece with respect to the base frame is $(25+t)$ mm. The following procedures are executed to place the origin of the reference frame at the top surface of the workpiece. The focal plane of the lens is established by the method as described in Sect. 2.9. The physical position of the focal plane (h mm) with respect to the Z home is recorded. The Z axis is sent home and the position counters are set to zero. The Z axis is moved to position h , and the position counters are again set to zero. The current Z position is redefined, with an offset command, in software to be $(25+t)$ mm. The Z position ; of the lens is now properly defined according to the base frame coordinates in software. Care should be exercise in setting the starting position variables when initializing the software. The position of the origin of the reference frame can be relocated by redefining the position vector P in software. It is of crucial importance that the physical position of the focal plane of the lens be maintained at the correct position after redefining the origin of the reference frame.

2.8 Choice of model material

The purpose of this study is to develop a laser machining process. Graphite was chosen as the model workpiece material for the following reasons:

1. It has homogeneous properties
2. It is relatively inexpensive
3. It is readily available in many forms and shapes
4. It does not generate hazardous by-products during vaporization
5. A simple vacuum cleaner system is sufficient to remove the by-products
6. It has high absorptivity at 10.6 micron
7. It consists of a single element (Carbon)
8. It can be easily handled

More specifically, Poco Graphite type CZR-1 was used throughout this study.¹¹ A preliminary set of experiments were conducted to demonstrate that it is possible to machine graphite with the CO₂ laser beam. Grooves were cut successfully in graphite blocks translating at 40 mm/sec with a beam of power level between 400 to 1000W, focussed with a 127mm(5 in) focal length lens. The grooves formed in graphite were comparable in size and shape to those machined in Si₃N₄ in previous studies.

In conventional machining processes such as turning, milling, drilling, various materials require different feeds, tool geometries, spindle speeds etc. It is reasonable to anticipate a similar variation in the set of control

variables when different materials are being laser machined. Identifying such parameters is an objective of this investigation.

2.9 Procedures in setting focus on workpiece

The focal plane of the focussing lens in the base frame is determined experimentally. A piece of carbon steel of known thickness is placed on top of the workpiece to be machined. The laser is set at an average power of 700 W cavity power, pulse-width of 10 ms, and a pulse repetition rate of approximately 1 Hertz. The Z axis is brought within range of focus manually using the jog buttons on the CNC system. A blue-white color plasma is generated when the lens is in the range of focus. After the lens is brought into range of focus, the "range of focus" software is executed to locate the focal plane of the focussing lens. The software follows the Z position of the lens from the physical home of the Z axis, fires a pulse at a specific X location and Z setting, moves the translation stages to new X and Z settings, fires the laser again and repeats the process till the defined range of Z has been covered. The steel sample is then removed from the workstation and studied under a microscope. The holes made by the laser pulses are compared to their respective Z positions with the computer print out. The focal plane is identified as the Z distance associated with the deepest hole. In the event that a group of holes have similar depth, the mean Z distance of the group is used to establish the focal plane. The focus on the top surface of the workpiece would be the Z distance determined by the above method plus the thickness of the steel plate. The amount of defocussing is determined in referenced to the established focal plane. Figure 2.9.1 is a diagram illustrating the convention used in defining the appropriate signs for defocussing.

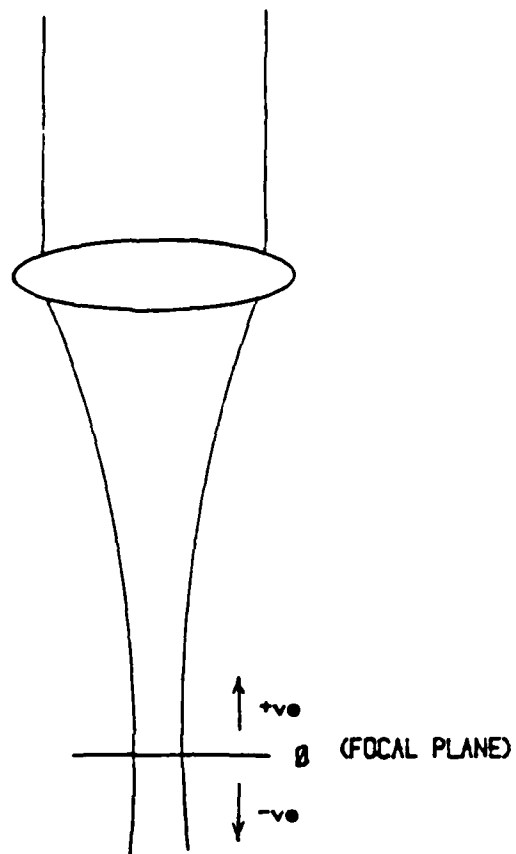


Fig 2.9.1 CONVENTION IN DEFINING AMOUNT OF DEFOCUS

3.1 Important Variables

One of the objectives of this study is to identify the essential control variables pertinent to laser shaping processes. Many of the variables are related to each other in a complicated fashion and can vary from material to material. Wallace has discussed how various variables affect the depth of material removed and surface roughness in a continuous wave laser machining process.⁶ The variables identified in Wallace's work can be summarized as follows:

1. focussed spot size(depends on the focal length of the focussing lens, the diameter of the unfocussed beam, and the wavelength of the laser);
2. focal plane position with respect to surface to be irradiated;
3. power of the laser;
4. velocity of translation of workpiece;
5. type of shielding gases and flow rate;
6. cross-feed when overlapping grooves; and
7. polarization of the laser beam.

When a workpiece is irradiated by a repetitively pulsed beam, the duty cycle of the pulses and the translation velocity of the workpiece together contribute to the actual dwell time of irradiation on the workpiece. In the case when machining is performed under pulse-move protocol, the dwell time of irradiation on the workpiece will depend only on the on-time duration of the laser pulse fired. Figure 3.1.1 shows the timing relationship

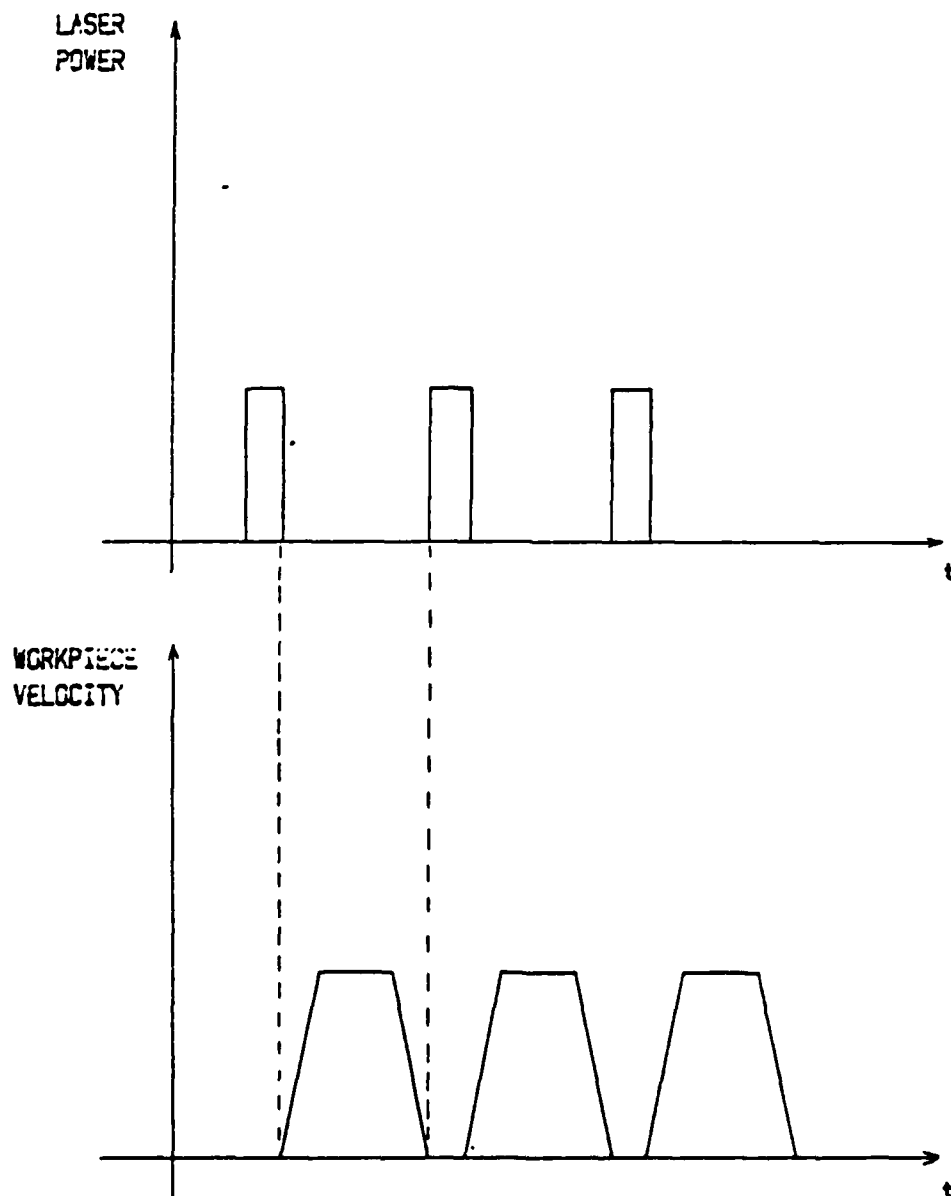


Fig. 3.1.1 TIMING RELATIONSHIP BETWEEN LASER PULSES AND MOTION OF WORKPIECE UNDER PULSE-MOVE PROTOCOL

between the laser pulses and the translation of the workpiece under pulse-move protocol and Fig. 3.1.2 shows the case when the workpiece is translated at constant velocity.

It is necessary to acquire quantitative data about the effects of various control variables on the laser machining process before experiments to machine contour shapes can be performed. A preliminary set of criteria based on surface finishes and depth of cuts were used to determine the settings of various key controlling variables. It is crucial to have sufficient overlap of holes when forming a groove and sufficient overlapping between grooves to form a surface with an acceptable finish. Furthermore, the depth of cut desired is chosen to be around 0.1 mm so that an accurate approximation of a contour can be produced. A sequence of parametric experiments were conducted to determine the appropriate settings of laser power, duty cycle of pulses, step sizes(feed) in X, Y and Z directions, amount of defocussing(focal plane position with respect to machining surface), translation velocity and orientation of the laser beam's polarization vector. The grooves and surfaces machined were studied under a microscope to determine when the desired settings had been found.

Several sets of experiments were conducted to determine the appropriate settings of laser power, duty cycle of pulses, and translation velocity for satisfactory overlapping of holes in forming grooves. Ranges of values of variables in various combinations were tried. Laser cavity power between 400 to 1100 W was investigated and a power of around 800 W was chosen for the experiments. The maximum translation speed was limited by

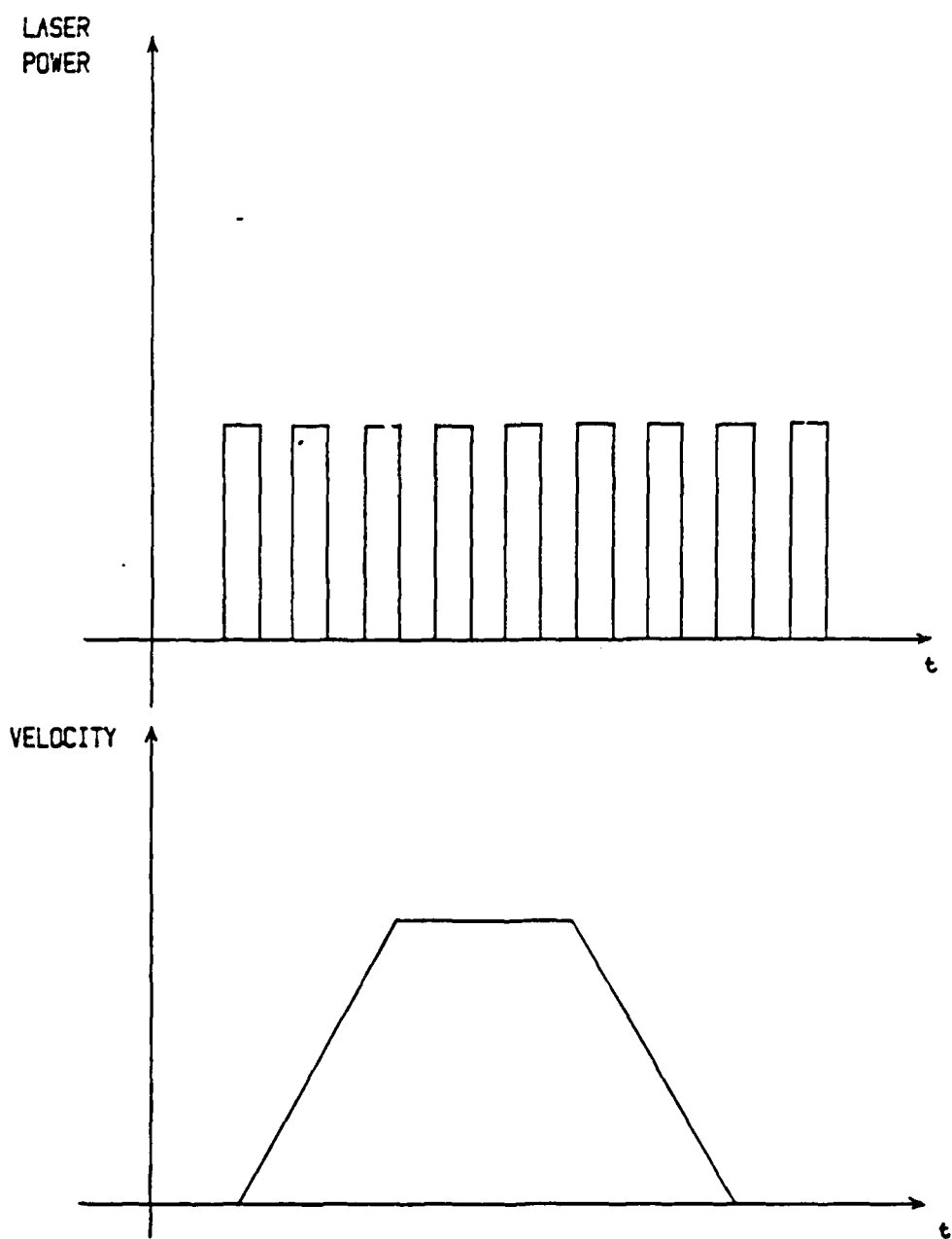


Fig. 3.1.2 TIMING RELATIONSHIP BETWEEN CONTINUOUSLY PULSED LASER AND MOTION OF WORKPIECE UNDER CONSTANT VELOCITY

the design of the X, Y tables to less than 5 cm/s, and it was found that the tables could be translated at a speed of 4 cm/s, reproducibly, and that speed was chosen for constant velocity translation experiments.

After values for laser power and translation velocity had been chosen, studies were conducted to determine the appropriate duty cycle settings of the laser pulses for workpiece moved at constant velocity at 72 degrees to the polarization vector. The grooves in this study were cut at focus and the focal plane of the lens on the workpiece was established according to the procedures described in Sect. 2.9. Ranges of on-time and off-time for the duty cycle of the pulses were tried. Effects of varying the on-time cycle was studied first. The on-time cycle was varied from 0.1 ms to 5 ms while the off-time cycle was fixed at 1 ms. It was discovered that the laser does not fire consistently at on-time cycles of less than 0.3 ms. At 0.5 ms on-time cycle, the grooves machined appeared to have sufficient overlap and depth (approximately 0.1 mm). At higher on-time cycle, the depth of the grooves became much deeper than 0.1 mm, which was not desirable for this machining process.

In the next set of experiments, the on-time cycle of the laser pulse was fixed at 0.5 ms and the off-time cycle was varied from 0.5 ms to 5 ms. It was discovered that at 1 ms off-time cycle, sufficient overlap of holes was obtained. At longer off-time cycles, insufficient overlapping of holes become apparent. Based on the results of these experiments, duty cycle settings of 0.5 ms on and 1 ms off were chosen for further experiments in this investigation.

It was also necessary to determine the appropriate pulse on-time and holes spacing when machining with the pulse-move protocol. The on-time of the laser pulse was fixed at 1 ms for this study. The distances between successive holes were varied from .05 mm to 0.3 mm. It was discovered that 0.1 mm between successive holes provide adequate overlapping in forming a groove under these operating conditions. Insufficient overlapping of holes become obvious when the distances between holes were set greater than 0.15 mm. A longer on-time pulse was needed in these experiments to produce similar overlap as in the repetitively pulsed experiments. The holes spacing were further apart than those in the repetitively pulsed experiments. The effective holes spacing in the continuously pulsed experiments were 0.04 mm.

After appropriate values of the essential variables to make grooves had been chosen, the effects of focal plane position and laser beam's polarization orientation with respect to machining surface were studied. A set of experiments with a repetitively pulsed beam at normal incidence were conducted. Different translation directions with respect to the polarized laser beam's electric vector were used in the experiments. Figure 3.1.3 is a series of pictures showing the profile of grooves machined with various amounts of defocussing and different translation direction orientations with respect to the electric vector of the beam.

It can be seen in Fig. 3.1.3 that within 1 mm of the focal plane(defocus=0 mm), the cross-sections of the grooves have very

TRAIL @ BRIGHT MOST DEFOCUS - 2 MM
 DIFFERENCE IN Z BETWEEN TRAILS = 0.25 MM
 LASER POWER = 700 W (5700)
 TRANSLATION SPEED = 4 CM/SEC (F880)
 DUTY CYCLE = 0.5 MS ON 1.0 MS OFF

1 MM

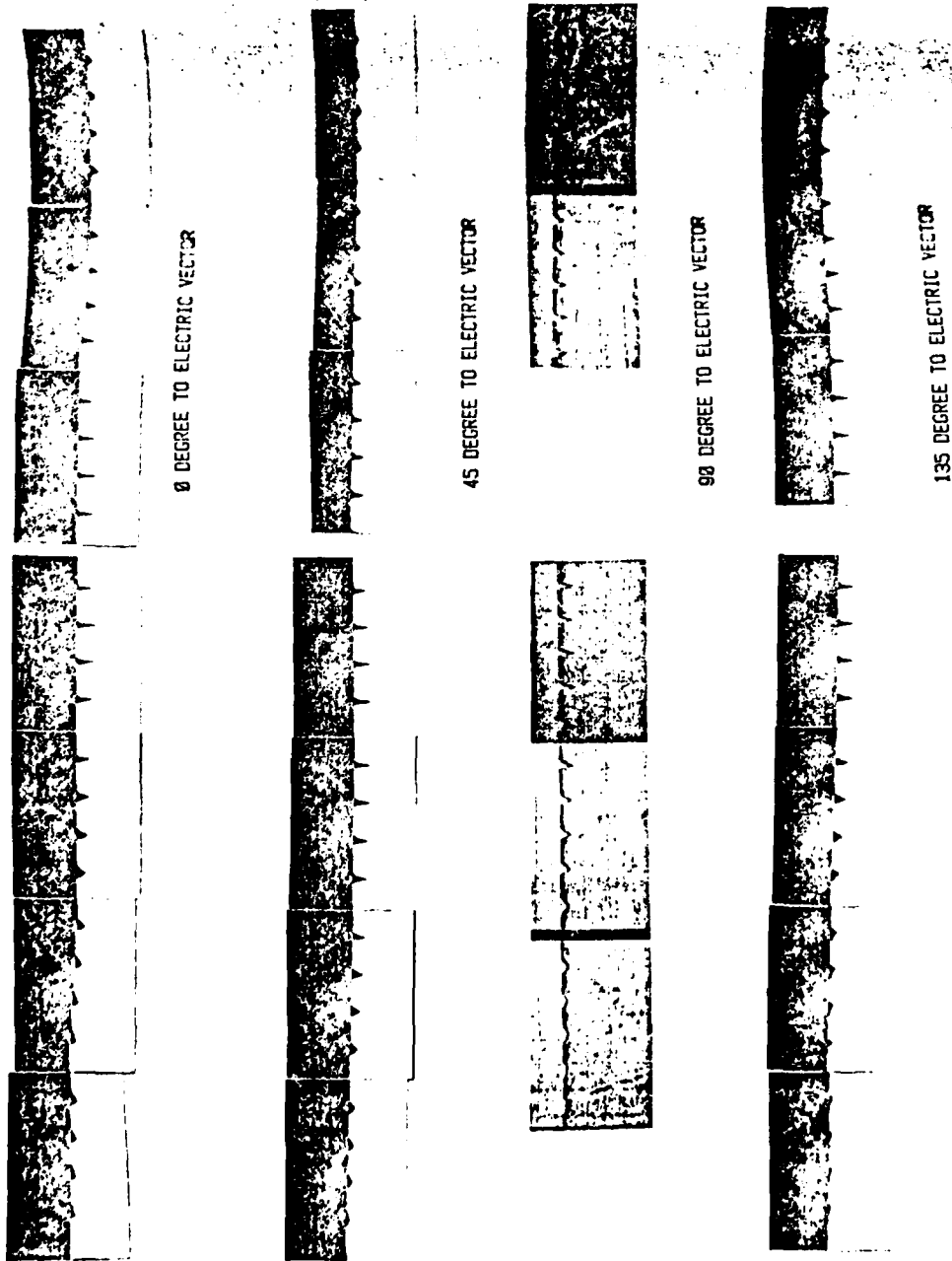


Fig. 3.1.3 GROOVES MACHINED WITH A NORMAL INCIDENCE BEAM AT VARIOUS FOCUS AND POLARIZATION ORIENTATION

little difference in appearance. In that region of the focussing range, the grooves have very sharp bottoms and depths in excess of 0.1 mm. Further away from the focal plane, the grooves have become broader in width, shallower in depth, and the bottom of the grooves are not as sharp. Such grooves are more desirable for this machining process than those with sharp bottoms. An unusual shape was observed for grooves cut at orientation of 135 degrees to the electric vector with defocussing greater than 2 mm. Similar profiles were seen in the beam scan experiment's results. The profile is presumably a characteristic spatial distribution of the laser beam at that particular orientation and level of defocussing.

Furthermore, it can be seen in Fig. 3.1.3 that there were significant differences in depth of cut among grooves machined with the beam defocussed between -1.5 mm and -2 mm. The grooves closer to the focal plane were relatively deeper. This observation suggests that focussing the laser beam above the surface might have a smoothing effect on the surface finish. In this case, the peaks of the surface would be closer to the focal plane than the valleys, and thus more material will be removed from the peaks than the valleys producing the smoothing effect.

A set of experiments to determine the overlapping distances between grooves to form layers were conducted. Continuously pulsed and pulse-move operations of the laser were used in this investigation. A range of overlapping distances between .05 mm to 0.3 mm were tried. The workpieces were machined at focus and above focus. In both mode of laser operations, it was found that a good surface finish was attainable with a

defocussed beam of ~ 2 mm with 0.1 mm overlap between grooves. The surface finish was fairly rough when the beam was at focus with the same overlapping distances. Insufficient overlap between grooves became apparent when the overlapping distances were greater than 0.15 mm.

All of the variables mentioned above affect the amount of material removed to some extent; however, laser beam power, pulse on-time, amount of defocussing, and the dwell time were found to be the dominant factors in vaporizing material. The choice of shielding gas such as nitrogen, carbon dioxide, oxygen and helium did not seem to have a significant effect on the amount of material removed. However, workpieces machined with oxygen as a shielding gas have the least carbon deposited on the finished surface.

3.2 Shaping Experiments

With knowledge gained from previous experiments about machining grooves and layers, this investigation proceeded to machine a common shape in making machine parts. A step as shown in Fig. 3.2.1 was attempted. The shape was machined by removing material layer by layer with a normally incident, focussed beam. The control variables settings used were those determined in Sect. 3.1. The laser was continuously pulsed at 780 W, with duty cycles of 0.5 ms ON and 1.0 ms Off. The workpiece was translated at 40 mm/s in an orientation of 72 degrees to the electric vector of the laser beam. It was discovered that the shape produced by this machining process was distorted from the designed shape. The distortions of the shape is shown in Fig. 3.2.2. Apparently, difficulties were encountered when the slope of the machined surface became steep. Materials were not removed as anticipated. The problem appeared to be a reduction of laser beam absorption on the steep sloped surface resulting in a decrease of material being removed on the surface. The effect propagates as more layers were removed and a sloped side wall was formed.

The material vaporization process requires the power density of the focussed beam to exceed a certain threshold. The amount of material removed depends on the amount of energy absorbed by the irradiated spot, which can be influenced strongly by the angle between the incident rays and the eroding surface. The reflectance of the beam increases with an increasing incident angle as stated in Fresnel's Law of Reflection.¹³ In

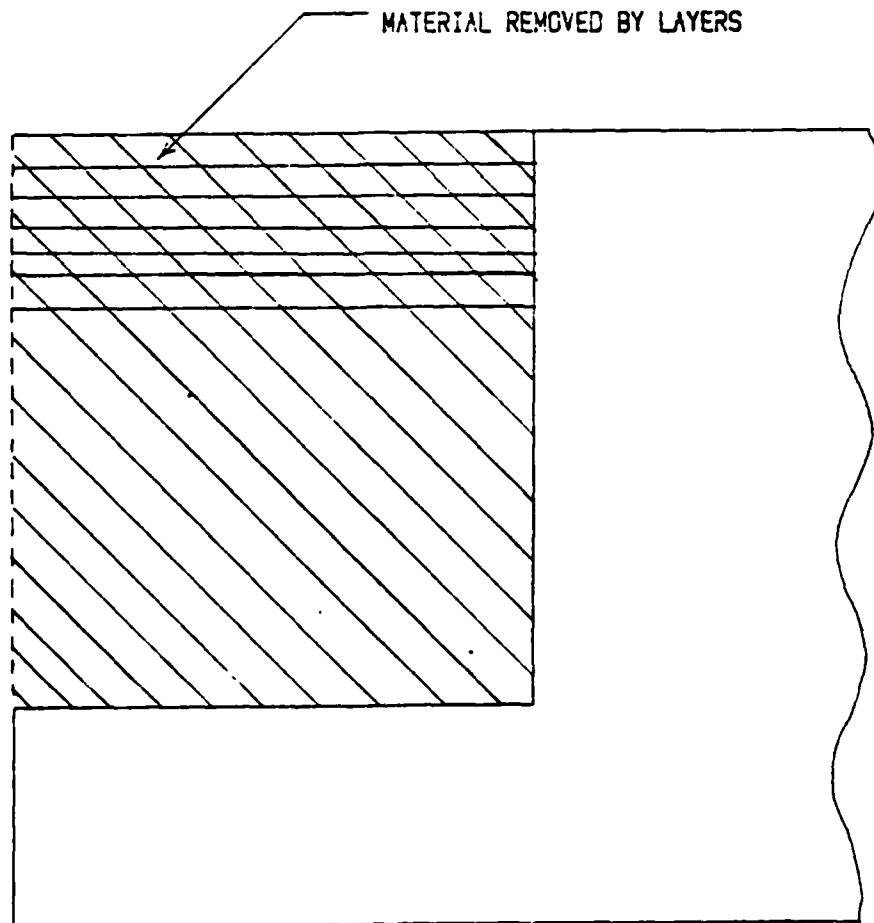


Fig. 3.2.1 LAYER REMOVAL TECHNIQUE TO FORM STEP

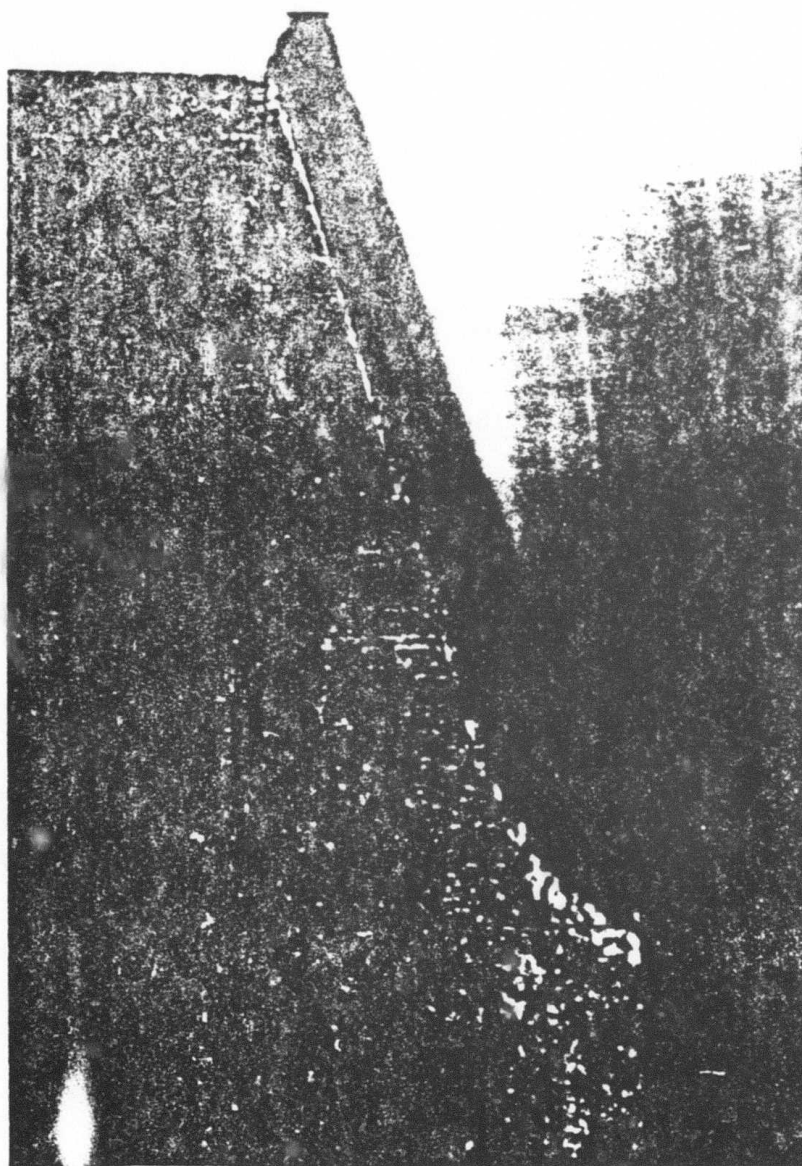


Fig. 3.2.2 DISTORTION IN STEP

Fig. 3.2.3, the cross-section of a trail as it was formed by a normally incident beam is illustrated. As the material was vaporized, the angle between the incident rays and the eroding right surface wall increases. After a small time of irradiation, the right surface will be making a very steep angle with the incident rays. Consequently, most of the beam energy was reflected and the relative material removal rate was drastically reduced at that surface. As more layers were removed, this slight slant at the end of each layer will reflect the beam and eventually formed the sloped side wall. Regardless of the shape being machined, this slight slant on the surface would be formed when the beam is vaporizing the end of a layer. The effect would be more pronounced when a blind corner is machined. Both side walls, forming the corner, would be sloped. Furthermore, due to the relationship of reflectance, the orientation of the incident plane and the electric vector as stated in Fresnel's Law, the orientation of the wall with respect to TE reflection of the beam should also affect the slope of the side wall. It may be possible to correct the sloped wall distortion by orienting the side wall appropriately with respect to the electric vector. The appropriate orientation of the side wall with respect to the electric vector so that TM reflections would be on the side wall. The increase in absorption may perhaps remove the sloped wall distortion as seen in early experiments.

Two crucial experiments were conducted to verify the reflection hypothesis. Experiments were performed to study the effects of polarization orientation on the slope of the side wall. Steps of a few

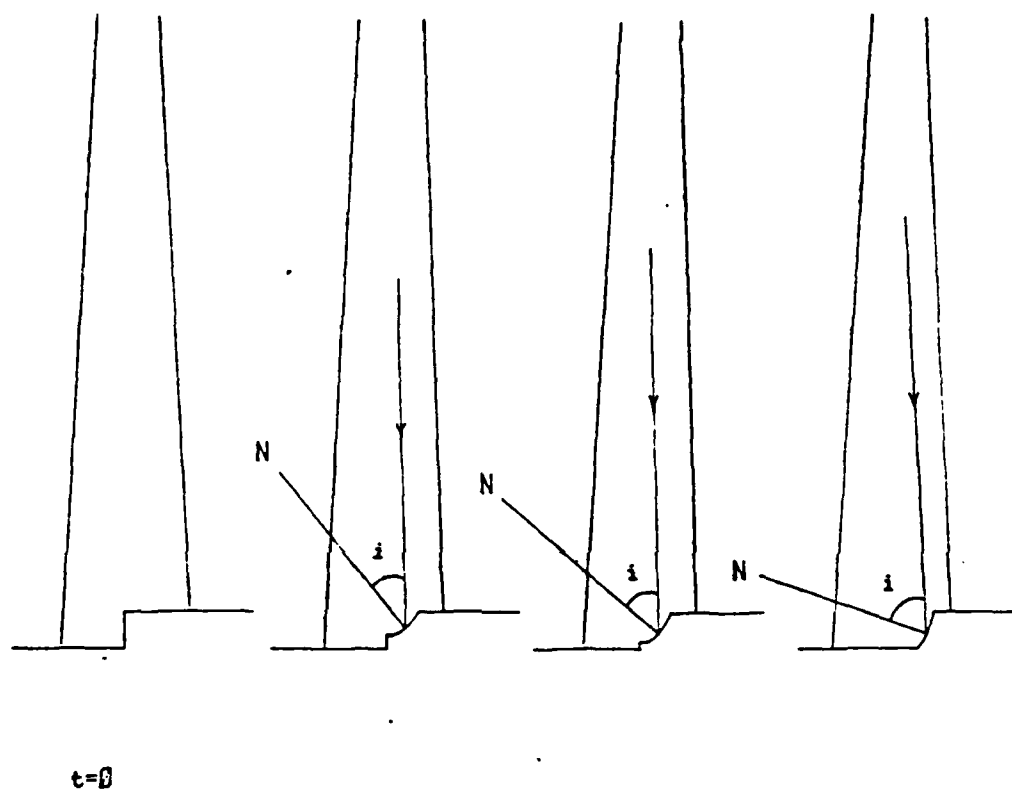


Fig. 3.2.3 SLOPED SIDE-WALL FORMATION

millimeters deep were cut with a continuously pulsed focussed beam at normal incidence with velocity vector parallel (0 degrees to TE) and perpendicular (90 degrees to TE) to the electric vector TE. The results were shown in Fig. 3.2.4 and Fig. 3.2.5. The slope on the side wall was more severe in the translation orientation of 0 degrees than that of 90 degrees. The findings were in good agreement with Fresnel's Law of Reflection. At the orientation of 0 degree, the side wall received TE reflections which were less absorptive than the TM reflections. Consequently, less material was removed and the side wall was formed with a greater slope. On the contrary, at orientation of 90 degrees, the side walls received more absorptive TM reflections, more material was removed and the side wall formed was not sloped as much. As can be seen in the data, reorientation of the velocity vector with respect to TE was not sufficient to correct the distortion in the side wall, extra measures have to be taken to further increase the absorption on that surface to remove the distortion completely.

This hypothesis suggested that increasing the absorption on the steep surface could probably correct the distortion. Reorientating the workpiece with respect to the optical axis of the laser beam could further reduce the angle of incident which in turn will increase the absorption on the steep surface. A schematic of the suggested solution is illustrated in Fig. 3.2.6. The workpiece was tilted at an angle θ with respect to the horizontal. As material was being vaporized away, the effective incident angle of the rays with respect to the right surface was reduced by angle

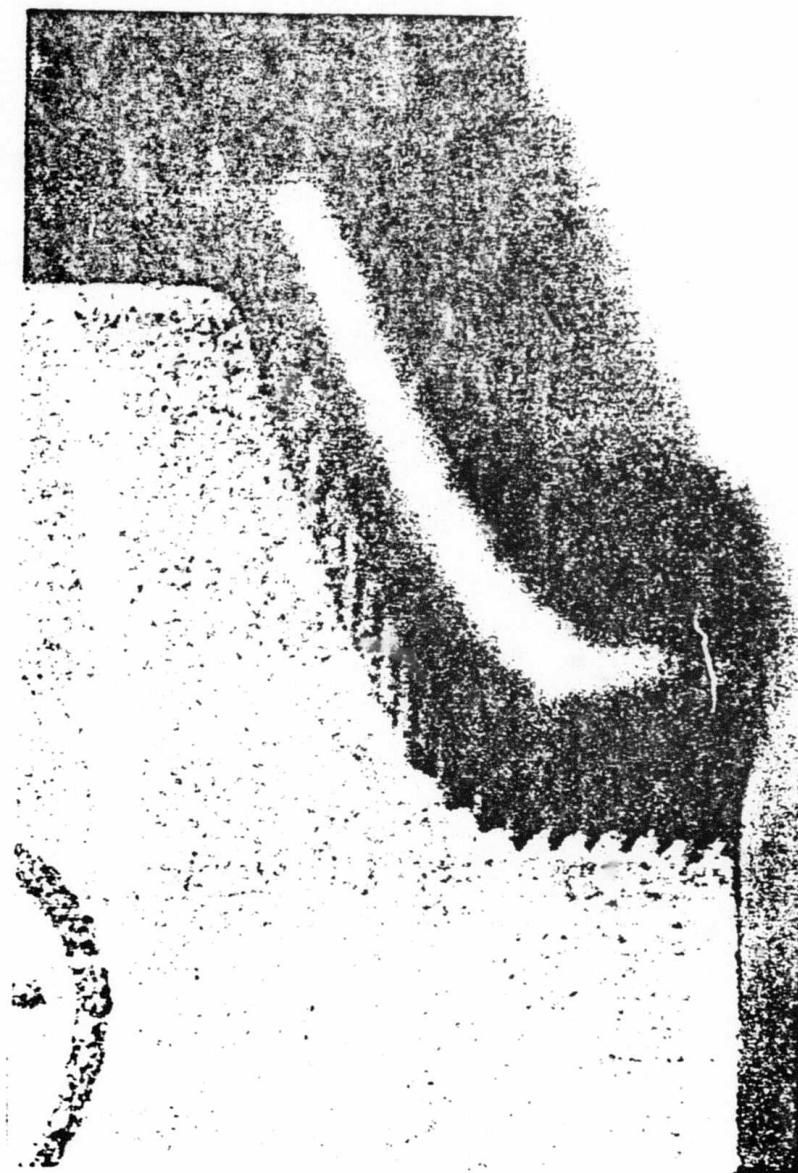


Fig. 3.2.4 STEP MACHINED WITH VELOCITY VECTOR PARALLEL TO
ELECTRIC VECTOR

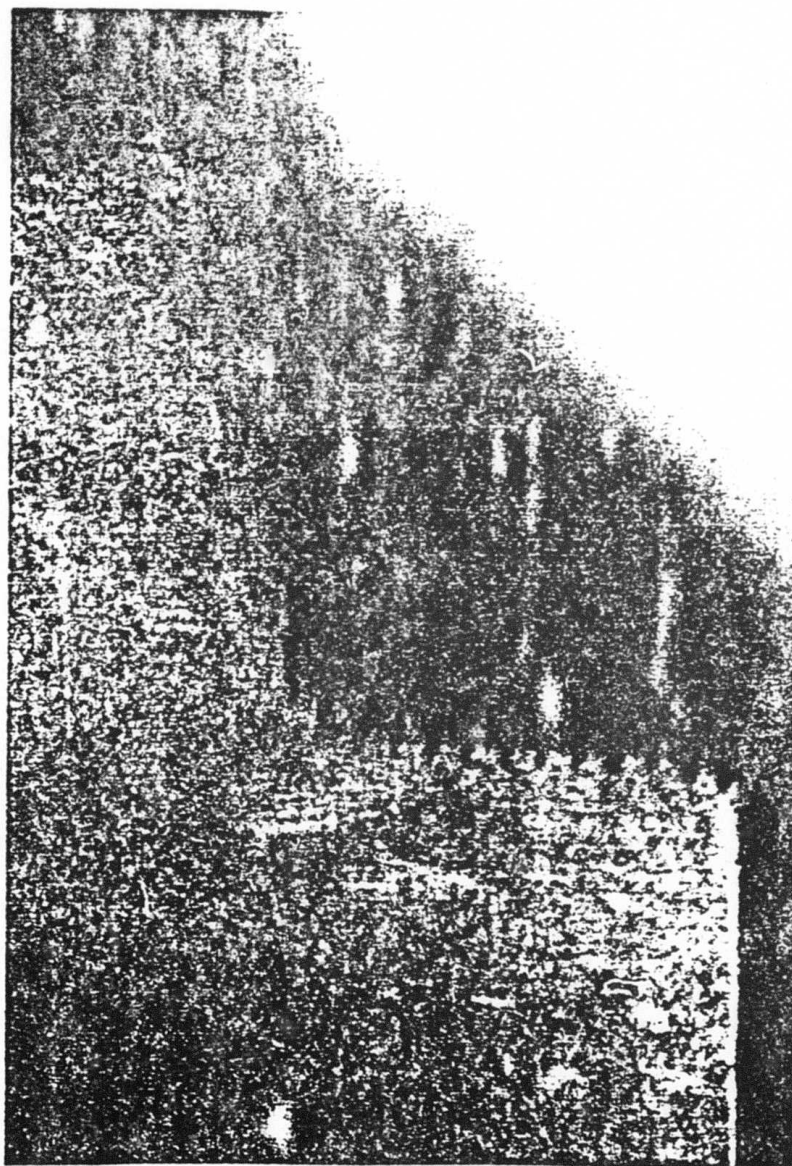


Fig. 3.2.5 STEP MACHINED WITH VELOCITY VECTOR PERPENDICULAR
TO ELECTRIC VECTOR

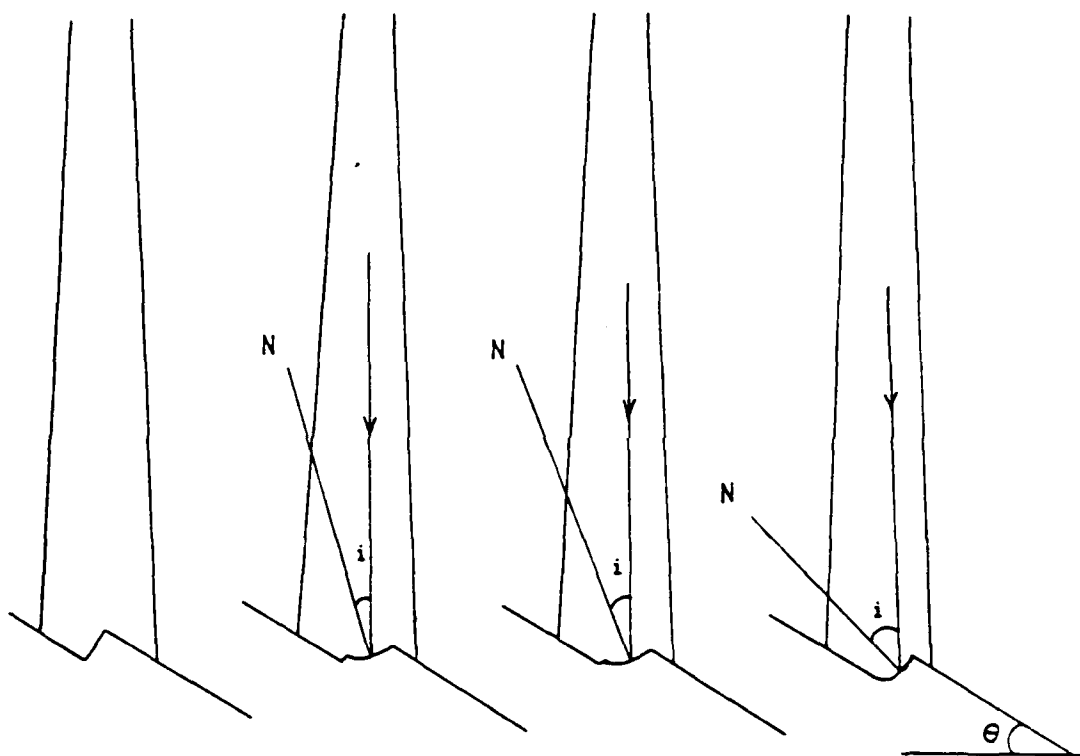


Fig. 3.2.6 INCREASE ABSORPTION ON SIDE-WALL BY TILTING WORKPIECE

theta because of the tilted workpiece. The reduced incident ray angle increases the absorption to that surface and hence relatively more material will be vaporized from the surface. Therefore, it is possible to cut a relatively vertical side-wall with a reoriented workpiece. As more layers are removed, the vertical side-wall can be preserved.

3.3 Effects of tilting workpiece

It has been postulated by the author that a vertical side-wall parallel to the xz plane of the reference frame can be machined if the workpiece was oriented appropriately to the optical axis of the beam (in the direction of vertical Z axis in base frame). A vertical side-wall parallel to the xz plane can be machined by tilting the workpiece about the x axis (translation direction) as shown in Fig. 3.3.1. Similarly, a vertical side wall parallel to the yz plane can be machined by tilting the workpiece about the y axis (translation direction) as shown in Fig. 3.3.2. The change in orientation between the beam and workpiece can be accomplished either by tipping the laser beam or tilting the workpiece. Beam tilting would have required extensive modification of the current beam delivery system whereas workpiece manipulation was less complicated and more adaptable to the CNC positioning system. The latter approach was chosen for this study.

A set of experiments was conducted to gain insight concerning the effects on a workpiece machined by a non-normal incident beam. The depth and shape of grooves formed on workpieces translating at different direction with respect to the polarization vector of the beam were studied. The experiments involve machining grooves at different tilt angles with translation direction (direction of X axis in base frame) at 0, 45, 90, 135 degrees with respect to the polarization vector of the laser beam. The workpiece was tilted about the X axis in a clockwise direction as shown in Fig. 3.3.1.

The laser was operated in continuous wave instead of pulsed mode

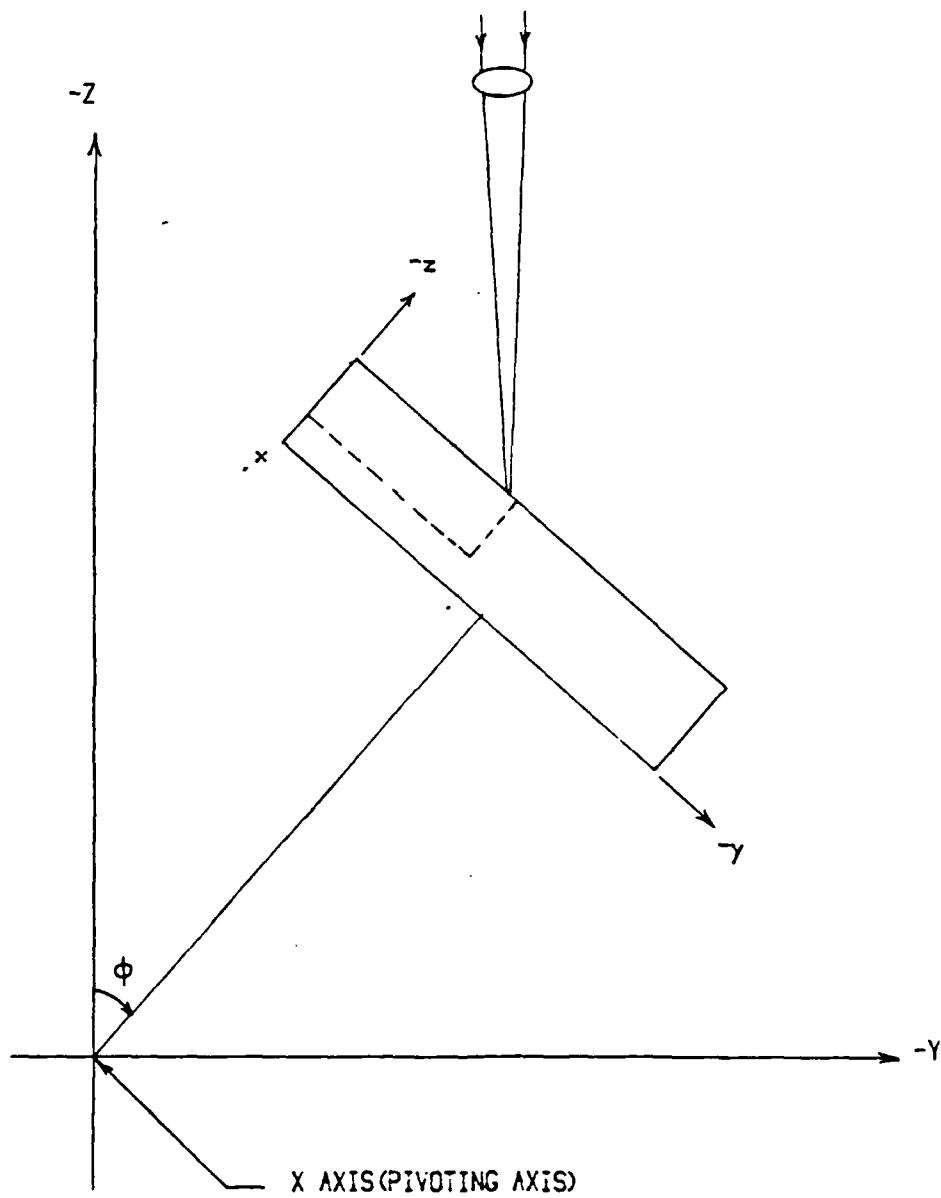


Fig. 3.3.1 TILT ANGLE ABOUT X AXIS

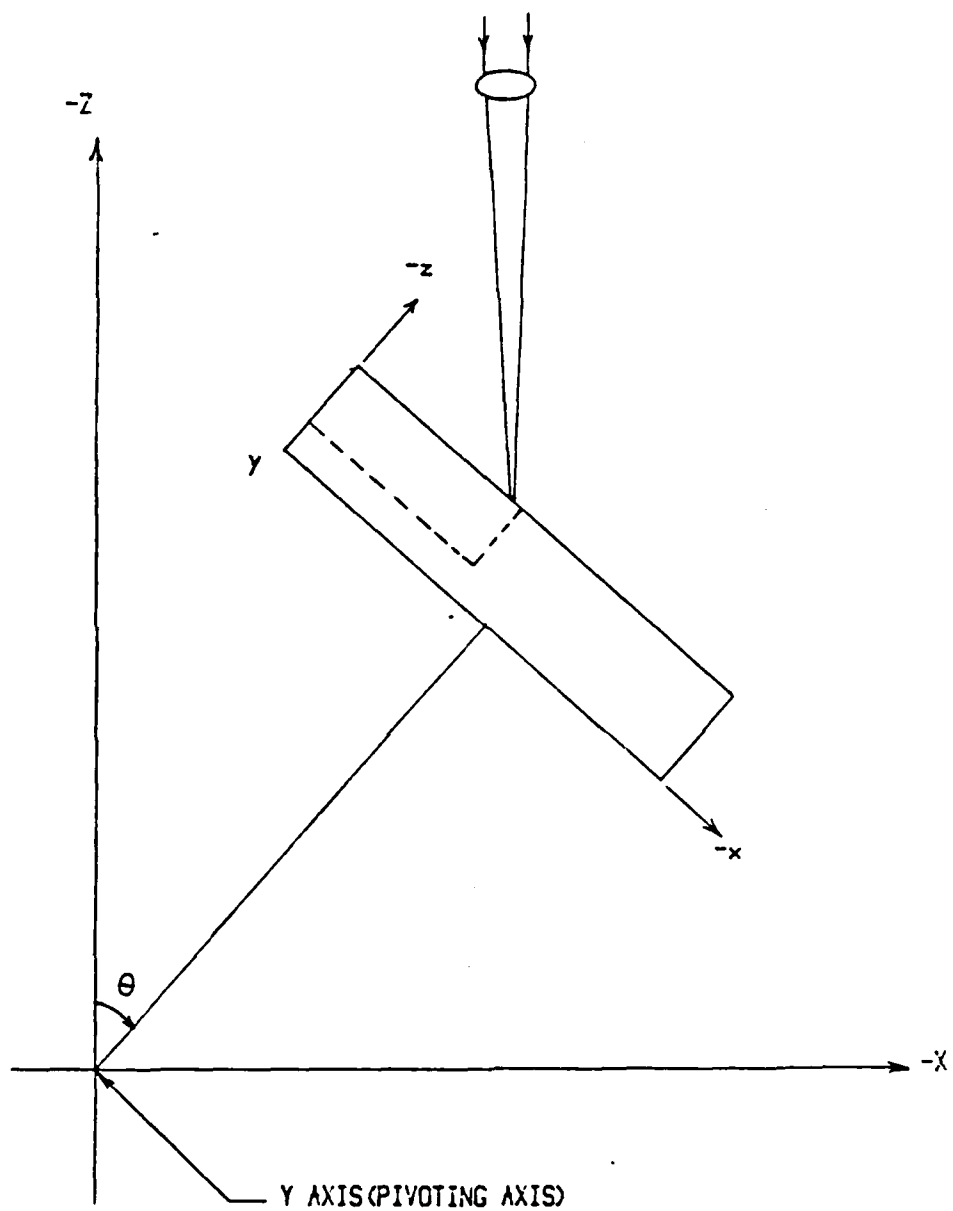


Fig. 3.3.2 TILT ANGLE ABOUT Y AXIS

to avoid the cross sections non-uniformity of grooves formed by overlapping holes. The power of the laser was set at 325 W to cut grooves of depth in the range of 0.1 to 0.2 mm.

Special handling of the laser power controls was necessary to stabilize the low power operating conditions. With the safety shutter closed, the laser was turned on at 700 W for 3 seconds to insure all the plasma tubes were firing, then the power was lowered to 325 W and held there for 3 seconds for stabilization at that power. The safety shutter was then open and a groove was cut in the workpiece that was translated under the beam at 5 cm/s. This process was repeated for every groove machined in the tilted/polarization orientation experiments.

The workpiece was mounted on the platform of the rotation table assembly and was rotated to the desired angle as needed. In the experiment, the tilt angle about X axis was set at 0 degrees initially and was incremented 2 degrees after a groove was cut. The proper position of focus was tracked by the CNC system as the tilt angle was changed. Figure 2.3.3 shows the conventions used in measuring the angles between the translation vector and the polarization vector for the experiments. In Fig. 3.3.3, the profiles of the grooves machined are shown in a series of photographs.

It can be seen in the series of photographs in Fig. 3.3.3 that there were significant differences between grooves machined at different orientations. Grooves machined at tilt angles of less than 10 degrees appeared symmetrical at different orientations. As the tilt angle is



0 DEGREE TO ELECTRIC VECTOR



45 DEGREE TO ELECTRIC VECTOR



90 DEGREE TO ELECTRIC VECTOR



135 DEGREE TO ELECTRIC VECTOR

Fig. 3.3.3 GROOVES MACHINED AT VARIOUS TILT ANGLES AND POLARIZATION ORIENTATION. POWER = 325 W CW, TILT INCREMENT PER TRAIL = 2 DEGREE
TRAIL Ø (RIGHT MOST) TILT = 0 DEGREE

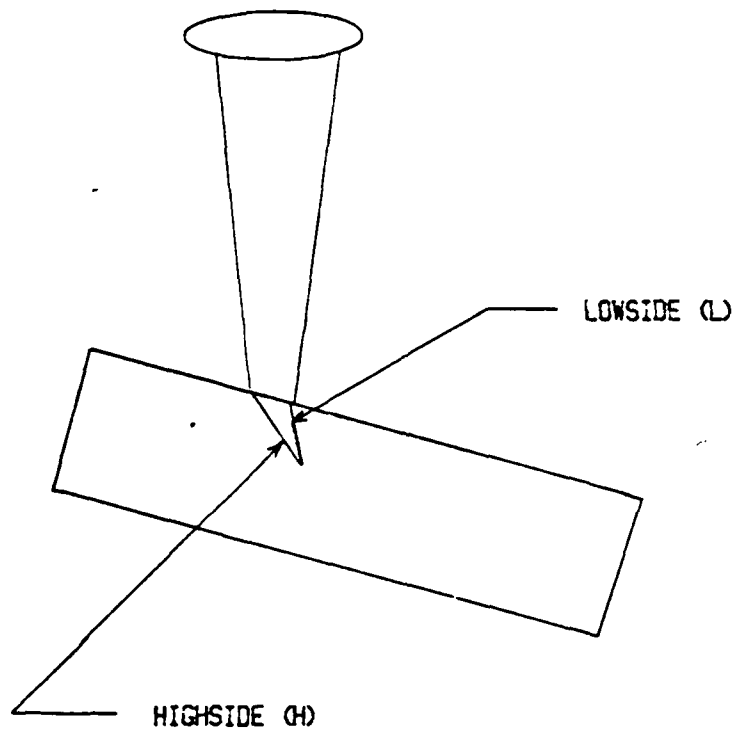
increased, grooves began cutting into the material in the direction of the incident beam. Furthermore, at tilt angles above 30 degrees, grooves translated at different direction with respect to the polarization vector of the beam have dramatically different profiles. At 0 degrees to the polarization vector, the grooves formed were sharp and curved into the material. At 45 and 90 degrees, the grooves were broader and flatter at the bottom. At 135 degrees, the grooves were narrow in width and sharply pointed at the bottom.

The formation of the shapes of grooves at different polarization orientation can be understood by applying Fresnel's Law of reflection of polarized light.¹³ Differences in reflectance between the TE and TM reflections of the polarized beam on the respective surfaces contribute to the variations in the shapes of the grooves formed. Wallace has discussed the formation of curve grooves cut by a normally incident beam.^{6,15} The extreme cases of reflections at tilt angles of greater than 40 degrees were examined in this study for the different polarization orientations.

The two reflection vectors are designated TM(transverse magnetic) and TE (transverse electric) reflections. The TM reflection is produced when the incident's beam E vector is in the plane of incidence while the TE reflection is produced when the E vector is perpendicular to the plane of incidence. The reflectance of TE and TM are the same at incident angles of 0 and 90 degree. For incident angles in between 0 and 90, TE has a higher reflectance than TM. In relative terms, TM would be more strongly absorbed on a surface than TE.

Figure 3.3.4 shows the effects of tilting on the side-walls of a groove. The effective incident angle is increased on the highside(H) and reduced on the lowside(L). The "H" and "L" notations are used in Fig. 3.3.5 and Fig. 3.3.6 to identify the tilt orientation for the grooves.

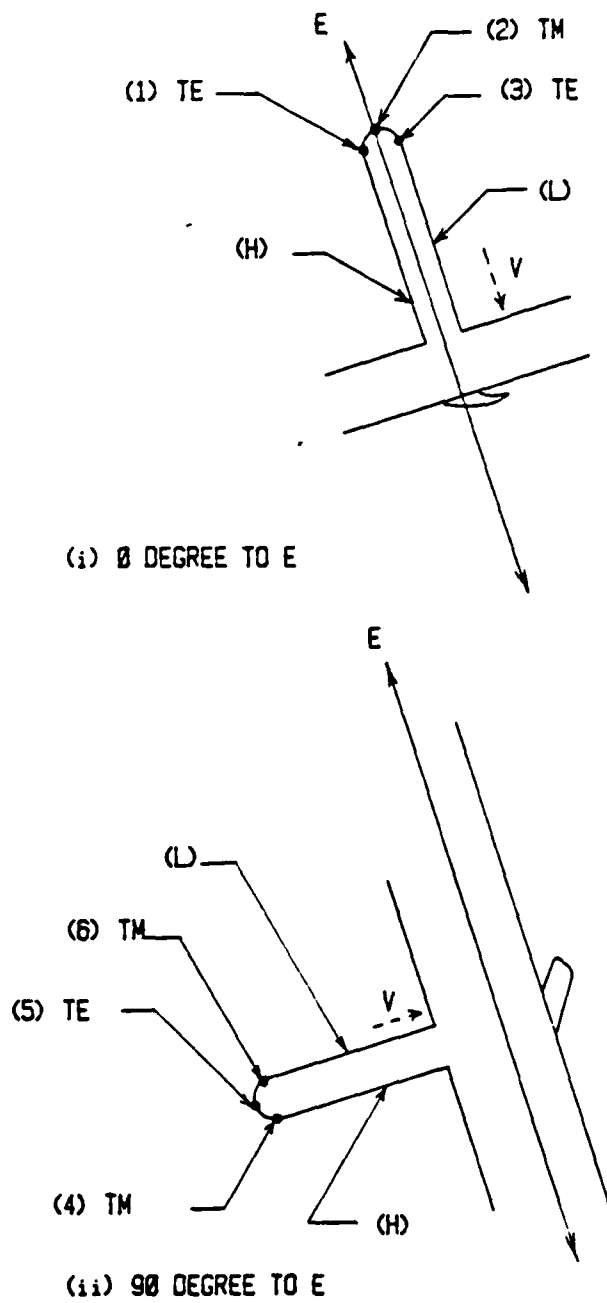
In Fig. 3.3.5 and Fig. 3.3.6, the top and side views of grooves formed in the four different polarization orientations are shown. The reflections at locations of interest are labelled from 1 to 14 in the figures. A plane of incidence is assumed at each labelled location. The tilt orientation can be determined from the "H" and "L" labels. In Fig. 3.3.5, for the case when the velocity vector is parallel to the E vector, the reflected rays at locations 1, 3 are TE reflections and 2 is a TM reflection. Due to the direction of the tilted angle and reflections from rays 1,2 and 3, the grooves formed are expected to be narrow and steep. For the case when the velocity is at 90 degrees to the E vector, the reflected rays at locations 4 and 6 were TM reflections and they were more strongly absorbed and a boarder groove with a smoother bottom was expected. In Fig. 3.3.6, for the case where the velocity vector is at 45 degree to the E vector, location 8 is a TE reflection whereas location 7 is a TM reflection. The surface at location 7 would be cut deeper relative to location 8 forming a broader and smoother bottom groove. If the velocity vector is reversed in direction, the TE and TM reflections would be switched on the side-wall as indicated by labels 9 and 10. For the case when the velocity vector is at 135 degree to E, location 11 is a TE reflection and location 12 is a TM reflection. The groove formed is expected to be sharp and narrow because most of the



HIGHSIDE (H)) INCREASED ANGLE OF INCIDENCE

LOWSIDE (L)) REDUCED ANGLE OF INCIDENCE

Fig 3.3.4 EFFECTS OF TILTING ON INCIDENCE ANGLES AT
SIDE-WALLS OF GROOVES



--> TRANSLATION DIRECTION OF WORKPIECE

Fig. 3.3.5 SHAPES OF GROOVE DEVELOPMENT AT 0 & 90 DEGREES TO E VECTOR

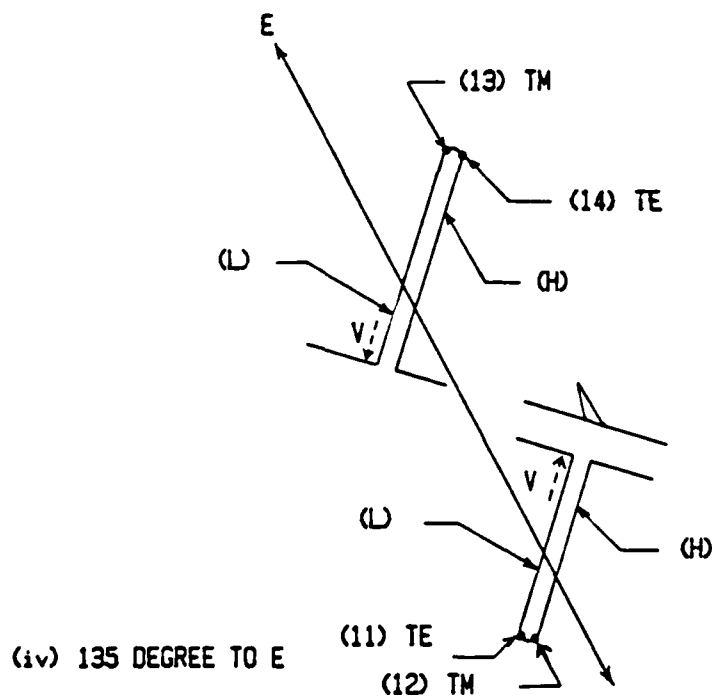
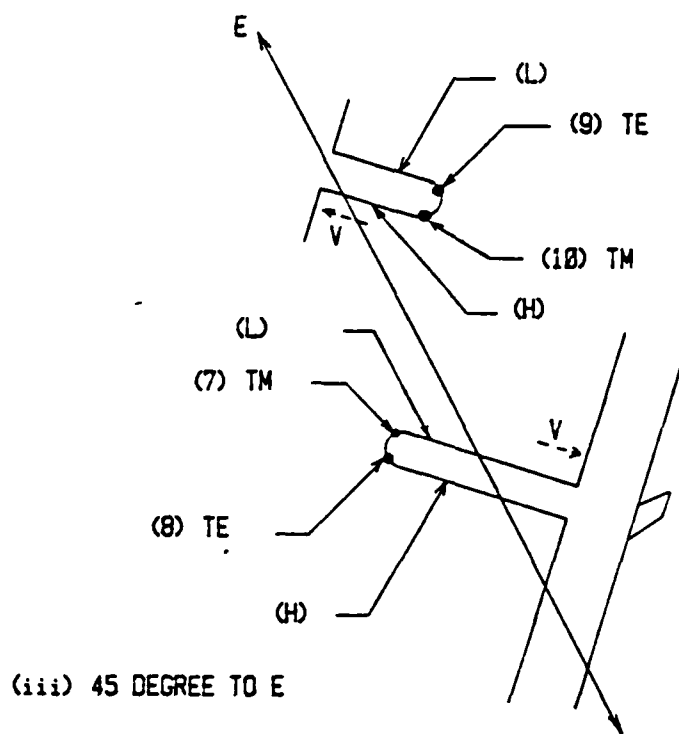


Fig. 3.3.6 SHAPES OF GROOVE DEVELOPMENT AT 45 & 135 degree to E VECTOR

material removed would be on the side of 12 due to absorption of TM and reflection of TE from 11. If the direction of the velocity vector is reversed in direction, the TM and TE reflections would be switched on the side-walls on the grooves as indicated by labels 13 and 14.

The data from these experiments supported the idea that tilting the workpiece could be used to control shape distortion. Studies were conducted to determine the effects of tilts on machining layers.

3.4 Layer removal on a tilted workpiece

Results of Sect. 3.3 suggest that tilting the workpiece can be employed to control the slope of the vertical side formed at the end of a layer. Maintaining that vertical geometry on each layer is crucial in forming a contour shape by stepwise approximation. The CNC positioning system operates in an orthogonal X-Y-Z coordinate system. If the workpiece's position and orientation are changed by tilting, it is necessary to transform the coordinates of the workpiece from the reference frame to the base frame of the CNC system. The transformation is accomplished by applying the corresponding transformation matrices to the coordinates in the reference frame.¹

The reference frame is a set of coordinates imbedded in the tilting mechanism to simplify the description of the shape to be made. The origin of the base frame was carefully chosen to be at the intersection of the X, Y rotational axes of the rotation table assembly in order to simplify the transformation computations.

A diagram showing the reference and base frames is given in Fig. 2.6.1. The position vector P points at the origin of the reference frame when there is no rotation about either the X or Y axis. The format of an empirical transformation equation is shown in Eq. 3.4.1.

$$X = T * x \quad \dots\dots (3.4.1)$$

where:

X = coordinate in base frame
T = transformation matrices
x = coordination in reference frame

Equation 3.4.2 is the matrix equation to compute the position of the workpiece in the base frame after rotation about the X axis.

$$(X,Y,Z,1) = \text{Rot}(x,\phi) * \text{Tran}(T) * (x,y,z,1)^T \quad \text{..... (3.4.2)}$$

Equation 3.4.3 shows the corresponding components in matrices of Eq.3.4.2.

$$\begin{bmatrix} X \\ Y \\ Z \\ 1 \end{bmatrix} \begin{bmatrix} 1 & 0 & 0 & 0 \\ 0 & \cos\phi & -\sin\phi & 0 \\ 0 & \sin\phi & \cos\phi & 0 \\ 0 & 0 & 0 & 1 \end{bmatrix} \begin{bmatrix} 1 & 0 & 0 & T_x \\ 0 & 1 & 0 & T_y \\ 0 & 0 & 1 & T_z \\ 0 & 0 & 0 & 1 \end{bmatrix} \begin{bmatrix} x \\ y \\ z \\ 1 \end{bmatrix} \quad \text{..... (3.4.3)}$$

The translation vector **T** points to the reference frame's origin after the rotation about the X axis. **T** can be computed by applying the rotational transformation matrices on vector **P** as shown in Eq. 3.4.4.

$$(T_x, T_y, T_z, 1) = \text{Rot}(x,\phi) * (P_x, P_y, P_z, 1)^T \quad \text{..... (3.4.4)}$$

In the case when the workpiece is tilted about the X axis, after focus on the workpiece has been established, motion in the X direction requires

no transformation computation to maintain proper focus at the spot of irradiation. However, any movement in the Y direction will require a corresponding movement, as defined by the transformation computations, in the Z direction so that proper focus on the workpiece is maintained.

In experiments where the workpiece is tilted about the X and the Y axis, an additional rotation about Y transformation matrix is needed in the matrix transformation equation. Equation 3.4.5 is the matrix transformation equation for computing the position of the workpiece after rotations about X and Y axis. The corresponding components of the matrices are shown in Eq. 3.4.6. The translation vector T in this case is computed by applying the rotational transformation matrices on vector P as shown in Eq. 3.4.7.

$$(X, Y, Z, 1) = \text{Rot}(y, \theta) * \text{Rot}(x, \phi) * \text{Tran}(T) * (x, y, z, 1)^T \quad \dots\dots (3.4.5)$$

$$\begin{pmatrix} X \\ Y \\ Z \\ 1 \end{pmatrix} = \begin{pmatrix} \cos\theta & 0 & \sin\theta & 0 \\ 0 & 1 & 0 & 0 \\ -\sin\theta & 0 & \cos\theta & 0 \\ 0 & 0 & 0 & 1 \end{pmatrix} \begin{pmatrix} 1 & 0 & 0 & 0 \\ 0 & \cos\phi & -\sin\phi & 0 \\ 0 & \sin\phi & \cos\phi & 0 \\ 0 & 0 & 0 & 1 \end{pmatrix} \begin{pmatrix} 1 & 0 & 0 & T_x \\ 0 & 1 & 0 & T_y \\ 0 & 0 & 1 & T_z \\ 0 & 0 & 0 & 1 \end{pmatrix} \begin{pmatrix} x \\ y \\ z \\ 1 \end{pmatrix} \quad \dots\dots (3.4.6)$$

$$(T_x, T_y, T_z, 1) = \text{Rot}(y, \theta) * \text{Rot}(x, \phi) * (P_x, P_y, P_z, 1)^T \quad \dots\dots (3.4.7)$$

When the workpiece is tilted about the X and Y axis, any movement in the X or Y direction will require a corresponding Z movement so that proper focus is maintained on the workpiece. The amount of movement in the Z direction is computed by the corresponding matrix equations.

3.5 Studies on machining a tilted workpiece

The basic approach of the laser machining process involves overlapping holes to form grooves and overlapping grooves to form a layer. The amount of overlapping of the holes and grooves strongly influence the smoothness of the resulting surface finish. As discussed in Sect. 3.1 a highly focussed beam cut very steep grooves. Overlapping steep grooves form a rather rough surface. Alternatively, a defocussed beam cuts grooves that are not steep and a smooth surface can be formed.

Surfaces machined on a tilted workpiece with a defocussed beam are most relevant to laser machining because this arrangement was used in experiments where attempts were made to form a defined shape. The layers in these experiments were formed by overlapping grooves machined in the X direction. Various tilted angles from the range of 0 to 40 degrees and defocussing of 0 to -2 mm were used in machining layers of material for the purpose of studying the edge formed at the end of the layer. It was found that tilting the workpiece 30 degrees and defocussing the beam -2 mm produce a relatively vertical edge and a very smooth surface on graphite. This combination was used in most of the shaping experiments for this investigation.

In Sect. 3.3, it was shown for tilt angles greater than 30 degrees, the angle between the translation direction of the beam and the electric vector of the beam could have a remarkable effects on the shapes of grooves formed. A set of experiments was conducted to determine if the

edge at the end of layers formed with a 30 degree tilt was influenced by the polarization of the beam. In the experiments, the workpiece was tilted at 30 degrees and two layers of material were machined from a free edge at each orientation. The workpiece was translated at a constant velocity of 40 mm/s. Translation direction of 0, 22.5, 45, 67.5, 90, 112.5, 135 degrees with respect to the electric vector of the beam were used in the studies. The laser was operated at 780W in continuously pulsed mode. The duty cycle of pulses were set at 0.5 ms on-time and 1 ms off-time. Two set of data were collected. One with the beam at focus on the surface and the other with the laser beam focussed 2 mm above the surface. The results were shown in Fig. 3.5.1 and Fig. 3.5.2 respectively.

With a focussed beam, undercutting was obvious and the surfaces formed were fairly rough. Furthermore, it can be seen in Fig. 3.5.1 that the slope of the side wall changed slightly as the translation direction was changed from 0 to 135 degree with respect to the electric vector. The unfocussed beam removed less material, the surfaces formed were smoother and there was no undercutting at the end of the layer. Effects of beam's polarization were not significant at the edges of layers removed on a tilted workpiece.



0 , 22.5

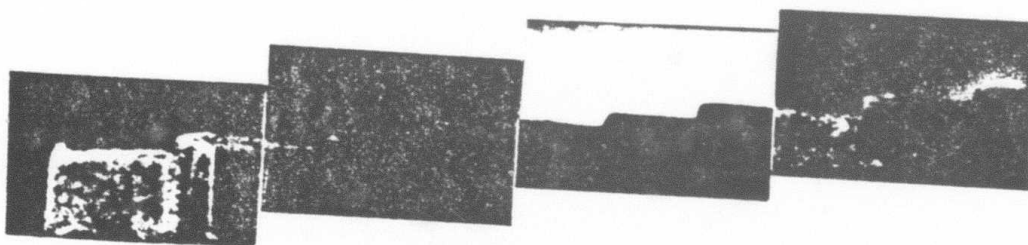
45 , 67.5

90 , 112.5

112.5 , 135

TO ELECTRIC VECTOR

Fig. 3.5.1 LAYERS MACHINED AT VARIOUS POLARIZATION ORIENTATIONS
(AT FOCUS) WITH TILT = 30 DEGREE



135

112.5 , 90

67.5 , 45

22.5 , 0

TO ELECTRIC VECTOR

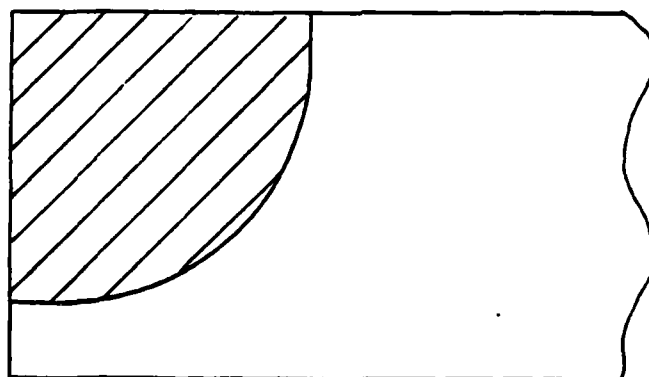
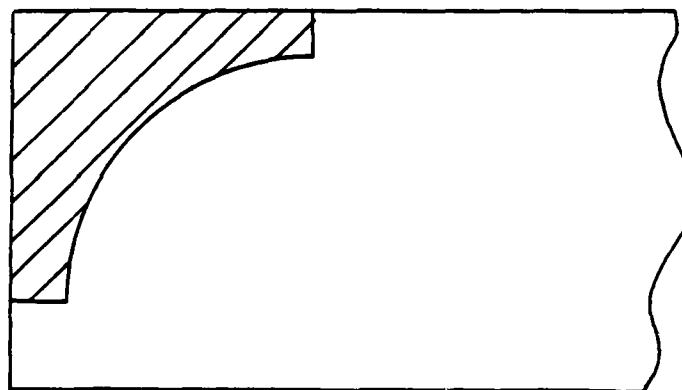
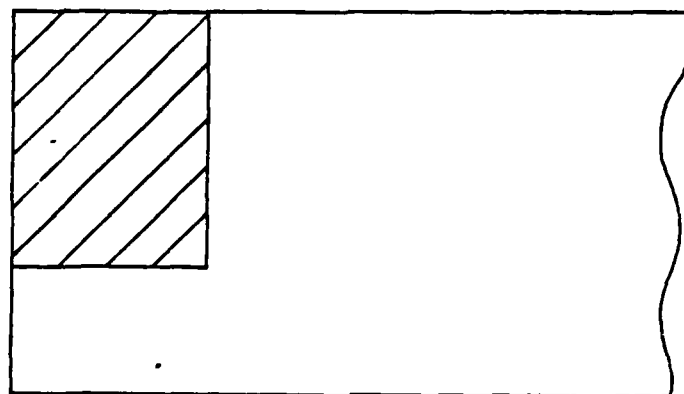
Fig. 3.5.2 LAYERS MACHINED AT VARIOUS POLARIZATION ORIENTATIONS
(DEFOCUS = -2 MM) WITH TILT = 30 DEGREE

3.6 Machining Shapes with tilting about one axis

The following approach was used in machining a step, a convex and concave cylindrical quadrants in graphite. The workpiece was tilted at 30 degrees about the X axis. The translation direction(X direction) of the workpiece was positioned at 45 degrees to the electric vector of the laser beam. The translation velocity was set at 40 mm/s and the laser was operated at an average power of 780W in repetitively pulsed mode with duty cycle of pulses set at 0.5 ms on and 1 ms off. The focus of the beam was placed at 2 mm above the surface to be machined. The feed in Y and Z direction were set at 0.1 mm. Different shapes were obtained by changing the Y limit of the layers removed. Tilting about the X axis was sufficient because of the geometries of the desired shapes to be formed.

The square corner of a rectangular block was machined off to form the specified shapes. Figure 3.6.1 is a diagram of the stock before and after the machining process. The CNC machine's software listings for these experiments can be found in appendix II.

The workpiece was mounted on the platform of the tilt mechanism as shown in Fig. 3.6.2. The right front corner of the block was used to position the workpiece in the proper location in the base frame. The alignment procedures in Sect. 2.7 were followed using the He-Ne laser system with tilt angle of rotation platform set at zero degrees. The focal plane of the lens was established as described in Sect. 2.9. After the alignment procedures, the workpiece was tilted 30 degrees about the X axis. The controlling variables in the software were initialized to their respective



 MATERIAL REMOVED

Fig. 3.6.1 STOCK BEFORE AND AFTER MACHINING

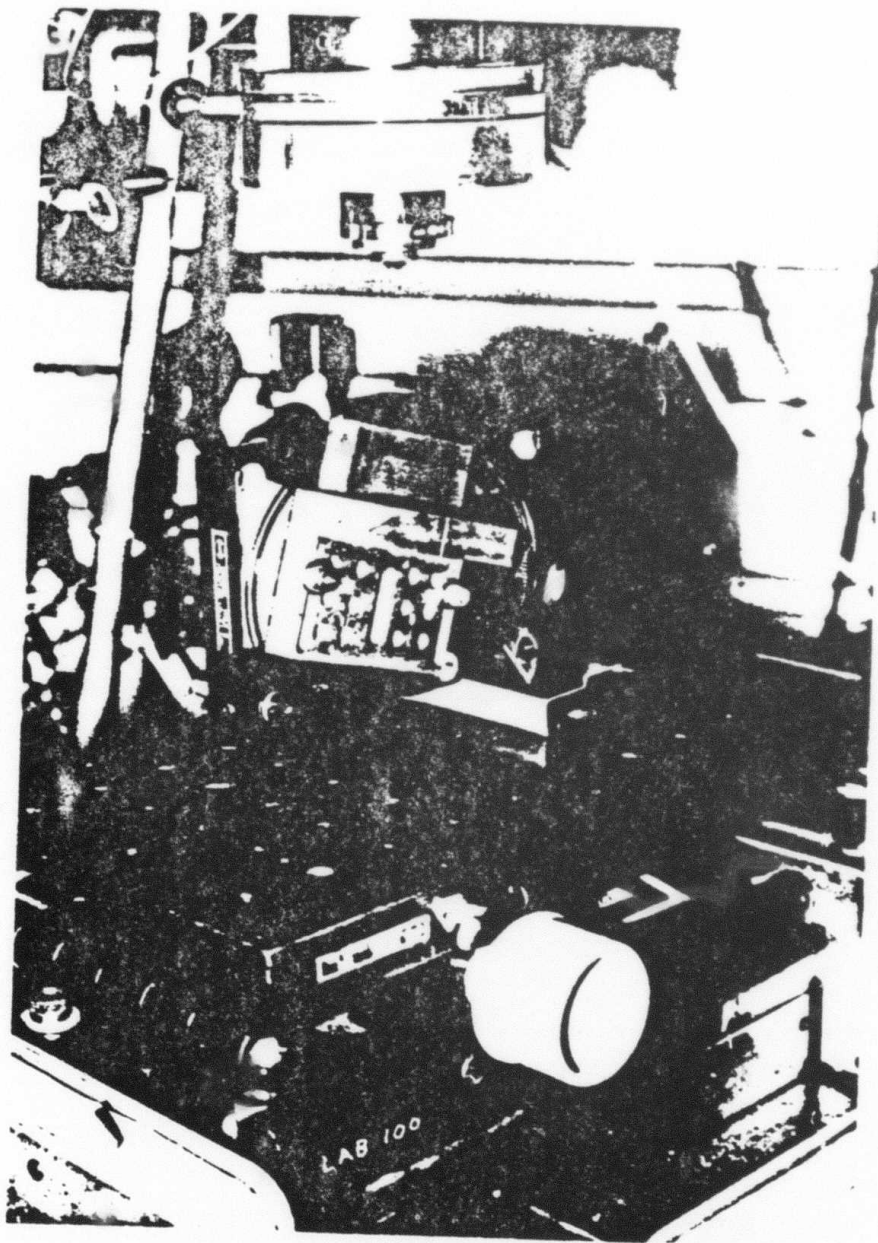


Fig. 3.6.2 WORKPIECE MOUNTED ON TILT PLATFORM

values, the laser was set at the appropriate operating conditions, and the program to form the respective shape was executed.

Figure 3.6.3 is a picture of the step shape machined in graphite by this process. It can be seen that the side wall is relatively smooth and vertical. Figure 3.6.4 and Fig. 3.6.5 are pictures of the convex and concave quadrants machined in graphite. The shapes formed were in good agreement with that designed.

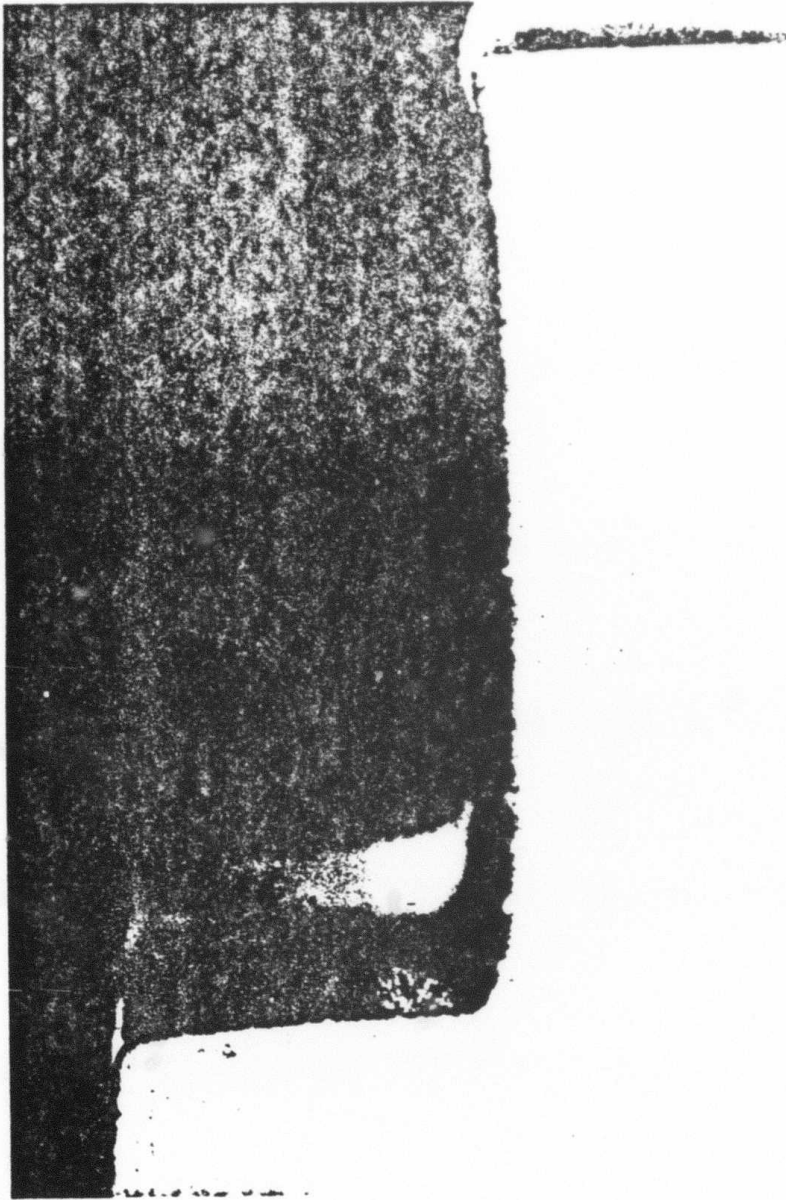


Fig. 3.6.3 STEP MACHINED WITH TILTING AND DEFOCUSING

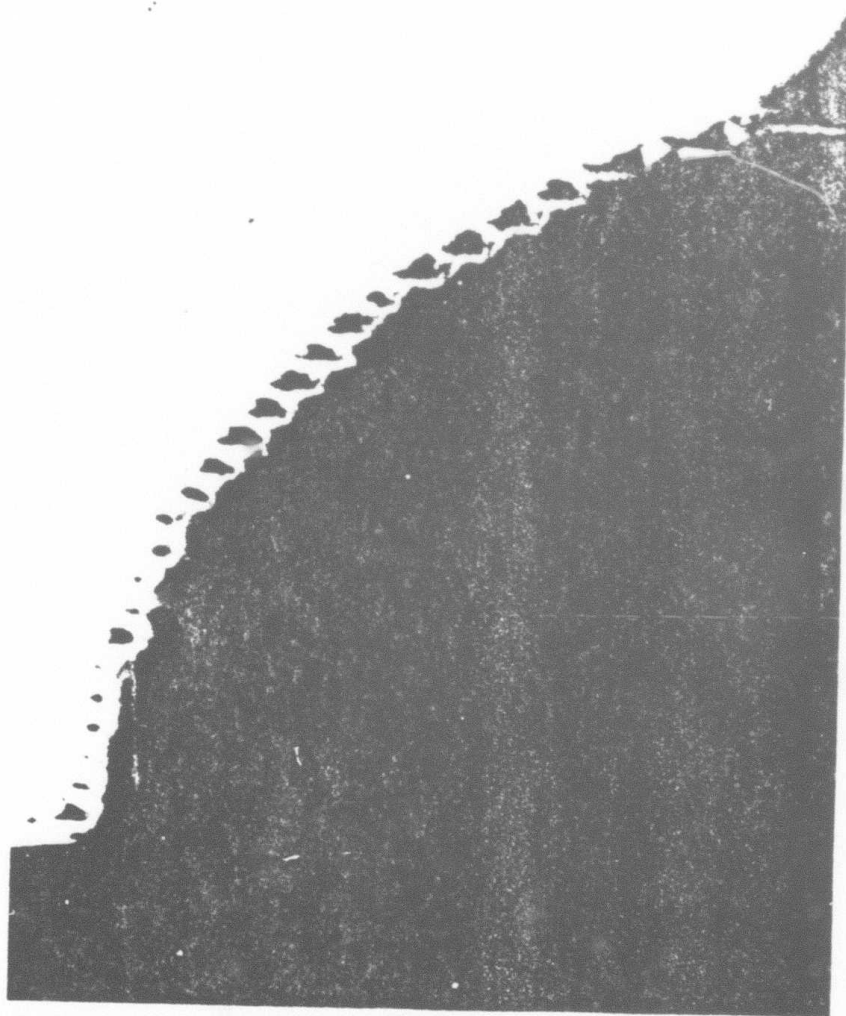


Fig. 3.6.4 CONVEX QUADRANT (GRAPHITE)

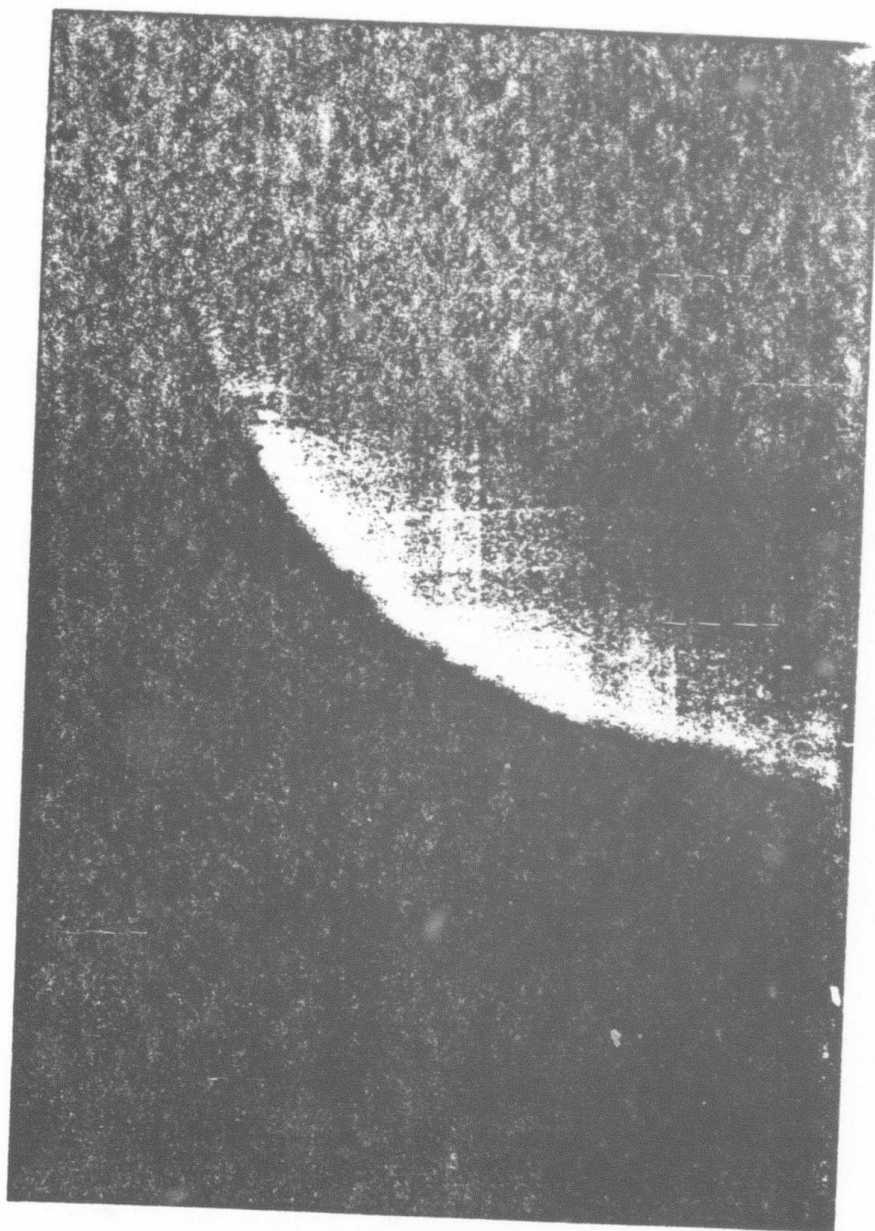


Fig. 3.6.5 CONCAVE QUADRANT (GRAPHITE)

3.7 Studies in machining workpiece tilted about 2 axis

Success in machining the convex/concave shapes encouraged investigation in the possibility of forming a more general shape. If it is possible to form a shape such as an ellipsoid, a broad class of shapes can be machined with this process. A general shape of that nature poses additional demands on the beam/workpiece manipulation techniques. A shape such as an ellipsoid would require stepwise approximation with steps preferably with orthogonal corners. It is foreseeable to form the orthogonal corner by tilting the workpiece about the X and Y axis simultaneously. Figure 3.7.1 shows the necessary rotations about the respective axis to obtain the orthogonal corner shown in the block of the diagram.

Experiments were conducted to verify if it is possible to machine an orthogonal corner by tilting the workpiece at appropriate angles about the X and Y axis. The relative straightness of XZ, YZ surfaces with respect to the top surface are of most interest in this experiment. Attempts were made to machine an orthogonal corner out of a block of graphite. The workpiece was tilted about the X and Y axis. Figure 3.7.2 shows the surfaces of interest in the experiment. The CNC machine's software listing for this experiment can be located in Appendix II.

Constant velocity translation was not possible for this experiment because of the limitation of the CNC system. The CNC system is incapable of completing the transformation computations of the trajectories on the fly. Pulse-move protocol for translation was necessary to conduct this

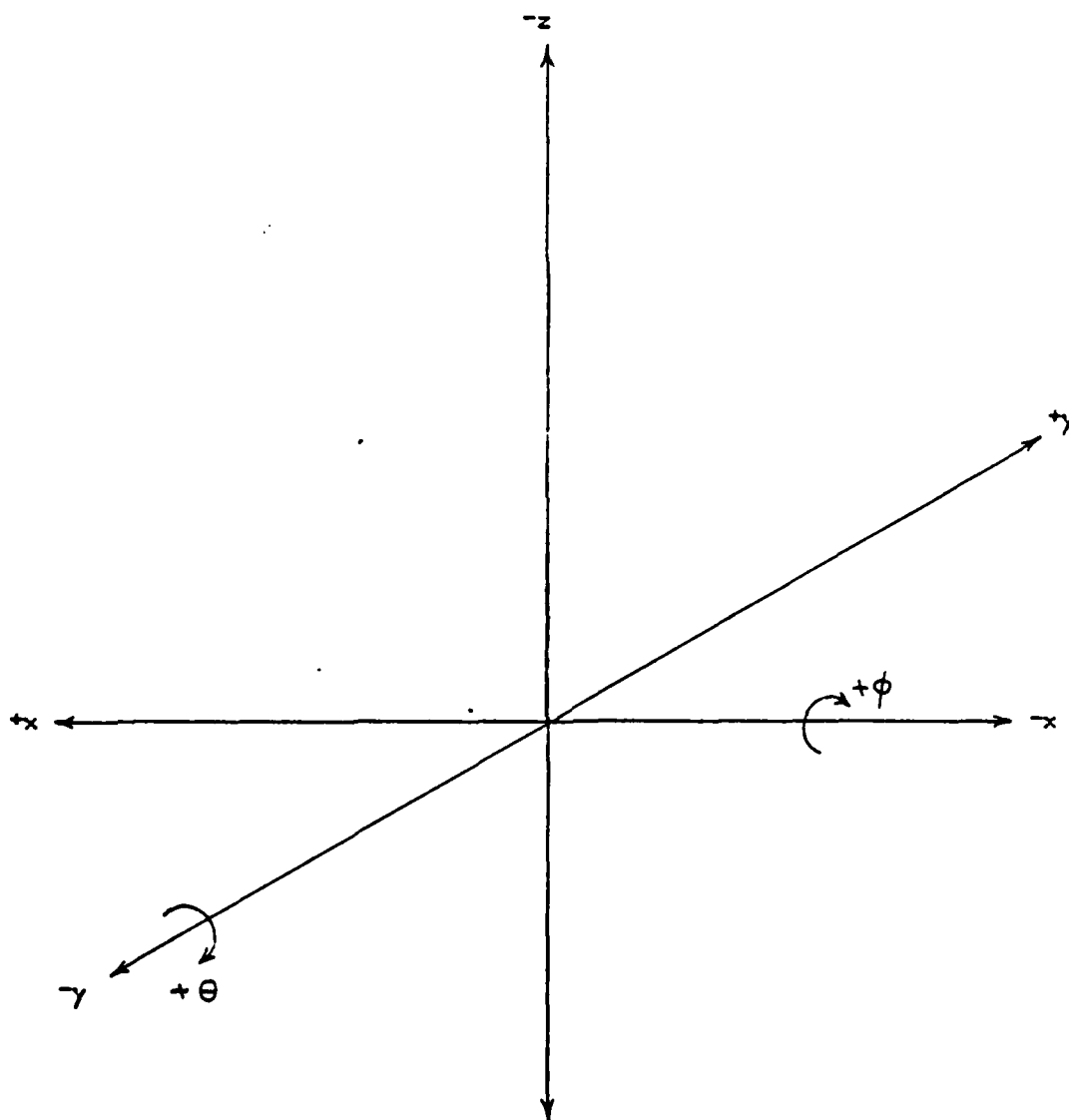


Fig. 3.7.1 SIGN CONVENTIONS IN TILT ANGLES

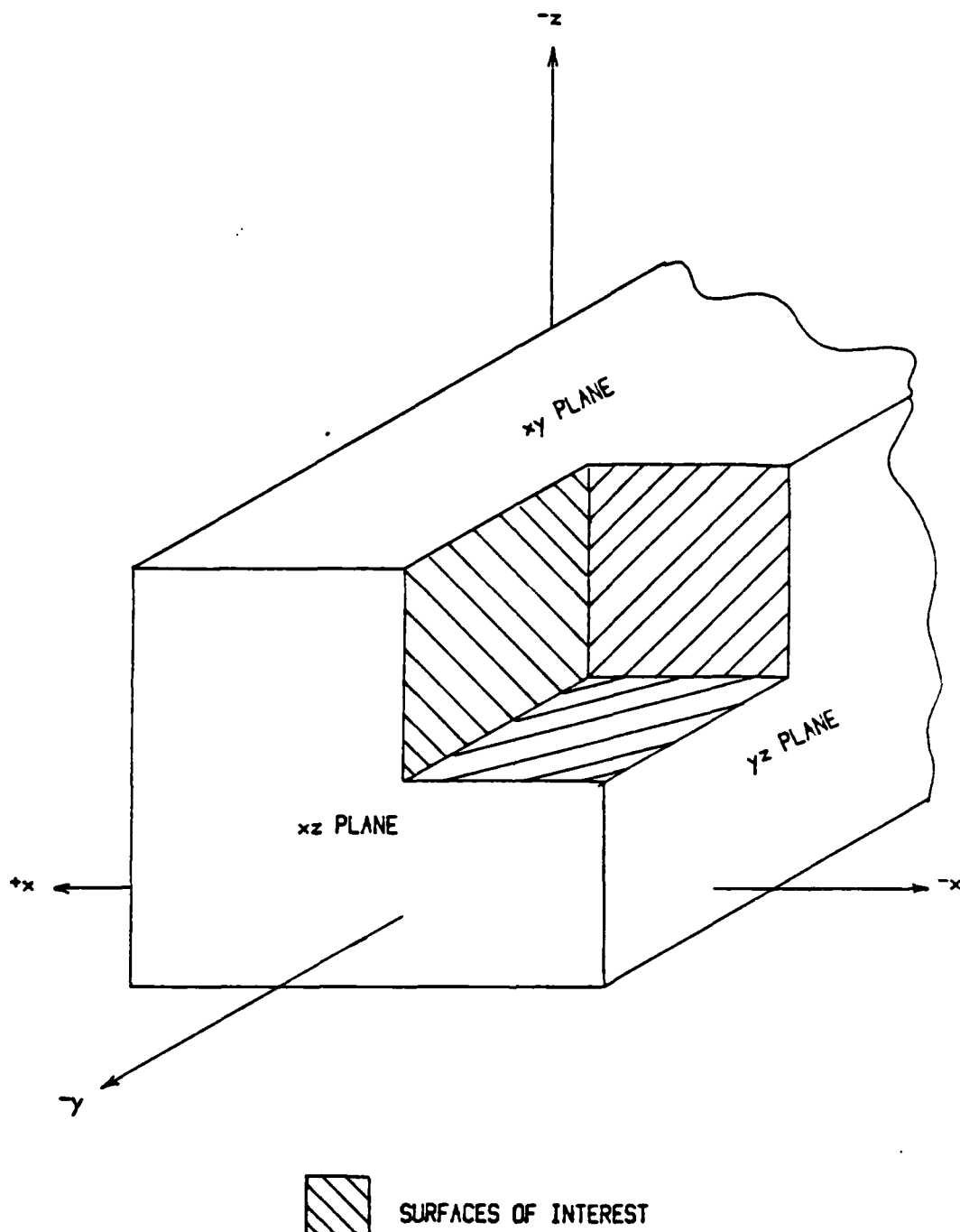


Fig. 3.7.2 SURFACES OF INTEREST IN SHAPING AN ORTHOGONAL CORNER

experiment.

The alignment procedures were similar to that described in Sect. 3.6. After the correct positions of the workpiece and the focal plane of the lens have been established in the base frame, the workpiece was tilted about the X and Y axis by 30 degrees respectively. The translation direction of the workpiece was positioned at 45 degrees to the electric vector of the beam. The laser was operated in time sequence mode II with 1 ms pulse on time at 780W. The output pulse count was set at 1. The X, Y, and Z feeds were set at 0.1 mm and the focus of the beam was placed at 2mm above the surface to be machined. Controlling variables in the software were initialized to their respective values, and the laser was set at the appropriate operating conditions. The program to machine an orthogonal corner with the workpiece tilted about two axis was executed.

Pictures of the XZ, YZ and XY plane of the corner machined are shown in Fig. 3.7.3, Fig. 3.7.4 and Fig. 3.7.5 respectively. It can be seen in the pictures that the surfaces of interest were very close to orthogonal with each other. Indeed, it is possible to form an orthogonal corner by orientating the workpiece appropriately with respect to the optical axis of the laser beam.

The tilting technique based on the idea if the locations to be irradiated are at the appropriate orientation with respect to the optical axis of the beam, it is possible to obtain an approximately orthogonal corner. The ideal situation would be to position the workpiece at the appropriate orientation on every spot to be irradiated. However, the orientation of the

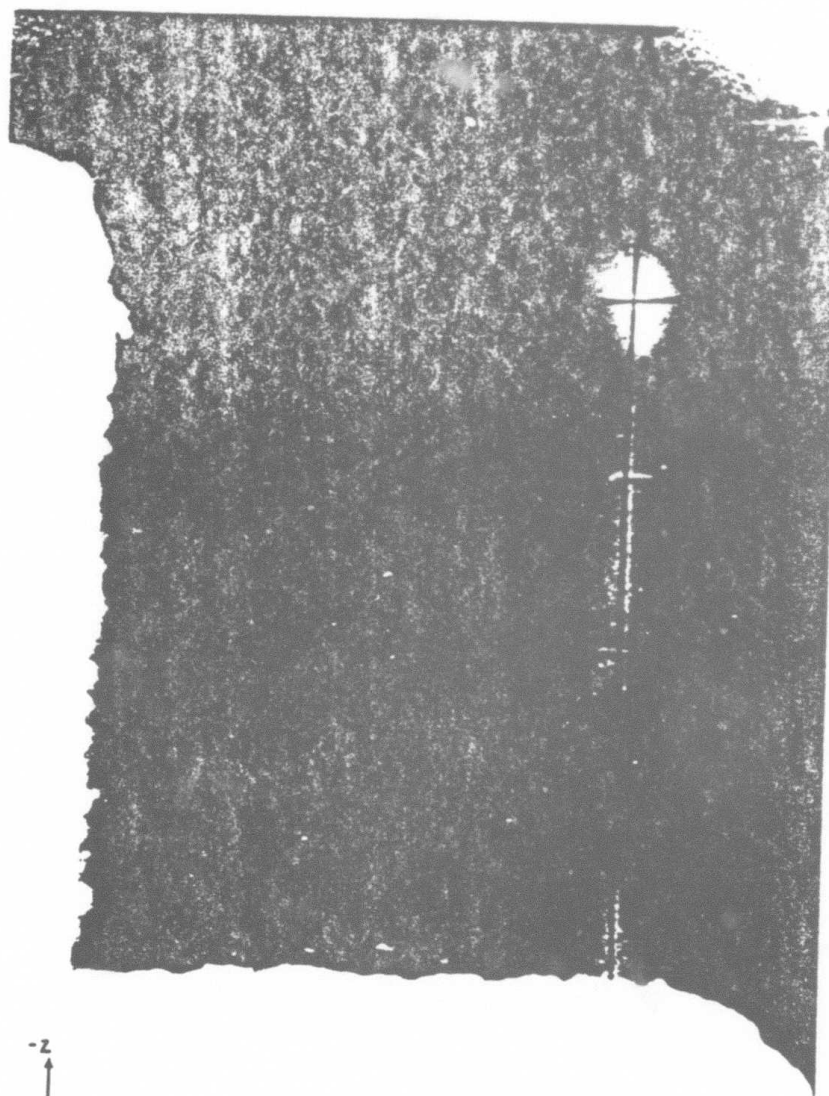


Fig. 3.7.3 xz PLANE

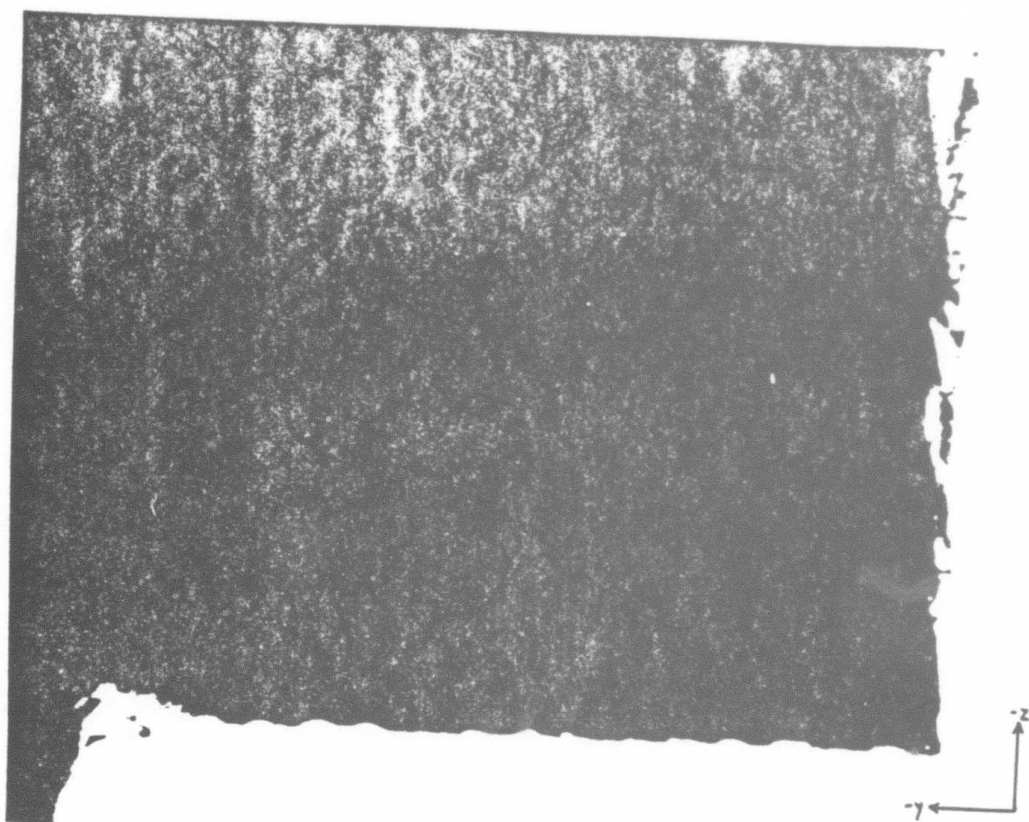


Fig. 3.7.4 yz PLANE

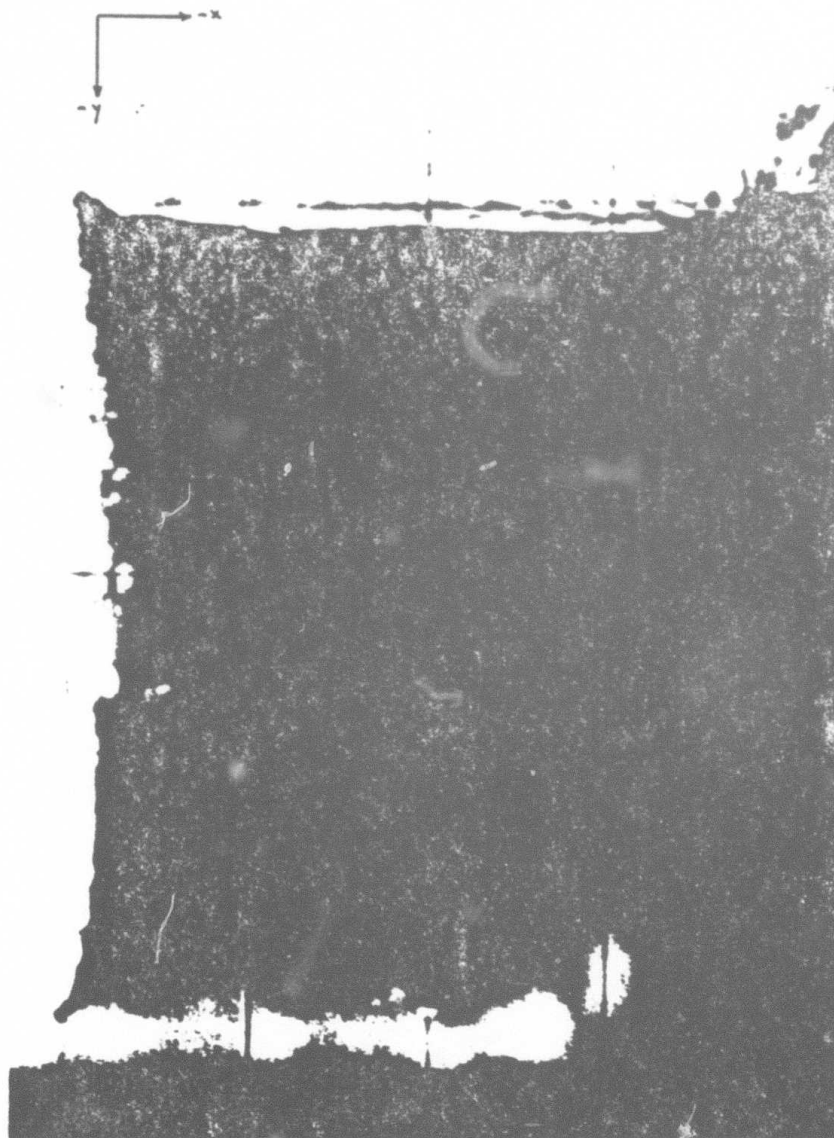


Fig. 3.7.5 xy PLANE

workpiece to approximate the orthogonal corner is not unique. A range of orientations in the neighborhood of the ideal could possibly produce the desired shapes of comparable quality. It is foreseeable to have a compromised orientation to machine a shape within a range of contour without losing much of the accuracy in forming the desired shape. The idea is illustrated in Fig. 3.7.6. Imagine that a half ellipsoid is to be machined out of a block. The ellipsoid to be formed can be conceptually divided into four quadrants. The workpiece will be positioned at a different orientation for each quadrant to be machined. This approach could simplify the task in reorienting the workpiece during machining.

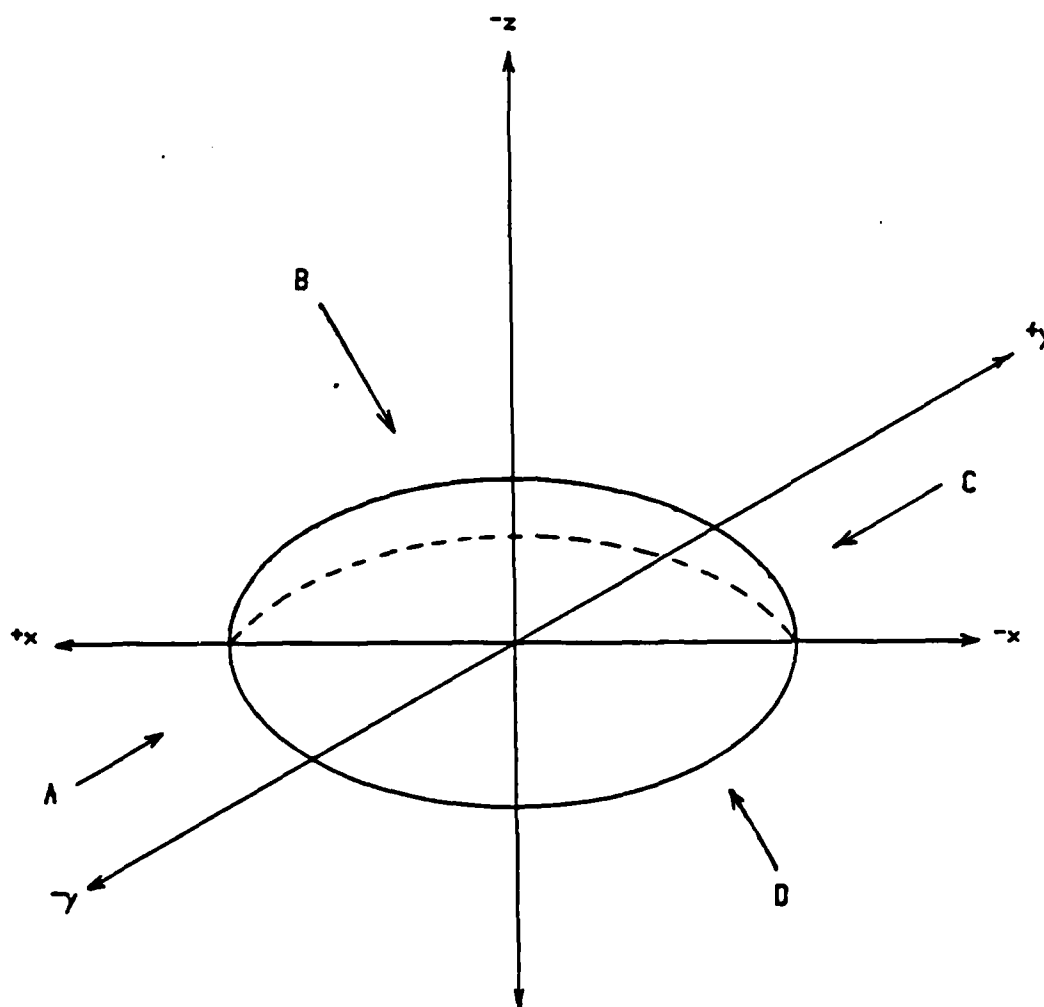


Fig. 3.7.6 SCHEMATIC OF 4 QUADRANT ORIENTATION APPROACH

3.8 Application to Si_3N_4

The findings of this investigation indicate that it is possible to form a contour shape in graphite with a high power laser beam. However, it is more efficient to shape graphite with conventional techniques. Nevertheless, the techniques developed could well be adopted to machine other materials which pose difficulties when conventional machining techniques are employed. One of these hard to machine materials is Si_3N_4 . Diamond grinding is the usual technique used to machine Si_3N_4 because of its high hardness. Experiments were conducted to shape Si_3N_4 with the techniques developed in machining graphite.

The same set of controlling variables to machine graphite were used in the experiments to machine Si_3N_4 . Several parameters were adjusted to tailor the process for Si_3N_4 . Convex and concave quadrants of 5 mm radius were machined in the ultra hard ceramic. The laser was operated in continuously pulsed mode with pulses of duty cycle of 1 ms on and 1 ms off at 780W. The workpiece was tilted at 20 degrees about the X axis, and was translated at 40 mm/s in a direction at 45 degrees to the electric vector of the laser beam. The focus of the beam was placed at 1.5 mm above the workpiece. Software listing of the program for this experiment can be located in appendix II. Table 3.8.1 list the operating conditions in machining graphite and Si_3N_4 .

The shapes formed are shown in Fig. 3.8.1 and Fig. 3.8.2. The curvatures formed were in good agreement with that designed.

	Graphite	Si ₃ N ₄
Laser Power:	780 W	780 W
Pulse Duty Cycle:		
On-time:	0.5 ms	1 ms
Off-time:	1.0 ms	1 ms
Angle of tilt about X axis:	30 deg	20 deg
Translation angle to TE:	45 deg	45 deg
Translation speed:	40 mm/s	40 mm/s
Y stepsize(feed):	0.1 mm	0.1 mm
Z stepsize(feed):	0.1 mm	0.142 mm
Amount of defocus:	-2.0 mm	-1.5 mm

Table 3.8.1 Operating Conditions

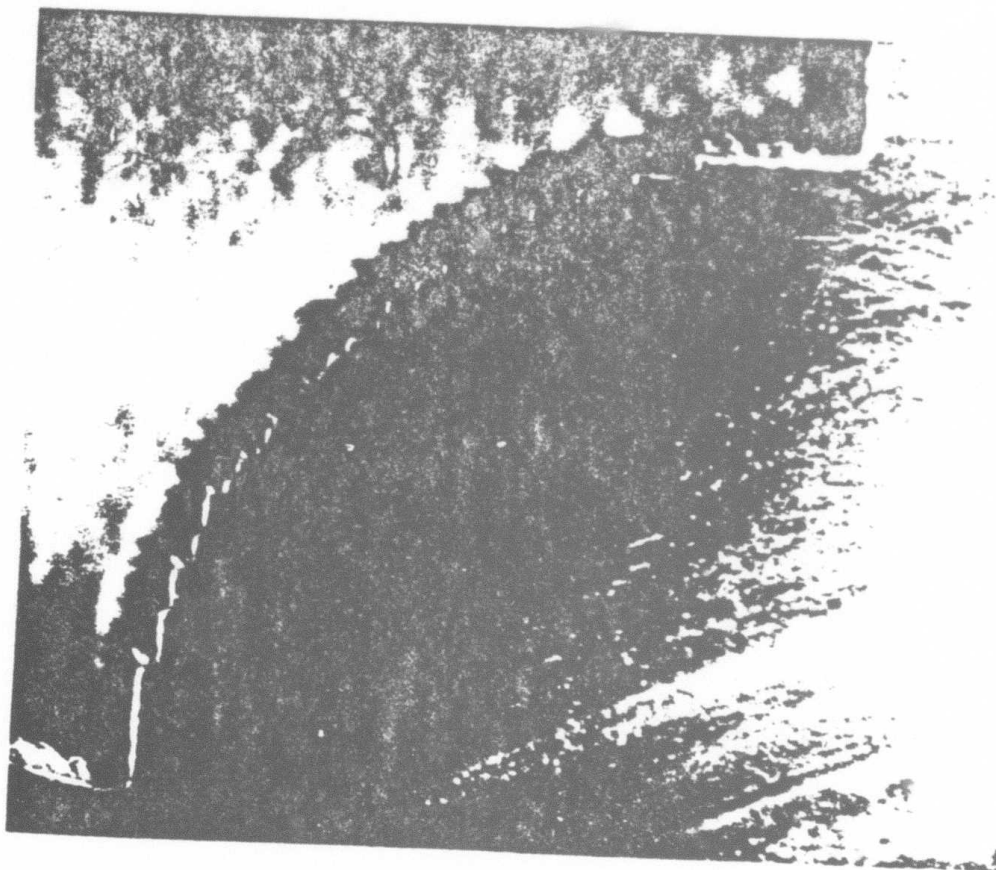


Fig. 3.8.1 CONVEX QUADRANT (Silicon Nitride)

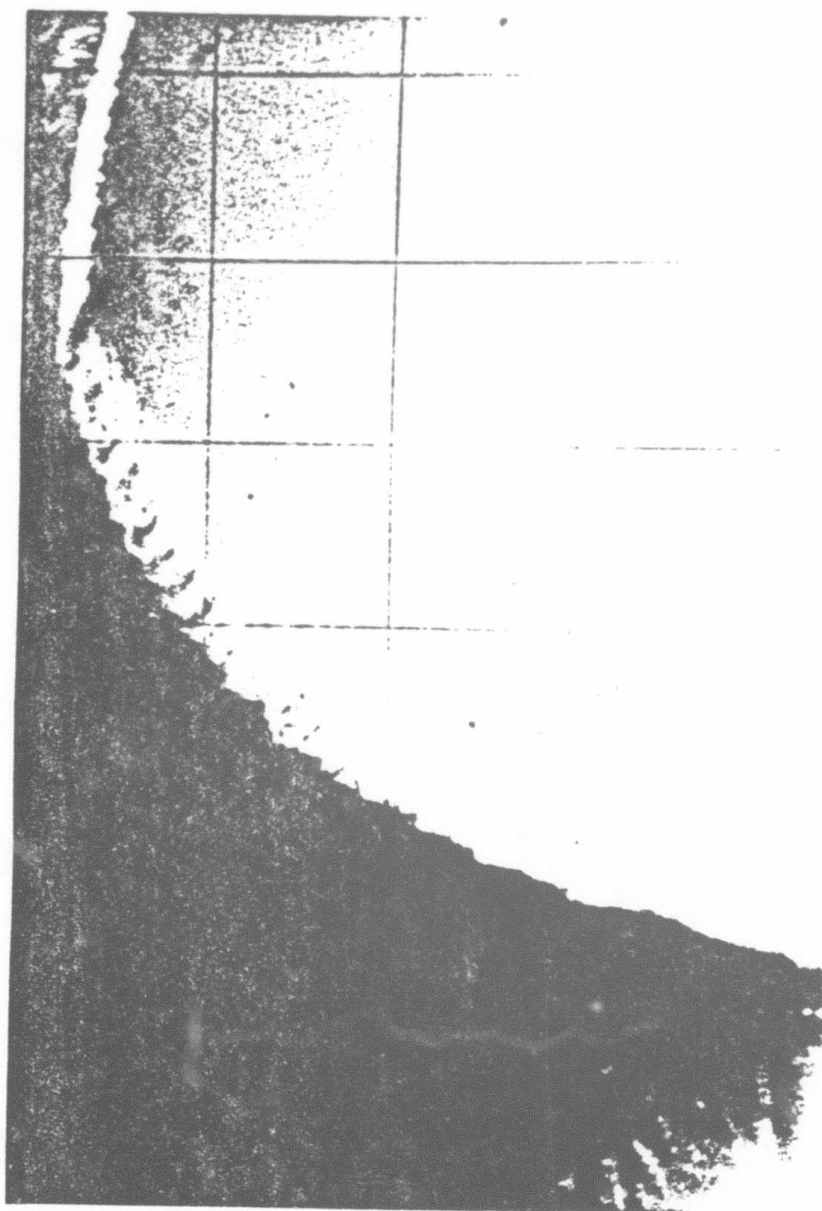


Fig. 3.8.2 CONCAVE QUADRANT (Silicon Nitride)

4.1 Assessment of Laser Shaping Process

This laser machining process like many other conventional machining processes requires a clear line of sight path to the area on the material to be machined. Shapes being machined should not develop into geometries that will obstruct the beam path. For example in the case of machining a slot in a block, the aspect ratio of the slot must be large enough to accomodate the beam. Care must be exercised to insure that the laser beam is not blocked off by the edge of the slot. Figure 4.1.1 illustrates the potential problem in machining a slot in a block. Similar situations can occur in making other shapes. With a few exceptions, shapes that can be formed by machining from the free sides of a block towards the middle can be done with this machining process.

The sloped wall distortion at the end of a layer can be corrected by increasing the absorption on the surface by workpiece manipulation techniques. Selective orientation with respect to the electric vector of a polarized beam to increase absorption on the side-wall was not adequate to correct the distortion. Reorientation of the workpiece was necessary to solve the problem. A circular polarized beam would require similar workpiece manipulation techniques to correct the distortion formed at the end of a layer.

The speed of this process is limited by the design of the positioning system. Due to reorientation of the workpiece, timely transformation computations between the reference frame's and the base frame's coordinates have to be performed when the workpiece is moved. In the

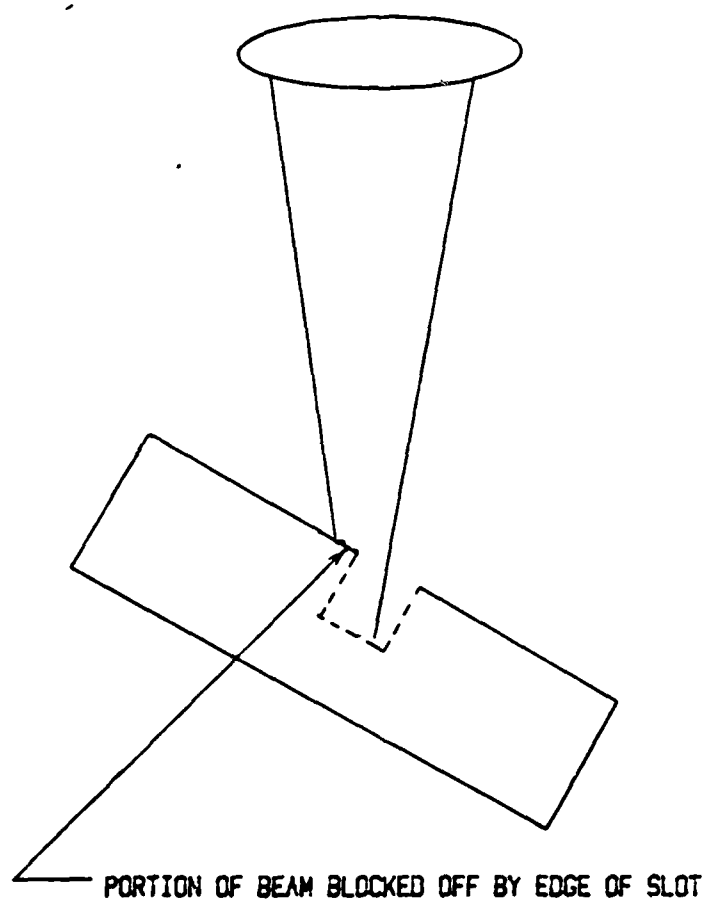


Fig. 4.1.1 DIFFICULTIES IN MACHINING A SLOT

case when the workpiece is tilted about the X axis, the transformation computation is performed whenever there will be a move in the Y direction. This will insure proper tracking of focus in the Z direction. The maximum speed of translation is limited by the mechanics and design of the CNC positioning system. At constant velocity, the CNC system software requires a minimum of 200 ms to process the interpolation data between points for the servo motors. An error condition will occur if the feedrate exceeds this limitation. To avoid making this error while machining, the software programs for experiments in this investigation have been written such that the transformation computations are done before and after, but not during the translation of the workpiece. This approach allows ample time for the CPU to complete the computations, while managing the system's overhead, without running into timing difficulties. In the case when the workpiece is tilted both about the X and the Y axis, the transformation computation is performed whenever the workpiece is to be moved to a new position. Due to the frequencies and extra time needed to do the transformation computations, the pulse-move protocol is used to circumvent the timing constraints of the CNC system. The calculations are done while the system is not in motion as mentioned earlier. Extra time is needed to do the start/stop motion for each move but in return the difficulties in managing velocity of translation are eliminated!

A multi-degree of freedom manipulator type of positioning system to move the beam or the workpiece would be more flexible for this

machining process.

It is possible to increase the speed of this machining process by reducing the number of passes necessary to remove a layer. Focussing the laser beam into a line with cylindrical optics, a small layer of material(wider groove) instead of a narrow groove could be removed on every pass. If the length of the focussed line of the beam is varied dynamically, it would be possible to change the width of the layer of material being removed on every pass. Further studies would be necessary to develop this approach.

The shapes machined with stepwise approximation in this process produce a coarse finish part. Post processing(fine finish) of the part will be necessary to make it into a finish product. Dynamic stepsizes control with a closed loop system could improve the accuracy on the shape formed. A non contact position sensor adaptable to this machining process for measuring the material removed on each pass would have to be developed to close the loop for this machining process. Furthermore, a broad data base of the effects on depth and width of cut in varying the controlling variables has to be generated for the closed loop control algorithm.

This process can be adopted to machine materials that change from a solid phase to vapor phase under intense radiation of a focussed carbon dioxide laser beam. The same set of control variables in machining graphite can be used to machine other materials. A parametric study on the material to be laser machined will have to be conducted to established

proper settings of the variables. In particular, it is necessary to determine the power settings, pulse duty cycle of the laser, amount of defocussing, feeds in the X, Y, Z directions, translation speed, proper orientation of the workpiece with respect to the optical axis and electric vector of the beam. These essential data have to be compiled on the material before shaping operations can be performed successfully with this process.

5. Conclusion And Suggestions For Further Work

The feasibility of machining non-solid of revolution shapes with a high power carbon dioxide laser operating in pulse mode has been demonstrated in this investigation. The shapes are machined out of a model material, graphite. The techniques and controls developed can easily be adapted to machine other materials as demonstrated in making shapes in Si_3N_4 . With tilting about the X/Y axis, it is possible to machine an orthogonal corner implying a more general shape such as an ellipsoid can probably be formed with this process. The polarized beam incident at angles other than normal produces grooves of different cross-sectional shapes depending on the angle between the direction of translation and that of the polarization vector. Nevertheless, the polarization of the beam does not pose serious problems in the machining process. The effects of tilting the workpiece overshadow that of the selective absorption between the TE and TM vectors on the side-wall at the end of a layer. Defocussing the laser beam above the workpiece can produce a smoother surface finish. The speed of the machining process is severely limited by the speed of the positioning system and can be dramatically improved if a faster system is employed. Furthermore, the two rotational axis should be automated so that more complicated manipulation of the workpiece can be programmed. Besides employing higher speed positioning system, alternative optical solutions to improve the speed of the machining process should be explored.

List of References

1. Richard P. Paul, "Robot Manipulators", MIT Press 1981.
2. Photon Source Inc., Model 1003 Laser Manuals, Livonia, MI.
3. Anomatic II hardware, software manuals, Anorad Corp., Haupaugge, N.Y..
4. Geoffrey Boothroyd, "Fundamentals of Metal Machining and Machine Tools", McGraw Hill, San Francisco, 1975.
5. "Thermal Machining Process", Society of Manufacturing Engineerings, 1st. ed..
6. R.J. Wallace, "A Study of the Shaping of Hot Pressed Silicon Nitride with a High Power CW Carbon Dioxide Laser", Ph.D. dissertation, University of Southern California (1983).
7. "Infrared Optics Catalog"(II-VI Incorporated, Saxonburg, PA).
8. J.F. Ready, Industrial Application of Lasers.(Academic Press, San Francisco, 1978).
9. J.F. Ready, Effects of High Power Lasers Radiation.(Academic Press, San Francisco, 1971).
10. Newport Corporation catalog, Fountain Valley, California.
11. Poco Graphite Inc., Decatur, Texas.
12. S.M. Copley, M. Bass, and R.J. Wallace, Proceedings of 2nd International Symposium on Ceramic Machining and Finishing. National Bureau of Standards Publication No. 562 (1978), pp. 283-292.
13. S.A. Jenkins, H.E. White, Fundamentals of Optics, 3rd. Ed., McGraw Hill, 1957
14. S.M. Copley, M. Bass, B. Jau and R.J. Wallace, "Shaping Materials with Lasers" in Laser Materials Processing, M. Bass, Ed., North Holland Publishing Co. (1983).
15. R.J. Wallace, M. Bass and S.M. Copley, "Effect of Beam Polarization on the Shape of Grooves in Si_3N_4 Produced by Laser

Machining," submitted to J. Appl. Phys. (1983).

16. R.J. Wallace, M. Bass and S.M. Copley, "Laser Machining of Si_3N_4 : I. Energetics," submitted to J. Am. Ceram. Soc. (1983).
17. R.J. Wallace, M. Bass and S.M. Copley, "Laser Machining of Si_3N_4 : II. Shaping and Material Properties," submitted to J. Am. Ceram. Soc. (1983).
18. S.M. Copley, "Laser Shaping of Materials" in Lasers in Materials Processing, E.A. Metzbaer, Ed., American Society for Metals, Metals Park (1984).

Appendix

The following sections include descriptions of the mechanical and electronic designs of the crucial interfaces that complete the connections between the laser's programmable digital controller (PDC) and the Anomatic II CNC positioning controller. These mechanical devices and interfaces have been custom designed and built at USC to integrate the two controller systems to work together. The schematics, drawings and literatures are supplements to those of the Laser and CNC controller manufacturers' manuals.

The software listings in Appendix II are some of the programs used for experiments in this work.

A.1.1 Interface Control Commands

The M100 (laser on), M101 (laser off) functions of the CNC controller are used to control the laser ON/OFF sequences. For safety reasons, the laser should be operating in Mode I when this function is invoked. If the laser is operating in Mode II, the CNC controller will not be able to turn off the laser. Once the laser is turned on in Mode II with the CNC controller, it will have to be turned off manually by pressing the sequence off button or be turned off by itself when the executed program is completed.

The M102 (shutter open), M103 (shutter closed) functions of the CNC controller are used to control the laser's safety shutter. The laser has to be in Mode I or Mode II; shutter mode select switch has to be in remote and the manual shutter switch turned on for this function to actuate the shutter properly.

The M200 function of the CNC controller is wired up for monitoring the status of the laser. When M200 is a "0", the laser sequence is off. whereas when M200 is "1", the laser sequence is on.

The S-function (Analog) of the CNC controller is interfaced to control the power of the laser. The range of S numbers that can be used are from 0 to 1250. S-numbers outside this range must not be used because serious damage to the laser could be done. The power control select switch inside the PDC must be set at external for this function to be active.

The respective interface cables from the CNC controller to the PDC must be connected for the above functions to work properly.



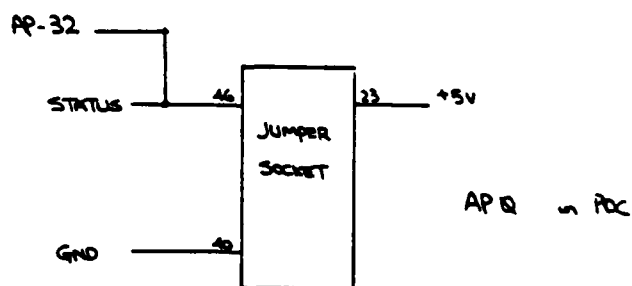
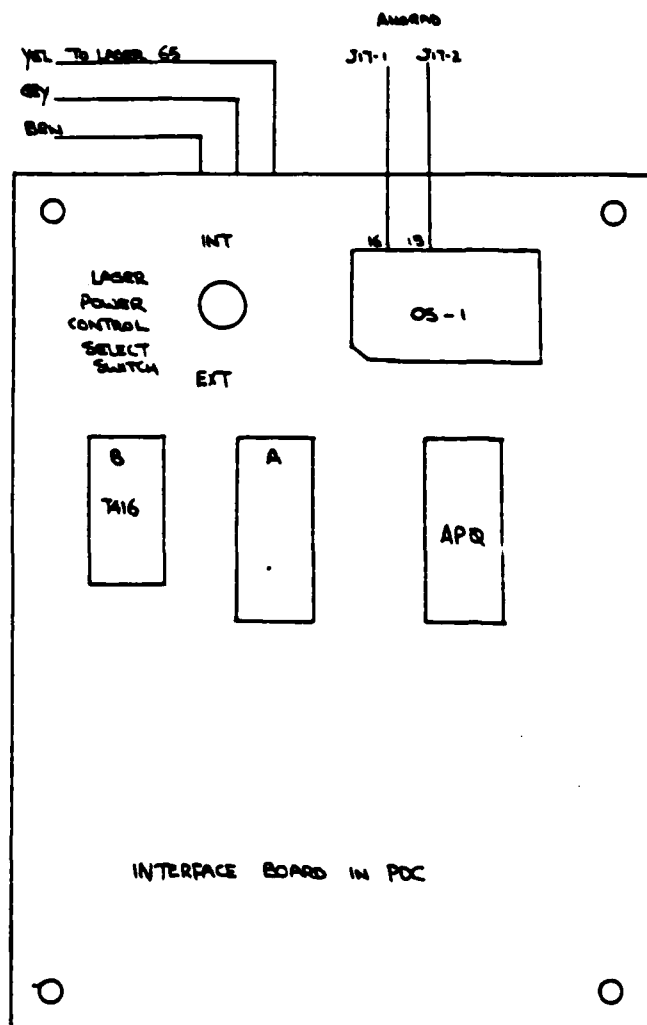
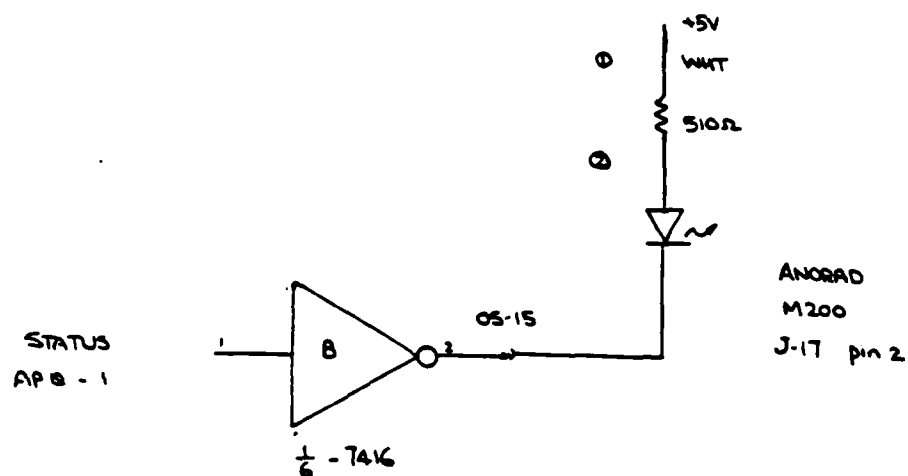
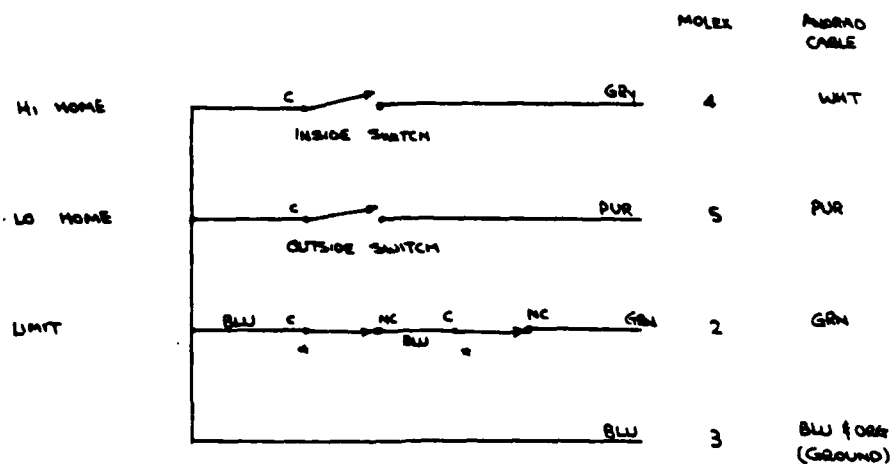


Fig A.I.2 INTERFACE BOARD LAYOUT IN PDC



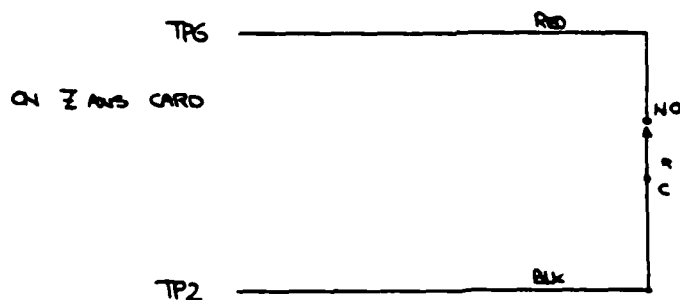
M200 is a "1" when Laser sequence is "ON"
M200 is a "0" when Laser sequence is "OFF"

Fig. A.I.3 LASER STATUS MONITOR BUFFER CIRCUIT



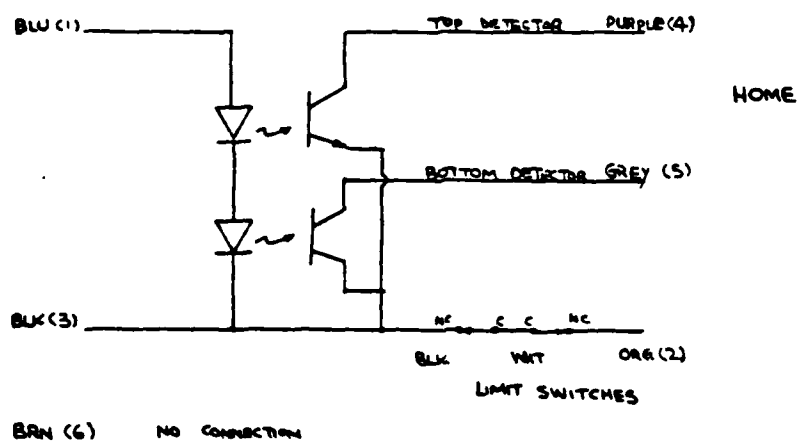
* CHERRY E-62 Type SWITCHES
LOW CAM IS ON INSIDE

HOME & LIMIT SWITCHES ON Z AXIS

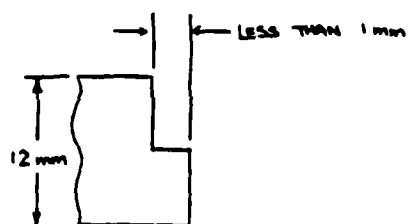


Z axis Adjustable Lower Limit SWITCH

Fig. A. I. 4 HOME AND LIMIT SWITCHES FOR TRANSLATION TABLES



4 LIMIT SWITCHES ARE CONNECTED IN SERIES [NC] ; AT LIMIT , SWITCHES OPEN



HOME ACTUATION CAM

Fig. A. I. 5 OPTO-ELECTRONIC HOME SWITCHES FOR TRANSLATION TABLES & ACTUATION CAM

A.II.1 Program for Beam Scan Experiment

N9900 G69 *BEAM SCAN V1.1* 10JAN 1984 *R HSU*

N9905 G69 V3 V4 V10 V25 V26 USED

N9910 G69 F.1=.005 MM/SEC

N7200 G69 SET UP

N7210 F100 S0 G90 M101 M103 M0

N7215 V3=0 V4=.1 G69 POWER/SPEED

N7220 V10=10 G69 INC VOLTAGE NO.

N7225 V25=.01 G69 X INTERVAL

N7230 V26=10 G69 XLIM

N7300 SV3FV4 M100M102 G69 SET POWER/SPEED LASER/SHUTTER ON

N7310 J(X-V26)N7350 G69 IF DONE

N7320 G9G91XV25 G69 BEGIN SCANNING

N7330 V3=V3+V10 SV3 G69 INC POWER

N7340 JN7310 G69 NEXT SCAN

N7350 G0F100 G69 END CV/RESET SPEED

N7360 G90M101M103 G69 ABS/LASER SHUTTER OFF

N7370 M0 G69 STOP/END PROGRAM

N10005 JN7200M7 G69 GO TO SET UP

A.II.2 Program To Determine Focal Plane On Workpiece

N9900 G69 ** RANGE OF FOCUS V1.1 ** 31 DEC 1983 R. HSU
N9905 G69 V3 V5 V27 V29 V30 USED
N9910 G69 LASER MODE 2/PULSE COUNT=1
N9915 G69 TIME SEQ/ 10 ms ON-TIME

N7200 M101M103 G69 LASER OFF/SHUTTER CLOSE
N7203 M0 G69 STOP
N7205 G69 SET UP
N7210 V3=800 SV3 F100 G69 POWER
N7215 V5=0 G69 PULSE COUNTER
N7220 V27=-1 G69 YSTP
N7225 V29=.1 V30=Z+2 G69 ZSTP/ZLIM

N7300 G69 MAIN PROGRAM
N7310 J(Z-V30)N7400 G69 IF DONE
N7330 M102M100 G69 OPEN SHUTTER/LASER ON
N7340 JM200N7340 G69 IF PULSE COMPLETED
N7350 M101 G69 LASER OFF
N7360 G58"PULSE NO "V5F3.0" Z POSITION IS"ZF5.3" MM"
N7370 V5=V5+1 G69 INC COUNTER
N7380 G90Y(Y+V27) G69 MOVE Y
N7385 Z(Z+V29)G4X.2 G69 MOVE Z
N7390 JN7310 G69 NEXT LOCATION
N7400 M103M0 G69 CLOSE SHUTTER/STOP

N10001 G90X0Y0M7 G69 START POSITION
N10005 JN7200M7 G69 RUN PROGRAM

A.II.3 Program For Cutting Trails In Regions Of Focus(Normal Incidence)

N9800 G69 VARYING FOCUS/TRAILS V1.1(PULSED)*
N9803 G69 *31 DEC 83* R.HSU
N9804 G69 NORMAL INCIDENT *31 DEC 83* R.HSU
N9805 G69 ORIGIN AT PIVOT
N9807 G69 V3-V4 V18-V65 ARE USED X1ST=KN20 Y1ST=KN150
N9809 G69 SETUP*X~V31=V25*Y~V32=V27
N9811 G69 KN700=TRANSFORM KN1000=CAL VEC T
N9815 G69 V25=XSTP V26=XLIM V27=YSTP V28=YLIM V29=ZSTP V30=ZLIM
N9820 G69 V31=CURX V32=CURY V33=CURZ V34=STRX V35=STRY V36=STRZ
N9825 G69 V37=OFSX V38=OFSY V39=OFSZ
N9827 G69 V43=DCR LIM
N9830 G69 V46=THETA DEG V47=THETA RAD
N9833 G69 V48=TX V49=TY V50=TZ *POSITION VEC
N9835 G69 V51 V52 V53*PASS PAR XYZ* V54 V55 V56*TRANSFORM XYZ*
N9840 G69 V57=PX V58=PY V59=PZ
N9850 G69 V63=PRERUN V64=ORIENT ANGLE

N300 G69 LAYX1ST
N310 G69 V32=V27
N320 KN1200 G69 CUT TRAIL
N330 M6 G69 RETURN

N378 G69 CAL Y-Z MOV
N380 V52=V32 V53=V33 KN700 G90YV55Z(V56+V65)
N390 V32=V32+V27 KN10002
N400 M6

N700 G69 TRANSFORMATION
N710 V54=V51+V48 G69 TRAN X
N720 V55=(V52*Q4(V47))-(V53*S(V47))+V49 G69 TRAN Y
N730 V56=(V52*S(V47))+(V53*Q4(V47))+V50 G69 TRAN Z
N740 M6

N1000 G69 CAL VECTOR T
N1010 V48=0 V49=0 V50=0
N1020 V51=V57 V52=V58 V53=V59 KN700
N1030 V48=V54 V49=V55 V50=V56
N1040 M6

N1198 G69 XLAY CV
N1200 G9XV54 G69 +X DIR
N1205 M100
N1210 XV26
N1215 M101
N1220 X(V26+V63)
N1225 G0 G69 END CV
N1230 J(V28-V32)N1240
N1235 M6
N1240 KN380 G69 MOV Y/Z
N1245 G9XV26 G69 -X DIR
N1250 M100
N1255 XV54
N1260 M101
N1265 X(V54-V63)
N1270 G0
N1275 J(V28-V32)N1285
N1280 M6
N1285 KN380
N1290 JN1200

N1500 G69 MOV TO START
N1510 V51=0 V52=V32 V53=V33 KN700 G90X(V54-V63)
N1512 YV55
N1515 Z(V56+V65)G4X.2
N1520 KN10002 G5
N1530 M6

N10001 G92X0Y0Z0F850G90X0Y0Z-30M103M7
N10002 G69 G58"CURY="V32" YLIM="V28" CURZ="V33
N9914 M6
N10005 JN7200
N10006 M99M98FZ200G90X-70Y-70 G69 SET ORIGIN
N9001 Z35.257G4X.8
N9902 M98
N9903 G92Z48.114
N9905 X20.4675Y50.4205Z-43M7

N7200 G69 MAIN PROGRAM SETUP
N7202 M101M103 J(Q2(167))N7206 G69 IF RESET G67
N7204 JN7208
N7206 G67
N7208 M0

N7210 V3=700 V4=800
N7212 V25=.1 V26=16 G69 X STEP/LIM
N7214 V27=1 V28=0 G69 Y STEP/LIM
N7216 V29=.125 V30=0 G69 Z STEP/LIM
N7218 V31=0 V32=0 V33=0 G69CUR X-Y-Z
N7220 V34=0 V35=0 V36=0 G69 START X-Y-Z
N7222 V37=0 V38=1 V39=-1 G69 OFFSET
N7224 V43=2 V46=0 G69X TILT ANGLE
N7226 V47=V46*P/180
N7228 V57=0 G69 PX
N7230 V58=-25 G69 PY
N7232 V59=-48.114 G69 PZ
N7234 V63=15 V64=0 V65=-2 G69 PRERUN/CTR/DEFOCUS
N7250 G69*** END SET UP ***

N7300 J(V65-1.9)N7440 G69 IF FINISH
N7350 KN1000 G69 CAL VEC T
N7360 SV3FV4 M102 G69 SET POWER/SPEED SHUTTER ON

N7400 KN1500 KN310 G69 CUT 1 TRAIL
N7405 G58"TRAIL NO"V64F3.0
N7406 G58" DIST FROM ORIGIN ="ZF5.3" MM
N7407 G58" DEFOCUS="V65F4.3"MM"
N7410 V32=V32+V27 V28=V32
N7420 V64=V64+1 V65=V65+.25 G69 INC CTR
N7430 JN7300
N7440 M0

N8000 G58"31 DEC 1983"
N8010 G58"XTILT 0 DEG"
N8015 G58"POWER=S700 (780 W)"
N8035 G58"PULSE 0.5 MS ON 1MS OFF"
N8040 G58"VELOCITY=F800"
N8045 G58"O2 SHIELDING 10 PSI"
N8065 M0

A.II.4 Program For Tilted/Orientation Studies

N9800 G69 POLARIZATION/ORIENT V1.1 (CW)
N9803 G69 *22 JULY 83* R. HSU
N9804 G69 VARY XTILT ANGLE/2 DEG INCREMENT
N9811 G69 KN700=TRANSFORM KN1000=CAL VEC 5
N9827 G69 V44=ANGLE COUNTER
N9830 G69 V46=THETA DEG V47=THETA RAD
N9833 G69 V48=TX V49=TY V50=TZ * POSITION VEC
N9835 G69 V51 V52 V52 * PASS PAR XYZ * V54 V55 V56 *
TRANSFORM XYZ *
N9840 G69 V57=PX V58=PY V59=PZ
N9850 G69 V64=TRAIL CTR V65=ANGLE LIM

N700 G69 TRANSFORMATION
N710 V54=V51+V48 G69 TRAN X
N720 V55=(V52*Q4(V47))-(V53*S(V47))+V49 G69 TRAN Y
N730 V56=(V52*S(V47))+(V53*Q4(V47))+V50 G69 TRAN Z
N740 M6

N1000 G69 CAL VECTOR T
N1010 V48=0V49=0V50=0
N1020 V51=V57V52=V58V53=V59 KN700
N1030 V48=V54V49=V55V50=V56
N1040 M6

N1500 G69MOV TO START
N1510 V51=0V52=0V53=0 KN700 G90XV54YV55ZV56
N1530 M6

N1600 G69 RUN CW TRAIL
N1610 SV3+400 G69 SET HIGH POWER
N1620 X0M100G4X3 G69 ON LASER/DELAY
N1630 SV3G4X3 M102 G69 SET LOW POWER/DELAY/OPEN SHUTTER
N1640 F1000X10 G69 CUT TRAIL
N1650 M101 M103 G69 OFF LASER/CLOSE SHUTTER
N1660 M6

N10001 G92X0Y0Z0F850G90X0Y0Z-30M103M7
N10005 JN7200
N10006 M99M98FZ200G90X-70Y-70

N9001 Z35.257G4X.8
N9902 M98
N9903 G92Z48.114
N9905 X20.4675Y50.4205Z-43M7

N7200 G69MAIN PROGRAM SETUP
N7202 M101M103J(Q2(167))N7206
N7204 JN7208
N7206 G67
N7208 M0 JN7500

N7500 G69 MAIN PROGRAM
N7510 V3=250 V46=0 V47=V46*P/180 V57=0 V58=0 V59=-48.114
N7515 V64=0 V65=70
N7520 G92X0Y0
N7530 FX1000FY1000FZ200 G90X0Y0G5
N7540 KN1000 KN1500 KN1600 G92YV58
N7560 G90X0Y0
N7570 G58"SET TILT TO"V46F3.0" DEG TRAIL NO."V64F3.0" POWER="V3F4.0
N7580 G66 32786 240 R5-
N7590 K(V65-V64)N7630
N7600 V46=V46+2 V47=V46*P/180 V58=V58-1 V64=V64+1
N7610 J(V65-V64)N7520
N7620 G92X0Y0 G90X0Y0
N7630 M0

N8000 G58"25 NOV 1983"
N8005 G58"defocussed 2 mm above"
N8010 G58"XTILT 30 DEG"
N8015 G58"POWER=S700 (780 W)"
N8020 G58"OVERLAP Y.1 Z.125"
N8035 G58"PULSE .5 MS ON 1MS OFF"
N8040 G58"VELOCITY=F800"
N8045 G58"O2 SHIELDING 10 PSI"
N8065 M0

A.II.5 Program For Tilt/Orientation (layer) Studies

N9800 G69 POLARIZATION/ORIENT V1.1(PULSED)*
N9803 G69 *25 NOV 83* R.HSU
N9804 G69 LAYERS/FIX XTILT ANGLE=30/DEFOCUSSED
N9805 G69 CHANGE TRANSLATION DIRECTION
N9806 G69 CONSTANT VELOCITY-CONTINUOUS PULSE
N9807 G69 V3-V4 V18-V65 ARE USED X1ST=KN20 Y1ST=KN150
N9809 G69 SETUP *X*V31=V25 *Y*V32=V27
N9811 G69 KN700=TRANSFORM KN1000=CAL VEC T
N9815 G69 V25=XSTP V26=XLIM V27=YSTP V28=YLIM V29=ZSTP V30=ZLIM
N9820 G69 V31=CURX V32=CURY V33=CURZ V34=STRX V35=STRY V36=STRZ
N9825 G69 V37=OFSX V38=OFSY V39=OFSZ
N9827 G69 V43=DCR LIM
N9830 G69 V46=THETA DEG V47=THETA RAD
N9833 G69 V48=TX V49=TY V50=TZ *TRANSLATION VEC
N9835 G69 V51V52V53*PASS PAR XYZ* V54V55V56*TRANSFORM XYZ*
N9840 G69 V57=PX V58=PY V59=PZ
N9850 G69 V63=PRERUN V64=ORIENT ANGLE

N300 G69 LAYX1ST
N310 V32=V27 G69 SET CUR Y
N320 KN1200 G69 CUT GROOVES
N330 M6

N378 G69 CAL Y-Z MOV
N380 V52=V32V53=V33KN700G90YV55Z(V56+V65)
N390 V32=V32+V27 KN10002
N400 M6

N700 G69 TRANSFORMATION
N710 V54=V51+V48 G69 TRAN X
N720 V55=(V52*Q4(V47))-(V53*S(V47))+V49 G69 TRAN Y
N730 V56=(V52*S(V47))+(V53*Q4(V47))+V50 G69 TRAN Z
N740 M6

N1000 G69 CAL VECTOR T
N1010 V48=0 V49=0 V50=0
N1020 V51=V57 V52=V58 V53=V59 KN700
N1030 V48=V54 V49=V55 V50=V56

N1040 M6

N1198 G69 XLAY CV

N1200 G9XV54 G69 +VE DIR

N1205 M100

N1210 XV26

N1215 M101

N1220 X(V26+V63)

N1225 G0

N1230 J(V28-V32)N1240

N1235 M6

N1240 KN380

N1245 G9XV26 G69 -VE DIR

N1250 M100

N1255 XV54

N1260 M101

N1265 X(V54-V63)

N1270 G0

N1275 J(V28-V32)N1285

N1280 M6

N1285 KN380

N1290 JN1200

N1500 G69 MOV TO START

N1510 V51=0V52=0V53=V33KN700G90X(V54-V63)YV55Z(V56+V65)

N1520 KN10002G5

N1530 M6

N10001 G92X0Y0Z0F850G90X0Y0Z-30M103M7

N10002 G58"CURY="V32" YLIM="V28" CURZ="V33

N9914 M6

N10005 JN7200

N10006 M99M98FZ200G90X-70Y-70

N9001 Z35.257G4X.8

N9902 M98

N9903 G92Z48.114

N9905 X20.4675Y50.4205Z-43M7

N7200 G69 MAIN PROGRAM SETUP

N7202 M101M103J(Q2(167))N7206

N7204 JN7208

N7206 G67

N7208 M0

N7210 V3=700 V4=800 V21=0 V22=5 V23=0

N7212 V25=.1 V26=16 G69 X STEP/LIM
 N7214 V27=.1 V28=16 G69 Y STEP/LIM
 N7216 V29=.125 V30=0 G69 Z STEP/LIM
 N7218 V31=0 V32=0 V33=-6 G69 CUR X-Y-Z
 N7220 V34=0 V35=0 V36=-6 G69 START X-Y-Z
 N7222 V37=0 V38=1 V39=-1 G69 OFFSET
 N7224 V43=2 V46=30 G69 X TILT ANGLE
 N7226 V47=V46*P/180
 N7228 V57=0 G69 PX
 N7230 V58=-25 G69 PY
 N7232 V59=-42.114 G69 PZ
 N7234 V63=15 V64=0 V65=-2
 N7250 G69 *** END SET UP ***

N7300 J(V64-157.5)N7370 G69 IF FINISH
 N7310 G66 32786 240 R500
 N7320 G58"SET ORIENTATION TO"V64F4.1" DEG"
 N7330 J(V64-72)N7360
 N7340 G58"***A(V64-72)F4.1" CLOCKWISE FROM ZERO ***"
 N7350 JN7370
 N7360 G58"***A(V64-72)F4.1" COUNTER CLOESWISE FROM ZERO ***"
 N7370 M0

N7380 KN1000 G69 CAL VEC T
 N7390 SV3FV4 M102

N7400 KN1500 KN310 G69 CUT 1 LAYER
 N7410 KN1500 G69 MOVE TO START
 N7420 V33=V33+V29
 N7430 KN310 G69 CUT LAYER 2
 N7440 V28=V28-V43 V33=V33+V29 V64=V64+22.5
 N7450 X20.4675Y50.4205Z-43 G69 ALIGN PT
 N7460 JN7300

N8000 G58"25 NOV 1983"
 N8005 G58"defocussed 2 mm above"
 N8010 G58"XTILT 30 DEG"
 N8015 G58"POWER=S700 (780 W)"
 N8020 G58"OVERLAP Y.1 Z.125"
 N8035 G58"PULSE 0.5 MS ON 1MS OFF"
 N8040 G58"VELOCITY=F800"
 N8045 G58"O2 SHIELDING 10 PSI"
 N8065 M0

A.II.6 Program To Machine Convex Quad In Graphite

N9800 G69 CV-TILT/CONVEX QUAD V1.1(PULSED)* *21 NOV 83* R.HSU
N9805 G69 GRAPHITE/BASE FRAME ORIGIN AT PIVOT
N9807 G69 V3-V4 V18-V65 ARE USED X1ST=KN20 Y1ST=KN150
N9809 G69 SETUP*X~V31=V25*Y~V32=V27
N9811 G69 KN700=TRANSFORM KN1000=CAL VEC T
N9813 G69 V21=A V22=B V23=C RADIUS
N9815 G69 V25=XSTP V26=XLIM V27=YSTP V28=YLIM V29=ZSTP V30=ZLIM
N9820 G69 V31=CURX V32=CURY V33=CURZ V34=STRX V35=STRY V36=STRZ
N9825 G69 V37=OFSX V38=OFSY V39=OFSZ
N9827 G69 V46=THETA DEG V47=THETA RAD
N9833 G69 V48=TX V49=TY V50=TZ *TRANSLATION VEC
N9835 G69 V51 V52 V53*PASS PAR XYZ* V54V55V56*TRANSFORM XYZ*
N9840 G69 V57=PX V58=PY V59=PZ
N9850 G69 V63=PRERUN V65=DEFOCUS

N300 G69 LAYX1ST
N310 V32=V27
N320 KN1200
N330 M6

N378 G69CAL Y-Z MOV
N380 V52=V32 V53=V33 KN700 G90YV55ZV56
N390 V32=V32+V27 KN10002
N400 M6

N700 G69 TRANSFORMATION
N710 V54=V51+V48 G69 TRAN X
N720 V55=(V52*Q4(V47))-(V53*S(V47))+V49 G69 TRAN Y
N730 V56=(V52*S(V47))+(V53*Q4(V47))+V50 G69 TRAN Z
N740 M6

N1000 G69 CAL VECTOR T
N1010 V48=0 V49=0 V50=0
N1020 V51=V57 V52=V58 V53=V59 KN700
N1030 V48=V54 V49=V55 V50=V56
N1040 M6

N1198 G69 XLAY CV
N1200 G9XV54 G69 +X DIR
N1205 M100
N1210 XV26
N1215 M101
N1220 X(V26+V63)
N1225 G0
N1230 J(V28-V32)N1240
N1235 M6
N1240 KN380
N1245 G9XV26 G69 -X DIR
N1250 M100
N1255 XV54
N1260 M101
N1265 X(V54-V63)
N1270 G0
N1275 J(V28-V32)N1285
N1280 M6
N1285 KN380
N1290 JN1200

N10001 G92X0Y0Z0F850G90X0Y0Z-30M103M7
N10002 G58"CURY="V32" YLIM="V28" CURZ="V33
N9914 M6
N10005 JN7200
N10006 M99M98FZ200G90X-70Y-70
N9001 Z33.392G4X.8
N9902 M98
N9903 G92Z48.114M7

N7200 G69 MAIN PROGRAM SETUP
N7202 M101M103J(Q2(167))N7206 G69 IF RESET G67
N7204 JN7208
N7206 G67
N7208 M0

N7210 V3=700 V4=800 V21=0 V22=5 V23=0
N7212 V25=.1 V26=16 G69 X STEP/LIM
N7214 V27=.1 V28=6 G69 Y STEP/LIM
N7216 V29=.1 V30=0 G69 Z STEP/LIM
N7218 V31=0 V32=0 V33=-6 G69 CUR X-Y-Z
N7220 V34=0 V35=0 V36=-6 G69 START X-Y-Z
N7222 V37=0 V38=1 V39=-1 G69 OFFSET
N7224 V46=30 G69 X TILT ANGLE
N7226 V47=V46*P/180

N7228 V57=0 G69 PX
N7230 V58=-25 G69 PY
N7232 V59=-42.114 G69 PZ
N7234 V63=15 V65=-2 G69 PRERUN/DEFOCUS
N7250 G69*** END SET UP ***

N7300 KN1000 G69CAL VEC T
N7310 SV3FV4

N7320 V51=0V52=0V53=V36KN700G90X(V54-V63)YV55Z(V56+V65) KN10002
N7330 J(A(V33)-(V22+V29))N7350
N7340 V28=V38+V22-R((V22*V22)-(V33*V33))JN7360 G69 CURVE LIM
N7350 V28=V38+V22 M102
N7360 KN310 G69 X-LAYER
N7370 V33=V33+V29 J(V33+(V29+V30))N7410
N7380 V51=0V52=0V53=V33KN700KN10002 G69 MOV TO START
N7390 G90X(V54-V63)YV55Z(V56+V65)G5
N7400 JN7330
N7410 X0Y0Z-60 M103
N7420 M0

N8000 G58*21 NOV 1983*
N8005 G58*CONT VELOCITY - CONVEX QUAD (PUSLED)*
N8007 G58*DEFOCUSED -- FOCAL PLANE 2 MM ABOVE WORKPIECE*
N8010 G58*XTILT 30 DEG*
N8015 G58*POWER=S700 (780 W)*
N8020 G58*OVERLAP Y.1 Z.1*
N8035 G58*PULSE 0.5 MS ON 1MS OFF*
N8040 G58*VELOCITY=F800*
N8045 G58*CO2 SHIELDING 10 PSI*
N8050 G58*ORIENTATION -- (27 DEG CW FROM ZERO)*
N8055 G58*VELOCITY VECTOR AT 45 DEG TO E VECTOR*
N8060 G58*08
N8065 M0

A.II.7 Program To Machine Concave Quad In Graphite

N9800 G69 CV-TILT/CONCAVE QUAD V1.1(PULSED)* *21 NOV 83* R.HSU
N9805 G69 BASE FRAME ORIGIN AT PIVOT
N9807 G69 V3-V4 V18-V65 ARE USED X1ST=KN20 Y1ST=KN150
N9809 G69 SETUP*X~V31=V25~Y~V32=V27
N9811 G69 KN700=TRANSFORM KN1000=CAL VEC T
N9813 G69 V21=A V22=B V23=C RADIUS
N9815 G69 V25=XSTP V26=XLIM V27=YSTP V28=YLIM V29=ZSTP V30=ZLIM
N9820 G69 V31=CURX V32=CURY V33=CURZ V34=STRX V35=STRY V36=STRZ
N9825 G69 V37=OFSX V38=OFSY V39=OFSZ
N9827 G69 V46=THETA DEG V47=THETA RAD
N9833 G69 V48=TX V49=TY V50=TZ *TRANSLATION VEC
N9835 G69 V51 V52 V53*PASS PAR XYZ* V54V55V56*TRANSFORM XYZ*
N9840 G69 V57=PX V58=PY V59=PZ
N9850 G69 V63=PRERUN V65=DEFOCUS

N300 G69 LAYX1ST
N310 V32=V27
N320 KN1200
N330 M6

N378 G69CAL Y-Z MOV
N380 V52=V32 V53=V33 KN700 G90YV55ZV56
N390 V32=V32+V27 KN10002
N400 M6

N700 G69 TRANSFORMATION
N710 V54=V51+V48 G69 TRAN X
N720 V55=(V52*Q4(V47))-(V53*S(V47))+V49 G69 TRAN Y
N730 V56=(V52*S(V47))+(V53*Q4(V47))+V50 G69 TRAN Z
N740 M6

N1000 G69 CAL VECTOR T
N1010 V48=0 V49=0 V50=0
N1020 V51=V57 V52=V58 V53=V59 KN700
N1030 V48=V54 V49=V55 V50=V56
N1040 M6

N1198 G69 XLAY CV
N1200 G9XV54
N1205 M100
N1210 XV26
N1215 M101
N1220 X(V26+V63)
N1225 G0
N1230 J(V28-V32)N1240
N1235 M6
N1240 KN380
N1245 G9XV26
N1250 M100
N1255 XV54
N1260 M101
N1265 X(V54-V63)
N1270 G0
N1275 J(V28-V32)N1285
N1280 M6
N1285 KN380
N1290 JN1200

N10001 G92X0Y0Z0F850G90X0Y0Z-30M103M7
N10002 G58"CURY="V32" YLIM="V28" CURZ="V33
N9914 M6
N10005 JN7200
N10006 M99M98FZ200G90X-70Y-70
N9001 Z33.392G4X.8
N9902 M98
N9903 G92Z48.114M7

N7200 G69 MAIN PROGRAM SETUP
N7202 M101M103J(Q2(167))N7206
N7204 JN7208
N7206 G67
N7208 M0

N7210 V3=700 V4=800 V21=0 V22=5 V23=0
N7212 V25=.1 V26=16 G69 X STEP/LIM
N7214 V27=.1 V28=6 G69 Y STEP/LIM
N7216 V29=.1 V30=0 G69 Z STEP/LIM
N7218 V31=0 V32=0 V33=-6 G69 CUR X-Y-Z
N7220 V34=0 V35=0 V36=-6 G69 START X-Y-Z
N7222 V37=0 V38=1 V39=-1 G69 OFFSET
N7224 V46=30 G69 X TILT ANGLE
N7226 V47=V46*P/180

N7228 V57=0 G69 PX
N7230 V58=-25 G69 PY
N7232 V59=-42.114 G69 PZ
N7234 V63=15 V65=-2
N7250 G69*** END SET UP ***

N7300 KN1000 G69CAL VEC T
N7310 SV3FV4

N7320 V51=0V52=0V53=V36KN700G90X(V54-V63)YV55Z(V56+V65) KN10002
N7330 J(A(V33)-(V22+V29))N7350
N7340 V28=V38+R((V22*V22)-((-V22-V33)*(-V22-V33)))JN7360 G69
CURVE LIM

N7350 V28=V38+V22 M102
N7360 KN310 G69 X-LAYER
N7370 V33=V33+V29 J(V33+(V29+V30))N7410
N7380 V51=0V52=0V53=V33KN700KN10002
N7390 G90X(V54-V63)YV55Z(V56+V65)G5
N7400 JN7330
N7410 X0Y0Z-60 M103
N7420 M0

N8000 G58"21 NOV 1983"
N8005 G58"CONT VELOCITY - CONCAVE QUAD (PUSLED)"
N8007 G58"DEFOCUSED -- FOCAL PLANE 2 MM ABOVE WORKPIECE"
N8010 G58"XTILT 30 DEG"
N8015 G58"POWER=S700 (780 W)"
N8020 G58"OVERLAP Y.1 Z.1"
N8035 G58"PULSE 0.5 MS ON 1MS OFF"
N8040 G58"VELOCITY=F800"
N8045 G58"CO2 SHIELDING 10 PSI"
N8050 G58"ORIENTATION -- (27 DEG CW FROM ZERO)"
N8055 G58"VELOCITY VECTOR AT 45 DEG TO E VECTOR"
N8060 G58"08
N8065 M0

A.II.8 Program For Machining Workpiece With 2 Rotations

N9800 G69 "X-Y TILT/PATCH V1.1(PULSE-MOVE)" *7 JAN 1984* R.HSU
N9802 G69 PLATFORM 3" ABOVE SLIDER/5"F.L SALT LENS
N9803 G69 GOOD FOR POSITIVE X Y -Z ONLY
N9805 G69 ROT ABOUT X BY FI AND Y BY THETA
N9806 G69 TRANSLATE BY VECTOR T
N9807 G69 V18-V65 ARE USED X1ST=KN20 Y1ST=KN150
N9809 G69 SETUP "X" V31=V25 "Y" V32=V27
N9811 G69 KN500=MOV KN700=TRANSFORM KN1000=CAL VEC T
N9815 G69 V25=XSTP V26=XLIM V27=YSTP V28=YLIM V29=ZSTP V30=ZLIM
N9820 G69 V31=CURX V32=CURY V33=CURZ V34=STRX V35=STRY V36=STRZ
N9825 G69 V37=OFSX V38=OFSY V39=OFSZ
N9827 G69 V44=THETA DEG V45=THETA RAD
N9832 G69 V46=FI DEG V47=FI RAD
N9833 G69 V48=TX V49=TY V50=TZ *TRAN VEC
N9835 G69 V51 V52 V53*PASS PAR XYZ* V54 V55 V56*TRANSFORM XYZ*
N9840 G69 V57=PX V58=PY V59=PZ*POSITION VEC

N4 G69 FIRELASER
N5 M100
N6 JM200N6 G69WAIT FOR PULSE TO COMPLETE
N7 M101
N8 M6

N20 G67N5 G69 CUT LINE X MOV R-L
N25 V31=V25
N30 KN500 V31=V31+V25
N35 J(V26-V31)N30
N40 G67
N45 J(V28-V32)N55 G69 IF END LAYER
N50 M6
N55 KN380 G69 INC/MOV Y
N60 G67N5
N70 V31=V31-V25 G69 MOV L-R
N75 KN500
N80 JV31N70
N85 G67
N90 J(V28-V32)N100
N95 M6

N100 KN380
N110 JN20 G69 END

N150 G67N5 G69 CUT Y
N155 V32=V27
N160 KN500 V32=V32+V27
N165 J(V28-V32)N160
N170 G67
N175 J(V26-V31)N185
N180 M6
N185 KN500 V31=V31+V25
N190 G67N5
N200 V32=V32-V27
N210 KN500
N215 JV32N200
N220 G67
N225 J(V26-V31)N235
N230 M6
N235 KN500 V31=V31+V25
N245 JN150 G69 END

N300 G69 LAYX1ST
N310 V32=V27
N320 KN20
N330 M6

N340 G69 LAYY1ST
N350 V31=V25
N360 KN150
N370 M6

N378 G69 CAL INC Y/MOV X-Y-Z
N380 V32=V32+V27 KN10002
N385 KN500
N390 M6

N500 G69 CAL/MOV TO NEW POSITION
N505 V51=V31V52=V32V53=V33KN700G90XV54YV55Z(V56+V65)
N510 KN10002M6

N700 G69 TRANSFORMATION(RY*RX*T)
N710 $V54 = (V51 * Q4(V45)) + (V52 * S(V45) * S(V47)) + (V53 * S(V45) * Q4(V47)) +$
V48G69TRAN X
N720 $V55 = (V52 * Q4(V47)) - (V53 * S(V47)) + V49G69TRAN Y$
N730 $V56 = (-V51 * S(V45)) + (V52 * Q4(V45) * S(V47)) + (V53 * Q4(V45) * Q4(V47)) +$

V50G69TRAN Z

N740 M6

N1000 G69 CAL VECTOR T

N1010 V48=0V49=0V50=0

N1020 V51=V57V52=V58V53=V59 KN700

N1030 V48=V54V49=V55V50=V56

N1040 M6

N1500 G69 MOV TO START POS

N1505 V51=V34V52=V35V53=V36KN700

N1510 G90XV54YV55ZV56

N1515 M6

N10001 G92X0Y0Z0F850G90X0Y0Z0M103M7

N10002 G58"CX="V31F6.4" XLIM="V26F6.4" CY="V32F6.4" YLIM="V28F6.4"

CZ="V33F6.3

N9914 M6

N10005 JN7200

N10006 M99M98FZ200G90X-70Y-70 G69 SETUP ORIGIN IN BASE FRAME

N9901 Z35.466G4X.8

N9902 M98

N9903 G92X27.925Z48.114M7

N10007 X-7.4405Y50.3305Z-45.160M7 G69 ALIGNMENT PT.

N7200 G69MAIN PROGRAM SETUP

N7202 M101M103J(Q2(167))N7206

N7204 JN7208

N7206 G67

N7208 M0

N7210 V3=700 V4=1000 V21=0V22=5V23=0

N7212 V25=.1V26=2 G69 X STEP/LIM

N7214 V27=.1V28=2 G69 Y STEP/LIM

N7216 V29=.125V30=0 G69 Z STEP/LIM

N7218 V31=0V32=0V33=-2 G69CUR X-Y-Z

N7220 V34=0V35=0V36=-2 G69START X-Y-Z

N7222 V37=0V38=1V39=1 G69OFFSET

N7226 V44=30 V45=V44*P/180 G69Y TILT ANGLE

N7228 V46=30 V47=V46*P/180 G69X TILT ANGLE

N7230 V57=-27.925 G69 PX

N7232 V58=-25 G69 PY

N7234 V59=-46.114 G69 PZ

N7236 V65=0 G69DEFOCUS

N7300 KN1000 G69CAL VEC T
N7310 KN1500 G69MOV TO START
N7320 SV3FV4 M102

N7330 J(V33+(V29+V30))N7380 G69IF FINISH
N7340 KN310 G69CUT 1 X-LAYER
N7350 V33=V33+V29 G69INC Z
N7360 V31=V34V32=V35KN500
N7370 JN7330

N7380 KN1500
N7390 M103
N7400 M0 G69END MAIN

N8000 G58"7 JAN 1984"
N8005 G58"PATCH (PUSLE-MOVE)"
N8007 G58"-- FOCAL PLANE 0 MM ABOVE WORKPIECE"
N8010 G58"X TILT 30 DEG Y TILT 30 DEG"
N8015 G58"POWER=S700 (780 W)"
N8020 G58"OVERLAP Y.1 Z.125"
N8035 G58"PULSE 1 MS ON"
N8040 G58"SPEED=F1000 ON CNC"
N8045 G58"OXYGEN SHIELDING 2 PSI/LONG NOZZLE"
N8050 G58"ORIENTATION -- (27 DEG CW FROM ZERO)"
N8055 G58"TRANSLATION DIRECTION AT 45 DEG TO E VECTOR"
N8060 G58"08
N8065 M0